FAU Studien aus dem Maschinenbau 360

Ralf Merkl

Closed-Loop Control of a Storage-Supported Hybrid Compensation System for Improving the Power Quality in Medium Voltage Networks

FAU UNIVERSITY PRESS

Ralf Merkl

Closed-Loop Control of a Storage-Supported Hybrid Compensation System for Improving the Power Quality in Medium Voltage Networks

FAU Studien aus dem Maschinenbau

Band 360

Ralf Merkl

Closed-Loop Control of a Storage-Supported Hybrid Compensation System for Improving the Power Quality in Medium Voltage Networks

Dissertation aus dem Lehrstuhl für Fertigungsautomatisierung und Produktionssystematik (FAPS)

Prof. Dr.-Ing. Jörg Franke

Erlangen
FAU University Press
2021

Bibliografische Information der Deutschen Nationalbibliothek:
Die Deutsche Nationalbibliothek verzeichnet diese Publikation in der Deutschen Nationalbibliografie; detaillierte bibliografische Daten sind im Internet über http://dnb.d-nb.de abrufbar.

Bitte zitieren als
Merkl, Ralf. 2021. *Closed-Loop Control of a Storage-Supported Hybrid Compensation System for Improving the Power Quality in Medium Voltage Networks*. FAU Studien aus dem Maschinenbau Band 360. Erlangen: FAU University Press. DOI: 10.25593/978-3-96147-403-5.

Der vollständige Inhalt des Buchs ist als PDF über den OPUS-Server der Friedrich-Alexander-Universität Erlangen-Nürnberg abrufbar:
https://opus4.kobv.de/opus4-fau/home

Verlag und Auslieferung:
FAU University Press, Universitätsstraße 4, 91054 Erlangen

Druck: docupoint GmbH

ISBN: 978-3-96147-402-8 (Druckausgabe)
eISBN: 978-3-96147-403-5 (Online-Ausgabe)
ISSN: 2625-9974
DOI: 10.25593/978-3-96147-403-5

Closed-Loop Control of a Storage-Supported Hybrid Compensation System for Improving the Power Quality in Medium Voltage Networks

Regelung einer speicherunterstützten hybriden Kompensationsanlage für die Verbesserung der Spannungsqualität in Mittelspannungsnetzen

Der Technischen Fakultät
der Friedrich-Alexander-Universität
Erlangen-Nürnberg

zur
Erlangung des Doktorgrades Dr.-Ing.

vorgelegt von

Dipl.-Wirtsch.-Ing. Ralf Merkl

aus Bad Kissingen

Als Dissertation genehmigt
von der Technischen Fakultät
der Friedrich-Alexander-Universität Erlangen-Nürnberg

Tag der mündlichen Prüfung:	23.10.2020
Vorsitzender des Promotionsorgans:	Prof. Dr.-Ing. habil. Andreas Paul Fröba

Gutachter:	Prof. Dr.-Ing. Jörg Franke
	Prof. Dr.-Ing. habil. Christian Rehtanz, TU Dortmund
	Prof. Dr.-Ing. Dirk Westermann, TU Ilmenau

Vorwort

Die vorliegende Arbeit entstand während meiner Tätigkeit als wissenschaftlicher Mitarbeiter am Lehrstuhl für Fertigungsautomatisierung und Produktionssystematik an der Friedrich-Alexander-Universität Erlangen-Nürnberg.

Herrn Prof. Dr.-Ing. Jörg Franke danke ich für die Freiheit zur Durchführung meiner wissenschaftlichen Arbeiten, das Vertrauen in meine Aktivitäten und die Gelegenheit zur Promotion.

Herrn Prof. Dr.-Ing. habil. Christian Rehtanz, Leiter des Instituts für Energiesysteme, Energieeffizienz und Energiewirtschaft der Technischen Universität Dortmund, danke ich für die vertrauensvolle, gemeinsame Beantragung und Durchführung der Forschungsarbeiten im Projekt HYBKomp, die stets wohlwollende Begleitung meiner Aktivitäten, die inspirierenden Dialoge und die Übernahme des Korreferrats.

Herzlich bedanke ich mich auch bei allen Wissenschaftlerinnen und Wissenschaftlern, mit denen ich zusammenarbeiten durfte. Herrn Prof. Dr.-Ing. habil. Christian Weindl danke ich für die Unterstüzung über mein Studium hinaus und den stetigen, freundschaftlichen Austausch. Den Kollegen und Freunden Timo Kordass, Julian Praß, Eva Bogner, Johannes Bürner, Lukas Baier, Thomas Braun und Adrian Fehrle danke ich für kreative Impulse, Unterstützung und akademische Diskurse. Björn Bauernschmitt, Michael Steglich und Willi Horenkamp von der Technischen Universität Dortmund danke ich für die konstruktive Zusammenarbeit bei Beantragung und Bearbeitung des Projekts HYBKomp. Friedmann Eppelein und Marco Krasser danke ich für fachlichen und freundschaftlichen Rat.

Auch allen Studierenden, deren Arbeiten wertvolle Beiträge zu den durchgeführten Forschungsaktivitäten geleistet haben, danke ich vielmals. Besonders danke ich Martin Paulsburg, dessen vielfältige Talente, Fähigkeiten und Interessen den Rahmen des Möglichen erweitert haben. Ebenfalls danke ich Sergey Datsevic und Benjamin Brunner für ihr Engagement.

Besonderer Dank gilt meiner Partnerin Christiane, meinen Eltern und meiner Familie für die immerwährende, bedingungslose Unterstützung.

Bamberg, 19.12.2018 Ralf Merkl

Contents

List of Tables

List of Figures

Nomenclature

Acronyms

AC	-	Alternating current
ADC	-	Analog-to-digital converter
CHPP	-	Combined heat and power plant
CTI	-	Charge transfer interconnect, here a DC link
DC	-	Direct current
DG	kW	Dispersed generation
DSO	-	Distribution system operator
EHV	V	Extra high voltage, above 220 kV
FFT	-	Fast Fourier transform
FSR	-	Full scale range value of an analog-to-digital converter
GWh	kW	Gigawatt hour, corresponds to 10^3 kWh
HV	V	High voltage, between 60 kV and 220 kV
LSB	-	Least significant bit
LV	V	Low voltage, below 1 kV
MV	V	Medium voltage, between 6 kV and 30 kV
PLL	-	Phase locked loop
RES	-	Renewable energy source
RMS	-	Root mean square value
SoC	-	State of charge
THD_i	-	Total harmonic distortion of the current signal
THD_u	-	Total harmonic distortion of the voltage signal
THD	-	Total harmonic distortion
TSO	-	Transmission system operator
TWh	kW	Terawatt hour, corresponds to 10^6 kWh
VUF	-	Voltage unbalance factor
VCO	-	Voltage controlled oscillator

Greek Symbols

δa	m	Width of an air gap
η	-	Efficiency
η_{c}	-	Charging efficiency of a storage
η_{d}	-	Discharging efficiency of a storage
η_{p}	-	Efficiency of a fluid pump
η_{rt}	-	Round-trip efficiency of a storage
η_{s}	-	Efficiency of energy storage
λ_{f}	-	Darcy friction factor or flow coefficient
$\nu_i(t)$	-	Instantaneous value of a phase or signal component i at time t
ω	rad s^{-1}	Angular velocity
$\Delta\Psi$	V	Donnan Potential
ρ	kg m^{-3}	Volumetric mass density
ρ_{el}	kg m^{-3}	Volumetric mass density of the electrolyte
ρ_{g}	kg m^{-3}	Volumetric mass density of a gas
σel	S m^{-1}	Electrolytic conductivity
σe	S m^{-1}	Specific conductivity of the electrode material
τ	N m	Torque
ϑ_{e}	K	Temperature of the electrolytes
$\vartheta_{\mathrm{g,H}}$	K	Temperature of the gas mixture in the flywheel housing
ζ_{Ω}	V	Ohmic overpotential
ζ_{cc}	V	Ohmic overpotential of the current collector
ζ_{c}	V	Concentration overpotential of the cell
ζ_{e}	V	Ohmic overpotential of the electrolyte
ζ_{m}	V	Ohmic overpotential of the membrane

Roman Symbols

$\underline{a}$	-	Complex rotation operator
a	-	Parameter of the characteristic polynomial of a function
$\vec{\mathbf{B}}$	T	Magnetic flux density
b	-	Parameter of the characteristic polynomial of a function
$\mathrm{c_d}$	-	Drag coefficient
c	-	Parameter of the characteristic polynomial of a function
c	$\mathrm{mol\,m^{-3}}$	Molar concentration
c_{ec}	€ $\mathrm{W^{-1}\,h^{-1}}$	Energy capital cost
c_{pc}	€ $\mathrm{W^{-1}}$	Power capital cost
c_{vu}	-	Voltage unbalance coefficient
CAPEX	€	Capital expenditure
d_{P}	m	Diameter of a fluid pipe
E	J	Energy
$E(t)$	-	Error signal of a control loop or a PLL at time t
$E^{\ominus\prime}$	V	Standard electrode potential
$E^{\ominus}$	V	Formal potential, potential actually measured in an electrochemical cell
E_{kin}	J	Kinetic energy
E_{max}	W h	Maximum amount of energy to be accumulated in a storage, capacity
e_{r}	-	Eccentricity
e_m	$\mathrm{W\,h\,kg^{-1}}$	Gravimetric energy density
E_t	W h	Energy present in a storage at time t
e_V	$\mathrm{W\,h\,m^{-3}}$	volumetric energy density
F	$\mathrm{C\,mol^{-1}}$	Faraday constant
f	$\mathrm{s^{-1}}$	Frequency
$F(t)$	-	Transfer function of a filter or a control loop
$f\mathrm{lh}$	$\mathrm{s^{-1}}$	Frequency of the lowest harmonic order to be filtered

$f\mathrm{r}$	s^{-1}	Real signal frequency
$f\mathrm{s}$	s^{-1}	Sampling frequency
F_m	N	Magnetic force of a magnet or electromagnet
f_u	-	Unbalance factor
F_w	N	Weight of an object
G	$\mathrm{mm\,s}^{-1}$	Coefficient representing the balance quality grade of an object
g	$\mathrm{m\,s}^{-1}$	Gravity constant
$G^{\ominus}$	J	Standard Gibbs free energy
h	m	Hydraulic head
h_f	m	Hydraulic head due to friction
h_m	m	Hydraulic head due to geometry parameters
$H_r^{\ominus}$	J	Standard enthalpy of reaction
$\hat{I}$	A	Peak value of the current
i_PQ	-	Aggregated index of power quality
Im	-	Imaginary part of a complex number
I_c	A	Current provided for compensation of power quality deviations
i_c	A	Current of the coil, for example in a magnetic bearing
I_g	A	Load current of the grid
I_RMS	A	Root mean square value of the current
I_sh	A	Shunt current within a redox flow battery
I_s	A	Current exchanged with the superordinate voltage level
k_f	-	Pipe friction coefficient
k_l	-	Loss coefficient in dependence of the geometry
l_P	m	Length of a fluid pipe
l_r	m	Height of the flywheel rotor
M	$\mathrm{kg\,mol}^{-1}$	Molar mass
m_r	kg	Mass of the flywheel rotor
n	$\frac{1}{60}\mathrm{s}^{-1}$	Number of revolutions per minute

n	mol	Amount of a substance
n_{ADC}	-	Number of steps of an analog-to-digital converter
N_{b}	-	Basic order of a filter
N_{c}	-	Number of windings of a coil
N_A	mol^{-1}	Avogadro constant
OPEX	€	Operational expenditure
Δp_{f}	Pa	Pressure drop due to friction
$\mathrm{d}PQ_{\mathrm{i}}$	-	Instantaneous deviation of power quality parameter i
P	W	Active power
P_{AMB}	W	Power for operation of the axial magnetic bearing
p_{a}	Pa	Ambient gas pressure
P_{c}	W	Charge rate of a storage, charge power
P_{d}	W	Discharge rate of a storage, discharge power
P_{FP}	W	Power for operation of the fluid pump
$P_{\mathrm{g,p}}$	W	Predictable or controllable generation power of the grid
$P_{\mathrm{g,t}}$	W	Total generation power of the grid
$P_{\mathrm{g,u}}$	W	Unpredictable and uncontrollable generation power the grid
P_{GF}	W	Losses due to gas friction
p_{H}	Pa	Gas pressure within the flywheel housing
$P_{\mathrm{L,SB}}$	W	Stand-by power loss
$P_{\mathrm{l,sc}}$	W	Load of metered special contract customers of the grid
$P_{\mathrm{L,SD}}$	W	Power loss due to self discharge
$P_{\mathrm{l,t}}$	W	Total load of the grid
P_{L}	W	Power loss
P_{RMB}	W	Power for operation of the radial magnetic bearing
P_{VP}	W	Power for operation of the vacuum pump
p_m	W kg^{-1}	Gravimetric power density

p_{Q_i}	-	Power for compensation of power quality parameter i
p_V	$\mathrm{W\,m^{-3}}$	volumetric power density
$\dot{V}_\mathrm{P}$	A s	Volume flow rate in a fluid pipe
Q	W	Reactive power
Q_1	W	Displacement reactive power
Q_CTI	A s	Electric charge present at the charge transfer interconnect (CTI)
Q_C	A s	Electric charge present at a capacitor with capacity C
Q_D	W	Distortion reactive power
Q_el	A s	Electric charge
Q_i	-	Dimension-less quality indicator of parameter i
Q_M	W	Modulation reactive power
Q_U	W	Unbalance reactive power
Re	-	Real part of a complex number
R	$\frac{\mathrm{kg\,m^2}}{\mathrm{s^2\,mol\,K}}$	Gas constant
R	Ω	Electrical resistance
r_1	m	Outer radius of a hollow cylinder
r_2	m	Inner radius of a hollow cylinder
R_ch	Ω	Electrical resistance of cell supply lines
R_c	Ω	Internal cell resistance
R_ext	Ω	Electrical resistance of external hydraulic components
R_m	Ω	Electrical resistance of lines and manifolds
Re	-	Reynolds number
S	W	Apparent power
$S_r^\ominus$	J	Standard entropy of reaction
t	s	time
$\hat{U}$	V	Peak value of the voltage
U_OCV	V	Open circuit voltage of a battery cell
U_RMS	V	Root mean square value of the voltage

U_r	V	Reference value of the voltage
u_i	m s^{-1}	i-component of veclocity $\vec{u}$
$\dot{V}_\mathrm{l}$	m^3 s^{-1}	Volume flow due to leakage
$\dot{V}$	m^3 s^{-1}	Volume flow
$\dot{V}_\mathrm{e}$	m^3 s^{-1}	Volume flow of the electrolyte
V	m^3	Volume
v	m s^{-1}	Velocity
v_f	m s^{-1}	Flow velocity of a fluid
v_P	m s^{-1}	Flow velocity of the fluid within a fluid pipe
$\overline{X^2}$	-	Quadratic mean value of an arbitrary, time-discrete signal
$\overline{X}$	-	Mean value of an arbitrary, time discrete signal
$x(t)$	-	Input signal of a control loop or a PLL at time t
X_RMS	-	Root mean square value of an arbitrary, time-discrete signal
Z	Ω	Impedance
Z_g	Ω	Equivalent impedance of the grid
Z_l	Ω	Equivalent impedance of the network branch, to which the compensator is connected
Z_max	-	Maximum digital value of an analog-to-digital converter

1 Introduction

Subject of this thesis is the elaboration, analysis and evaluation of a control concept of a device for the simultaneous provision of various system services and of an approach for the energy and power management of the energy storage of this plant. A focal point of the examination is the determination of the present level of power quality, the derivation of suitable power quality indicators as well as the power distribution to the system services. In addition, an important subject of the research activities is modeling of the investigated storage technologies, combining them to a hybrid storage system and evaluating it.

1.1 Initial situation and presentation of the problem

System services in the electricity supply are necessary for proper functioning of the system and determining the quality of supply. They are provided by the grid operator in addition to transmission and distribution of electrical energy. According to the definition, a subdivision of system services into frequency stability, voltage stability, supply restoration and operational management of the grid is possible. [1, 2] Ensuring frequency stability is a task of the transmission system operators (TSO) by the means of primary balancing power, secondary balancing power and minute reserve power. Plants with a rated power above 100 MW are obliged to provide primary balancing power. Smaller generation units may participate by agreement with the TSO. In the future, decentralized plants, loads and storages in distribution networks could also contribute to frequency stability [3]. Each grid operator is responsible for ensuring voltage stability within the permissible voltage band. To provide the demand of reactive power of the grid and the loads, generation plants, reactive power compensation plants, transformer staging and changes in the grid topology are available. Up to now, distribution grid operators (DSO) draw the majority of the required reactive power from the transmission grid. The scope of the obtainable reactive power is contractually agreed between the TSO and the DSO. Due to the increasing decentralized feed-in, it is aimed at flexibly involving plants within the distribution grid in ensuring voltage stability by providing reactive power. Thus, the required reactive power is partially generated locally and does not have to be drawn from the superordinate grid level [4]. It is possible to provide reactive power by generation plants, reactive power compensation systems, adjustable power transformers and changes in the network topology. At present, local measures of supporting voltage stability are still in the experimental stage. [4, 5, 6] Although the task of providing system services is in the responsibility of TSO, impairments of power quality are caused predominantly on distribution network level. Accordingly, it appears reasonable to locate measures and the responsibility for ensuring a suitable level of power quality at this network level. In particular, this concerns impairments of the signal form of voltage and current signals, the balancing of demand and generation as well as the provision of reactive power.

In Germany, the share of electricity generation using renewable sources is expected to increase from 30 % today to at least 35 % in 2020 [7]. The German government plans to use at least 80 % renewable energies for generation of electricity by 2050. According to studies by the Federal Environment Agency, however, it is possible to cover the total German electricity demand from renewable sources only by 2050 [8]. The planned phasing out of lignite-fired power plants for the generation of electrical energy by 2038, which accounted for 24.1 % of the total electricity generated in 2018, is expected to significantly reduce carbon dioxide emissions of electricity generation [9]. In order to achieve these ambitious targets, a variety of renewable generation plants, load management services and system services are to be coordinated. In order to compensate for fluctuations in renewable energy sources, it is necessary to couple these technologies with energy storage systems [10]. Decentralized, grid-integrated storage systems have already been investigated in various research projects. Predominantly conventional storage systems for supporting the grid by drawing and feeding active power have been subject of investigation [11, 12]. The use of small decentralized storage systems is politically promoted to increase private consumption of photovoltaic system operators and aims in particular at energy balancing in the range of minutes to hours. Lithium-ion batteries, which are still too expensive for widespread use in distribution networks with costs between 600 € and 2.500 € per kilowatt hour, are the major storage technology used. In addition to small decentralized storage systems, large central battery storage systems are currently being installed with the aim of compensating for power fluctuations by providing primary control power, which is traded at attractive market prices. As a consequence of the installation of large battery storages, however, the average capacity charge for primary control power has dropped from 2.657 €/MW in 2016 to an average below 2.000 €/MW. [13, 14]

Hybrid storage systems, which provide supplementary system services in addition to active power injection, have not yet been exhaustively examined. A combination of storage technologies with different, complementary properties, has been considered in a variety of cases yet, for example by combining a lithium-ion storage and a redox flow battery. Available concepts differ in terms of controlling the storages. [11, 15, 16] The combination of a vanadium redox-flow battery and a flywheen storage has been investigated regarding wind energy integration into microgrids [17]. Single-phase earth faults are by far the most frequent cause of faults in medium-voltage networks. Those earth faults are present, if a conductive connection of a conductor and the earth arises due to isolation damage. Common reasons for isolation damage of cables are mechanical damages caused by construction works or malfunction due to dielectrical stress. A quick error detection and correction is crucial in order to prevent the fault from spreading, causing damage and personal injury. The type of handling earth faults in three-phase systems depends on the way in which the neutral point is connected to earth. The neutral point can be operated isolated, directly earthed, low-impedance earth, or connected to earth via an arc suppression coil. Conventional arc suppression coils are designed to compensate for the capacitive earth-fault current of the 50 Hz fundamental oscillation. If voltages and currents in the network are affected by harmonics, the earth fault current often also features harmonics that cannot be adequately compensated by conventional arc suppression coils. Depending on the network situation, the limit value for the automatic extinction of an arc caused by an earth fault may already be exceeded [18]. The use of converters to supplement or replace earth fault compensation systems has already been investigated using an adaptive compensation controller for earth fault compensated high-voltage networks [19]. In addition, harmonic components in the residual current are reduced using a three-phase converter for compensating the voltage harmonics in the grid [20].

A large number of studies has been carried out yet in which different types of converters, for example unifying power controllers (UPFC), have been used to improve power quality [21, 22]. For example, a static synchronous compensator (STATCOM) was used to compensate for voltage fluctuations and flicker [23]. Inverters of renewable power plants were used as STATCOM, for example when the plant is inactive [24] or in addition to regular operation [25]. Power quality improvement using the converters of renewable plants is also possible according to the voltage injection method in order to adjust the power factor [26]. In other cases, additional power converters were investigated at the connection point of renewable generation plants, for example to compensate for reactive power and power factor correction [27]. Also, a unified power quality conditioner was used to compensate current harmonics, current unbalance, load reactive power, voltage sag, voltage swell and voltage interruption, including an energy storage system consisting of battery storage and super capacitor [28]. Other approaches, in which a hybrid energy storage system with a UPFC to improve the voltage quality was investigated, referred to small island grids [29]. PV battery storage systems for the provision of additional functionalities in industrial networks have also been considered [30]. While the majority of studies focuses on the investigation of special converter types and converter topologies, the application of commercial components receives less attention. Therefore, the present work considers the composition of a device from available components using their proprietary functions.

In comparison to other, already examined approaches, the system serves to influence the voltage quality at the transfer point to the superimposed network level. Depending on the present requirements, the converter of the system is used for different purposes such as the storage and feed-in of active power, the compensation of different types of reactive power and other services. The system is tuned using current measured values for the existing voltage quality as well as load and feed-in forecasts of the grid. Especially for the storage of active power, the plant is provided with a storage system that is operated with maximum efficiency. Storage operation is based on measurable efficiency variables of the stores, which depend on power values as well as the state of charge. Thus, the presented approach allows the integration of arbitrary energy stores.

Reliable operation of electrical networks requires various prerequisites, equipment and system services. The demand for system services is rising due to an increased level of decentralized feed-in as well as power electronic components at producers, energy storages and consumers. Within this thesis it is investigated, which system services can be provided by an integrated device.

1.2 Structure of thesis

After the relevance of the research work was indicated with reference to challenges posed by the transition to an electrical energy supply based on renewable energy sources, in the following **chapter 2** basics of the electrical energy supply and the structure of electrical transport as well as distribution networks are introduced. Structure and properties of the medium-voltage distribution network are presented. Furthermore, definitions and standards of power quality are elaborated. Subsequently, phenomena of power quality disturbances are described. Available system services are explained which are used to ensure reliable network operation and limit the fluctuation of relevant power quality parameters to the permissible range.

In order to enable a continuous adjustment of the behavior of a system that simultaneously provides various system services, according to the present parameters of power quality, it is necessary to observe and analyze the signals within the electrical network using methods of digital signal processing. **Chapter 3** therefore presents approaches for understanding the processes in three-phase AC systems and elucidates the procedure for digitizing analog input signals. In addition, algorithms enabling spectral analysis of digitized signals are introduced and basic constructs of control engineering required for control of the plant to be developed are delineated. In addition, an overview of available energy storage technologies is provided, which includes a characterization based on key performance indicators.

Chapter 4 presents the structure of the hybrid compensation system. Requirements for functional groups as control, signal processing, power electronics and storage system are presented. Models of the storage technologies used within the hybrid storage system, a vanadium redox flow battery and a flywheel storage system are elaborated. Furthermore, the electrical connection of the storages with the grid power converter of the plant is described.

Applicability of selected methods for determining relevant parameters of power quality is verified in **chapter 5**. It is shown how effective values, frequency, phase angle, unbalance and harmonic spectrum are calculated reliably and accurate. Based on these quantities, the behavior of the grid converter of the system is determined by elaborating an approach for distribution of the available power of the converter to individual system services.

In **chapter 6** an approach for combining long-term energy management of the storage system with short-term power distribution is developed. For this purpose, functional interrelationships are developed, by means of which energy quantities are translated into target values of power. Subsequently, using the developed storage models, it is shown how a particular target value of power is distributed to the storages of the hybrid storage system with the highest possible efficiency. The presented approaches are evaluated by comparing the efficiencies and the state of charge.

The thesis concludes with a critical appraisal of the results, a summary of the topic and an outlook for further need for research.

2 Electrical energy supply and power quality

The term electrical energy supply covers all areas of handling electrical energy, from generation via transport and distribution to application for a wide variety of purposes. The electrical energy supply is considered as a value chain. Main activities are the provision of energy sources, the generation of electrical energy, its transport and distribution and finally its application. In the introduction it was postulated that the transition to an electrical energy supply based on renewable energies increases its volatility, has effects on the quality of supply and requires the introduction of measures to increase quality. Therefore, it is examined how renewable power plants and power electronic devices affect the energy supply, what is meant by the term power quality and which phenomena of power quality deviation are known.

2.1 Electrical energy distribution

The German electrical energy supply system is integrated into a supranational association of the European Network of Transmission System Operators for Electricity (ENTSO-E). In total 36 European countries are comprised and 43 TSO are involved as members in ENTSO-E. Figure 1 a visualizes the countries involved in ENTSO-E and subdivides them into the regional groups continental Europe (dark green) Nordic (light green), Baltic (black green), United Kingdom (dark orange) Ireland (orange).

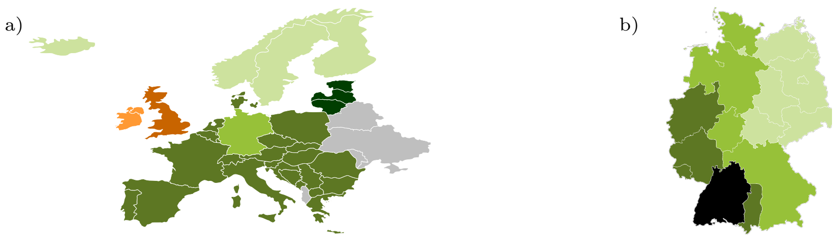

Figure 1: Overview map of the regional groups of the European Network of Transmission System Operators for Electricity (ENTSO-E) (a) and visualization of the control zones in Germany of Transnet BW (black green), amprion (dark green), Tennet (green) and 50hertz (light green) (b)

In Germany, the electrical energy supply system is divided into four control zones (Fig. 1 b), each of which is in responsibility of a TSO. In each control zone, various DSO distribute electrical energy to the customers. In 2018, a total of 888 DSO were registered with the Federal Network Agency.

2.1.1 Voltage levels of transmission and distribution grids

The electrical energy generated in the power plants is transported and distributed to consumers predominantly via an extensive alternating current (AC) network of lines, switchgear and transformers. Direct current (DC) grids represent a further technical option of transporting and distributing electrical energy. For high power transmission over large distances, in particular high voltage direct current (HVDC) systems are advantageous [31]. Aside from individual pilot projects, for example for connecting offshore wind farms, HVDC today has little relevance for german electricity transport and distribution. In fact, the existing infrastructure for the transmission and distribution of electrical energy consists of an AC system, in which four voltage levels are distinguished as visualized in Fig. 2 a. The topmost grid level is the extra-high voltage (EHV) grid with a voltage range between 380 kV and 220 kV, which serves primarily for national and international energy exchange as well as for transmission of electrical energy from large power plants to subordinate grids. In some cases, consumers with extraordinarily high power input are also supplied by the EHV grid.

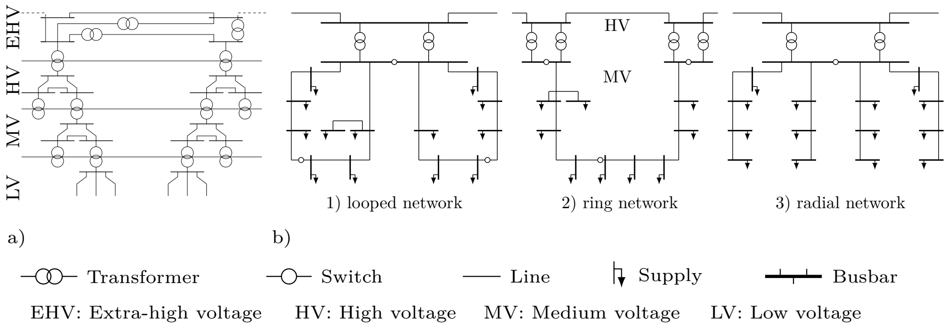

Figure 2: Voltage levels in electrical networks (a) and basic topologies of medium voltage grids (b) [32]

As a second level of electrical energy distribution, high-voltage (HV) networks with a voltage range between 60 kV and 110 kV are used for of both transmission and regional distribution, known as primary distribution. Conventional small and medium-sized power plants are connected to the high-voltage level as well as special contract customers as industrial customers and municipal utilities with significant power input [33]. As a next lower network level, medium-voltage (MV) networks constitute the secondary distribution layer with voltages in a range between 1 kV and 60 kV. The most common voltages are 10 kV and 20 kV. Main tasks of medium-voltage level are supply of local low voltage distribution networks with voltages between 230 V and 40 V as well as supply of special contract customers. Low-voltage (LV) networks represent the lowest network level and supply households, agriculture, small commercial enterprises and other customers. [33]

2.1.2 Medium voltage grids for local distribution

In the recent past medium voltage grids obtained electrical energy from superimposed grids on high voltage level and distributed the electrical energy to subordinate low-voltage grids. Today, renewable plants, cogeneration plants and other plants with a rated power between several kilowatts and a few megawatts are installed within MV grids. Further, even smaller plants feed electrical energy into the subordinate low voltage grids. Accordingly, multi-directional energy flows occur within MV grids. Typical topologies of MV grids are radial networks, ring lines or looped networks as visualized in Fig. 2 b. Radial networks represent the most simplistic network structure, as they consist of one or more stubs connecting the transformer station to sub-stations along the line. As there is only one supply path between the loads and transfer station, radial networks represent an unfavorable network topology with regard to the continued operation of the network in the event of a fault. From the perspective of the transfer station, on occurrence of a fault the sub-stations after the fault location are cut off from supply until suitable repair measures have been implemented. The lack of redundant supply paths increases the risk of supply interruption, prolongs the necessary time for supply restoration and thus reduces overall supply reliability. Apparently, radial networks can be regarded poorly suited to supply network areas featuring high load density and high requirements regarding supply reliability. If both ends of a supply line are connected to the same transfer station, a looped network is present. Accordingly, for all substations, feeders and consumers connected alongside the supply line there are two transmission paths to the transfer station. In the event of a fault that does not affect the transfer station, the faulty line section is disconnected and the supply is continued. In ring networks one supply line connects two transfer stations. Several substations, consumers or feeders are connected along the length of the supply line. If switchgears are installed between all stations, in the event of a fault the fault location is disconnected from the line. As the line sections on both sides of the fault location are still connected to one transfer station, it is possible to continue supplying the rest of the network once the fault location has been disconnected. As two transfer stations are involved, supply reliability of ring networks is higher in comparison to looped networks. [32]

2.1.3 Key figures on electricity production and consumption

In 2017, a 541 terawatt hours (TWh) of electrical energy have been generated in Germany. Approximately 40.2 % of which are assigned to renewable plants and 59.8 % to conventional plants. The major share of electricity generated from renewable plants originates from wind turbines with a share of 20.2 %. Biogenic plants contributed 8.3 %. Photovoltaic systems accounted for 8.5 % of total generation and hydroelectric power plants contributed 3.2 %. Regarding conventional generation plants, lignite-fired power plants accounted for the largest share of 24.1 % of total generation. A share of 14.0 % was produced in hard coal-fired power plants and a share of 13.3 % was supplied by nuclear power plants. Gas-fired power plants contributed 7.4 %. [9]

2.2 Challenges of the electricity sector

The transition to an electricity supply based on renewable sources is concomitant to a structural change regarding type, behavior and location of the generating plants. Conventional steam power plants, fired by fossil or nuclear fuels and featuring a controllable power output are being replaced by large numbers of plants using renewable energies. Here, electricity generation depends on the availability of environmental factors. As a consequence, they are preferably built in areas with auspicious occurrence of the required environmental factors. Energy sources powering renewable plants commonly feature a low energy density or low power density. Therefore, those plants are characterized by relatively high spatial requirements. As a consequence, renewable plants are predominantly installed in rural areas. For these reasons, the term dispersed generation (DG) is used, which includes both renewable energy sources (RES) and cogeneration of heat and power plants (CHPP).

2.2.1 Information on the distribution networks considered

Analysis is based on recorded power values of renewable plants, customers and the transfer stations of two rural distribution grids in northern bavaria. Both grids are located at approximately 50°2′ north.

In grid one, photovoltaic plants with a nominal power of 9.8 MW, wind power plants of 5.0 MW, biogas plants of 1.5 MW, biomass plants of 1.5 MW, natural gas CHPP of 1.6 MW and hydropower plants of 0.1 MW were installed. Moreover, approximately 12.000 households as customers with standard load, special contract customers with total maximum power of 12.8 MW and storage heaters with total nominal power of 10 MW were supplied. Within the observation period, the maximum value of the load recorded at the transfer station was 12.6 MW. Grid one includes both medium voltage level and low voltage level and is connected to the superordinate high voltage grid via two transfer stations. Both earth cables and overhead lines are present. The grid is operated as arc-suppression-coil-grounded network.

In grid two, which features a smaller spatial extent in comparison to grid one, photovoltaic plants with a nominal power of 10.1 MW, wind power plants of 30.1 MW, biogas plants of 1.5 MW and natural gas CHPP of 1.5 MW were installed. Approximately 13.000 customers with standard load and roughly 100 special contract customers featuring a total maximum load of 33 MW were supplied. Grid two is operated as cable network with low-impedance grounding. It is connected to the superimposed high voltage network via one transfer station.

2.2.2 Fluctuation and behavior of renewable power plants

Electricity generation using renewable energies is subject to a number of restrictions. As environmental factors as insolation and wind speed influence electricity production of renewable plants, generation is limited both seasonally and throughout the day. Accordingly, the number of possible full load hours differs considerably from the annual maximum of 8.760 hours. Analysis is based on recorded power values for all 15-minute time intervals during one year. Accordingly, 35.040 power values per year are present for all plants under consideration. Those power values are then sorted in descending order and the prevalence of individual power intervals is analyzed, which are introduced with an increment of 5 % relative to the nominal power of the plant. Photovoltaic plants in Germany may attain an annual utilization degree of 12.8 %, which is equivalent to 1.100 full-load hours annually. For illustration, in Fig. 3 a the power output of a real photovoltaic system is statistically evaluated over a period of one year. Here, the recorded power values of a field-installed photovoltaic plant with a rated power of approximately 500 kW are analyzed, which is located at 50°2′ north.

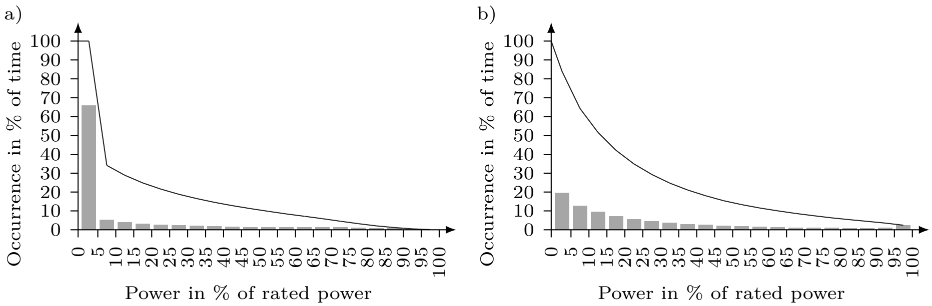

Figure 3: Histogram of fed in power compared to nominal power (gray) and load duration curve (dark gray) of a photovoltaic system (a) and a wind power plant (b)

For the analysis of the distribution of a plant's power output, the prevalence of certain power intervals in percent of rated power is depicted as a bar plot. The line visualizes the percentage of time during which a certain percentage of the rated power is produced. Immediate dependence on environmental factors is also observed for wind turbines. In Germany, for onshore wind power plants an annual utilization degree of approximately 18.8 % equaling 1.650 annual full-load hours is assumed. The distribution of power output per year is statistically evaluated for a wind turbine in Fig. 3 b with a nominal power of 3.1 MW based on power values recorded during the year 2017. A quite different behavior is observed for renewable plants, where the source of energy is controllable supplied to the plant or stored in the vicinity of the plant. Accordingly, there is no shortage of the energy source and thus the plant is operated similarly to a conventional plant. Statistical analysis is carried out for biogas plants (Fig. 4 a) and biomass plants (Fig. 4 b).

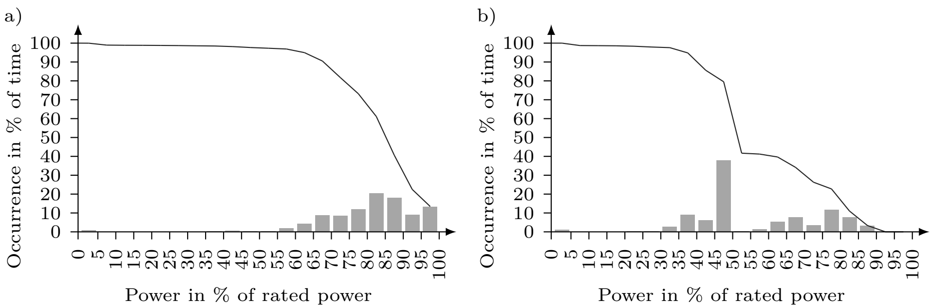

Figure 4: Histogram of fed in power compared to nominal power (gray) and load duration curve (dark gray) of a biogas plant (a) and a biomass plant (b)

The depicted prevalence of feed-in power indicates, that these plants are capable of continuously providing power in contrast to fluctuating plant types. Both biogas plants and biomass plants in particular are often operated as CHPP, where residual heat is used for heating purposes. Due to seasonal variations in heat requirements, CHPP are often not operated all year round. In order to assess the feed-in behavior of different plant types, it is not sufficient to consider only one individual plant per type. As depicted in Figure 5 a for wind power plants, the feed-in behavior of different plants differs considerably. Here, recorded power values are depicted for conventional wind turbines and weak wind turbines installed at different locations in northern bavaria at approximately 50°2′ north.

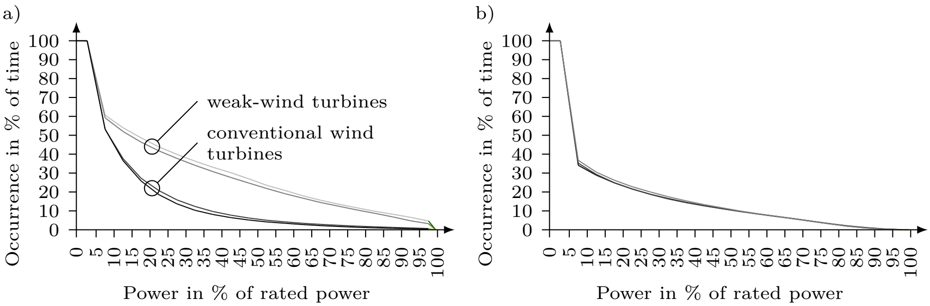

Figure 5: Load duration curves for various power plants of wind power plants (a) and photovoltaic systems (b) installed at different locations in northern bavarian distribution grids

Weak-wind turbines represent a particular plant specification, where the rotor is oversized in relation to the nominal power of the generator. Therefore, the power maximum of the plant is reached at lower wind speed. As a downside, for higher wind speeds the power is constant.

Figure 5 b visualizes the load duration curves of three photovoltaic systems located geographically close to another within the same medium-voltage grid and it becomes clear that the load duration curves of these systems are very similar. Nevertheless, it is possible that the instantaneous power of the systems differs significantly due to varying cloud cover and thus the impression created by the illustration of a uniform behavior of several of these highly fluctuating generation plants is to be contradicted. Biogas plants (Fig. 6 a) and biomass plants (Fig. 6 b), are operated continuously or seasonal [34].

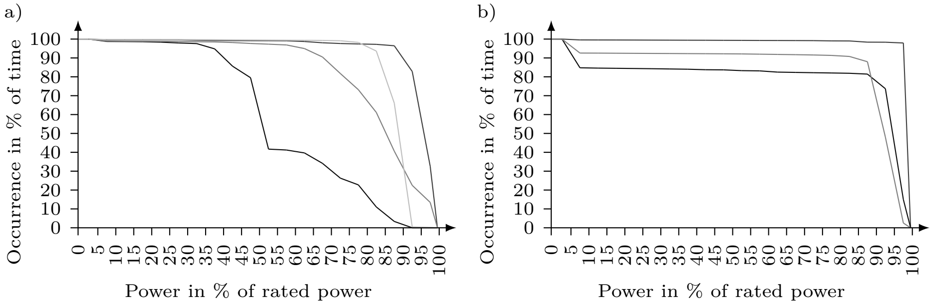

Figure 6: Load duration curves for different power plants of the same type for biogas plants (a) and biomass plants (b)

The investigation of the feed-in characteristics of different renewable plant types indicates that a continuous electricity generation is not to be expected, especially for photovoltaic plants and wind power plants. Due to significant installed capacity of these plant types, it is either required to adapt the load to the generation or to install storages.

2.2.3 Controllability of decentralized renewable power plants

If the power provided by all generating capacities within the two distribution grids under consideration is analyzed, both short-term fluctuations and seasonal fluctuations become obvious. As depicted in Figure 7 a and b predictable generating capacities reliably generate a base fed-in power of approximately 3 MW in both grids.

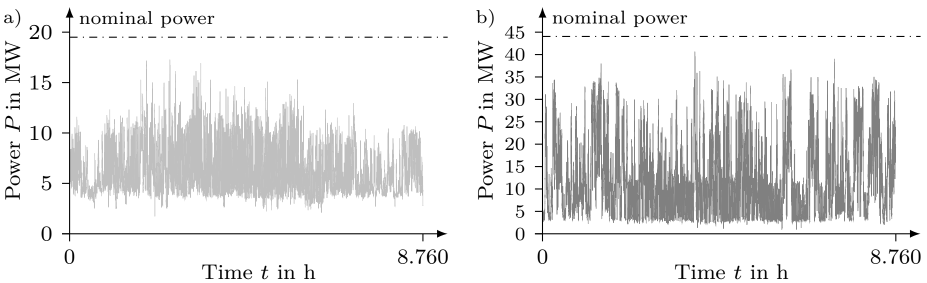

Figure 7: Interpolated course of the fed-in power of all generation plants in medium voltage grids with total generation capacity of 19.5 MW during 2014 (a) and 43.5 MW during 2017 (b)

By photovoltaic systems and wind power plants, additional power is provided whenever the required environmental factors are available. Renewable plants are usually operated without remote control by the control center and feed the available power into the grid. Accordingly RES are considered as negative loads, as there are no active control, communication, or other interaction options between those plants and the grid operator or the electricity market [35]. As an example, small photovoltaic systems feed electrical energy into the grid if the frequency is within a permissible frequency range. In the event of supply restoration, as soon as the frequency is within the permissible range again, a significant amount of feed-in power is provided uncontrollable. The fluctuation range of the output provided by fluctuating regenerative generation plants is large. Periods with significant supply alternate with periods of low supply.

2.2.4 Temporal structure and development tendency of the load

Within an arbitrary distribution grid, load is not constant but varies over time. When considering the feed-in power of fluctuating photovoltaic and wind turbine generators, it is noticeable that their installed power is several times greater than the load of the consumers in the medium-voltage networks under consideration. For this reason, the power drawn from the superordinate grid is partly reduced to zero in some cases or periods with regenerative generation surplus alternate with periods of excess demand. Therefore, for individual distribution grids a quite different load flow can be observed at the connection point to the superordinate grid. For the purpose of visualization, the load flow of two rural distribution grids is visualized over the period of a year based power values measured at the transfer station in 15 minute intervals. Both diagrams are based on data provided by distribution grid operators. In Fig. 8 a the load flow of grid 1 recorded during the year 2014 is visualized

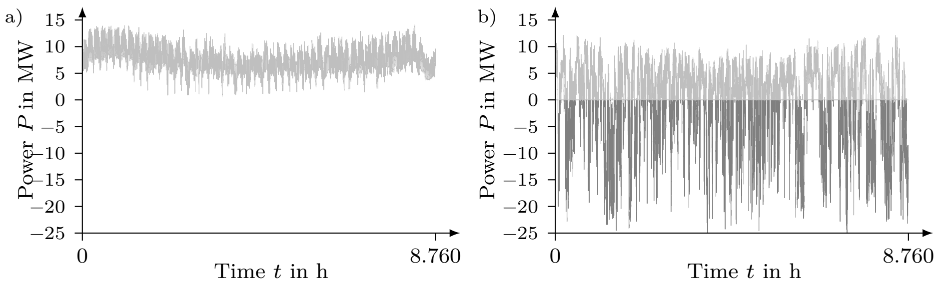

Figure 8: Load metered in the transfer stations of medium voltage grids during one year. Grid (a) with 19.5 MW of fluctuating generation capacity measured during 2014 and grid (b) with 43.5 MW measured during 2017

A substantially different load flow was recorded in a second rural distribution grid during the year 2017 as visualized in Fig. 8 b.

The fluctuations of the load flow measured at the transfer stations, however, are not only caused by variations of the fed in power, but due to the consumer behavior. Seasonal fluctuations are attributed to varying demands for electrical room heating, for example. Diurnal fluctuation are determined by typical periods of time for distinct human activities during a day or other requirements with conjunction to daytime. Diurnal fluctuations feature periodic nature, the typical load of certain customer groups is represented by standard load profiles. Those standard load profiles are available for different customer groups as for example regular households, households using electrical room heating, farms, dairy farms, small shops. Furthermore, a variation of diurnal load patterns is observed on different days of a week. In Fig. 9 a, the standard load profile for small shops (G4) and as a comparison, metered load profile of real small shops are visualized. Figure 9 b presents the standard load profile for bakeries (G5) and metered load profiles of real bakeries. Standardized load profiles depict load curves, whose integral corresponds to a certain amount of energy. For comparing the load of real consumers to standardized load profiles, all profiles are normalized regarding the amount of energy. [36, 37]

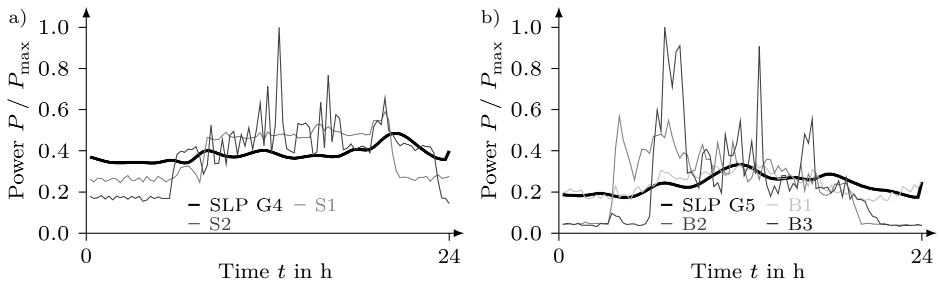

Figure 9: Comparison of stadardized load profiles (green, bold) and normalized metered consumption profiles of bakeries (a) and small shops (b) for 24 hours [37]

For example, working days feature a different load-time course in comparison to days of the weekend. In the available standard load profiles, diverging load patterns of different weekdays are included. In the past, those standard load profiles have been used by grid operators for load prognosis. Today, communication-capable smart meter enable online metering as well as generation of grid specific load profiles. When evaluating the metered load profiles of consumers, it is noticeable that the individual consumption behavior deviates considerably from the load profiles (Fig. 9 a and b). Accordingly, for comparable customers, the consumption of an equal amount of energy features completely different load curves. Despite the available forecasting possibilities, there is uncertainty about the instantaneous feed-in and load. Accordingly, unsteady behavior occurs at the transfer station to the superimposed grid level. As shown by the example of the medium-voltage networks, at the local level significant deviations between the electrical power generated and the electrical power required by the consumers occur. If it is aimed at using as much of the electrical energy generated by local regenerative generation plant as possible, either the demand is to be adapted to the generation or the energy is to be stored.

2.2.5 Analysis of the volatility of load and supply

In order to visualize the volatility of load and supply both distribution grids, data on fed-in power and load is analyzed graphically using box plots (Fig. 10). Analysis is based on measured values of plants, consumption metering of customers and the load flow recorded in the transfer stations of the aforementioned distribution grids.

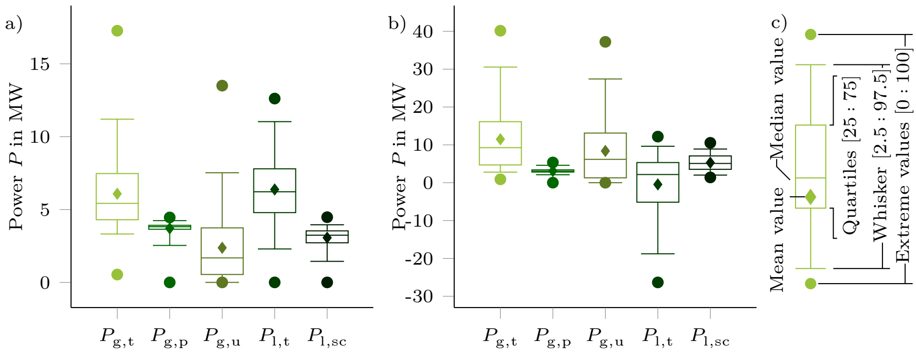

Figure 10: Distribution of total generation power $P_{g,t}$, generation power of predictable plants $P_{g,p}$, uncontrollable plants $P_{g,u}$ as well as the load in the transfer station $P_{l,t}$ and load of all metered special contract customers $P_{l,sc}$ in grid 1 for the year 2014 (a) and grid 2 for the year 2017 (b). In (c) elements of a boxplot are visualized, stating the enclosed range of samples as percentages

The box plot representation allows for a simple estimation of the fluctuation range. For each parameter considered, two points indicate the maximum value and the minimum value. The 97.5 % quantile as well as the 2.5 % quantile are plotted as so-called whiskers, connected transverse lines. A central rectangle marks the area between the 25 % quartile and the 75 % quartile. Within the rectangle, a transverse line marks the median of the distribution. The arithmetic mean is marked by a hash. For the distribution grids under consideration, the approximated total generation $P_{\mathrm{g,t}}$, the approximated generation from fluctuating generation plants $P_{\mathrm{g,u}}$ as well as the approximated generation from predictable generation plants $P_{\mathrm{g,p}}$ were investigated. In comparison, the load observed in the transfer stations of the grids $P_{\mathrm{l,t}}$ to the superimposed grid level as well as the distribution of the load of the special contract customers $P_{\mathrm{l,s}}$ are shown.

It becomes evident that in both cases the fluctuation range of generation from unpredictable feeders exceeds the fluctuation range of the load. At the same time, important distribution parameters of the generation power values, which are assumed to be normally distributed, are located at lower values in comparison to the load.

2.2.6 Circuit feedback by loads

If in an electric network in addition to purely ohmic loads capacitive loads, inductive loads and loads supplied by power electronic circuits are present, circuit feedback on the supplying network is observed. In particular, the non-sinusoidal currents caused by converter circuits cause reactive power and harmonics [38]. Power quality is significantly influenced by circuit feedback. It is obvious that the consumers, which are connected to the grid, influence power quality. For this reason, the permissible interference emissions of equipment and loads is limited according to the series of standards EN 61000-x-x [39]. For loads with switched-mode power supplies, signal characteristics of the current, which in some cases deviate considerably from the desired, ideal sinusoidal shape, are measured. As an example, the current of a switched-mode power supply (Fig. 11 a) and a flat screen (Fig. 11 b) were measured using a current sensor.

In general, these loads exhibit non-linear or time-variant current-voltage characteristics and thus cause voltage harmonics and voltage fluctuations in power supply networks. Such loads draw non-sinusoidal currents in systems of initially purely sinusoidal supply voltage, causing non-sinusoidal voltage drops at the impedances. Those voltage drops excite distortions of the sinusoidal shape of the mains voltage or to its harmonic content [40]. For consumers which are supplied with electrical energy by switching power supplies or that are otherwise connected to the grid via semiconductor circuits, virtually any current-time course is possible.

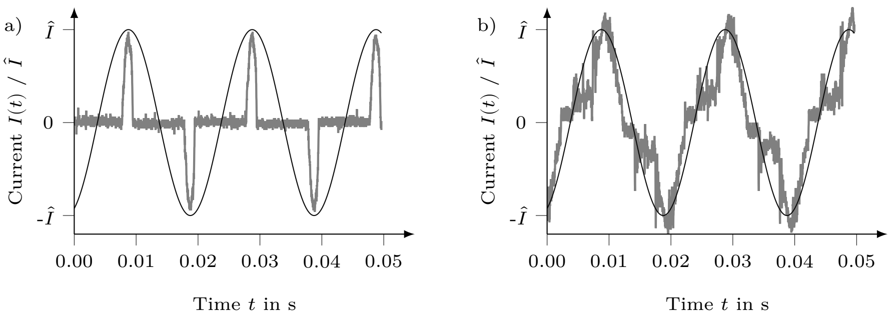

Figure 11: Measured current-time curve (gray) of a flat screen (a) and a switched-mode power supply (b) over a period of 0.05 seconds in comparison with ideal sine wave (dark gray)

Due to the large number of small consumers that are connected to the grid at the same time, there are overlaps and partial extinction of the disturbances. In general, circuit feedback is regarded as a disturbance of the network, which is caused by loads, consumers, equipment and other installations connected to the grid. Circuit feedback is introduced into the grid on different network levels and may affect other voltage levels.

2.2.7 Influence of power quality on ageing of equipment

The life of equipment in electrical networks is limited. As almost 70 percent of equipment failures are caused by insulation failures, ageing of insulation materials is a determining factor in equipment life [41]. This applies to underground cables, cable sleeves, cable terminations and transformer windings. Moreover, electrical generators and motors, both as equipment of electrical grids and as customer appliances, are affected. As most important ageing factors, electrical stress, thermal stress, mechanical stress and environmental stress are known. Distortions of the voltage as non-sinusoidal voltage signals due to superimposed oscillations favor the occurrence of partial discharges [42]. Transient events due to switching operations or lightning strikes also affect the ageing of insulation materials [43]. For transformers, harmonics cause increased losses in the iron core, increased copper losses in the windings, malfunctions of the protection relays, a reduced power factor and ageing of the insulation materials [44]. In addition, the occurrence of overvoltages also represents a strain on the insulation of equipment. Both transient overvoltages with short duration and large voltage amplitudes and longer voltage strokes with low amplitudes, caused for example by decentralized feeders, have a negative effect on equipment [45, 46]. Further stress of the insulation materials is caused by fluctuating electrical loads over time. Analogous to the electrical load, the power loss also occurs discontinuously and according to that the temperature of the equipment parts changes. This temperature change places thermal and mechanical stress on the insulation material.

2.2.8 Analysis of power quality in AC and DC grids

At first glance, DC power systems appear to be unaffected with power quality issues introduced for AC power systems. This assumption is caused by the circumstance, that in DC systems power is transmitted as pure active power according to equation (2.1).

$$P = U \cdot I \tag{2.1}$$

Voltage is regulated to the nominal value and is relatively constant. Therefore, load currents occur in dependence of the power required by the connected loads. As in DC power systems, currents and voltages are in-phase, no reactive power is present. Furthermore no inductive or capacitive phase shift occurs, as there is no periodic reversal of the voltages and currents. DC power systems are commonly single-phase systems consisting of a supply conductor and a return conductor. Accordingly, there is no voltage unbalance between phases. Moreover, frequency control is unneeded. Rather, it is possible to couple arbitrary AC power systems with different frequency using DC power systems. [31, 47, 48] Aside from the mentioned advantages in comparison to AC power systems, DC power systems feature several characteristic challenges regarding power quality. Those are voltage transients, harmonic currents, electromagnetic interference compatibility, inrush currents, DC bus fault currents, circulating currents or voltage unbalance in bipolar DC bus systems. [49, 50, 51] Voltage transients are caused by the AC grid or repeatedly connecting and disconnecting loads or feeders to the DC grid, such as large numbers of storages or photovoltaic plants [49, 52]. Resonant frequencies are caused by the presence of capacitors in converters connected to the DC grid and impedances of the DC bus cables [53]. Harmonic oscillations occur when one of the resonant frequencies is within the frequency range, in which one of the converters generates harmonics [49]. Capacitors comprised by converters and filters installed for electromagnetic compatibility (EMC) feature inrush currents, which occur on connection to the grid in uncharged condition. Inrush currents evoke voltage oscillations influencing other appliances connected the

DC bus [54]. Unbalance of the voltage in bipolar DC bus systems, as for AC systems, is caused by asymmetric distribution of loads or by feedback of the AC grid on the DC grid [49, 55, 56].

2.3 Definitions and standards of power quality

According to the Institute of Electrical and Electronic Engineers (IEEE) Standards 1100-2005 power quality is defined as the entirety of conducted electromagnetic disturbances in AC electrical supply networks and aims to ensure appropriate powering and grounding of sensitive electronic equipment [57, 58, 59]. Moreover, it is regarded as a concept of powering and grounding sensitive electronic equipment in a manner suitable for the equipment. The International Electrotechnical Commission (IEC) defines electromagnetic compatibility as the ability of an equipment or system to function satisfactorily in its electromagnetic environment without introducing intolerable electromagnetic disturbances to anything in that environment [60]. A further approach which includes performance and life expectancy of equipment as relevant dimensions defines power quality as a set of electrical boundaries that allows a piece of equipment to function in its intended manner without significant loss of performance or life expectancy [58]. Power Quality, also frequently referred to as Electric Power Quality (EPQ) in general is a generic term that summarizes issues of power quality, current quality, reliability of service, quality of power supply and other related topics [61].

Most cited and most important organizations at international level are IEC and IEEE. In IEC standards 61000-1-x an overview of standards and definitions regarding power quality is provided [62]. The standards 61000-2-x contains requirements regarding environmental compatibility levels for low-frequency conducted disturbances and signaling in public low-voltage power supply systems and in the standards 61000-3-x permissible interference limits of harmonics, voltage fluctuations and flickers are denoted [63, 64]. Techniques for testing and measurement of interferences, distortions and interference immunity are found in the standards IEC 61000-4-x [65]. Remedial measures for improvement of power quality are contained in the standards IEC 61000-5-x and in IEC 61000-6-x generic standards regarding immunity are delineated [66, 67, 68]. In the standards 1100-2005 the IEEE expresses recommendations for powering and grounding electronic equipment [57]. A comprehensive classification of power quality phenomena is provided in the standard IEEE 1159, where events related to power quality are categorized with regard to duration, magnitude and their spectral content [69]. Requirements regarding power quality for Europe are defined in the standards EN 50160, EN 61000-2-2 and EN 61000-2-4 [63, 70].

Power quality is mainly associated with the dimensions voltage stability, voltage waveform and continuity of power supply [71]. The best possible level of power quality and current quality in AC systems is achieved when voltage has an ideal sinusoidal shape of the fundamental at a constant frequency, all phases form a symmetric power system, and the root mean square (RMS) value of the voltage is constant over time. Magnitudes of all voltages as well as currents are constant at an operating point. For three-phase systems, a constant phase difference of 120° is observed and voltages and currents feature equal magnitude. Furthermore, the voltage within the system is supposed to be unaffected by changes of load and energy is provided reliably. Deviations from the ideal operating conditions or state variables represent disturbances and reduce quality.

2.4 Classification of power quality disturbances

Power quality is a general term covering a variety of disturbances in power systems. Most common categories of power quality events are transient voltage changes, long duration and short duration voltage variations (Fig. 12).

Power quality variations are variations of frequency, voltage and current magnitude, power factor, unbalance of voltage and current, voltage fluctuations and flicker as well as distortions of voltage waveform [72, 73]. The entirety of phenomena concerning deviations of voltage, current or frequency that affect customer equipment by failure or malfunction is attributed to problems of power quality [74]. In AC systems, PQ disturbances either affect voltage amplitude, frequency of the voltage signal or even both. Further distinction is possible by considering the temporal structure of the disturbances [61]. Power quality events are those occurrences which are limited in time and are considered as single events. Power quality variations on the other hand are phenomena with a permanent character and are not attributable to individual events as a cause.

2.4.1 Types of transient phenomena

Unforeseen, non-periodic mutations of the signal with finite life that occur within an interval of duration between 50 ns and 50 ms are referred to as transients. Impulsive and oscillatory transients are distinguished. In three-phase AC systems with separate neutral conductor transients are furthermore distinguished by their mode.

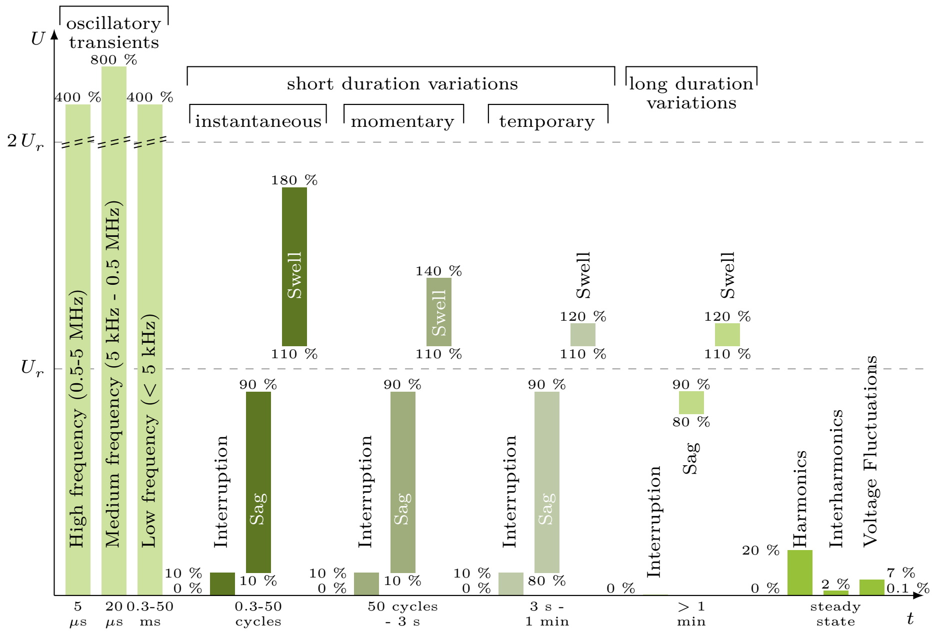

Figure 12: Systematization of PQ disturbances with regard to the voltage by magnitude and duration [72]

Common mode transients occur between line or neutral and ground, whereas normal mode transients affect line and neutral [75]. A characterization of transients is possible based on the waveform through analyzing for example peak magnitude, primary frequency or rate-of-rise of the transient signal components [76]. Transients are caused by lightning strikes, switching operations as well as switching events and may cause damage to equipment of electric energy supply, protective devices or insulation. Mitigation is possible using transient attenuators, avalanche diodes or surge arresters [72].

Impulsive transients (Fig. 13 a) are characterized as a sudden, onetime variation of the steady-state condition of voltage, current, or both that is unidirectional in polarity.

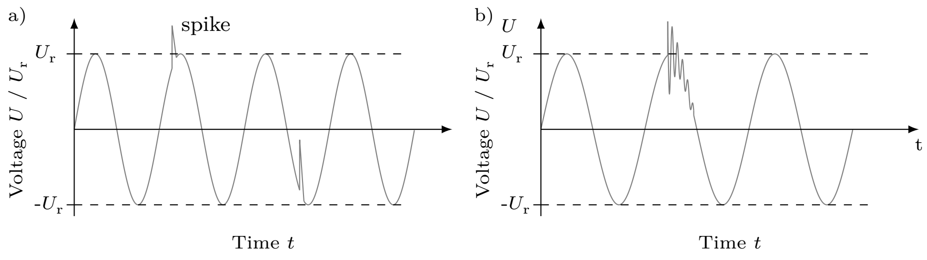

Figure 13: Visualization of impulsive transients (a) and oscillatory transients (b)

They are distinguished by their rise and decay times and are also detected by spectral analysis. As impulsive transients are short-time events and occur in high frequencies, their shape is often significantly altered by the equipment of the network so that their shape differs depending on the observation point. Due to dampening effects, for example in equipment acting as low-pass filters, transients are generally not transmitted over long distances. However, it is possible that impulsive transients cause an excitation of the network in its frequency range and thus evoke oscillatory transients. [75]

Oscillatory transients (Fig. 13 b) differ from the aforementioned in the fact that both positive and negative polarities occur within the fluctuation in rapid temporal change. This enables oscillatory transients like all oscillations to be described by their amplitude, duration and frequency spectrum. A distinction is made between three subcategories of oscillatory transients, in particular high-frequency transients, medium-frequency transients and low-frequency transients [75]. High frequency oscillatory transients feature a primary frequency in range greater than 500 kHz. For medium frequency oscillatory transients the primary frequency occurs in a range between 5 kHz and 500 kHz. If the primary frequency of the transient is below 5 kHz, a low frequency oscillatory transient is present.

2.4.2 Characteristics of superimposed harmonic oscillations

In general, harmonics are distortions of the waveform, which are attributed to sinusoidal oscillations at frequencies that are multiples of the system's fundamental frequency [72]. In particular, multiples $\nu = 1, 2, .., \infty$ of the fundamental frequency f_1 with $\nu = 1$ for which the system is designed are referred to as harmonics. Further, superimposed oscillations with non-integer conjunction to the fundamental frequency are called interharmonics. As a special case of the interharmonics, subharmonics include the frequency range below the fundamental frequency. Those oscillation components deviating from the fundamental cause distortions of the waveform. [72, 77, 78]

The periodic, sinusoidal voltage curve of the fundamental in AC systems is induced in the coils of generators, which rotate at a constant angular speed in a constant magnetic field. For a known angular velocity ω of such a system, the instantaneous value of the voltage $u(t)$ at a certain time t is calculated based on the peak value $\hat{u}$.

$$u(t) \quad = \quad \hat{u} \cdot \sin(\omega t + \varphi_{\mathrm{u}}) \tag{2.2}$$

Graphically, the emergence of the sinusoidal voltage represents the projection of a pointer with length of the peak value of voltage $\hat{u}$ onto the y-axis, which rotates around the origin of coordinates (Fig. 15 a).

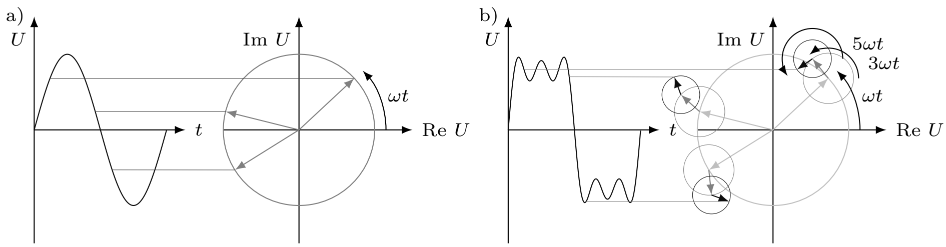

Figure 14: Emergence of a sinusoidal signal due to a rotating voltage pointer (a) and construction of a signal containing harmonic oscillations by superposition (b)

Harmonics, which are periodic oscillations with different periods in comparison to the fundamental frequency are represented as individual pointers with a corresponding RMS value and angular frequency. The resulting total voltage is determined by vector addition of the fundamental pointer and the harmonic pointers. The instantaneous value of the total voltage is calculated considering the time-dependent angles of the pointers (Fig. 15 b). Any time-dependent signal $x(t)$, repeating with period T, is represented exactly or approximately as a sum of trigonometric functions. This notation is called a Fourier series and formulated as follows [79]:

$$x(t) \quad = \quad c_0 + \sum_{\nu=1}^{\infty} c_\nu \sin(\nu\omega_1 t + \varphi_\nu) \tag{2.3}$$

Within this equation $\omega_1 = 2\pi f_1$ denotes the fundamental angular velocity of the observed signal and ν its harmonic order. Furthermore, c_0 denominates the direct component of the signal. For all harmonics $\nu = 1, 2, ..., \infty$ the expression c_ν indicates the amplitude and φ_ν the phase angle [77]. In order to asses the magnitude of total distortion, there are two essential indicators. Most commonly the total harmonic distortion factor THD is used, which is defined as the relation between the geometric sum of the quadratic means of all harmonics and the quadratic mean of the fundamental [78].

$$\mathrm{THD} = \frac{\sqrt{\sum_{\nu=2}^{\infty} X_n^2}}{X_1} \qquad \forall\, \nu = 2, 3, ..., \infty \tag{2.4}$$

Harmonics, which are integral multiples of the fundamental frequency, are caused by power electronic devices as well as loads and equipment, that feature non-linear characteristics of voltage and current as transformers, arc furnaces or induction furnaces. A further important source of harmonics are all kinds of power electronic feeders or loads connected to a grid as switched-mode power supplies or inverter-based feeders. Those harmonic distortions cause losses in electricity transmission, additional heating or malfunction of equipment, resonance excitation and faulty tripping of surge protection devices. Interharmonics with non-integer linkage to the fundamental occur in a broad frequency spectrum and are caused by static frequency converters, induction engines, welding machines or arc generators. Interharmonics interfere with power line carrier signals and evoke problems as resonance excitation, heating of equipment, torsional oscillation in rotating generators or flicker. Attenuation is possible using active and passive filters. [72, 80]

2.4.3 Notching due to switching or commutation

According to the IEEE notching is defined as a recurring power quality disturbance which is caused by the normal operation of power electronic devices by switching or commutating current from one phase to another [69]. Those actions cause a disturbance in the wave-shape of the signal which are referred to as notching (Fig. 15 a).

Thus, the normal voltage waveform is distorted and the shape of the deviation is of opposite polarity in comparison to the ideal waveform. Each notch last for a duration of less than 0.5 of the signal period. Notching is a phenomenon of power quality disturbance which shows characteristics of transients and harmonics. Similar to harmonics, notching is a steady-state phenomenon and is comprised in the harmonic spectrum of the signal. As for transients signal components of notching are not in the frequency range of common measurement and thus detection is not possible. [81]

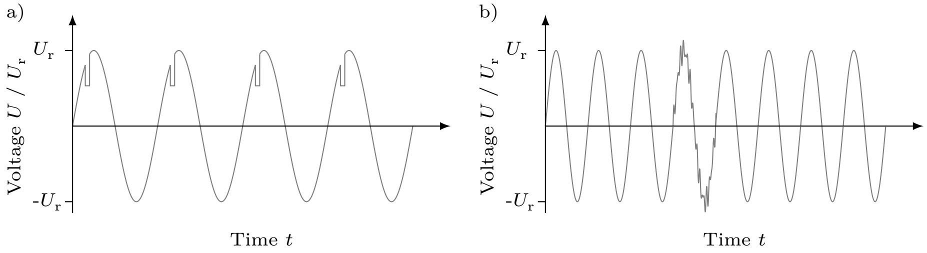

Figure 15: Visualization of an electric signal containing notching (a) and noise (b)

2.4.4 Noise caused by superimposed signals with high frequency

If unwanted signal components of high frequency are superimposed to the ideal waveform (Fig. 15 b), the signal is described as noisy. The noise components of the signal cover a wide frequency range up to 200 kHz. Noise is caused by electromagnetic waves in the wavelength range between 10 km and 1 cm, which occur for example in broadcasting, microwave appliances, radiation due to welding machines, arc furnaces and other electronic equipment. Furthermore, improper grounding is a reason for noise. Noisy power signals induce disturbances in sensitive electronic equipment, which disrupt the operation, but do not destroy the devices in most cases. In equipment of electronic data processing data loss as well as data processing errors may occur due to noise. [81, 82]

2.4.5 Voltage deviations and interruptions

If the voltage of a bus differs in comparison to its reference value, there is a voltage deviation. Those deviations are categorized based on the magnitude of the voltage deviation and the duration of the deviation as shown in Fig. 12. In general, short-term voltage deviations feature a period of up to 3 minutes. Any deviations exceeding this are referred to as long duration variations.

Voltage sag (IEEE) and voltage dip (IEC) describe a phenomenon of short-term variation of voltage waveform, which is characterized by reduced magnitude of the voltage (Fig. 16 a) [62, 69].

Caused by connecting loads, faults or switching the voltage of the network falls below the RMS value. Duration of voltage sags is usually between half a period of the fundamental and up to one minute. The voltage ranges between 10 % and 90 % of the RMS value. [61, 83]

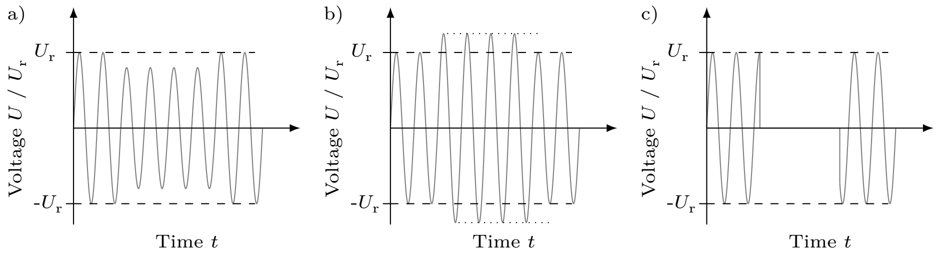

Figure 16: Visualization of a short-time voltage sag (a), a short-time voltage swell (b) and a short interruption (c)

During a voltage swell, the magnitude of voltage is increased for a short period (Fig. 16 b). In this case, the voltage ranges in an interval between 110 % and 180 % of the RMS value. Similar to voltage sags the duration of voltage swells is usually between 0.5 cycles of the fundamental frequency and 1 minute. Voltage swells are caused by system faults as single line-to-ground faults, disconnection of large loads or energization of capacitor banks with high capacitance. By voltage sags, the function protective systems and controls are disturbed. [61, 72, 83]

If the voltage drops to zero or a value below 10 % of the design specification, there is an interruption (Fig. 16 c). Interruptions with a duration of the voltage drop between a few milliseconds and a few seconds are short interruptions. Short interruptions are caused by switching of protection devices in order to decommission a defective section of the grid. Tripping of protection devices and data loss or malfunction of electronic data processing equipment are consequences of short interruptions.

2.4.6 Voltage fluctuations and flicker

Voltage fluctuations are variation in the amplitude with a duration that is longer than the period of the voltage signal (Fig. 17 a). The magnitude of voltage fluctuations is denoted as percentage of the voltage magnitude of the fundamental. They are caused by loads with varying power demand as starting drives, resistance welders and arc furnaces. Voltage fluctuations evoke alterations of rotational speed in drives and harm sensitive electronic equipment. [69, 84]

As a special case of short-term voltage fluctuation flicker (Fig. 17 b) are perceptible to the human eye as they cause a transient variation of the brightness of electrical lights.

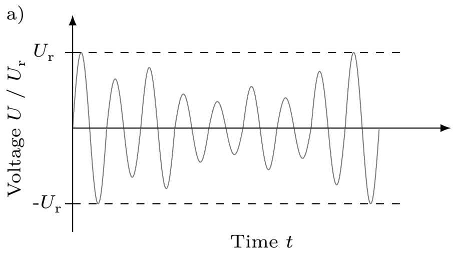

Figure 17: Illustration of a voltage fluctuation (a) and a flicker (b)

However, the visibility of a flicker depends on the magnitude of the voltage fluctuation, on the type of lamp and on the frequency of the signal component causing the flicker. Voltage fluctuations of flickers occur in a frequency range between 0.05 Hz and 35 Hz [84]. Flicker are caused by sudden variations of load or feed-in power and it is possible to asses loads and generating plants regarding their flicker potential. Facilities with high flicker potential are for example arc furnaces, welding devices, drives with high rated power and wind power plants [85]. Similar to other power quality disturbances, flicker are assessed based on the RMS magnitude of the flicker signal, which is usually denoted as percentage of the fundamental [75].

2.4.7 Voltage unbalance between the phases

If a deviation of the voltage magnitude of the different phases in AC systems occurs as visualized in Figure 18 a or the angle between the phases is changed (Fig. 18 b), voltage unbalance is present [84].

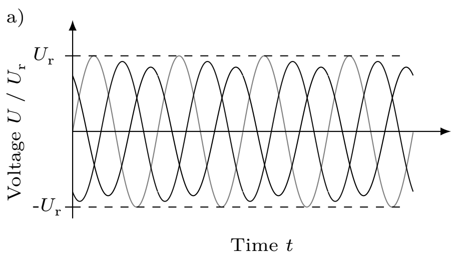

Figure 18: Illustration of voltage unbalance due to voltage deviations of the phases (a) and an angular deviation of 15 degrees for one phase (b)

Voltage unbalance, which is commonly also referred to as asymmetry or imbalance, is defined as the ratio of the negative or zero sequence component to the positive sequence component. As exact balance of voltages between the phases is difficult to achieve in real networks, slight unbalances are common. Major deviations, however, cause problems for polyphase loads as motors, adjustable speed drives and other. Voltage unbalance is caused by asymmetry of the equipment and asymmetry of the load. This includes single-phase connection of equipment and loads to phase conductor and neutral conductor or to phase conductor and earth, as well as the connection of industrial loads to two phase conductors, which is common for arc furnaces or welding systems. In distribution grids, unbalance is commonly caused by connecting electric storage heaters to one phase of the grid or by singe-phase charging of electric vehicles. Moreover, the arrangement of the three conductors of an overhead line may cause mutual influence and different phase-to-earth capacities. As a consequence, in contrast to a symmetrical system (Fig. 19 a), the voltage phasors of the system no longer feature equal absolute values and angles of 120 degrees with respect to the other phasors (Fig. 19 b).

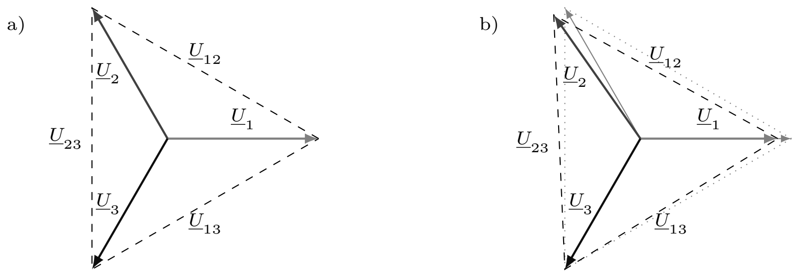

Figure 19: Voltage pointer representation of a symmetrical three-phase system (a) and an unbalanced three-phase system (b)

As provided in the definition, unbalance is associated with the ratio of negative sequence component to positive sequence component of the system. In order to understand the definition, three phase AC systems are represented by symmetrical components. It is assumed, that each three phase AC system consists of a superposition of two symmetrical three phase systems and one AC system. One of the two symmetrical three phase systems is referred to as the positive sequence system, the other one rotating counterclockwise is the negative sequence system [84]. A simplistic approach for assessment of voltage unbalance is to measure the deviation of voltage Δu for all three phases and to determine the voltage unbalance coefficient c_{vu} by comparing them to the average phase voltage $\overline{u}$ [66].

$$c_{\mathrm{vu}} = \frac{\Delta u}{\overline{u}} \qquad (2.5)$$

A variant of determining the voltage unbalance coefficient c_{vu} is based of the symmetric components by relating the absolute value of the negative sequence component to the absolute value of the positive sequence component. Determination of positive sequence component and negative sequence component on the basis of the line voltages is possible. The permissible extent of voltage unbalance is defined in the standards EN 61000-2-2, EN 61000-2-4 and EN 50160, which agree in a maximum degree of unbalance of 2 % for medium voltage networks [63, 70]. Observation is based on mean values over 10 minutes. [84]

2.4.8 DC offset

If a DC voltage is present in an AC system which is superimposed on the AC voltage and which results in a displacement of the mean value relative to zero, a DC offset is present (Fig. 20 a).

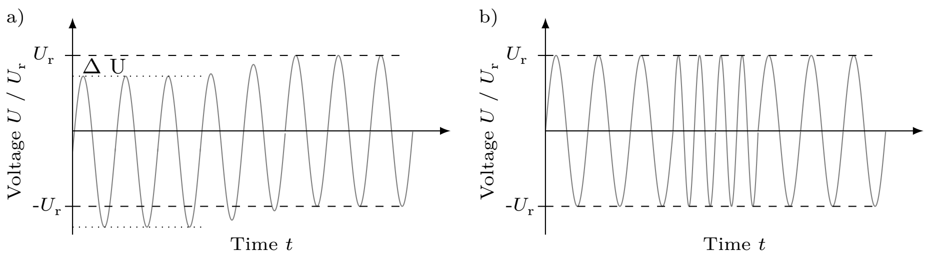

Figure 20: Illustration of a DC-Offset (a) and frequency variation (b)

A significant source of DC injection into AC grids are grid connected converters. Although modern converters generate AC voltage signals with a low distortion factor, a slight DC voltage input cannot be completely avoided. By increased use of power electronic components in generating plants this problem is exacerbated [86]. For this reason, it is stipulated in the standard IEEE 1547-2003 that DC injection any distributed resource must not exceed 0.5 % of the full rated output current. An DC offset causes a series of undesired effects, such as saturating transformer cores, erosion of grounding electrodes, evoking even harmonics as well as additional heating of equipment and appliances. [61, 75]

2.4.9 Alteration of the power system frequency

AC power systems are operated at a certain frequency determining the duration of a full period of voltage alteration. All devices and the entire equipment are specified for being operated at the design frequency. Different definitions are available for frequency. In physics, frequency is known as the inverse value of the period duration of a periodic signal. Thus, it is a measure for the temporal period from the beginning of an individual, entire oscillation until its ending. For signals in AC systems both beginning and ending of a signal period are in many cases associated with zero crossings. For determination of the frequency of polyphase systems, however, the observation of period duration of a single phase signal is not sufficient, as the polyphase AC system is not represented by one individual phase. Additional zero crossings may occur due to harmonics or phase jumps [87]. At any time, fed in power is supposed to equal the demand. If the demand exceeds the generation, the frequency decreases. The frequency tends to increase whenever the generation exceeds the demand. Fault on transmission lines, disconnection of large loads, shutting down or going off of large generators may also result in frequency fluctuations. Frequency variations (Fig. 20 b) outside the tolerance range of $\pm$ 5 % may lead to a system collapse [83]. Frequency deviations are considered temporal voltage distortions. Their magnitude depends on the load and thus the duration of the distortion varies from a few cycles to several hours. Typical duration of frequency variations is below 10 s.

2.4.10 Active and reactive power

In AC systems real power, also known as active power and reactive power is transmitted. Based on active power P and reactive power Q, the total power designated as apparent power S is determined.

$$S = \sqrt{P^2 + Q^2} = U \cdot I \tag{2.6}$$

Purely active power is transmitted, if the phase angle φ between the voltage signal and the current signal is zero, as visualized in Figure 21 a. If the φ is different to zero, reactive power occurs as depicted in Figure 21 b. Reactive power is represented by the shifting of the power function in comparison to the x-axis.

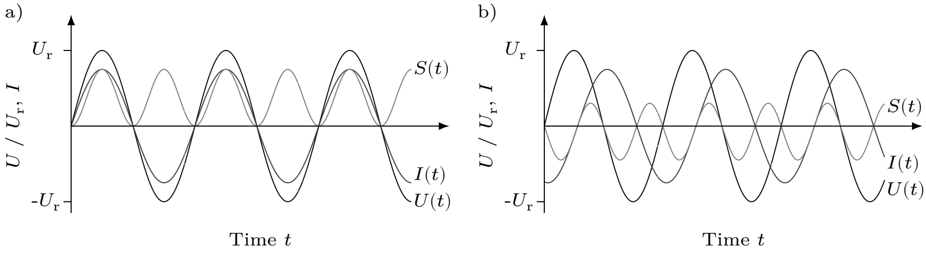

Figure 21: Illustration of power transmission in AC systems with pure active power (a) and combined active and reactive power transmission due to a phase shift (b)

The term reactive power in general denotes the reactive displacement power, which arises due to the phase shift of currents in comparison to the voltages and refers to the fundamental oscillation of the network. The power factor is a measure of the proportion of reactive power and is defined as the fraction of reactive power and the transmitted active power. Reactive power is required for field generation in electrical equipment such as transformers and rotating machines such as electric motors or generators. However, a high proportion of reactive power causes transmission losses and voltage drop [72].

2.4.11 Depiction of power quality deviations as reactive power

In addition to reactive displacement power, other reactive power types are known, which are introduced subsequently. Distortion reactive power occurs due to harmonics. Unbalance reactive power is caused by single-phase and two-phase loads as well as feeders. Modulation reactive power is caused by consumers with a strongly fluctuating power consumption. Causes of the reactive power types mentioned are harmonics in the supply current and in the supply voltage, commutation dips in the voltage caused by power electronics, flicker, brief voltage dips and unbalances in the supply voltage [88]. Total reactive power Q is composed of the reactive power types displacement reactive power Q_1, distortion reactive power Q_D, modulation reactive power Q_M and unbalanced reactive power Q_U [89, 90, 91]. The amount of the total reactive power Q is calculated as follows:

$$Q = \sqrt{Q_1^2 + Q_D^2 + Q_M^2 + Q_U^2} \tag{2.7}$$

$$Q_D = U \cdot \sqrt{\sum_{\nu=2}^{N} I_\nu^2} \qquad \forall\, \nu = 2, 3, ..., \infty \tag{2.8}$$

Distortion reactive power Q_D occurs whenever the wave-shape of current drawn by a consumer or fed in by a generator is no longer ideally sinusoidal but distorted by harmonics, notches or other modifications. Therefore, a further distinction is possible into harmonic reactive power including all integer superimposed sinusoidal oscillations with a frequency deviating from the fundamental oscillation and modulation reactive power comprising all non integer oscillations superimposed to the fundamental. Modulation reactive power results from pulsating current components, as they occur with cyclical power consumption. Those load fluctuations are often noticeable in the form of subharmonic and interharmonic components. Unbalance reactive power is detected by comparing the state variables of the individual phases and is a measure of present unbalance. It is therefore an indicator for the efficiency of power transmission in a multi-phase network. Unbalance reactive power is due to the presence of single-phase and two-phase loads or feeds in three-phase systems.

2.5 System services and ancillary services

Grid operators are aiming at a reliable supply of their customers and provision of electrical energy in compliance with defined standards of power quality. Furthermore, they are interested in safe and economic operation of the grid. To ensure those requirements, grid operators apply system services. According to the standard IEC 60050-617, system services are services, which are provided by the system operator or by power system users and necessary for the operation of an electric power system. A more detailed definition of system services is provided by the European Union of Electric Industry, which includes all necessary measures to support the transmission of electrical energy from producers to consumers [3]. Target of those measures is to ensure the integrity and stability of the transmission or distribution system as well as the power quality [92]. A distinction is made between system services, which are provided by the network operator and ancillary services, whose provision is task of network users [92, 93]. However, the subdivision is not strictly adhered to in the literature. A further vagueness is caused by the circumstance that system operators often buy ancillary services in order to provide system services [94]. In Germany, the Distribution Code postulates that provision of system services is task of transmission system operators and subdivides them into voltage stability, frequency stability, supply restoration and grid operation [1]. Even though transmission system operators are responsible for provision of system services, distribution system operators are likely to become increasingly involved in terms of support and responsibility [95]. A further subdivision of system services in Germany distinguishes between frequency stability, voltage stability, supply restoration and operational management. Moreover, it is implied that new technical solutions and further system services are required for reliable network operation in the future [96].

2.5.1 Static and dynamic voltage stability

The task of voltage stability measures is to ensure that the voltage within the system remains in a permissible band. A further task of voltage stability is the limitation of the voltage drop in the event of a short-circuit. A basic distinction is made between static voltage stability and dynamic voltage stability. Static voltage stability is achieved by the supply system independently returning to its initial steady state in the event of a minor disturbance, which is particularly associated with provision of reactive power. In contrast to this, dynamic stability refers to the continued operation of network operation in the event of considerable disturbances, which is why the provision of short-circuit power is of major importance. Dynamic stability includes transient voltage stability, dynamic voltage stability and long-term voltage stability [97]. Measures in the area of voltage stability include provision of reactive power, voltage-related redispatch or load shedding, provision of short-circuit power as well as voltage control [96].

2.5.2 Frequency stability by provision of balancing power

Within an AC power system, arbitrary variation of the frequency is not permitted. It is required, that the frequency is kept within a narrow range nearby the reference value. However, fluctuating consumer loads, feed-in capacities or disturbances cause frequency deviations in the power grid that have to be balanced by the frequency power control by adjustment of the fed active power. Therefore, the availability of balancing power in reserve power plants is required. Different types of balancing power are differentiated in dependence of their activation time, provisioning time and scope. Although the provision of balancing energy has up to now been task of large power plants, decentralized renewable feeders are increasingly used for provision of balancing power. Particularly for network frequencies above 50.2 Hz, the ability to reduce the feed-in capacity is demanded [98]. Measures of frequency control aim at maintaining the network frequency within the permitted range by controlling the active power output of the generating plants [93]. Positive frequency control reserve indicates additional capacity for provision of power in order to increase the frequency. Negative frequency control reserve is characterized as the ability to decrease the frequency by reducing the fed-in active power [94]. In dependence on their temporal characteristics, measures of frequency control are subdivided into the categories instantaneous reserve, primary reserve, secondary reserve and tertiary reserve.

2.5.3 Supply restoration in case of a blackout

In case of a voltage collapse or a blackout, the grid is out of function and loads are not supplied with electrical energy. By measures of network restoration it is attempted to resume a stable network operation. Usually the network restoration of distribution networks is established by renewed connection with the transmission network. Due to the increasing installation of decentralized plants DSO are increasingly interested in islanded operation capability and black start capability of their systems. Black start capability is the ability of a plant to put itself into operation in absence of voltage of the grid and to operate stably in a low operating point as idling or for providing on-site power demand. Accordingly, all required resources and auxiliaries have to be on site and have to be kept available in a sufficient scope to enable plant operation for a desired time. Furthermore, those plants independently attain an operational status in which they are ready for synchronization with the grid [99]. The islanded operation capability of a plant presupposes the ability to permanently provide a stable supply of an independent system, including voltage and frequency regulation. Compared to black start capability the implementation of the island operation capability is a comprehensive task as the control of the plant generators have to provide active and reactive power throughout the entire design range of the grid. This includes voltage surges on putting different types of equipment into operation such as transformers and overhead lines. The tolerance range of the control systems has to satisfy further requirements, as considerable voltage and frequency fluctuations may occur. [99, 100]

2.5.4 System services provided on distribution grid level

According to a study of German Energy Agency (DENA) on system services, decentralized renewable plants and storages were identified as suitable for provision of system services prospectively [96, 101]. It is assumed that those devices are capable of supporting harmonic compensation as active power filters, contribute static reactive power and reduce network unbalance as a result of asymmetric supply and load, given an appropriate design of their converters [102]. Qualification of those plants for ancillary services as voltage amplitude regulation, reactive power compensation and active parallel filtering has been investigated and discussed [103, 104].

As distribution grids undergo a change in dynamics caused by fluctuating renewable plants resulting in unwanted operating states, it is advisable to decouple those plants from the main system using power electronic interfaces. In some cases, decentralized renewable plants and storages are advantageous in provision of ancillary services in comparison to conventional systems due to their location and lower opportunity costs [105]. Improved coordination between TSO and DSO in provision of system services appears to be beneficial and cost-cutting, provided a suitable regulatory framework exists [106].

2.5.5 Present and future tasks of network operation

The task of network operation comprises measures of grid analysis, monitoring, congestion management and feed-in management by the grid operator. Network operation measures also include cross-network level system services. Continuous monitoring of network security is an important element of network operation according to the Transmission Code [2]. Thus, it is ensured, that malfunctions are limited using available operational resources. Furthermore, operational safety has to be guaranteed for maintenance measures as well as for modifications or new installations of equipment. Tasks of the TSO include organizing the injection of control power for frequency stability, controlling the ratio of reactive power in order to stabilize the voltage in the transmission grid, carrying out congestion management measures in the grid and executing supply restoration after interruptions [1]. Today, the DSO are responsible for voltage stability and network restoration within their networks and in addition are obliged to support the measures of the TSO [1]. Ensuring reliable network operation includes planning, installing and operating of protective equipment. Considerations concerning application of arc suppression coils, filters or other systems are task of network operation. Furthermore, network operation comprises suitable dimensioning of those devices and determination of their coupling point in accordance with planning of the future grid structure.

2.6 Technical measures for improving power quality

In addition to the four classic areas of system services, the field of improving power quality is introduced. All measures in this area aim at mitigation possible deviations from the ideal level of power quality, that are not covered by the aforementioned areas. Services in this area are of a rather technical nature, so that their provision depends on the availability of suitable equipment. Harmonics, which are induced for example by power electronic devices, cause undesirable effects on the transmission system, its equipment, generators and consumers. If circuit feedback cannot be avoided and if permissible operating limits are violated, compensation measures are required. Numerous approaches are available for the compensation of these disturbing signal components. Available approaches for harmonic compensation are subdivided into active systems, passive systems and hybrid systems. According to their position within the grid, a further distinction is made into serial and parallel filters. In addition, the possibility of continued operation of the distribution network in the event of a single-phase earth fault depends on the selected method of neutral point treatment and requires the presence of devices for limiting the residual current. [107, 108]

2.6.1 Power filters to influence the waveshape

Filters are typically used between the grid and a load. They retain unwanted circuit feedback or mitigate the negative effects of disturbed current and voltage signals from the network on sensitive loads. An adjustment or regulation of the filters is necessary regarding specific requirements of a distinct point within the network or a specific branch of the network where power quality parameters are to be influenced. Compensation currents or voltages fed in by filters may affect power quality in other system parts of the system. [109]

Passive filters

Passive filters utilize the frequency-related behavior of capacitors and inductors, which are integrated into the network with suitable dimensioning for elimination of unwanted signal components as harmonics. For each frequency that is to be blocked, a separate filter circuit is provided. Passive filter systems feature a number of disadvantages. First, they are preset to individual frequencies that are to be compensated and dynamic adjustment is not possible. Second, parallel resonances may be excited and therefore ripple control systems are influenced. A third disadvantages consists in the aging of passive filters. Moreover, tolerances of the components used and relatively high losses are regarded as further disadvantages [110]. Passive filters are designed according to different functional principles. For unchoked compensation, a purely capacitive branch is added to the system, which contains capacitors and enables limitation of line and transformer losses. For choked compensation, an inductance is introduced into the capacitive branch, which limits the occurrence of current overloads due to resonances and compensates for selected, low-frequency harmonics. If several, differently tuned filters are combined, a simultaneous compensation of multiple harmonics is possible. Furthermore, a high-pass filter for higher order harmonics can be set up. A separate filter stage is required for each single harmonic to be filtered. [88]

Active filters

Power electronic systems used for improving power quality are referred to as active filters. They are used in a wide variety of applications as for compensation of harmonics, capacitive and inductive reactive power compensation as well as the compensation of unbalance [88]. Active filters feature measuring equipment with high-resolution and high sampling frequency, suitable computing power for signal processing and power semiconductors with high switching frequencies. They are distinguished into the function groups measurement, control, energy storage and power semiconductors. In comparison to passive filters, one advantage is that the output currents are set as desired by parameterizing the converter. Furthermore, power dissipation of active filters is considerably reduced [111]. Active power filters are realized using voltage source inverters based on pulse-width modulation. In case of proper adjustment active filters reduce harmonics by feed-in or deduction of power from the grid. Electrical energy gathered from voltage peaks caused by harmonics is buffered in capacitors or inductors of an intermediate circuit and recovered for compensation of voltage dips. Active filters are capable of providing several functions simultaneously and reacting to changes in power quality at the measuring point. For reactive power compensation, the compensation is highly dynamic, so that flicker compensation is possible. [88]

2.6.2 Available concepts of earth-fault compensation

During operation of electrical networks short circuits between conductors or a conductive connection to the environment occur. Those short circuits are due to external effects such as lightning or mechanical impact as well as internal effects such as failure of insulation material. As a consequence, grid operation is transferred to fault mode and currents and voltages deviating from normal operation appear. Transient voltages and currents are observed during transition to a stationary fault mode [112]. A common fault scenario in medium voltage grids is single-phase ground fault. In addition, ground faults of two of the three conductors or of all three conductors are possible.

Moreover, a short circuit between two conductors without earth contact or even a short-circuit of all three conductors without earth contact is possible [113]. In medium voltage networks, grounding is realized via neutral points of the systems. A variety of possibilities to implement grounding is available. Those are isolated neutral, resonant neutral grounding and low impedance grounding. Depending on the neutral point treatment, a fault current $\underline{I}_\mathrm{F}$ occurs on ground fault. [112]

Medium-voltage networks with low spatial expansion are partially operated with isolated neutral points (Fig. 22 a). This is possible because only low capacitive earth fault currents are to be expected due to the low earth capacitances. Neutral point treatment by low-resistance grounding is particularly suitable for medium-voltage networks in which all stations are connected to at least two independent lines. This enables minimization of the duration of supply interruption in the event of a fault and restoration of the supply of all consumers by excluding the line affected by the fault from operation. Due to voltage surges, arcs arise, carrying a fault current. These arcs extinguish, if both the voltage and the earth fault current are below certain maximum values. [47, 85, 114]

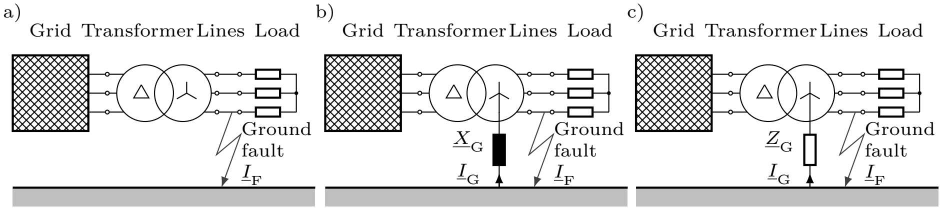

Figure 22: Earth fault in isolated neutral system (a), in arc-suppression-coil-grounded neutral system (b) and earth fault in low-impedance-grounded network (c)

In spatially extended medium-voltage networks, the capacitive earth-fault current is increased as a result of the capacitances of the equipment. In order to limit the reactive current required for generation of electric fields in equipment, in the event of a ground-fault at least one neutral point of a transformer is connected to the ground via an inductor (Fig. 22 b). In most cases, a coil is used as inductor, which is tuned to the line frequency of 50 Hz. The reactive current of the coil partially compensates the capacitive ground-fault current in case of a single phase ground-fault. [47, 84, 85, 114]

In the case of low-impedance neutral grounding, the neutral point of at least one transformer within the medium-voltage network is connected to earth

(Fig. 22 c) featuring a low impedance $\underline{Z}_G$. This leads to a reduced voltage surge in the remaining intact conductors during a single-phase ground fault. However, significant fault currents occur and continued operation of the network segment affected by the fault is impermissible. Therefore, the network section at which the fault is located has to be disconnected from the grid as quickly as possible, usually within 0.1 to 0.2 seconds. Neutral point treatment by low-resistance grounding is particularly suitable for medium-voltage networks in which all stations are served by at least two independent lines. This enables minimization of the duration of supply interruption in the event of a fault and restoration of the supply of all consumers by excluding the line affected by the fault from operation. [47, 85, 114]

2.7 Deduction of the need for research

In the previous sections, challenges for operators of medium voltage grids have been introduced. The number of feeders and loads, that are connected using power electronic devices is increasing. As a result, non-sinusoidal current waveshapes occur, which cause non-sinusoidal voltage curves at the impedances of the grid. The installed capacity of the regenerative generation plants is already large and still increasing.

Due to the fluctuation of the generated power, fluctuations in the load flows appear. Moreover, the direction of load flows in medium-voltage networks is being reversed with increasing frequency. In these circumstances, measures are required, which allow for balancing of generation and load as well as readjustment of the signal forms of the current and voltage signals to the tolerable range.

For that reason, the ideal level of power quality was characterized and important parameters of power quality were discussed. As a result it appears desirable to develop an integrated type of equipment, which provides selected system services in order to improve particularly relevant power quality parameters, as visualized in Fig. 23, at once.

Beyond influencing the signal parameters, a further task of this system is the compensation of active power. This is achieved by equipping the system with an energy storage.

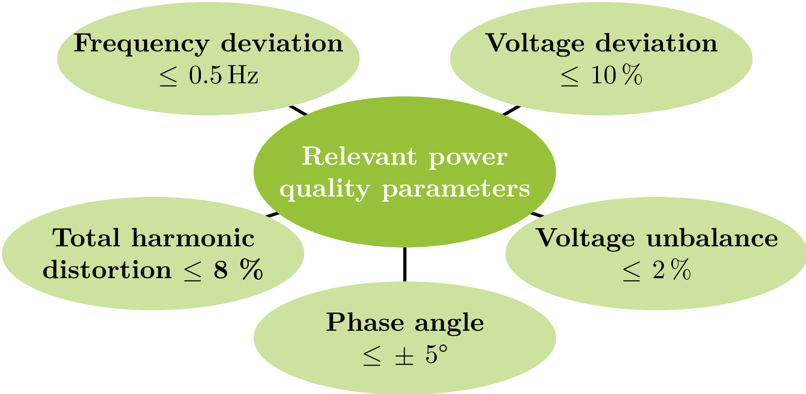

Figure 23: Visualization of relevant power quality parameters in medium voltage networks

By providing several system services by an integrated device, certain advantages are suspected (Fig. 24). First of all, it is assumed that by combining several system services in one single integrated device, capital expenditures for conventional resources are reduced. Secondly, it is assumed that by improving the power quality the lifetime of equipment in the network is increased and capital expenditures for replacement are reduced. In addition, by improving the power quality at the transfer station to the superimposed grid level, possible contractual penalties or, for instance, fees for the purchase of reactive power may be avoided.

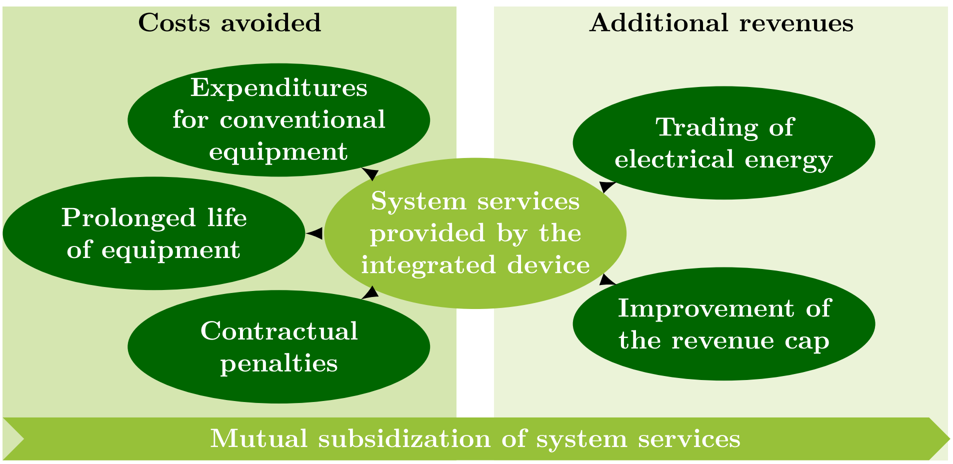

Figure 24: Assumed advantages of providing several system services by an integrated device

Profits are expected by using the system's energy storage unit for the provision of active power and trading electrical energy. The system is assumed to contribute to a reduction of network downtime and supports the achievable revenue cap by improving the quality element. Finally, a mutual subsidization of the individual system services is assumed. The exploration of such a system is concomittant by the following, definite research tasks:

1. In a first step, available approaches for calculating relevant power quality indicators using digital measuring technology are to be investigated and assessed.
2. Secondly, an approach for making different power quality deviations comparable is to be derived. Based on all considered individual power quality deviations, an indicator for total power quality is calculated.
3. Subsequently a concept for distributing the available nominal power power of a converter to individual system services, which are provided in parallel, is to be developed. The power distributed to each individual system service corresponds to the share of the individual power quality deviation in total power quality deviation.
4. Characteristics of individual system services under consideration are to be investigated and it is to be determined whether the provision is associated with active power or reactive power.
5. An approach for distributing power with highest possible efficiency to individual storages of a hybrid storage system is required.
6. The impacts of different charging- and discharging strategies concerning both the efficiency and the state of charge of the energy storages are to be investigated.

In addition to the research work presented in this thesis, further tasks were elaborated by cooperating researchers in the same project. Therefore, the energy storage technologies redox flow battery and flywheel storage are investigated within the present thesis based on simplified models coordinated with the research partners. Development, precise modeling and optimization of the energy storages is carried out by cooperating researchers. The present thesis includes relevant parameters of the energy storages concerning specifications and power ratings.

Likewise, the selection and evaluation of a suitable converter as well as adaptation of the converter control in order to provide the system services is task of cooperating researchers. Testing of the converter is carried out in a laboratory grid. Time behavior is assessed in the test grid and in simulation. There, provision of system services by the converter is investigated and simulated. Based on those findings, the approach presented within this thesis enables distribution of power to individual system services in order to improve the total power quality. Relevant specifications concerning control variables and set values are defined in cooperation.

3 Methods of signal analysis and technologies of energy storage

For the determination of power quality parameters within an electrical network, its signals are to be analyzed. Therefore, basics for mathematical representation of alternating current (AC) systems and essential information on measurement as well as digital signal processing are provided. Fundamentals of control theory and power electronic converters are introduced. Moreover, an overview of available technologies for storing electrical energy is provided. To enable objective technology selection, available storage technologies are characterized by suitable performance indicators. With regard to the demand for action, this chapter examines the questions how the present level of power quality can be determined using procedures of digital signal processing and which key performance indicators are available for assessing the suitability of energy storage technologies.

3.1 Mathematical modeling of three-phase systems

Electrical energy is obtained by conversion from other primary energy sources [115]. As pure exergy it is the most valuable form of energy and can be converted into all other forms of energy with low losses [116]. In addition to its versatility, electrical energy is characterized by its convertibility, low-loss transportability, simple measurability and controllability [85, 115]. Electric power supply systems are operated in Germany as AC voltage systems with few exceptions only. AC systems are characterized by the fact that the progressions of the voltage or current signals are not constant over time, but fluctuate periodically with a defined amplitude. A polyphase system represents an electrical coupling of several single-phase systems. Here, the number of necessary transmission lines is reduced in comparison to single-phase systems and it is possible to provide rotating magnetic fields on the consumer side [117]. Coupling of the independent circuits is implemented in the form of star-connection as well as in the form of delta connection. Both have in common that for symmetrical systems the alternating line voltages $u_1\,(t)$, $u_2\,(t)$ and $u_3\,(t)$ add up to zero at any time.

$$u\,(t) \;=\; \hat{u}\sin\omega\,t \;+\; \hat{u}\sin\Big(\omega\,t-\frac{2\,\pi}{3}\Big) \;+\; \hat{u}\sin\Big(\omega\,t-\frac{4\,\pi}{3}\Big) \;=\; 0 \qquad (3.1)$$

3.1.1 Basic principles of three-phase systems

Depending on the desired application, electrical energy of different voltage is required. In order to implement a comprehensive network for the transport and distribution of electrical energy, a simple and low-loss transformation of the voltages is required. AC voltage systems offer this advantage and are therefore used in the form of three-phase systems for electrical power supply. A symmetrical three-phase system with three voltages of equal amplitude and a phase angle of $\varphi = 120^\circ$ degrees is created by three rotating coils in a constant, homogeneous magnetic field, each of which is also arranged at an offset of 120° degrees or $2/3\,\pi$ towards the other coils. [118, 119]

3.1.2 Pointer representation of periodic signals

If the voltage at the terminals of a coil rotating at a constant angular velocity ω in a homogeneous and temporally constant magnetic field $\vec{\mathbf{B}}$ is observed, the voltage induced in the coil can be represented as a time-dependent, periodic quantity. This is due to the circumstance that the magnetic flux through the coil is associated to the angle that the normal vector $\vec{\mathbf{n}}$ perpendicular to the coil plane includes with the directional vector of the magnetic field as visualized in the figures 25 a and b [113].

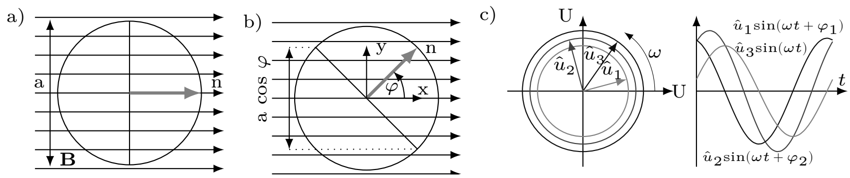

Figure 25: Visualization of directions of pointers in the context of AC systems (a) and pointer diagram for visualization of the addition of sinusoidal AC voltages [89, 118, 119]

The voltage $u\,(t)$ induced in the coil rotating at an angular velocity ω with a cross-sectional area $\vec{\mathbf{A}}$ at time t, which is described by the plane vector, is determined according to the induction law as a trigonometric function of the phase angle φ depending on the time t and the maximum value of the voltage $\hat{u}$ [118]. If it is furthermore taken into account that a shift of the voltage phase may occur at time t by a zero phase angle φ, the equation describes the instantaneous value of voltage for all points in time.

$$u(t) = -\frac{\mathrm{d}}{\mathrm{d}t}\iint\limits_A \vec{\mathbf{B}} \cdot \mathrm{d}\vec{\mathbf{A}} = \hat{u}\sin\omega t = \hat{u}\sin(\omega t + \varphi_u) \quad (3.2)$$

A system consisting of the original voltage pointers $u_1(t)$, $u_2(t)$ and their corresponding zero phase angles of φ_1 and φ_2 rotating at a common angular velocity ω as well as the pointer of the sum of both voltages $u_3(t)$ is visualized in Fig. 25 c. Instantaneous values of the voltages are projected onto the axis of ordinates. In order to analyze and calculate arbitrary AC systems using pointers, calculation using complex values is introduced. [89, 119]

3.1.3 Complex calculation of AC systems

A time-dependent voltage signal can be represented by a sum of a sine wave and a cosine wave without zero-phase angle. Using the addition theorem (3.3), the voltage equation $u(t) = \hat{u}\sin(\omega t + \varphi_u)$ can be converted to the form (3.4).

$$\sin(\omega t + \varphi_u) = \cos\varphi_u \cdot \sin\omega t + \sin\varphi_u \cdot \cos\omega t \quad (3.3)$$

$$u = (\hat{u} \cdot \cos\varphi_u)\sin\omega t + (\hat{u} \cdot \sin\varphi_u)\cos\omega t \quad (3.4)$$

Result of this transformation is a unified, simplistic representation of the voltage $u(t) = \hat{u}\sin(\omega t + \varphi_u)$ as a pointer diagram that consists of two voltage arrows $u_1(t) = (\hat{u} \cdot \cos\varphi_u)\sin\omega t$ and $u_2(t) = (\hat{u} \cdot \sin\varphi_u)\cos\omega t$ perpendicular to each other (Fig. 26 a) [119].

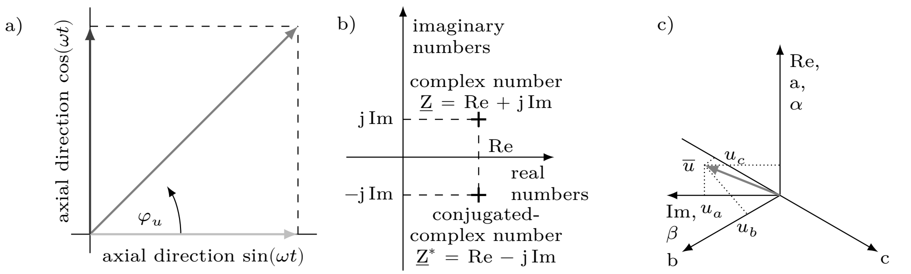

Figure 26: Illustration of a pointer diagram (a), visualization of the complex number Z in the Gaussian plane of numbers (b) and transformation of a three-phase system into a space phasor in complex plane (c) [119]

Voltages, currents and other variables of electrical networks are represented as complex numbers in the complex number plane (Fig. 26 b) by indicating their real part (Re) and their imaginary part (Re). The imaginary part is identified by the letter j. Complex quantities are indicated by an underline. In contrast to rotating pointers, voltage pointers in the complex plane are subsequently described as static pointers according to the symbolic method [89].

$$\underline{u}(t) = \mathrm{Re}\{\underline{u}(t)\} + \mathrm{j}\,\mathrm{Im}\{\underline{u}(t)\} \tag{3.5}$$

$$= \hat{u}\cos(\omega t + \varphi_u) + \mathrm{j}\,\hat{u}\sin(\omega t + \varphi_u) = \hat{u}\,\mathrm{e}^{\mathrm{j}\,\varphi_u}\,\mathrm{e}^{\mathrm{j}\,\omega t} \tag{3.6}$$

By excluding $\hat{u}$ and using the Euler formula $\mathrm{e}^{+\mathrm{j}\,\varphi} = \cos\varphi + \mathrm{j}\sin\varphi$, both the trigonometric form and the exponential form of the complex voltage are obtained. The exponential representation comprises a time-dependent part $\mathrm{e}^{\mathrm{j}\,\omega t}$ and a non-time-dependent part $\hat{u}\,\mathrm{e}^{\mathrm{j}\,\varphi_u}$. For analysis of electrical networks, in which the alteration of all variables depends on a common frequency ω only, it is not necessary to consider the time-dependent variables. A network analysis is then possible using the time-independent variables called complex amplitudes, in this case $\hat{u}\,\mathrm{e}^{\mathrm{j}\,\varphi_u}$. [89]

Complex representations of voltages and currents within this thesis are used for determining the angle between voltage signals and current signals.

3.1.4 Space phasors for three-phase AC systems

Mathematical description and modeling of the behavior of three-phase systems can be simplified by space vector representation in state space. Space phasors are considered complex modal components and are increasingly used to study transient phenomena in three-phase systems. Any three-phase AC system represents three independent instantaneous values $\nu_1(t)$, $\nu_2(t)$, $\nu_3(t)$ in current or voltage. The dependence of the variables introduced by the time is for reasons of clarity eliminated by separation of a variable $\nu_0(t)$. [120, 121]

$$(\nu_1 - \nu_0) + (\nu_2 - \nu_0) + (\nu_3 - \nu_0) = \nu_1' + \nu_2' + \nu_3' = 0 \tag{3.7}$$

By rearranging and solving results for ν_0 the well-known expression:

$$\nu_0 = \frac{1}{3}(\nu_1 + \nu_2 + \nu_3) \tag{3.8}$$

By introduction of the rotation operator $\underline{a} = e^{j\frac{2\pi}{3}} = (-\frac{1}{2} + j\frac{\sqrt{3}}{2})$ and acknowledgment of the connectedness $1 + \underline{a} + \underline{a}^2 = 0$, the complex space phasor $\underline{\nu}$ can be composed as follows: [38, 85, 120, 121, 122]

$$\underline{\nu} = \frac{2}{3}\left(\underline{a}^0\nu_1 + \underline{a}^1\nu_2 + \underline{a}^2\nu_3\right) = \frac{2}{3}\left(\underline{a}^0\nu_1' + \underline{a}^1\nu_2' + \underline{a}^2\nu_3'\right) \quad (3.9)$$

The complex plane is spanned by the two axes α and β, representing the real parts and imaginary parts of the complex space phasors (Fig. 26 c). Space phasor components consist of the space phasor $\underline{\nu}$, the complex conjugate space phasor $\underline{\nu}^*$ and a real double zero component $\nu_h = 2\,\nu_0$. The previously introduced values of the three phase system are transferred into components of the space vector by the following transformation. [120]

$$\begin{bmatrix}\nu_1\\ \nu_2\\ \nu_3\end{bmatrix} = \frac{1}{2}\begin{bmatrix}\underline{a}^0 & \underline{a}^0 & \underline{a}^0\\ \underline{a}^2 & \underline{a}^1 & \underline{a}^0\\ \underline{a}^1 & \underline{a}^2 & \underline{a}^0\end{bmatrix}\begin{bmatrix}\underline{\nu}\\ \underline{\nu}^*\\ \nu_h\end{bmatrix} = \frac{1}{2}\begin{bmatrix}1 & 1 & 1\\ \underline{a}^2 & \underline{a}^1 & 1\\ \underline{a}^1 & \underline{a}^2 & 1\end{bmatrix}\begin{bmatrix}\underline{\nu}\\ \underline{\nu}^*\\ \nu_h\end{bmatrix} \quad (3.10)$$

The space phasor introduced above is used for determination of the power system frequency.

3.1.5 Symmetrical components facilitate analysis of unbalance

The description of multi-phase AC systems using symmetrical components was invented by the Canadian electrical engineer Charles Legeyt Fortescue, who used symmetrical subsystems to analyze any unsymmetrical, polyphase signal [120, 123]. Three-phase systems can therefore be subdivided into positive sequence component, negative sequence component and zero sequence component.

$$\begin{bmatrix}\underline{V}_1\\ \underline{V}_2\\ \underline{V}_0\end{bmatrix} = \frac{1}{3}\begin{bmatrix}1 & \underline{a}^1 & \underline{a}^2\\ 1 & \underline{a}^2 & \underline{a}^1\\ 1 & 1 & 1\end{bmatrix}\begin{bmatrix}\underline{\nu}_1\\ \underline{\nu}_2\\ \underline{\nu}_3\end{bmatrix} \quad (3.11)$$

Symmetrical three-phase systems can be represented by positive sequence component only. Negative sequence component and zero sequence component do not occur in symmetrical case [120]. Here, the complex vector of the symmetrical components contains elements for positive sequence component $\underline{V}_1$, negative sequence component $\underline{V}_2$ and zero sequence component $\underline{V}_0$. The symmetrical components introduced are the symmetric used to determine present voltage unbalance.

3.2 Measurement of power quality disturbances

As delineated in the previous section, various phenomena of PQ disturbance with individual characteristics are distinguished. In order to ensure reliable network operation within the tolerance ranges, limits and compatibility levels defined by applicable standards, detailed information on the present disturbances is required. Accordingly, proper detection and precise measurement of those PQ disturbances is necessary [84]. If the analog signals to be analyzed are examined by using tools of digital signal processing, appropriate conversion of the continuous-time signal into a discrete-time signal with appropriate temporal resolution is to be executed first. In contrast to analog signals, digital signals contain only a limited quantity of values. Quantization converts the analog signal into the appropriate value of the digital value range. In summary, a continuous signal with an unlimited range of numerical values is converted into a discontinuous signal with a limited range of numerical values. There is a discretization both in time and amplitude as visualized in Figure 27.

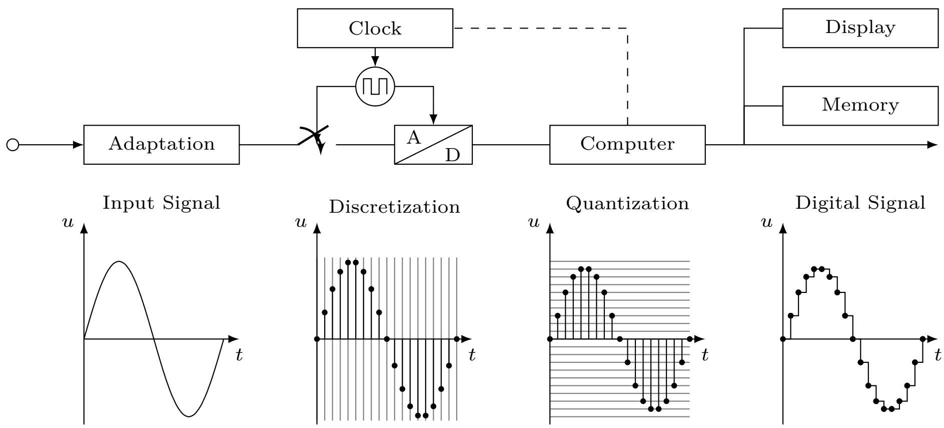

Figure 27: Structure of a digital measurement system and visualization of processing steps required for digitizing analog signals

Deviations of the signal may occur in an arbitrary frequency range. In order to detect all possible deviations, an unlimited frequency band is to be observed. This requirement is counteracted by restrictions of digital signal processing. A basic law of signal processing, the sampling theorem by Nyquist and Shannon, requires a minimum sampling rate greater than twice the frequency of the signal component with the highest frequency to be sampled. As this requirement cannot be met by an unlimited frequency band, a limitation of the frequency band is necessary. As the computation effort required for signal analysis and the computation time increases with the amount of data to be interpreted, narrowing of the frequency range to the frequencies of interest is advisable. A reasonable approach is to consider only the frequency range of the phenomena which are particularly relevant in terms of power quality. The frequency range required for sampling of important power quality disturbances is between a few mHz and several kHz. [84] Equally important is the definition of the number of distinguishable signal stages, which is also referred to as the resolution of the signal. The required resolution determines the size of the binary numbers to be processed. By quantization, the instantaneous value of the input signal is assigned to the closest stage of possible signal steps according to predefined rules. In order to substantiate the decision regarding the required signal levels, it seems promising to consider the amplitudes of the relevant disturbances. It is to be ensured that the specified resolution permits at least a reliable detection of violation of limits specified in the standards and moreover identification of events that have undesirable effects on the electrical power system.

3.2.1 Inaccuracies of analog-to-digital conversion

Errors occurring in the context of analog-to-digital conversion are divided into static errors that remain after all transients have subsided and dynamic errors which occur on converters when they are operated under non-static conditions. Main types of static errors are quantization error, zero error, gain error, non-linearity, differential non-linearity, monotonicity error and dependency of converter parameters on operating voltage, which is commonly referred to as power supply sensitivity. Due to the limited number of signal steps that can be distinguished by the ADC according to its resolution, the quantization error (Fig. 28 a) of each sample ranges in an interval between 0 and $\pm$ 0.5 LSB. After analog-to-digital conversion, there is an error signal with similar characteristics in comparison to noise. [124]

An offset-error is present, if the characteristic curve of the converter is shifted in parallel towards the ideal signal curve (Fig. 28 b). Offset-errors cause a deviation with constant magnitude of the position of all converted values throughout the entire signal range. As offset-errors are constant, they are eliminated by shifting the converted values by the known offset-value [125]. Gain errors are characterized by the circumstance that the first derivative of the function of the converted signals deviates to the first derivative of the ideal function (Fig. 28 c).

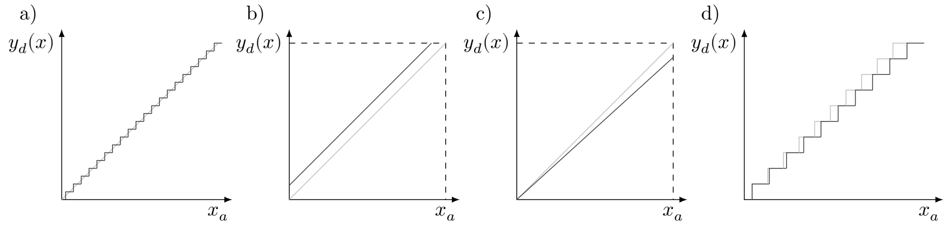

Figure 28: Errors of converting an analog input signal x_a into a digital output signal $y_d(x)$ using an ADC. Here, quantization error (a), offset error (b), gain error (c) and non-linearity error (d) are visualized

Accordingly, there is a slope of the transfer curve in comparison to the original signal curve. As all output values are shifted by the same percentage compared to the input values, a correction by appropriate amplification or attenuation is possible [125]. Non-linearity, also referred to as integral non-linearity is associated with the maximum deviation of the ideal linear transfer function in comparison with the real transfer function after elimination of offset error and gain error (Fig. 28 d). A reason for non-linearity is unequal size of quantization intervalls. Non-linearity of an analog-to-digital converter (ADC) is usually represented as a fraction of LSB [124]. Differential non-linearity of an ADC is considered as the presence of deviations regarding the range of values with respect to the input signal within the distinguishable stages of the converter. As for real converters the width of the converter stages deviates from the ideal values, a measure of deviation is required to estimate the conversion error of the sampled signals [126]. Analog-to-digital converters comply to monotonicity, if the characteristic curve of the ADC increases incrementally monotonous for growing input values. monotonicity is sufficient, if non-linearity remains below 2 LSB [124]. If the results of analog-to digital conversion are influenced by variations of the supply voltage, power-supply sensitivity is present. In order to obtain useful conversion results, a constant supply voltage must be supplied at all times. Power-supply sensitivity of an ADC is calculated as a change in the output variables in relation to the change in the supply voltage. [124, 126]

3.2.2 Analog-to-digital converters

Analog-to-digtal converters assign each analog input value to a corresponding step of the possible value range. The number of steps n_{ADC} represents the resolution of the ADC and determines the maximum digital value $Z_{\max} = 2^{n_{\mathrm{ADC}}}$ of the output signal provided by the ADC. As output values of the ADC all possible combinations of the digital value range occur as binary numbers. The specified signal range, for which an ADC is designed, is limited and a maximum input value or full scale range value (FSR) exists, which is attributed to the maximum digital value. Based on the FSR value and n_{ADC} the smallest possible difference between values of the analog signal distinguished by the ADC are calculated. [127, 128]

$$\mathrm{LSB} = \frac{\mathrm{FSR}}{2^{n_{\mathrm{ADC}}}} \tag{3.12}$$

Analog-to-digital converters are implemented in different ways. Parallel converters, serial converters, integrating converters and delta-sigma converters represent the four main design types [129]. The different approaches deviate considerably in terms of effort and speed [124].

3.2.3 Phase-locked loops for adaptation of sampling frequency

Sampling of the input signal with a fixed sampling frequency, which is independent of the frequency of the input signal, is insufficient in some cases of digital signal processing. In particular, there is a variety of applications, where it is relevant to ensure the sampling of entire signal periods. For this purpose it is necessary to establish a coupling between the frequency of the input signal and the sampling frequency (Fig. 29 a).

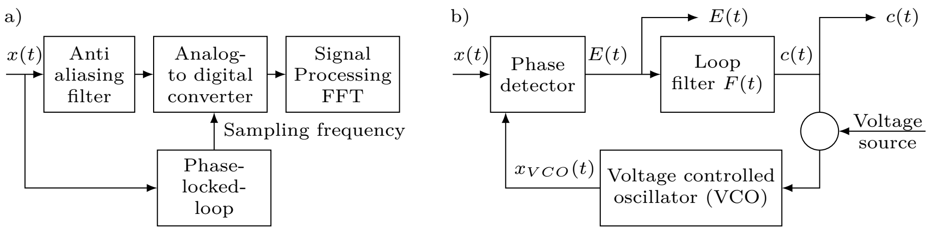

Figure 29: Elements of a system for digital signal processing of analog input signals containing a phase locked loop (PLL) for adapting the sampling frequency to the frequency of the input signal (a) and visualization of the functional principle of a PLL (b)

Phase-locked loops (PLL) are used for this purpose. In a PLL (Fig. 29 b), coupling between the input signal and the internal oscillation is established by iteratively changing the frequency of the internal oscillator until the input signal and the signal of the internal oscillator have a constant phase angle or the relationship between the two signals remains constant. [130, 131, 132]

PLL are nonlinear feedback systems, which always consists of the same elements. First, the input signal $x(t)$ is fed to a function block in which the input signal is compared with the signal from the internal oscillator (Fig. 29 b). The output signal of this phase comparator indicates the instantaneous deviation between input signal and output signal and is referred to as error signal $E(t)$. If the error signal fluctuates strongly or is unstable for other reasons that it cannot be used directly for controlling the internal oscillator, it is reasonable to set up a time-invariant filter between the phase comparator and the oscillator. The transfer function $F(t)$ of this element, known as a loop filter, is to be tuned for each individual PLL. Usually the loop filter is configured as an averager in order to transmit an average value of the error signal as a control signal $c(t)$ to the controllable oscillator. As a last functional group, there is an adjustable oscillator, which is called a voltage controlled oscillator (VCO). In digital circuits, this is usually a numerically controllable oscillator whose output frequency $x_{\mathrm{VCO}}(t)$ can be influenced by a control signal within its specification [132, 133]. At the beginning, when the PLL is started, the initial frequency of the VCO $f_{\mathrm{VCO},0}$ is set. The initial frequency is likely to differ from the frequency of the input signal f_x. In a first step, the frequency of the VCO is adjusted, until it is equal to the frequency of the input signal. This phase is referred to as frequency pull-in. In Figure 30 a the progression of the input signal and the signal of the VCO is visualized.

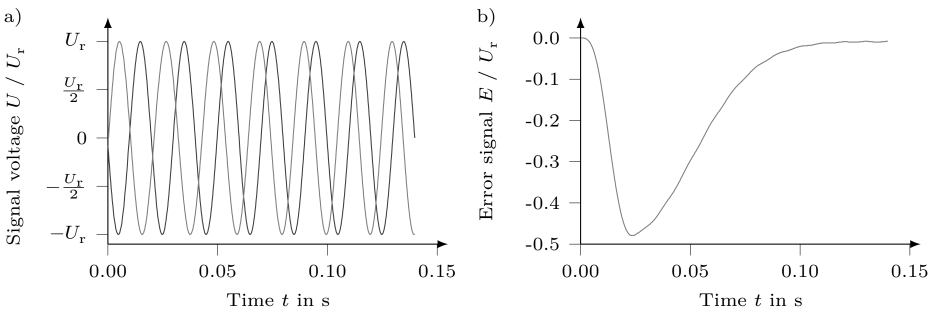

Figure 30: Coupling of the frequency of the voltage controlled oscillator of a PLL to the frequency of the input signal (a) and visualization of the corresponding error signal (b)

The frequency of the VCO is altered, until the phase-shifted signals have an identical frequency. Correspondingly, the error signal regarding the frequency assumes a constant value (Fig. 30 b), as the frequency of the VCO is set to a particular value deviating from its original value.

3.2.4 Fundamentals of digital signal processing

In Section 3.2 it has been explained how analog signals are converted into digital signals. Before interpretation of signal attributes is possible, the application of digital signal processing methods is required. Digital signal processing is concerned with time-discrete as well as amplitude-discrete signals and features advantages in terms of susceptibility to faults, stability, reproducibility, dynamics and flexibility in comparison to analog signal processing [134]. Digital signal processing (DSP) includes all available methods and procedures for generation, transmission, transformation, filtering, analysis and interpretation of digital signals. Subsequently, essential methods of DSP are presented, which are used to obtain information on power quality from sampled electrical input signals. DSP is associated with processing of sampled, discretized input signals, which are obtained from analog input signals by analog-to-digital conversion. Time-continuous signals with unlimited resolution (Fig. 31 a) are converted into time-discrete, quantized digital signals with a limited value range. For sampling of analog input signals different approaches as equidistant sampling or random sampling are available.

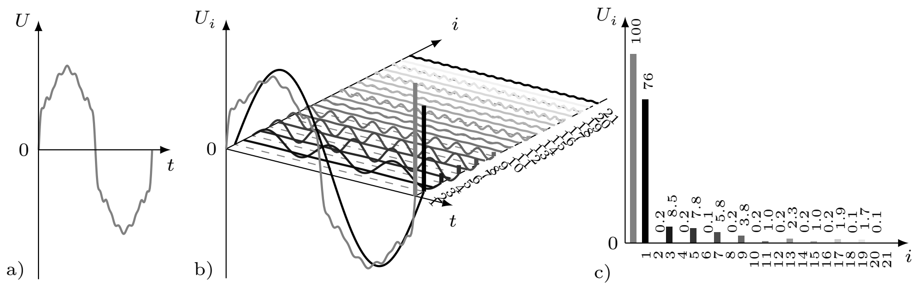

Figure 31: A signal with harmonic distortion (a) is transformed from time-domain into frequency domain (b) and the harmonic spectrum is analyzed regarding the magnitudes (c)

However, for correct signal reconstruction, the sampling theorem by SHANNON is to be respected [135].

$$x_k(t)|_t \quad = \quad kT_\mathrm{S} = x_k(kT_\mathrm{S}) =: x(k) \tag{3.13}$$

Here, $T_A = \frac{1}{f_\mathrm{S}}$ represents the sampling interval and f_S the frequency of sampling $k \in \mathbb{Z}$ in the domain $-\infty < k < +\infty$. The discrete signal is represented by $\{x(k)\}$. It is possible to transform signals from time domain into frequency domain by multiple approaches of Fourier-transform. In frequency domain, the entirety of oscillations contained into the input signal becomes manifest

(Fig. 31 b). Accordingly, main purpose of Fourier-Transform approaches is to determine the frequency spectrum of a signal (Fig. 31). By definition, the Fourier-Transform of an arbitrary signal $f(t)$ is denoted as follows [136]:

$$F(\omega) = \mathfrak{F}\{f(t)\} = \int_{-\infty}^{\infty} f(t)\mathrm{e}^{-j\omega t}\,\mathrm{d}t \tag{3.14}$$

Both $\mathfrak{F}(\omega)$ and $f(t)$ are complex functions of variables. For computation of Fourier-Transforms using digital computers, instead of time-continuous analog input signals, time-discrete and quantized digital signals are basis of calculation. Fourier-Transform for discrete signals or discrete Fourier Transform (DFT) is defined as indicated in equation (3.15) below [137]:

$$X(\mathrm{e}^{j\Omega}) = \sum_{k=-\infty}^{\infty} x(k)\mathrm{e}^{-j\Omega k},\ \Omega = \omega T \tag{3.15}$$

$$x(k) = \frac{1}{2\pi}\int_{-\pi}^{\pi} X(\mathrm{e}^{j\Omega})e^{j\Omega k}\,\mathrm{d}\Omega \tag{3.16}$$

For the general definition of a Fourier-Transform, which is represented by equation (3.16), a series of samples $x(k)$ in time domain is transformed into a continuous spectral function $X(\mathrm{e}^{j\Omega})$. In order to distinguish between the classic Fourier-Transform, which links the continuous functions in time and frequency domain, and the DFT, where discrete series in time and frequency domain correlate with each other, the transform is referred to as discrete-time Fourier-Transform (DTFT) [137].

In order to assess the computational time required for execution of the DFT in dependence of the number of samples provided as input data, the algorithm was implemented on a microcontroller and for different sample numbers the duration from beginning to end of execution was measured [138]. As the computational effort depends on the number of samples, a comparative analysis was carried out. Here, the number of samples is varied between 2^0 and 2^{11}. As for each additional sample within the vector of readings the number of multiplications executed in DFT calculation rises by two. Accordingly, processing time increases quadratic as depicted in Figure 32. The calculations were executed on a microcontroller of the type Atmega AT91SAM3X8E, which is installed on a prototyping board Arduino Due, has a clock frequency of 84 MHz and a word length of 32 bits. [138]

Samples	Processing time $[\mu s]$
1	6
2	105
4	662
8	4,255
16	19,937
32	89,877
64	385,886
128	1,763,361
256	7,227,423
512	29,212,845
1,024	117,565,305
2,048	434,243,282

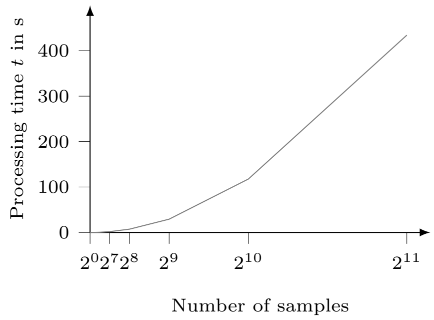

Figure 32: Time required to execute the DFT in dependence of the number of samples

A variant of discrete Fourier-Transform with lower demands regarding computational power is fast Fourier-Transform (FFT). Performance is increased by replacing multiplications by simpler operations as additions. Approaches of FFT are distinguished into procedures of decimation in time and procedures of decimation in frequency [137]. Minimum requirement for the application of FFT is that the number of input values is power of two. A wide variety of alternative approaches to the FFT algorithm have been developed. As important procedures the Radix-2 algorithm, the Radix-4 algorithm, the Radix-8 algorithm, the Prime-Factor algorithm (PFA), the Sparse Fast Fourier-Transform (SFFT), the Split Radix Fast Fourier-Transform (SRFFT) or the Winograd Fourier-Transform Algorithm (WFTA) are known. [137, 139, 140, 141]

In order to verify the assumed reductions of calculation time of FFT in comparison to DFT, a Radix-2 FFT algorithm was implemented and required processing time was measured based on identical sampled data (Fig. 33) [138].

Samples	Processing time $[\mu s]$
1	2
2	28
4	134
8	598
16	2,083
32	6,111.5
64	16,312
128	41,004
256	106,273.5
512	249,568
1,024	573,341
2,048	1,295,672

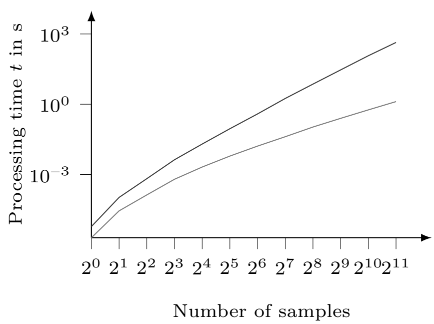

Figure 33: Comparison of the time required to execute the FFT in dependence of the number of samples in comparison to execution of the DFT

All calculation were executed on the microcontroller of the Arduino Due board for identical conditions. The time requirement for calculation of the FFT is depicted in dependence of the number of samples. The previously introduced conventional methods as FFT are designed for stationary, non-variable amplitude, frequency or phase as boundary conditions.

If deviations in frequency, amplitude or phase occur in the measured signal, the results of those transformations are faulty. In order to remedy this deficiency, the Taylor Fourier transform has been developed by José Antonio de la O Serna [142]. TFT is suitable for determining the harmonic signal components under transient conditions [143]. Furthermore, the momentous frequency of the signal is calculated and thus deviations in comparison to the reference frequency. Simplistically the TFT approximates the Taylor components of the oscillation at fundamental frequency over short time intervals by polynomial fitting. [142, 143, 144]

The transformations for determining the harmonic spectrum of any input signal are used for determining the magnitudes of power system harmonics. Based on the results of a FFT, the total harmonic distortion is calculated.

3.3 Introduction of power electronic circuits

Power electronics enable a transformation of electric energy into a required form using electronic switches. The general system layout of power electronic converters is shown in Figure 34 a.

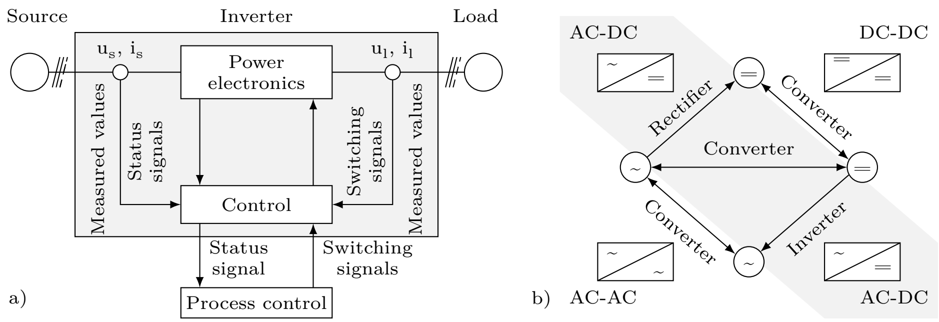

Figure 34: Basic layout of power converters (a) [145] and distinguishable converter types (b)

They are subdivided into four basic functional principles as depicted in Figure 34 b. Rectifiers convert alternating current into direct current (DC). Inverters unidirectionally transform DC into AC and enable energy to flow from

DC systems to the AC systems. DC converters allow bi-directional energy transport between DC systems and transform DC of given voltage and polarity into DC with different voltage and different polarity. AC converters enable bidirectional energy transport between AC systems by converting a system with given voltage, current and frequency into a system with different voltage, current and frequency. [38, 146]

Most commonly used in grid-connected applications are three-leg converters. For special applications, extraordinary converter layouts such as four-leg converters are available. Here three legs of the converter are connected to the three phases of the grid and a fourth leg provides zero sequence voltage to either a fourth conductor in four-wire power grids, a shunt-type active power filter or an earth fault compensator [147]. The necessary calculations to properly control the PWM for the approximation of the desired signal curves on all four legs of the converter requires a powerful software and hardware equipment of the digital signal processor of the controller [148, 149]. This is even more difficult for four-legged converters, which are considered under-determinate systems due to the fact that three reference voltages have to be transformed into four derived control commands [150]. In addition to three phase converters, variants for special applications have been developed. A three-phase four-wire converter with split DC link topology features a layout similar to conventional three-phase three-stage converters. However, a fourth wire is present connecting the center point of the converter to a load or the neutral conductor of a four wire three phase network (Fig. 35 a). [151]

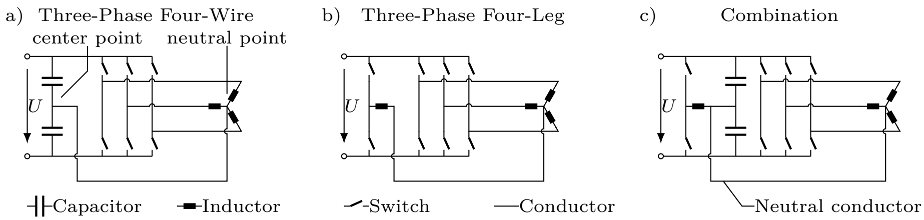

Figure 35: Layouts of converter types with interconnection of the neutral point of the grid to a split DC link of the converter (a), a neutral leg of the converter (b) or a hybrid approach of both (c) [151]

The three-phase four-legged converter extends the layout of the three-phase four-wire converter by additional switches between the two potentials of the DC link and the medium point (Fig. 35 b). A third possible design is a combination of the three phase four wire converter and the three phase four leg converter, in which both the insulation of the center point by capacitors and the power electronic switches are provided (Fig. 35 c). [151]

Application of four-wire converters of four-leg converters is reasonable, in cases where a four-wire three-phase network is present and symmetry is not granted due to connection of both single-phase and three-phase loads, feeders or other devices. In those cases, the connection of the converter to the neutral of the network is required for drawing or providing zero phase currents. The zero sequence current contains components for harmonics occurring in the neutral point. [152]

Converters are digitally controlled power semiconductor devices, which emit high-frequency voltage pulses in variable width. The method of controlling the pulse width for the approximation of a desired waveform is referred to as pulse width modulation (PWM). For control of the switching states of a converter and alignment of input signal and switching, several approaches are known. PWM is an approach of modulation by defining the duration of valve activation by comparing an input signal to a carrier signal, for example a triangular signal (Fig. 36 a). For each time step it is analyzed, whether the amplitude of the scaled input signal is higher or lower in comparison to the reference signal. [77, 153]

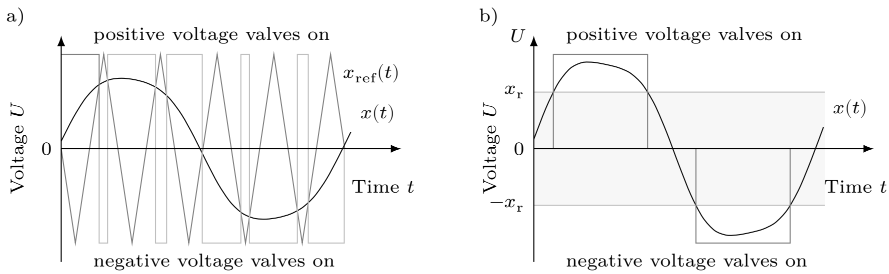

Figure 36: Illustration of basic concepts for converter control PWM (a) and hystersis band control (b)

As visualized, positive voltage valves are activated if the amplitude of the input signal is greater than the amplitude of the reference signal, otherwise the negative voltage valves are activated. In hysteresis band control, it is determined whether the input signal violates a defined voltage range (Fig. 36 b). [77, 153]

3.4 Control systems engineering and control loops

Any system dedicated to improve power quality in electrical networks is required to detect present deviations of the analog electrical signals in comparison to the reference values. Based on the detected deviations, suitable measures for compensation are to be initiated. For this purpose, the deviation of the signal component under consideration initially is to be identified by comparing the actual value and a target value of the signal and subsequently a suitable system response is to be determined in order to reduce the deviation. The calculated response is then effected on the system. Hereinafter it is to be analyzed in to what extent the impressed system response has changed the signal variables in the system and the procedure shown is to be repeated in a loop. In control engineering, this is referred to as a closed control loop. Two fundamental concepts of control loops are known. As previously indicated, for closed-loop control there is a coherence between the systems response and the present characteristics of the input variables. This connection is established as a feedback loop that allows evaluation of the effect of the impressed system response. On the contrary, open-loop controllers lack feedback on the effects of the system response and thus the system to be controlled is influenced without analyzing the results. [154, 155, 156]

3.4.1 Structure and elements of a closed-loop control

Information on the state of the system to be controlled $y(t)$ are referred to as input or control input. Initially, the control input measured using a sensor and its metered value $y_m(t)$ is compared to the reference value $r(t)$. In the present case, for example, the specified reference values originate from power quality standards. Subsequently, the difference of both $e(t)$, the so called control difference, is forwarded into the controller or control signal processing unit for signal analysis as visualized in Figure 37. [156, 157]

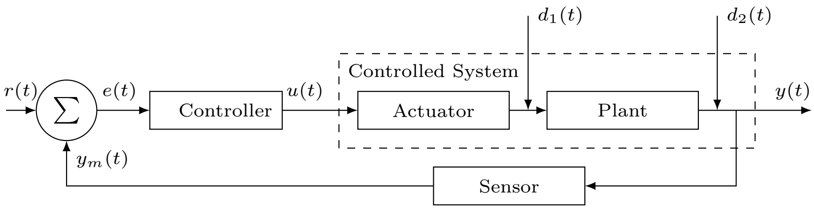

;

Figure 37: Structure of a closed-loop control system

There, a command signal $u(t)$ is calculated based on the transfer function implemented in the controller, which is then fed to an actuator that exerts an influence on the controlled system. In addition to the actuator controlled according to $u(t)$, interference variables $d(t)$ may also have an effect on the controlled system. A distinction is made between interference variables at the inlet $d_1(t)$ and at the outlet $d_2(t)$ of the controlled system. Based on the effect of the actuator on the controlled system, the disturbing variables and the inherent reaction of the controlled system, the instantaneous value of the system status $y(t)$ changes, which in turn is measured by the sensor and repeatedly fed to the comparator as input signal $y_m(t)$ to determine a new error signal. [155, 156]

3.4.2 Subdivision of controller types

Depending on the properties of their transfer function, controllers are distinguished into controllers with a continuous course of the output variable and discontinuous controllers with a graduated course of the output variable. The transfer function of the controller represents a proportional gain of the input signal (P), correspond to a temporal integration of the error signal (I), react to the rate of change of the error signal (D) or be realized as a combination of these individual transfer types. If the transfer function of the controller has only a proportional component, the output variable of the controller $u(t)$ is described as a product of the error signal and the controller constant E.

$$u_P(t) \quad = \quad K_D \cdot e(t) \tag{3.17}$$

If the controller features integrative behavior only, the control value of the controller is generally obtained as an integral of $e(t)$ over time.

$$u_I(t) \quad = \quad K_I \cdot \int_0^T e(t)\,\mathrm{d}t \tag{3.18}$$

In addition, the command signal of the transfer function of a controller operating as a differentiator reflects the rate of change of the error signal, but does not allow any conclusion to be drawn about the amount of deviation represented by the error signal. As no information on the magnitude of the deviation is possible, but only the rate of change is represented in the system response, it is not possible to regulate a controlled system with a pure differentiator. For this reason differentiators are only used in combination with other controller types.

$$u_D(t) = K_D \cdot \frac{\mathrm{d}}{\mathrm{d}t} e(t) \tag{3.19}$$

3.5 Energy storage technologies

An energy storage is defined as an installation with the purpose to store energy recoverable. During charging, the energy to be absorbed is converted into the accumulated form of energy and transferred to the storage medium, thereby increasing the energy content of the storage. On discharging, the energy to be discharged is reconverted and transferred from the storage medium to the accepting system, thereby reducing the energy content of the storage. If the storage is in a completely charged state, it has reached its maximum energy content. In an entirely discharged state its energy content is zero and thus no useful energy is provided. The entirety of all required conversion steps and processes from generation to consumption are depicted in the process chain shown Fig. 38 a.

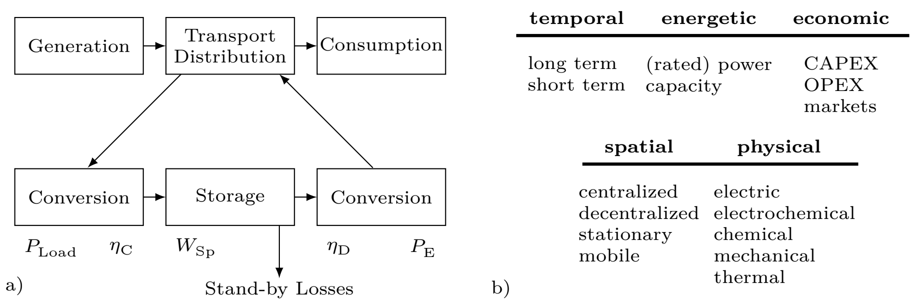

Figure 38: Visualization of the electrical energy storage process chain (a) [158] and subdivision of energy storage systems according to physical, energetic, temporal, spatial and economic aspects (b) [159]

A significant factor for the selection of storage technologies is efficiency. During charging and discharging of a storage device, lossy energy conversions occur. Furthermore, storage itself causes stand-by losses reducing the amount of energy available for reconversion [158].

3.5.1 Systematization of energy storage technologies

As a vast number of different storage technologies is available, systematic classification facilitates technology selection [160, 161, 162]. Storage systems are classified by physical, temporal, spatial, economic and energetic aspects as visualized in Fig. 38 b [159]. Energy occurs in various forms and therefore is stored using different physical principles. Mechanical, chemical, electrical, electrochemical and thermal energy storage systems are distinguished. Available technologies of storing electrical energy are classified according to the criteria type of energy, duration of storage and technical parameters [163]. A further distinction is possible based on functions, response time and duration [164]. Regarding function, a subdivision is possible into application for support of power quality, reliability and energy management [165]. Energy storage technologies for application in the area of power quality and reliability are supposed to feature high power ratings. As provision of power is required for short duration only, storage capacity can be low. In contrast, application of storage technologies for energy management is associated with high capacity and relatively low rated power. Target of storage application in energy management is load balancing and seasonal storage, where long-term energy provision is one of the important contributions [166]. From the perspective of a grid operator, storage technologies are applied on the areas of system services, peak shaving, load balancing, long-term storage, seasonal storage, islanded grids and other sectors as electromobility [167].

Regarding system services, application of energy storages is possible for frequency stability by balancing generation and demand, for supporting voltage stability by providing reactive power and for ensuring compliance with the voltage limits. Furthermore, they are capable of providing rotating reserve in the form of virtual inertia, standing reserve by providing capacity not synchronized with the grid and of black start capability by providing power in the event of a fault in order to assist supply restoration. In peak shaving, energy storages contribute to reducing peak values of electricity demand or supply, which is concomitant by a reduction in costs for electricity and transmission capacities. Long-term storage facilities are required in times of low energy supply by renewable feeders, which are capable of providing energy for several weeks. [167]

3.5.2 Functional principles of important storage technologies

In the following, essential technologies for the storage of electrical energy are presented. Each technology is assigned a number, which is used for identification in diagrams and illustrations to characterize the storage technologies. Flywheel energy storage (FES, 1), vanadium redox flow battery (VRFB, 2), lithium-ion battery (LIB, 3), nickel metal hydride battery (NiMH, 4), supercapacitors (SCPs, 5), superconducting magnetic energy storage (SMES, 6), lead acid battery (LAB, 7), compressed air energy storage (CAES, 8), pumped hydroelectricity storage (PHS, 9) and zinc bromide redox flow battery (ZnBr, 10) are presented. [160, 161, 162]

Flywheel energy storage (1)

In flywheel storages, energy is stored as kinetic energy of a rotating flywheel. In general, flywheel energy storage devices can be distinguished into the two categories high speed flywheels and low speed flywheels. High speed flywheels operate at rotational speeds of tens of thousands revolutions per minute and are designed to enable the highest possible energy density. Costly composite materials that endure high stress caused by centrifugal force are used in high speed flywheels [168]. Furthermore they require auxiliary systems as magnetic levitation bearings as well as devices for evacuation of the flywheel housing in order to reduce mechanical losses. Those auxiliary systems are to be supplied with energy and reduce the efficiency of the system. Low speed flywheels rotate at thousands of revolutions per minute [168]. To achieve adequate rated power and capacity at lower angular velocities, greater moments of inertia are required, resulting in larger rotor diameters and heavier weights. Even though low speed flywheels do not require vacuum for operation, partial vacuum or the replacement of the air in the flywheel housing by gas with low density is reasonable. [166, 169, 170, 171, 172, 173, 174, 175]

Flow batteries as vanadium redox flow battery (2) and zinc-bromide redox flow battery (10)

Flow batteries, which are often referred to as redox flow batteries, are regarded hybrid systems of fuel cells and rechargeable batteries that feature two fluid electrodes. During charging and discharging, electrons are exchanged between the fluids and the electrodes and the ions in the battery cell are converted between different oxidation stages. A unique feature of flow batteries is the fact that the electrolyte is stored separately in fluid tanks and thus outside the battery cell. Accordingly, flow batteries are considered the only battery type where power and capacity are separate and can be expanded independently. Since neither the electrolyte nor the electrodes of the flow batteries are subject to significant aging effects, flow batteries achieve long service lives and cycle numbers. Due to the persistent charge separation in the battery cell, flow batteries achieve fast reaction times. Disadvantages of flow batteries are low specific energy and low energy density of the fluids or high capital costs. As most important types of flow batteries the vanadium redox flow battery (VRB), the zinc bromide (ZnBr) redox flow battery and the polysulfide bromide battery (PSB) are distinguished. As a recent novelty, polymer-based redox flow battery (pRFB) use a battery fluid based on organic polymers instead of metals. Focus of current development of flow batteries are efficiency as well as reliability of electrodes and management of power or energy for large-scale system. [159, 176, 177, 178, 179]

Lithium-ion battery (3)

Lithium-ion battery cells consist of two electrodes, which are separated by a porous membrane containing an ion-conductive electrolyte. The material of the cathode is usually aluminium and the anode consists of copper. During charging and discharging, lithium ions migrate between the electrodes and are stored in active materials adjacent to the electrodes [180]. Due to their high energy density and the resulting low weight, lithium-ion batteries are widely used in mobile phones, notebooks and all types of electric vehicles. [170, 177, 180, 181, 182, 183]

Nickel–metal hydride battery (4)

Nickel-metal hydride (NiMH) accumulators are a technological successor of nickel cadmium accumulators in which the environmentally harmful material cadmium has been replaced by a metal hydride. One electrode of each galvanic cell of these batteries consists of nickel, the other of a metal hydride. Caustic potash is used as electrolyte between the electrodes [180]. NiMH batteries are increasingly being replaced by lithium-ion accumulators and are now used primarily in hybrid vehicles. Previously, they were often also installed in portable devices such as mobile phones or notebooks. [159, 166, 180, 184, 185, 186]

Capacitors and supercapacitors (5)

The functional principle of a capacitor is based on charge separation. Two opposing conductive plates, which are separated from each other by a dielectric, are electrically charged. The charges present on the conductive plates of the capacitor cause an electric field with a field strength proportional to the feeding voltage. Capacity and maximum voltage of a capacitor are determined by the area of the conductive plates, the distance between the conductive plates and properties of the dielectric. Electrolytic capacitors feature an oxide layer as dielectric material, ceramic capacitors have a ceramic dielectric and film capacitors use a plastic film. Supercapacitors are considered an advancement of conventional capacitors and feature both electrostatic and electrochemical energy storage. Essential characteristics of capacitors and supercaps are their ability to provide power and energy very quickly and to withstand high numbers of charging and discharging cycles. [166, 167, 170, 177, 187, 188]

Superconducting magnetic energy storage devices (6)

Superconducting magnetic energy storage devices consist of a superconducting coil, power conditioning and a coolant system that keeps the temperature of the coil below the transition temperature of the superconductor. Energy is stored in the magnetic field of the coil generated by direct current in the coil. Power output is proportional to the variation of the current through the coil. SMES feature the highest number of cycles and best efficiency at high number of cycles. The capacity of SMES is relatively small. [189, 190]

Lead-acid battery (7)

Unlike the other types of accumulators, both electrodes of the lead-acid accumulator are made of the same material, lead. A low-concentrated sulfuric acid serves as electrolyte. Due to their low price, lead-acid batteries are still used today in stationary energy storage systems, although technologies such as lithium-ion batteries are far superior in terms of energy density and power density. Lead-acid batteries are widely used as vehicle starter batteries, as backup source for telecommunication systems, uninterruptible power supply and emergency power supply systems. [191]

Compressed air energy storage (8)

Another possibility for storing energy is compression of gases, where electrically driven compressors induce a pressure difference of the working fluid between a lower pressure level and the storage pressure. The differences in pressure are due to differences in density, as the compressors increase the amount of particles per volume of gas contained in the reservoir. Ambient air is usually used as working fluid. Prerequisite for accumulating energy is the presence of sufficiently dimensioned pressure vessels. Underground salt caverns are used to store large quantities of compressed air. According to the combined gas law, the ratio between the pressure-volume product and the temperature of a system remains constant. As the compression of gases is accompanied by heating as a result of the increase in internal energy, which is released into the environment during storage, compressed air storage systems are associated with low efficiency. [172, 184, 192, 193]

Pumped-storage hydroelectricity (9)

In pumped-storage hydroelectric power plants, the electrical energy supplied is converted into gravitational potential energy by pumping water into a upper reservoir. To recover the energy supplied, the water is fed back into the valley basin via a turbine. This type of energy storage is widely used and implemented in large-scale plants. Due to considerable spatial requirements and the demand for adequate differences in altitude between lower reservoir and upper reservoir, the expansion of storage capacities is limited. Currently, in Germany pumped-storage hydroelectric power plants with a capacity of 40 GW h and a rated power of seven GW are in operation. [164, 171, 194]

3.5.3 Performance indicators of energy storage technologies

The behavior of the available storage technologies differs significantly, due to the individual functional principles. Selection of a storage technology suitable for an individual purpose of energy storage is facilitated and objectified by evaluating available storage technologies based on applicable key performance indicators (KPI). For assessment of storage technologies, a broad variety of performance indicators is available. Hereinafter economical KPI, technical KPI and other KPI are introduced.

Economic performance indicators

CAPEX is an abbreviation for capital expenditure and refers to investment costs including all costs incurred for purchase, installation and connection of the energy storage device. Moreover, for stationary energy storage systems, CAPEX includes costs of power electronic devices, wiring, system periphery, project planning, grid connection, protection devices, energy storage control and sensors. The term OPEX stands for operational expenditure and thus covers all operating costs, which are also referred to as operation and maintenance costs. OPEX consists of fixed annual costs and variable costs. In comparison to an indication of CAPEX or OPEX of a storage system, however, the consideration of costs related to power or energy indicators is more meaningful. Energy capital costs c_{ec} indicate the costs associated with the purchase of a unit of capacity. Power capital costs c_{pc} represent the necessary expenses per unit of power. A subdivision into CAPEX and OPEX per unit of the desired reference quantity is possible as well. In Figure 39 power capital costs and energy capital costs of the selected storage technologies are visualized.

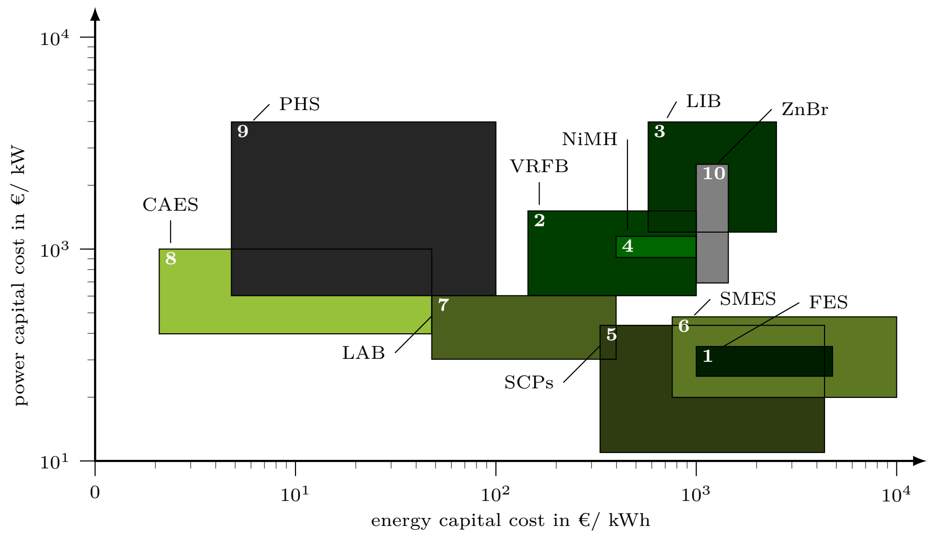

Figure 39: Characterization of the selected storage technologies by their energy capital cost and power capital cost [164, 165, 166, 167, 170, 171, 172, 184, 185, 189, 192, 195, 196, 197, 198, 199, 200, 201, 202, 203]

Technical performance indicators

An important parameter for characterizing energy storage systems is power P, which describes the energy transfer per unit of time and is a measure of how quickly a storage system absorbs or releases energy. A further differentiation is possible between the storage charging rate P_c and the storage discharging rate P_d. Another group of performance-related parameters are storage losses. The power loss $P_\mathrm{L,S}$ represents all losses that occur during energy storage and includes self-discharge losses $P_\mathrm{L,SD}$ and stand-by losses $P_\mathrm{L,SB}$. The capacity of a storage E_max denotes the maximum quantity of energy that can be absorbed into an energy storage system and represents the difference between the highest possible energy level in the fully charged state and the lowest possible energy level in the discharged state. In addition, the stored energy E_t reflects the amount of energy available in the storage at a certain point of time. A comparison of storage technologies regarding rated power and rated energy is provided in Figure 40.

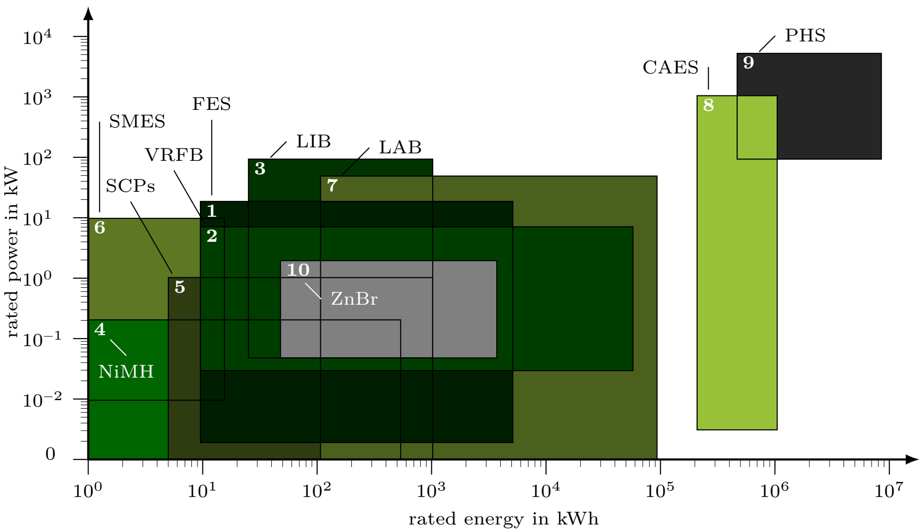

Figure 40: Characterization of the selected storage technologies by their rated energy and rated power [164, 165, 166, 167, 170, 171, 172, 184, 185, 189, 192, 195, 196, 197, 198, 199, 200, 201, 202, 203]

By relating the rated power of an energy storage to the mass of the storage or its volume, power densities are obtained. Gravimetric power density p_m, which is also referred to as specific power, is calculated as rated power per mass. By relating the power to the spatial requirement, the volumetric power density p_V is calculated. For determination of the power densities, commonly the maximum discharging power P_d is used. [165, 171]

$$p_m = \frac{P_\mathrm{d}}{m} \tag{3.20}$$

$$p_V = \frac{P_\mathrm{d}}{V} \tag{3.21}$$

Analogously, the capacity of a storage is related to the mass or the volume of the system in order to obtain energy densities. The gravimetric energy density e_m corresponds to the energy per unit of mass and the volumetric energy density e_V relates the energy to the volume. [167, 204] In Figure 41, selected storage technologies are characterized by their gravimetric energy density and gravimetric power density.

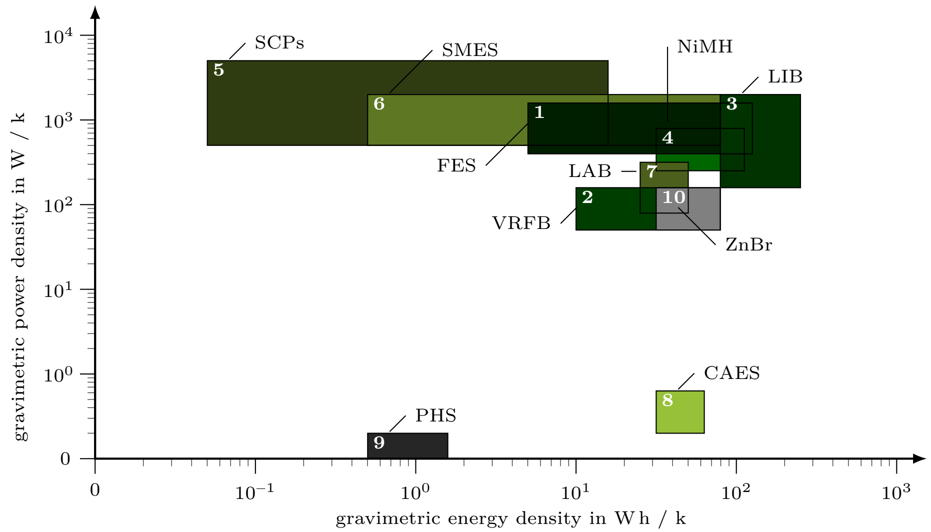

Figure 41: Characterization of the selected storage technologies by their gravimetric energy density and gravimetric power density [164, 165, 166, 167, 170, 171, 172, 184, 185, 189, 192, 195, 196, 197, 198, 199, 200, 201, 202, 203]

In Figure 42 densities of energy and power of selected storage technologies are related to the volume.

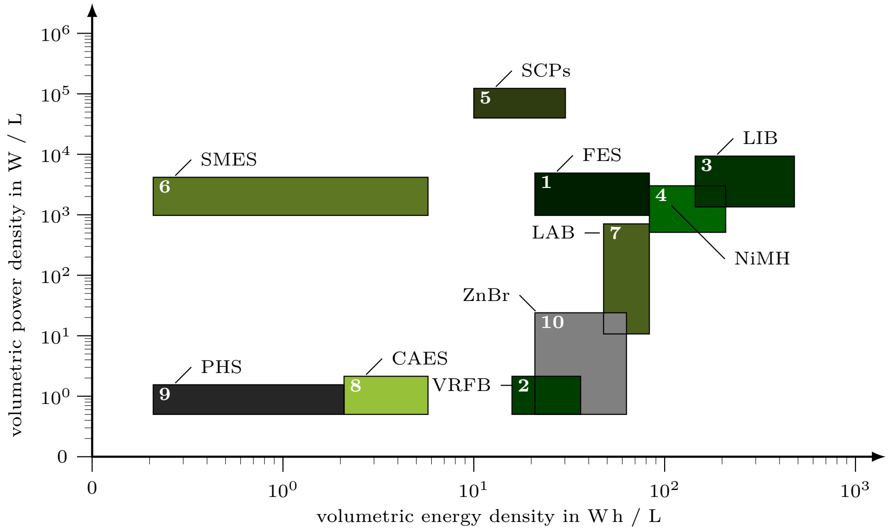

Figure 42: Characterization of the selected storage technologies by their volumetric energy density and volumetric power density [164, 165, 166, 167, 170, 171, 172, 184, 185, 189, 192, 195, 196, 197, 198, 199, 200, 201, 202, 203]

For estimation of the energy present in a storage the indicator state of charge (SoC) has been established, which relates the amount of energy available in the storage E_t to the maximum possible energy quantity E_{max} [177].

$$\mathrm{SoC} = \frac{E_t}{E_{\mathrm{max}}} \tag{3.22}$$

Of particular importance are efficiencies η, as they characterize the performance of a storage by representing the extent of losses in storage processes. Calculation of efficiencies is reasonable, as all processes of energy conversion and storage are accompanied by losses, so that less energy is recovered from the storage in comparison to the amount that has been absorbed. If a discharged energy storage is charged until the maximum possible energy content is reached and then completely discharged again, the round-trip efficiency η_{rt} (Fig. 43 a), also referred to as overall efficiency, is determined by measuring the total energy supplied E_{c} and the total energy recovered E_d.

$$\eta_{\mathrm{rt}} = \frac{E_{\mathrm{d}}}{E_{\mathrm{c}}} \tag{3.23}$$

Charging efficiency η_c is calculated as the quotient of the energy absorbed in the storage, represented as the change of the energy content of the storage ΔE_S and the energy supplied to the storage E_c.

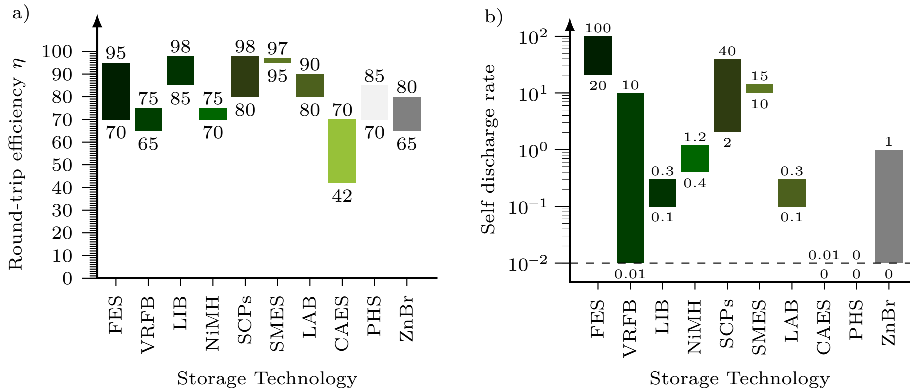

Figure 43: Characterization of the selected storage technologies regarding their round-trip efficiency (a) and their self discharge rate (b) [164, 165, 166, 167, 170, 171, 172, 184, 185, 189, 192, 195, 196, 197, 198, 199, 200, 201, 202, 203]

The same applies to the discharging efficiency η_d based on the recovered energy quantity and the amount of energy present in the storage ΔE_s. Beyond, the efficiency of energy storage η_s is determined by placing the amount of energy present before the start of discharging in relation to the amount of energy present in the storage after the end of charging. The introduced efficiencies are well suited to subdivide the storage technologies with regard to their intended use. Storage applications with a high number of cycles are therefore suitable for storage units with high charging efficiencies η_c and discharging efficiencies η_d. Storage applications with long storage duration require storage technologies with high storage efficiencies η_s. The storage efficiency is usually represented by the self discharge rate, which is defined as the duration within which a completely charged storage is completely discharged due to internal losses (Fig. 43 b.).

Further KPI are available for comparing storage technologies with regard to their lifetime. The lifespan describes the period for which the system is expected to be usable without replacement of core components or complete failure. Lifetime denotes how many years a technology is capable of serving efficiently. Cycle life of a storage technology describes the number of full cycles it is expected to endure under specified conditions before it fails to conform with specified performance criteria.

Other

The maturity of an energy storage technology represents its degree of commercialization, technical risks and economic benefits, which arise of learning effect from mass production and lower production costs. Maturity is distinguished into the five classes developing, demonstration, early commercialized, commercialized and mature. Transportability of a storage system indicates the effort involved in dislocating a storage system. Transportable systems and systems which are built on site are distinguished. Storage systems that involve a distinctive geographic situation for energy storage are not transportable. Storage systems with good transportability commonly feature both high gravimetric energy density and high volumetric energy density.

Further important performance indicators of energy storage technologies concern sustainability. Here, environmental compatibility, recyclability, emission of CO_2 or are to mentioned. Recyclability indicates the extent to which an energy storage system or parts thereof may be reused after the end of its lifespan. Indications on recyclability are commonly qualitative data or assignments to characteristic classes on a scale. Environmental impacts arise from the emission of noise, vibrations or substances during production and operation of a storage. [166, 199, 205]

4 Design of a hybrid compensation system

In the previous chapters, problems of power quality, methods for determining power quality and system services for increasing power quality have been introduced. Now a novel type of equipment is conceptualized, which provides several system services for network operation. As the system compensates for various undesirable occurrences within the electrical network and thus merges an entire bundle of services, it is referred as a hybrid compensation system [206]. Aim of this chapter is to present answers to the questions how the hybrid compensation system has to be constructed and how the storages of the storage system are modeled.

4.1 System services and technical restrictions

The possible functional scope of the system depends on technical restrictions of the components used. Both temporal structure and quantitative structure of power quality deviations are known. It is required that the plant is capable of contributing to improvement of the parameters of power quality both in terms of time and the required power. The rated apparent power of the system is 200 kW. However, the load of the medium-voltage grid is up to 15 MW and the maximum power fed in by renewable plants is up to 25 MW. Due to the relatively low rated power of the hybrid compensation system, exhaustive compensation of power quality deviations is only possible if the power associated with the deviations is low. For example, when at a total grid load of 20 MW distortion reactive power of 200 kW is present due to harmonics, which corresponds to a THD of 1 %.

4.2 Requirements for system control

A contribution of the components used for improvement of power quality is possible only if their interaction is coordinated. This is task of the control system, which collects status information as well as user inputs and generates control commands. Control loops to be used in real systems are more complex in comparison to the basic types introduced in Section 3.4. On the one hand, in many cases it is not sufficient to evaluate only a single input signal of the system, but the controlled system is characterized by multiple state variables. In particular this applies to control tasks of state variables of the electrical three-phase AC systems, where several voltage variables and current variables are to be analyzed. Furthermore, control structures with different time horizons may be intertwined and control tasks of completely different system functions are to be executed contemporaneously. Therefore, the system response of a closed-loop control, represented by an actuator acting on the controlled system according to the command signal, in case of a system operated in order to improve power quality within an AC power system features a proportional conjunction to the magnitude of the error signals. This error signal correspond to the detected deviation from the ideal value of a certain parameter of power quality. Accordingly, structures for controlling such a system will contain a proportional element. Integrating control elements are required where the monitoring of a deviation during a certain time interval is relevant. As an example, the control of the energy exchange between a storage and the grid requires integrating control elements.

4.2.1 Hierarchical structure of the control tasks

The task of control is divided into four subtasks as calcultion of the present power quality, determination of system services to be provided, energy management of the storage system and monitoring of the plant status, as visualized in Fig. 44. A first important area is digital signal processing of the voltage and current signals. Target of signal processing is determination of essential signal attributes for assessing power quality. As a second task, based on the calculated power quality parameters, the system services to be provided by the plant are calculated. Power quality parameters are analyzed by comparing them to limits defined in respective standards. After making individual power quality parameters comparable, an integrated power quality indicator is calculated. Power is distributed to individual system services according to the proportion of the deviation of individual power quality parameters in the integrated power quality indicator. A third task is energy management of the storage system and coordination of power flows. Energy is to be held available in accordance with a forecast and needs to be stored with the highest possible degree of efficiency. Therefore, external information as forecasts of the energy supply, electricity prices or other requirements of the grid operator are included in energy management. Monitoring of safety-relevant status variables and functions is a fourth major task of control. It is important to ensure that the system is always operated in a safe operating condition. Negative mutual interference or excitation of components is to be prevented and the system is to be transferred to a safe state in the event of critical internal or external conditions.

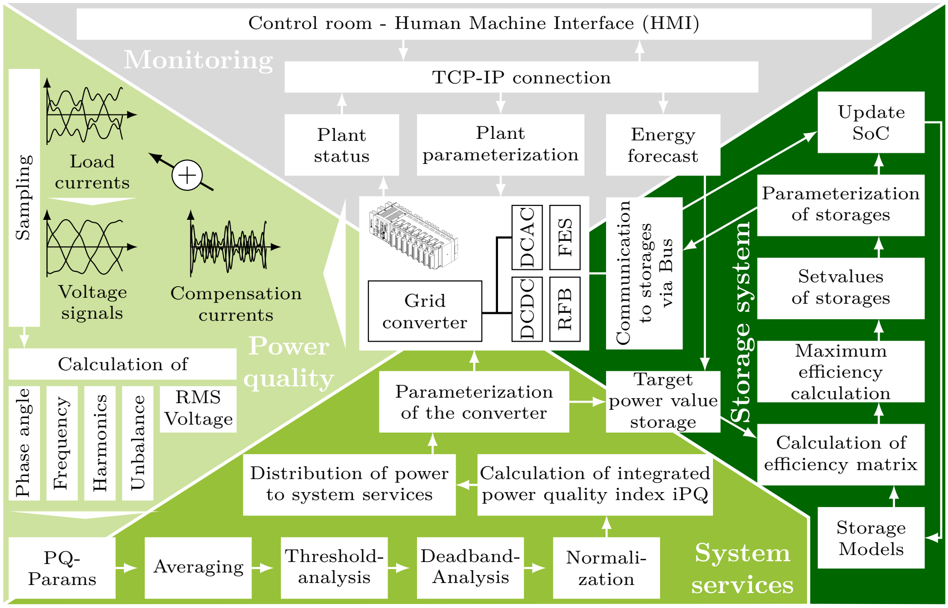

Figure 44: Visualization of major control tasks

The three preceding tasks are surveilled and communication between them is enabled. This includes communication with the network operator's control room and other authorized computers via a TCP-IP based connection. Furthermore, storage and archiving of operational data as well as control of user interfaces are part of this task.

4.2.2 Control hardware and network within the system

The controller of the system is the embedded controller Compact RIO 9038 from National Instruments (Fig. 45 a), which is programmed using the LabView development environment. A dual core CPU with 1.33 GHz clock frequency and 2 Gigabyte RAM are available for the execution of the control algorithms. In addition, signal processing tasks can be performed efficiently on a field programmable gate array (FPGA). In addition, the controller features 8 slots for connection of measurement and communication modules, so that analog measured variables can be digitized directly. The controller also comprises proprietary RS 232, RS 485, Ethernet, USB and display port interfaces, so that the controller can be monitored directly by connecting a monitor and input devices.

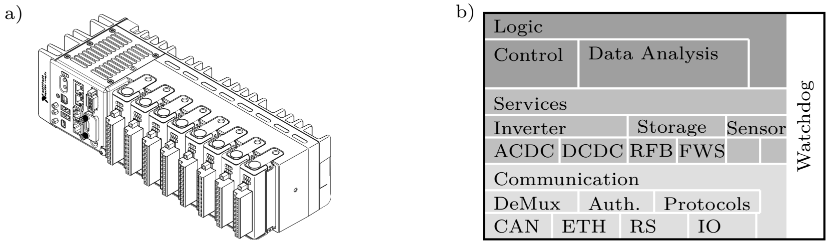

Figure 45: Illustration of the used controller (a) and representation of the layered software architecture (b)

A Modbus-TCP system and a CANopen bus system are available as information networks within the system. Via CANopen, the superordinate control is linked to the controler of the flywheel storage. Modbus-TCP is used to connecting the grid converter, the DC-to-DC converters and the control unit of the redox flow battery.

Field programmable gate arrays (FPGA) are devices that contain an array of programmable fields or of small logic blocks. FPGA are adopted to the desired task after manufacturing by programming. The operations executed by the FPGA are customized by a programmer similar to a dedicated IC designed for an individual purpose. It is possible to implement mathematical operations, calculations and other tasks by combining logical blocks or programmable gates of the FPGA directly. Thus, a variety of problems can be implemented with higher computational efficiency in comparison to using the more abstract instruction set of conventional CPU or microprocessors [207, 208]. At first, FPGA are to be programmed using a configuration bitstream which defines the behavior by specifying the connection between the individual function blocks. Operations executed during one cycle are defined by the configuration bitstream allowing parallel processing of the input data. The scope of tasks is limited by the number of available logic gates [207].

4.2.3 Information structure within the control system

The control system executes numerous operations in parallel. In addition to determination of control commands using algorithms and control loops, tasks of data acquisition, data processing, data storage or communication are continuously required. This includes converting calculated set points into suitable control commands for the respective devices. For structuring the control tasks, a multi-layer software model is developed by distinguishing logic layer, service layer and communication layer (Fig. 45 b). All algorithms for calculating the control variables are executed in the logic layer. This is where the main tasks of controlling system services, energy and power management and plant monitoring are located. These tasks are executed in parallel. Via interfaces to other layers, input data is supplied or results are transported onwards. The service layer contains all services accessed by the logic layer for execution of control tasks. For similar services, object classes are created, for which individual services are instantiated as objects. For example, converters and energy storage devices are created as classes, as they offer similar functions and share a set of identical state variables. Individual services are addressed by the logic layer on the basis of the reference to the corresponding object using assigned functions. The communication layer contains all routines, protocols and libraries required for data exchange via the installed external communication interfaces. This includes information on the structure of the messages exchanged via interfaces and the knowledge of the addresses of the communication partners. Program parts for splitting data packages into several messages, if the information exceeds the permissible word length of a single message, are also located here. Similarly, coherent messages are combined here to form a complete piece of information. Hierarchies of the bus access are also implemented here. Furthermore, access control is implemented in order to ensure that information is only passed onward after authentication and if authorization is present. In addition to communication via bus systems and interfaces, gathering and processing of analog measured variables is carried out via integrated measuring modules. Therefore, the parameterization of the measuring instruments with regard to the sampling rate and the multiplexing or demultiplexing of channels is task of the communication layer.

4.3 Measurement variables required for control

As introduced for basic structures of control engineering, determination of a control signal is based on existing deviations between reference values and actual values of considered parameters. In order to determine the error signal, the instantaneous values are determined using a suitable measurement procedures. Figure 46 below shows which state variables are observed in the electrical grid and in components of the system. In the present case, major control task is to adjust the power output of the converter and the waveshape of the emitted signals with the aim of minimizing the deviations from the ideal level of power quality in the grid.

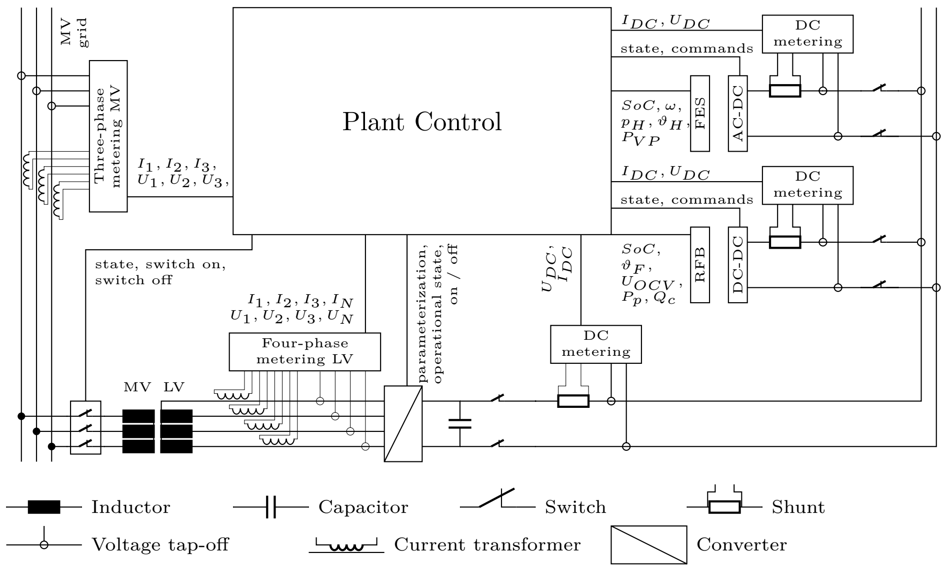

Figure 46: Visualization of observed variables in the grid as well as the compensation system and connection of both measurement equipment and system components to the control system

In addition to the measured parameters of the electrical network to be influenced, measured quantities of internal systems are to be processed as visualized in Figure 47. This is necessary in order to be able to monitor the current plant status and to control the operating parameters within the permissible limits.

4.3.1 Electrical measurands in the grid

The hybrid compensation system is connected to a branch of the medium-voltage network in the immediate vicinity of the transfer station. Accordingly, the state variables of the branch at the connection point to the busbar of the transfer station are interesting input variables. They contain both the voltage of the busbar and the current of the network branch. As the medium-voltage network is a three-phase system without neutral conductors, current and voltage signals per phase are measured. Measurement of electrical signals and determination of power quality parameters at the transfer station is essential for providing system services. On the one hand, the compensation of harmonics always takes place with respect to a certain point in the network, at which the shape of voltage or current signals is analyzed. If the busbar of the transfer station is selected as the point of compensation, it is assumed that a reduction of the harmonic content at this location causes a reduction

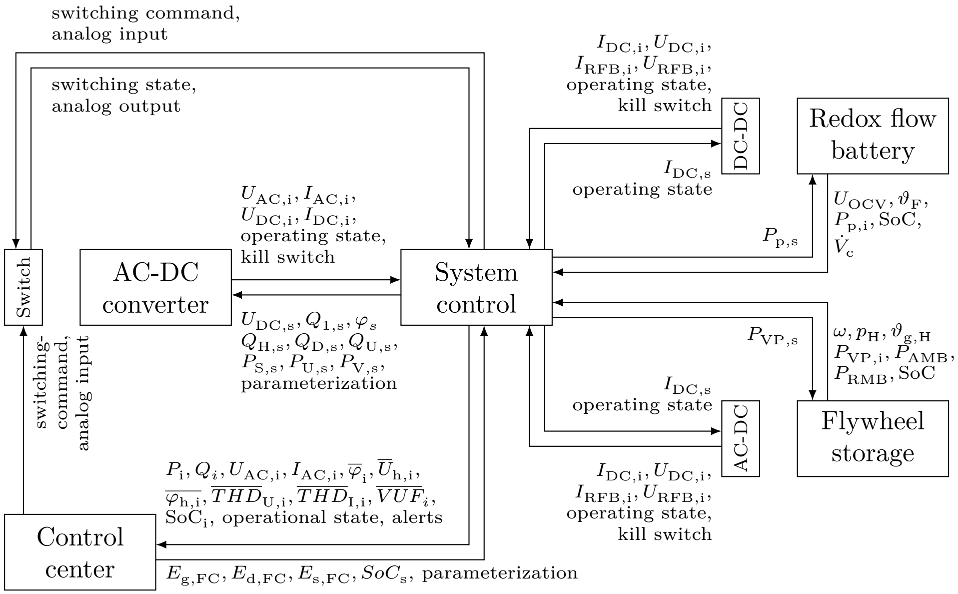

Figure 47: Overview of the information to be exchanged between the components of the hybrid compensation system

of feedback on other network branches without harmonic distortion due to connected devices.
Power quality parameters are usually measured using the per-unit system (p. u.), referring the values of power quality parameters to the corresponding state variable of the network. Relevant parameters are to be determined with suitable resolution. Two decimal places are regarded as suitable resolution. In this range, analog-to-digital converters with a resolution between 16-bits ($2^{16} = 65,536$ steps) and 24-bits ($2^{24} = 16,777,216$ steps) are used. High-precision power quality analyzers with a sampling frequency of 200 kHz per channel and resolutions of 16 bits are used as measuring instruments. Instantaneous values of voltage and current per phase, DC offset per phase, phase angle between voltage and current per phase and spectrum of harmonics per phase are determined. The amplitudes of the integer harmonics up to the 40$^{\text{th}}$ harmonic and their phase angles are derived from the spectrum. The frequency of the fundamental oscillation is also determined, as the line frequency provides information on the overall ratio of generation and load in the grid.

4.3.2 Measured variables in the electrical system of the plant

The electrical system within the installation includes a low-voltage AC system and a DC system between the converter and the battery converters. With regard to the DC link, it is relevant that the voltage U_{DC} remains within a permissible range. By measurement, it is to be determined which power is exchanged over time between the grid and the plant as well as between the storages and the DC link by monitoring the currents at all components $I_{\mathrm{DC},i}$. A voltage measurement is required for control of the DC link voltage. For evaluation of the power flow, however, the currents of the storage converters are relevant. Furthermore, currents I_{LV} and voltages U_{LV} of the AC system are measured.

4.3.3 Processed measured variables of the redox flow battery

To observe and monitor the condition of the redox flow battery, the terminal voltage U_{OCV} of battery cells or battery stacks is measured. The current provided by or drawn from the battery I_c is also measured. A further important parameter is the temperature of the electrolytes ϑ_F, as it has a major influence on the operation of the battery and is directly related to the cell voltage. The power drawn by the fluid pumps P_{p}, which are used to determining the volume flow of the electrolytes through the battery cells, is also used as the input variable for the controller. Furthermore, the concentration of vanadium isotopes in the electrolyte circuits within the battery is observed in order to determine the real state of charge of the battery.

4.3.4 Processed measured variables of the flywheel storage

An essential parameter for assessing the present state of charge of the flywheel storage is the angular velocity ω of the flywheel, which is observed in the unit hertz. In addition, the pressure of the mixture of gases inside the flywheel housing p_{H} is measured, as it exerts an influence on the gas friction of the flywheel. Furthermore, the power consumption of the active magnetic axial bearing P_{AMB} and the active magnetic radial bearings P_{RMB}, which are processed by the flywheel controller and only indirectly passed on to the overall system controller, are relevant, as they provide information about the correct functioning of the flywheel storage. The power consumption of the vacuum pump P_{VP} is also passed on to the system control. In addition, the temperature of the flywheel storage system is transmitted to the control, as deviations from the specified limit values indicate a malfunction of the cooling system.

4.4 Temporal structure of data acquisition and control

The majority of the observed input variables fluctuate over time. Accordingly, a continuous evaluation in suitable temporal resolution is necessary. Time specifications for measurement are based on the rate of change of the quantities as well as on the relevance of alterations for the operation of the plant.

Suitable observation of power quality parameters is most important, as inadequate or faulty analysis results in inadequate control of the system. As a consequence, power quality is either increased insufficiently or, as a worst case scenario, reduced due to operation of the hybrid compensation system. Internal status variables, whose deviation from the target values exert immediate impact on the operation of the plant are of great importance. This applies to the voltage of the DC link, which is incapable of transferring power between the storages and the converter or to serve as a short-term buffer for signal generation in the event of a impermissible voltage deviation. Parameters with slower fluctuation are fluid temperature of the electrolytes, gas pressure in the flywheel housing or temperatures of the flywheel storage as well as the power converters. On occurrance of intolerable deviations, those are transmitted to the control immediately using interrupts.

4.4.1 Temporal structure of calculating power quality parameters

Determination of power quality parameters is coupled to entire signal periods of the fundamental oscillation of the analog input signals. Accordingly, the temporal structure of gathering measured values is oriented to the period duration of the signals of 20 ms. In order to transmit a measurement result to the controller at intervals of 100 ms, 5 signal periods of the observed signals are jointly evaluated. The calculated power quality parameters are averaged in control over time in order to enable smooth adaptation of the system behavior to changes of the power quality parameters.

4.4.2 Monitoring and control of the DC link voltage

Voltage and current values at the DC link measurement locations described are measured at intervals of 100 ms and with a resolution of 16 bits. From these quantities, the exchanged power is also calculated in a time step of 100 ms and compared with the target values. Finally, the power of the power converters on the DC link is adjusted in steps of one second. The control system forwards set points for the DC link currents to be set to the storage converters.

4.4.3 Processing of power quality parameters to control commands

According to the approaches for determining parameters of power quality introduced, in general, not individual metered values are analyzed for control of the plant, but a series of samples over a number of complete signal periods are evaluated. For control of the converter regarding provision of system services, immediate adjustment of parameterization is not necessary in normal operation. Therefore, within the plant control, a distinction is made regarding the length of periods over which average values of power quality parameters are calculated and time intervals of parameterization. This is executed in time steps of one second or 100 milliseconds. In case the present values of the considered parameter of power quality are within the permissible range determined by the applicable standards, the period of averaging is one second. On violation of the permissible range of a power quality parameter, in addition to long-term analysis a fast adjustment of the behavior of the plant is required. For this purpose, the level of deviation in comparison to the ideal value is analyzed over a suitable, shorter period and a new set of variables for parameterization of the converter is generated. As a last case, on occurrence of a severe disturbance, immediate adjustment of the plant behavior is required. In order to be able to handle those events, beyond the procedures for calculation of power quality parameters methods for fast detection of disturbances are implemented, which may trigger instantaneous changes in the plant behavior.

4.4.4 Time horizon of energy management

In energy management, planning intervals are oriented to the usual regulatory interval of 15 minutes. Forecast variables in temporal resolution of 15 minutes are fed, the target state of charge are planned for all interval boundaries and energy quantities to be exchanged are calculated. The observed consumption or provision of energy of the system is transmitted to the grid operator with a resolution of 15 minutes for billing purposes. Planned target values of energy management are converted into target power values for the active power to be exchanged throughout any 15-minute time interval. For this purpose, target power values are calculated in steps of one seconds. Based on distribution functions, whose parameters are determined in dependence on the amount of energy to be exchanged during a 15-minute time interval, for each second of the interval a target power value is derived.

4.4.5 Control of the power output of the storage system

According to the temporal structure of target power values, the power provided by the storage system is supposed to be adjusted in time steps of one second. As deviations of the actual power values of the storages occur, for example due to fluctuations of the DC link voltage or state variables of the storages, tracking is required in shorter time to ensure compliance with targets. Therefore, currents and voltages are analyzed in a period of 100 ms and discretized power adjustments are parameterized to the storages.

4.4.6 Status monitoring of the storage system

The real energy storages of the hybrid storage system are simulated using models, which are introduced in Section 4.7 and Section 4.8 in the plant control system. These models are used for monitoring of the plant condition, determine the effects of different charging and discharging capacities on the charging conditions and determine the power distribution to the storages with the highest possible efficiency. In addition, the storage models are used to control the auxiliary units according to the functions determined. As deviations between calculated values and real quantities occur, state variables in the model are periodically overwritten with measured values. The measurement interval of the state variables fluid temperature, ion concentration, internal housing pressure and power consumption of the magnetic bearings is one second each. If the measured quantities lie within the permissible intervals, the quantities in the models are overwritten in a time step of 10 seconds. If the limit value is exceeded, a reaction is initiated immediately.

4.5 Derivation of the design from the function range

The target pursued by development of the hybrid compensation system is to influence the signal parameters of the current and voltage signals in the medium-voltage network. By appropriately influencing these signals, they are approximated to their ideal values or ideal courses. Consequently, it is necessary that the system is equipped with devices capable of influencing the signal characteristics as well as for their measurement. The structure of the plant and its components is visualized in Figure 48. The electrical network under consideration is a three-phase AC system.

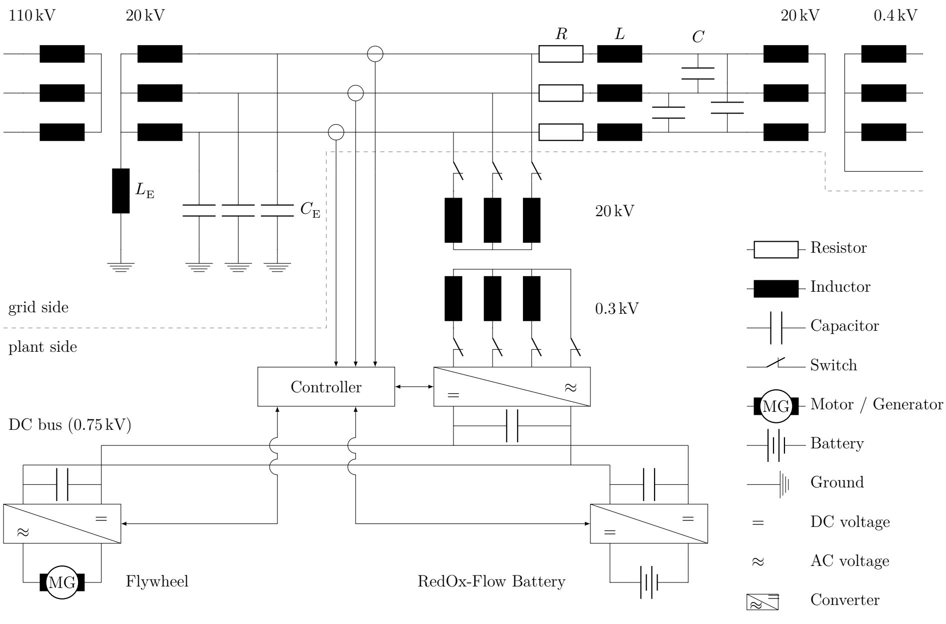

Figure 48: Draft of the hybrid compensation system and its components

The system is installed at the transfer station to the superordinate high-voltage grid in the medium-voltage network. Compensation currents are to be injected there. The signal characteristics of the compensation currents are set according to the power quality parameters present at the connection point. Power converters are devices capable of providing arbitrarily adjustable current signals. As the operating voltage of power converters is limited and an energy storage, which is operating at a lower voltage level, is connected via the power converter, a transformer is provided between the grid and the converter. In order to be able to provide current signals to compensate for power quality deviations, an energy storage is required. Short-term energy storage, for instance to provide distortion reactive power or displacement reactive power, is effected using capacities. Active power is provided from energy storages connected to the converter my means of a intermediate circuit, which is designed as a DC voltage system. By using a DC link as intermediate circuit, the total capacity for provision of short-term energy storage is increased due to the capacities of the storage converters. Furthermore, regulation of a DC link is simpler in comparison to a AC voltage system.

A suitable instrument for influencing the signal parameters are programmable three-phase power converters with DC link and sufficient switching rate. By appropriately controlling the PWM of the converter, current flows are drawn from or supplied to the grid and thus voltage signals are influenced. By buffering energy in the DC link and then feeding it back into the grid with a time delay, a temporal shift of power is accomplished within a phase or between different phases. Central component of the system is therefore a programmable converter with adjustable pulse width modulation. Here, a converter featuring a switching frequency of 20 kHz is used, which is capable of compensating harmonics up to the 40th harmonic within the scope of the power quality standards. Compensation of reactive power and unbalance is possible without temporal problems as well. Specification of an angular deviation of the fed-in voltage signal from the signal curve observed in the network is possible. By drawing electrical energy from individual phases, feeding it into the DC link of the converter and supplying it into another phase from the DC link, it is possible to compensate present unbalance. By installing the system at the transfer station to the superimposed grid level, the currents exchanged with the feeding grid are balanced. Balancing of the currents in the direction of the loads of the grid is not possible. As it is aimed at enabling storage as well as feed-in of active power and to include provision of active power in the provision of system services, the system also includes an energy storage. The storage system serves various purposes with different temporal requirements. Therefore, it is required that the installed storage is able to meet both short-term and long-term requirements and that it is capable of providing or absorbing power and energy in sufficient scope. For that reason, the storage system is designed as a hybrid storage system and includes two independent energy storage technologies with different characteristics. As elaborated in KPI analysis of available, individual storage technologies feature characteristic advantages and disadvantages. However, there is no storage technology available that exhibits the best overall performance in terms of all relevant indicators. According to the presented KPI lithium-ion storages are in many cases feature good values. They combine high energy density, power density, as well as large capacity. In addition, lithium ion batteries have high efficiencies, low losses, fast response times and low investment costs. Redox flow batteries moreover feature lower self discharge rates as lithium ion batteries as well as lower energy capital costs and power capital costs as visualized in Figure 49 a.

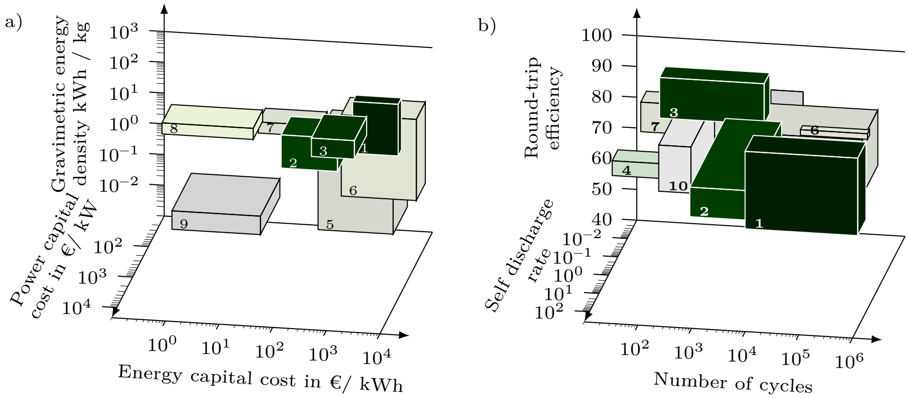

Figure 49: Characterization of the selected storage technologies as introduced in Section 3.5.2 by their volumetric energy density and volumetric power density (a) as well as their gravimetric energy density and gravimetric power density (b) [164, 165, 166, 167, 170, 171, 172, 184, 185, 189, 192, 195, 196, 197, 198, 199, 200, 201, 202, 203]

The storage technologies nickel-metal hydride battery (4) and zinc-bromide redox flow battery (10) are hidden by the other storage technologies and are not shown due to their low relevance. Accordingly, they are better suited for the long-term storage of large amounts of energy. A further argument for the application of a redox flow battery is the separation between energy storage and energy conversion, so that an expansion of the capacity is possible. Redox flow batteries and flywheel storages surpass lithium-ion storages in terms of cycle numbers (Fig. 49 b). It also becomes evident that the self-discharge rate of the flywheel is by far the highest. Vanadium redox flow batteries, however, achieve comparably good values as a lithium ion accumulator.

In order to support system operation, the storage is connected to the converter. Technically, this is solved by designing the converter as a bidirectional converter, being capable of providing power flows between the grid and the storage. In order to decouple the storage from the DC link, to transfer power between the storage and the DC link, and to control the power output and consumption, the DC link is separated from the storage by further power converters connected to the storages. As a hybrid storage system consisting of short-term storage with high rated power and long-term storage with large capacity is used, it comprises two converters connected to the DC link. The redox flow battery features a DC-DC converter and the flywheel comprises an AC-DC converter. The DC link capacities of the storage converters increase the total capacity of the DC link.

The voltage level of the medium-voltage network is 20 kV. Available IGBT converters with appropriate switching rates feature voltage limits of 1000 V. The cell voltage of a single cell of a redox flow battery varies between 1 V and 2 V. In order to use a converter for the provision of system services and to achieve an acceptable size of the battery stacks, in which several battery cells are connected in series for voltage increase, a voltage transmission between the grid and the other system components is required. For this purpose, a transformer is provided between the medium-voltage grid and the converter. It transforms the grid voltage of 20 kV into low voltage with an effective value of 300 V. For connection to the three-phase AC system, it is necessary that the converter is capable of generating both positive and negative voltages. Accordingly, the voltage difference of the DC circuit is split by isolating the center point from the bus bars and grounding it using two capacitors. The nominal value of the potential difference of the DC circuit of 750 V is thereby converted into a maximum positive and a maximum negative voltage amplitude of 375 V each. This voltage amplitude corresponds to the maximum peak value of an alternating voltage signal generated by the converter. According to the relationship between peak value $\hat{U}$ and effective value U of an alternating voltage $U = \hat{U}/\sqrt{2}$, the effective value of the alternating voltage is 265 V. A phase-to-neutral voltage level of 265 V for each phase conductor is suitable for feeding into the medium voltage grid via a standard transformer between 400 V low voltage and 20 kV medium voltage. The effective voltage value of 400 V refers to the phase-to-phase voltage of the three phases of the AC voltage system and corresponds to a phase-to-neutral voltage of 230 V each. In three-phase systems, the interlinking factor between phase-to-neutral voltage and phase-to-phase voltage is $\sqrt{3}$. Consequently, the maximum phase-to-phase voltage, that can be achieved based on the voltage difference of the DC circuit, is 460 V. As the DC link voltage does not remain constant if input or output power changes, but fluctuates, it is to be ensured that an adequate voltage level is maintained for converter operation. The permissible fluctuation band of the DC link voltage is set to the range between 720 V and 780 V. Based on those default values, permissible fluctuation of the maximum possible phase-to-neutral voltages is in the range between 255 V and 275 V and the fluctuation of maximum possible phase-to-phase voltage is between 440 V and 477 V.

The voltage level of the low voltage system with an effective value of 300 V is provided, even if a further reduction, for example due to the modulation depth of the converter, is taken into account.

The electrical system comprises all components involved in the transmission of electrical power between the medium-voltage grid and the converter as well as the energy storages. Within the plant, the medium-voltage system, the low-voltage system and the DC voltage system are distinguished. In addition to the described electrical structure of the plant, an IT structure is required for controlling plant operation. This includes recording of measured values at suitable points in the network and within the plant. Furthermore, transmission lines for measured variables or measurement data are required. As, for example, the storages and the converter feature proprietary control units, the connection between these components and the system control is established via bus systems.

4.5.1 Structure and components of the medium voltage system

The medium voltage AC system connects the system to the grid at the coupling point and to the medium voltage side of the transformer (Fig. 50).

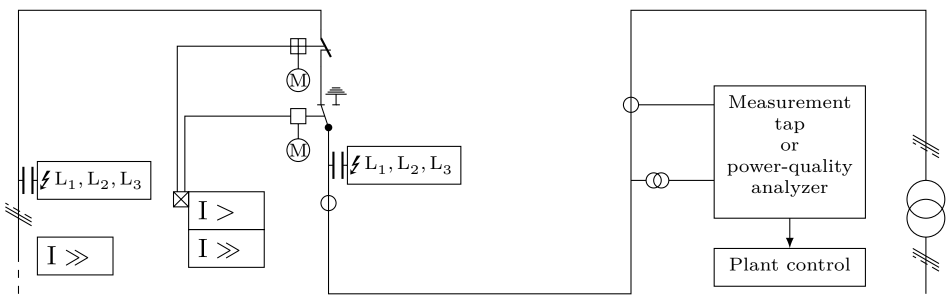

Figure 50: Circuit diagram of the medium voltage AC system of the plant

It comprises all necessary elements, in particular cables, lines, busbars, switchgear and isolating devices, measuring taps or measuring transformers for current and voltage as well as protective equipment. A further task of the AC system at medium voltage level is controlled and safe connection and disconnection of the system to the grid. For this purpose, the AC system includes switches and disconnectors for each phase or conductor connected to the grid. The following requirements are to be met by the devices for switching and disconnecting. It is required to be able to trigger the separation of the system from the grid by the control center. Restarting and reconnection is possible by means of a switching command emitted by the control center of the grid only. In addition, a manual switching possibility is provided for emergencies. Automatic restarting in the event of a fault is prohibited.

First, a fault indicator is connected, which serves to locate faults in the entire network. As on occurence of faults the current in individual conductors rise significantly ($I \gg$, as visualized in Figure 50), the functional principle of those fault indicators consists in detecting those overcurrents. For visualization whether voltage is present at the medium voltage system, an integrated, three-phase voltage detector (⚡) is subsequently connected. The medium-voltage system is then passed through a motor-operated switch-disconnector, which acts both as a circuit breaker and disconnector. It enables both the switching of loads while suppressing arcs and creating an adequate isolating distance that prevents accidental reconnection. A manually operated grounding switch is subsequently provided, which enables electrical interlocking. Accordingly, it can only be switched when the disconnector is off. In order to be able to check whether voltage is present at the medium voltage system behind the switchgear, an additional voltage detector is installed. This is followed by a measuring tap for an overcurrent protection device, which is capable of tripping the switch-disconnector of the system if impermissible current loads are present. In addition to overcurrent protection, other functions of the device are frequency protection, negative-sequence protection, breaker failure protection and sensitive ground-fault direction detection. Furthermore, the medium voltage system includes measuring taps for current and voltage, to which a power quality analyzer is connected in order to determine relevant power quality parameters. Finally, the medium voltage system ends at the terminals of the transformer to the low voltage system. Requirements are to be met by the measuring instruments or measuring taps of the AC voltage system at medium voltage level. A requirement for current measurements is angular accuracy of the measuring instruments. Any angular deviation between the phase angle of the metered signal and the phase angle of the measurement signal is to be avoided. Otherwise, the indication of the angular deviation caused by the measuring instrument is to be denoted. High-precision, capacitive voltage dividers are suitable for connection of voltage measurement devices.

4.5.2 Structure and components of the low voltage system

The low-voltage AC system connects the transformer to the AC side of the converter. Therefore, the AC voltage system comprises all necessary elements, in particular cables, busbars, switchgear, isolating devices, measuring taps or measuring transformers for current and voltage as well as protective equipment (Fig. 51).

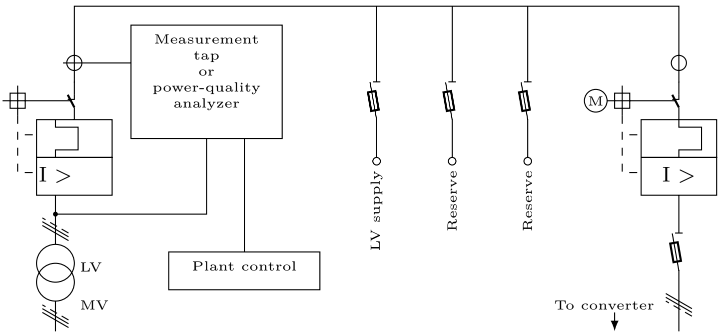

Figure 51: Circuit diagram of the low voltage AC system of the plant

After the transformer, there is a metering tap for the voltage signals, to which both a surge detector and measuring inputs of the system control are connected. After that, a manually operated circuit-breaker with overcurrent detection (I >) and temperature-sensitive protection tripping is installed. Current transformers are present behind the circuit-breakers to measure the phase currents, which are also connected to the measuring inputs of the system control. A low-voltage busbar is supplied comprising four connector panels, one of which is used for the low-voltage supply of the system components. Another one is used to connecting the converter and two connector panels remain unused as a reserve. All connector panels are protected by fuses. Another motor-operated circuit-breaker with overcurrent detection (I >) and temperature-sensitive protection tripping as well as a current transformer are installed at the connector panel for the converter.

4.5.3 Structure and components of the DC system

The DC voltage system connects the DC side of the converter to the DC link of the plant, to which both the DC-DC converter of the redox flow battery and the machine drive of the flywheel storage are plugged. In Figure 52 the structure of the DC system is visualized. Starting at the terminals of the converter, a motor actuated DC circuit-breaker with overcurrent detection (I >) and temperature-sensitive protection tripping switch is connected. In order to determine the current exchanged with the converter, a shunt is installed after the switch.

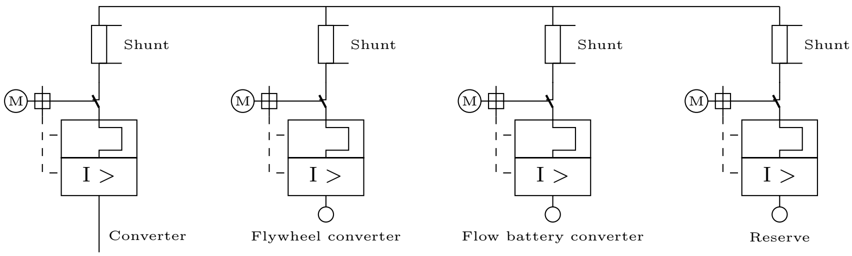

Figure 52: Circuit diagram of the DC system of the plant

Then a DC busbar is supplied which connects three connector panels. Each connector panel comprises a shunt and a motor actuated circuit breaker. One of the connector panels is connected to the machine drive of the flywheel storage. A second connector panel serves to connect the DC-DC converter of the redox flow battery. The third connector panel remains unused. For purpose of determining the currents within the DC system, the shunts are connected to measurement inputs of the system control.

The current carrying capacity of the DC system is to be designed according to the expected power values of the components connected. The total nominal power of the energy storages is 100 kW. Moreover, the nominal value of the voltage level of the DC bus is set to 750 V. Voltage fluctuations within a range of $\pm$ 30 V to the nominal value are permissible, as all components endure variations in this range. Assuming a maximum power value of 150 kW and a minimum voltage level of 720 V, the lower limit of current load capacity is 210 A. Arbitrary fluctuation of the DC link voltage is not permissible, as a violation of voltage restrictions of the components is a consequence. Therefore, deviations of the DC link voltage are corrected using closed loop control. The DC link is designed as earth symmetric system. Therefore, the absolute value of the line-to-earth potential is equal for both bus bars. Charges are supplied to the DC link or drawn from it by the power electronic devices. The voltage of the DC link corresponds to the charge Q_C which is present at the capacity C_{CTI} of the DC link.

$$U(Q) = \frac{Q_C}{C_{\mathrm{CTI}}} \tag{4.1}$$

If the voltage of the DC link is at its set point, a charge Q_{CTI} is present at C_{CTI}. In case that supplied power and drawn power differ, the quantity of charge supplied is not equal to the quantity of charge drawn. The charge quantity of the capacity of the DC link is altered and accordingly the voltage of the DC link changes. Voltage control of DC links is usually based on control algorithms using proportional–integral controllers (PI), proportional–integral–derivative controllers (PID) or fuzzy-PD controllers [209, 210].

The task of controlling the DC link voltage is provided by the converter connected to the grid. It continuously measures the DC link voltage and compensates for deviations towards the default value by supplying or discharging charges. Accordingly, a current between the grid and the DC link is invoked by the converter in such a way that the voltage remains within defined limits. Associated with this control concept is the circumstance that the power exchange between the converter and the DC link can no longer be set arbitrarily by the control. If provision of a desired power value is parameterized to a power electronic device, its control system measures the terminal voltage and aims at establishing a current corresponding to the requested power value. For a given DC link voltage, a target current between the DC link and the converter is a consequence, disregarding current flows required for voltage control. Accordingly, control of the DC link voltage is not possible in this scenario.

To enable control of the DC link voltage by the converter, planned power exchange between the grid and the storage system is set indirectly by parameterizing the current output of the storage converters to the DC link. In order to keep the voltage of the DC link constant, the converter balances the currents fed in or drawn by the storage converters and the grid.

4.5.4 Characteristics of the AC-DC converter

The AC-DC converter is a 3-level IGBT with DC link, which is designed as a three-phase four-wire converter. Accordingly, three bridges of the converter are connected to the three phases of the AC voltage system and the center of the earth-symmetrical DC link is connected to the neutral conductor of the AC voltage system (Fig. 53).

The efficiency of the converter is 97.7 % in normal operation and 97.4 % in operation at maximum load [211]. The switching frequency of the converter is 20 kHz, its reaction time is less than one millisecond and the pulse pattern is set by a proprietary controller [211]. Operation of the power converter is permissible in a temperature range between 0 °C and 40 °C. At higher temperatures, the output power is throttled. Communication between the power converter and the control system of the hybrid compensation system is possible via Modbus-TCP.

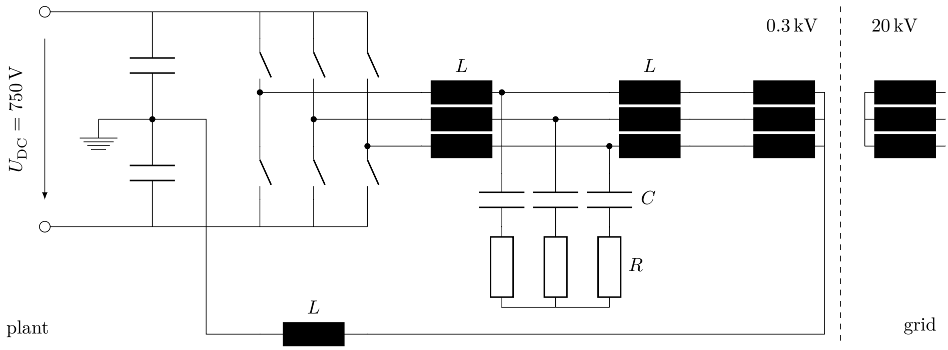

Figure 53: Layout of the grid converter of the hybrid compensation system and its connection to the transformer of the plant [212].

To provide system services, the converter is operated in current-controlled mode, in which no active power control is possible on the AC side. However, reactive power, unbalance between phases and harmonics are compensated in parallel and simultaneously. Harmonic compensation is performed either at the connection point or at any reference point, the point of common coupling, at which the signal parameters are measured. For compensation at the point of common coupling, the degree of compensation of individual harmonics is set. Unbalance is reduced by compensating the difference between the fundamental oscillations of the three phase currents, in order to obtain a symmetrical network load. Displacement reactive power is controlled based on a constant reactive power specification by providing a defined reactive power at the system connection point. If the system control detects a change of the phase angle, the power converter is provided a different setpoint for the reactive power.

4.5.5 Properties of the converter of the redox flow battery

A bidirectional, modular converter is used to connect the redox flow battery to the DC link. This allows charging of a battery connected to the DC link as well as feeding energy back into the DC link. Voltage limits are set for both charging and discharging. Each converter module features a minimum efficiency of 95 % and a maximum efficiency of 97.5 % [213]. The reaction time of the converter to changes in the parameterization including dead beat is less than 10 ms. Overloading of the converter is permissible up to 150 % for one minute, or up to 125 % for a maximum of 10 minutes. The rated power of each converter module of 8 kW is achieved in a temperature range between −5 °C and 40 °C. Operation of the converters below −5 °C is not permitted.

With a further increase in the converter temperature above 40 °C, the permissible power drops linearly to 50 % of the rated power, until the maximum permissible temperature value of 60 °C is reached. Continued operation is not permitted above this level [213]. For power exchange between redox flow battery and DC link, 6 modules of the DC-DC converter are used. These are parameterized via ModBus-TCP. Between the system control and the modules of the DC-to-DC converter, a proprietary control unit is required, which translates the communication between the system control and the control unit via an Ethernet connection into communication between the converter modules and the control unit via the RS 485 interface standard. Minimum and maximum current values are specified by the controller. Likewise, for each individual converter module a target current is set in an increment of one ampere. The target current refers to the battery current. If a battery voltage in the range of 100 V is assumed, this results in power steps of 100 W. As the battery voltage fluctuates constantly depending on the state of charge and the operating modes charging or discharging, the power changes accordingly.

4.5.6 Features of the flywheel machine-drive

The machine drive of the flywheel storage is an IGBT between a DC voltage system and a three-phase AC voltage system of the motor-generator unit. The DC link voltage fluctuates between 720 V and 750 V and the switching frequency is 10 kHz. The capacity of the converter on the DC link is 400 mF. As operating modes of the AC-DC converter, in addition to an idle mode, torque control mode and a mode for controlling the voltage of the DC link are available. The torque control mode allows a preset power value to be converted into a corresponding torque, accelerating or decelerating the flywheel rotor. Thus, controlled charging and discharging of the flywheel is possible. In voltage control mode, the converter of the flywheel storage controls the voltage of the DC link, provided that sufficient power is stored in the flywheel for this purpose. This mode is not required in normal operation of the hybrid compensation system, as voltage control of the DC link is task of the grid converter. [213]

4.5.7 Properties of the transformer

For connection of the hybrid compensation system to the medium voltage grid, a transformer is required to overcome the difference between the voltage levels. The layout of the transformer has to comply to restrictions defined by functions of the plant. It has to transform the AC voltage from 20 kV of the grid to the system voltage of 0.3 kV. As standard low voltage level is 0.4 kV, a custom-made design of the transformer is required. As depicted in Figure 48, the AC circuit on low voltage side features a neutral point and on the medium voltage side no neutral point is present. The neutral point of the low voltage side is connected to the converter.

4.6 Hybrid storage system

Provision of system services is associated with influencing both amplitude and wave shape of current and voltage signals by provision or deduction of power. Hence, suitable provision of power or the ability to accumulate the power in the storage according to the current requirements is task of optimized operation of the hybrid storage system. Availability of the hybrid storage system in terms of the ratio of time, in which the storage can cover the hybrid compensations systems energy demand to total time is to be maximized. A further target of optimization is energy efficiency. By the control of the hybrid energy storage system it is to be ensured, that the amount of energy that is recovered from the storage is maximized. Accordingly, the amount of energy which is lost due to processes of energy conversions is to be minimized. As the system is continuously operated and charging and discharging of the storages takes turns in short temporal periods, complete charging and subsequent complete discharging is rare. Consequently, it is task of plant control to ensure the highest possible energy efficiency despite varying short-term power flows as well as unknown storage duration. Within the hybrid storage system under investigation, a redox flow battery with a nominal power of 40 kW and a capacity of 20 kW h is used. As a second storage, a flywheel storage with a nominal power of 60 kW and a capacity of 3.6 kW h is present.

4.6.1 Requirements regarding the storage system

First and foremost, the hybrid storage system is intended to adequately supply or absorb electrical energy according to the demand of the hybrid compensation system. Secondly and similar to a conventional energy storage, the hybrid storage system is supposed to contribute to balancing of supply and demand by absorbing amounts of electrical energy during periods of generation surplus and to provide energy in times of excess demand. Third, energy is to be handled as efficiently as possible in order to avoid losses. Time steps of consideration for energy exchange with the grid is defined in accordance with the regulatory framework. During operation of the hybrid compensation system, power demands with varying temporal structure are expected. Both power variations in a timescale of 100 ms and energy management with a scope of several hours are to be met. Accordingly, the storage is supposed to feature excellent cycle life and fast reaction times for reactions to power variations at low standby losses. Losses of energy conversion are supposed to be low. Furthermore, high operating life as well as low cost of the storage is desirable for economic feasibility of the system.

4.6.2 Architectures of hybrid energy storage systems

As already introduced, hybrid energy storage systems consist of at least two storage technologies. However, no statement has yet been made as to how the storage technologies are connected within the storage system. Subsequently, the architecture of a hybrid storage system describes the mode of connection of the individual storages within the hybrid storage system. In general, a distinction is made between the approaches passive parallel connection, cascaded converter and shared bus topology [214]. In passive parallel connection (Fig. 54 a), the individual storages of the system are connected to the peripheral system in parallel via a common converter. Accordingly, the storages share a common terminal voltage level and are permanently connected to one another. Direct control of the distribution of power to individual storages by the converter is not possible. Control of power distribution is possible by influencing of the storages only. Furthermore, it is possible to connect

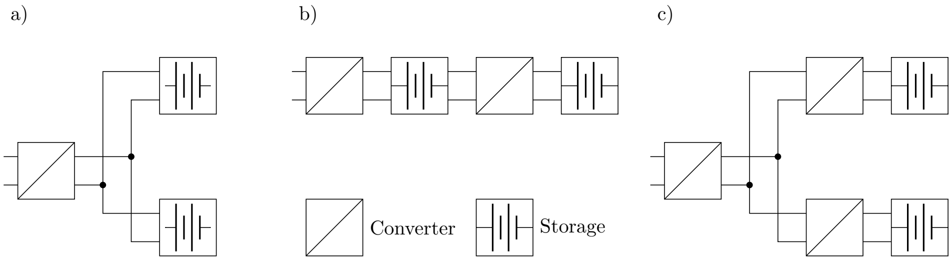

Figure 54: Structure of the available charge transfer interconnect (CTI) concepts passive parallel connection (a), cascaded converter (b) and single shared bus (c)

the storages of the system in series, with power converters located between the storages. This architecture is called a cascaded converter and has a basic structure as depicted in Figure 54 b. As several power converters are required, one disadvantage of this concept is higher conversion loss. A characteristic of shared bus architecture is that all storages of the hybrid energy storage system are connected via a power converter to a bus bar, which is connected to the peripheral system using a common power converter (Fig. 54 c). This approach allows the highest degree of freedom with regard to the control of the individual storages, as here energy can arbitrarily be exchanged via the bus bars, also referred to as charge transfer interconnect (CTI). A CTI is defined as a medium carrying an electric current which flows among components of a hybrid energy storage system as storage devices or a power converter towards the peripheral system [215, 216]. With regard to the design of the CTI, different concepts are available which have a considerable influence on the operation and efficiency of the hybrid energy storage system [217]. Single shared bus systems are considered cost-efficient solution appropriate for hybrid energy storage systems comprising few storage devices. In case of numerous simultaneous power flows caused by a lager number of storages, however, their efficiency is reduced. Systems featuring several independent CTI, also referred to as multiple shared bus topology, are better suited for this application [217]. For the hybrid energy storage system of the hybrid compensation system, a single shared DC bus architecture is chosen due to its advantages for hybrid energy storage systems comprising only few energy storage systems. Here, the grid-side power converter is connected to the storage devices via a common DC bus bar carrying all power flows among the components. Accordingly, all components connected to the single shared DC bus are designed to an equal voltage level and it is ensured that a limited voltage range is maintained by means of a controller.

4.6.3 Strategies for optimized operation of hybrid energy storage systems

A variety of different optimization strategies is available for controlling storage systems [218, 219]. Optimization is carried out analytically, if a mathematical description of the optimization problem is possible. Otherwise, numerical methods for approximative calculation or other simplifying methods are used. Fuzzy functions allow simplification of the interrelationships by expressing the degree of affiliation to certain attribute classes. Fuzzy functions are used when an exact description of the mathematical relationships is not possible or very complex. As a disadvantage, the results of fuzzy functions feature a low degree of precision. Advantages consist in fast, realistic modeling of complex systems, which can also be used for systems with non-linear behavior, clarity and good comprehensibility. In mathematical optimization, a mathematical model is required, including all relevant parameters and boundaries conditions. This type of optimization is a minimization task. In order to simplify the mathematical model, it is attempted to include as few variables and constraints as possible. Simplification reduces the computational effort and increases the velocity, however, a lower level of accuracy and meaningfulness of the results is a consequence. Mathematical optimization has successfully been implemented for control of a battery-supercapacitor storage system or for optimization of sizing and battery cycle life in a battery-ultracapacitor storage system [220, 221]. Artificial neural networks (ANN) represent a parallel computing model with numerous, simple arithmetic units and versatile application areas [222, 223]. They are used to detecting visual or acoustic patterns, control robots or predict various data [224]. Depending on the type of ANN, one or more future values are predicted [225]. ANN feature the ability of machine learning and are considered capable of handling complex tasks that are difficult to solve using regular programs in a time- and resource-saving manner [224, 226]. A further frequently used optimization method is the so-called dynamic programming, which is used if the optimization problem consists of several similar sub-problems and an optimal solution of the overall problem consists of optimal solutions of the sub-problems. Accordingly, sequential optimal solution of the sub-problems leads to an optimal overall solution [227, 228, 229]. Another optimization method is maximum efficiency point tracking (MEPT), where controllable system parameters CP_i are modified under observation of efficiency η in order to detect the parameter combination of maximum efficiency [230]. MEPT is about finding the optimum operating point or the best combination of values. In the case of a hybrid storage system, distribution of power with maximum efficiency to the two storages is to be determined [231, 232]. In this thesis, a derivative of MEPT is used for controlling the hybrid storage system. It is aimed at distributing an external power request with maximum efficiency to the individual storages of the hybrid storage system. As controllable parameters the power values fed to or drawn from the individual storages are varied. [233, 234]

4.7 Modeling of a flywheel energy storage

Objects in motion posses kinetic energy E_{kin}. Kinetic energy stored in the object is increased by acceleration and decreased by deceleration. A special form of motion is rotation, where a mass rotates with certain angular velocity ω about a space axis. Flywheel energy storage deploy axial mass moment inertia of flywheels that are connected to an electric machine. Alteration of angular velocity of the flywheel is achieved by torque load by the electric machine by means of absorption or release of electrical energy [235]. The maximum amount of kinetic energy to be stored in a flywheel is determined by the maximum angular velocity ω_{max} of the flywheel, its mass m and its geometry-dependent moment of inertia J [236].

$$E_{\mathrm{kin}}^{\mathrm{max}} = \frac{1}{2} \cdot J \cdot \omega_{\mathrm{max}}^2 \tag{4.2}$$

Maximum power P_{max} that can be provided by the flywheel is calculated based on the maximum possible angular velocity ω_{max} and J [237].

$$P_{\mathrm{max}} = -J \cdot \omega_{\mathrm{max}} \cdot \frac{\mathrm{d}\omega_{\mathrm{max}}}{\mathrm{d}t} \tag{4.3}$$

Available storage capacity depends on the speed range in which the flywheel is operated. The energy to be stored in a flywheel is defined by the upper ω_{max} and the lower ω_{min} boundary of angular velocity [238].

$$\Delta E = \frac{1}{2} \cdot J \cdot \left(\omega_{\mathrm{max}}^2 - \omega_{\mathrm{min}}^2\right) \tag{4.4}$$

Rotationally symmetric geometries with large moment of inertia are primarily used as flywheels. Hollow cylinders, in which the mass is located as far away from the axis of rotation are particularly suitable. Axis mass moment of inertia is calculated according to equation (4.5) for a hollow cylinder (Fig. 55 a) with outer radius r_2, inner radius r_1, height h and mass m [236].

$$J = \frac{1}{2} \cdot \rho_{\mathrm{f}} \cdot h \cdot \left(r_2^4 - r_1^4\right) = \frac{1}{2} \cdot m \cdot \left(r_2^2 + r_1^2\right) \tag{4.5}$$

Based on those equations, it is obvious that the storable energy increases quadratic with both the radius and the angular velocity. However, arbitrary expansion of those influencing variables in order to increase $E_{\mathrm{kin}}^{\mathrm{max}}$ is limited by material properties, restrictions of bearings, material cost based on quantity and restraints concerning installation space. Below, the design of a high-speed flywheel storage is visualized. (Fig. 55 b).

Flywheels predominantly rotate around the vertical axis, as horizontal orientation would result in a circumferential bending of both the axis and the rotor. For a flywheel designed as hollow cylinder rotating around a horizontal axis, the circulating occurence ot the weight force in the bearing points imposes further mechanical stress on the rotor material. During operation of a high-speed flywheel energy storage, several loss mechanisms occur.

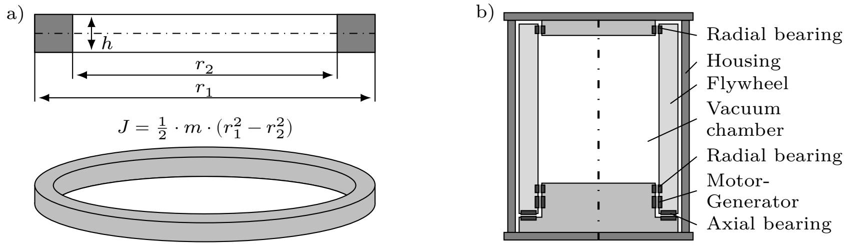

Figure 55: Determination of the moment of inertia of a circular ring (a) and layout of a high speed flywheel using active magnetic bearings (b)

On the one hand, a constant power requirement of the active axial magnetic bearing P_{AMB} is to be mentioned, which keeps the rotor of the flywheel in suspension. Furthermore, the radial active magnetic bearing of the rotor is to be supplied with power. Here, the power consumption P_{RMB} depends on the rotational speed of the rotor. Beyond, there is a power loss in the form of the gas friction of the rotor P_{GF}, depending on the rotational speed of the rotor and the gas pressure inside the housing. In addition, losses for operation of the vacuum pump P_{VP} reduce the efficiency. A further loss is caused by the efficiency of the electrical motor / generator unit P_{MG}, that depends on the rotational speed and the instantaneous power value. Losses of an electric engine are due to copper losses of currents at the ohmic resistances of the coils, iron losses at magnetic conductors guiding the magnetic flux in metal packages of the rotor and the stator as well as further losses in bearings or commutators. Metal losses are subdivided in hysteretic loss, eddy current losses and remagnetization losses. Finally, there is a power loss in the converter of the flywheel storage P_{PE}. [239, 240, 241, 242]

4.7.1 Losses of active magnetic levitation bearings

As illustrated in Figure 55 a the rotational axis of the flywheel is oriented vertically. Accordingly, the axial bearing of the flywheel has to absorb a force corresponding to the weight force of the flywheel. A particularly elegant approach is the use of passive bearings based on permanent magnets, as no supply of power is required. Concepts of equipping flywheel storages with passive magnetic levitation bearings have been investigated in theory, where permanent magnets are often arranged as so-called Halbach-arrays [243, 244, 245]. As conventional permanent magnetic bearings are considered unstable, passive superconductive magnetic bearings are investigated as a promising alternative. [246] Those, however, feature the disadvantages of high cost and the necessity for cooling. Passive magnetic levitation bearings today do not represent the state of the art for flywheel storage systems. As the research activities were provided a flywheel with active axial bearing, this type of levitation bearing is investigated. An active magnetic levitation bearing capable of axially supporting the flywheel is required to permanently provide a constant magnetic force F_m suitable to compensate the weight force F_w. This is true, if the vertical component of F_m is equal to F_w. In order to approximate the power required for operating the axial active magnetic bearing of the flywheel as a simplistic example an electromagnet is investigated. An electromagnet consists of a coil with a defined number of windings N_c, a ferrite core of a pole surface A_p which corresponds to the bearing area A_b. In addition, there is an air gap δ_a between the pole surface and the counterpart of the electromagnet, in this case the flywheel rotor. It is possible to calculate the magnetic force F_m provided by the electromagnet considering the electric current within the coil i_c [247]:

$$F_m \quad = \quad \mu_0 \cdot \frac{(N \cdot i_\mathrm{c})^2}{(2 \cdot \delta_\mathrm{a})^2} \tag{4.6}$$

Calculation of the electric power required for operation of the axial levitation bearing is possible based on the current i_c and the voltage u_c of the coil. By isolating i_c in equation (4.6), inserting the required bearing force F_w and considering u_c an approximation of the power loss is accomplished.

$$P_\mathrm{AMB} \quad = \quad u_\mathrm{c} \cdot i_\mathrm{c} \quad = \quad u_\mathrm{c} \cdot \sqrt{\frac{F_m \cdot (2 \cdot \delta_\mathrm{a})^2}{\mu_\mathrm{a} \cdot N^2}} \tag{4.7}$$

4.7.2 Radial active magnetic bearings

If the center of gravity is not located on the rotational axis, dynamical unbalance occurs on rotation of the object. In order to keep the rotating object in its position, radial bearings are required which are capable of compensating the revolving radial force. The radial force depends on the mass of the object m, the angular velocity ω and a factor representing the unbalance f_u. The standard ISO 1940 defines quality levels for the balancing quality of different rotor types [248]. Although the standard ISO 21940 has replaced the standard ISO 1940, the balance quality grades contained in this standard are helpful for the models developed. A balance quality grade G_U is specified for each rotor class, representing the maximum permissible value of the product of angular velocity ω and eccentricity e_r of the rotor according to $e_\mathrm{r} = \omega_\mathrm{max} \cdot G_\mathrm{U}$. The unbalance factor f_u represents the product of the mass of the rotor m_r and e_r. Based on these fundamentals, the radial force caused by the unbalance is calculated for any angular velocity.

$$F_r = \frac{f_\mathrm{u} \cdot \omega^2}{2} \cdot m_\mathrm{r} \tag{4.8}$$

The bearing force in dependence of the angular velocity is to be absorbed by an active radial magnetic bearing. Analogously to calculation of the power required for operation of the active axial bearing (Fig. 56 a), the power of the radial bearing is calculated as a function of the angular velocity.

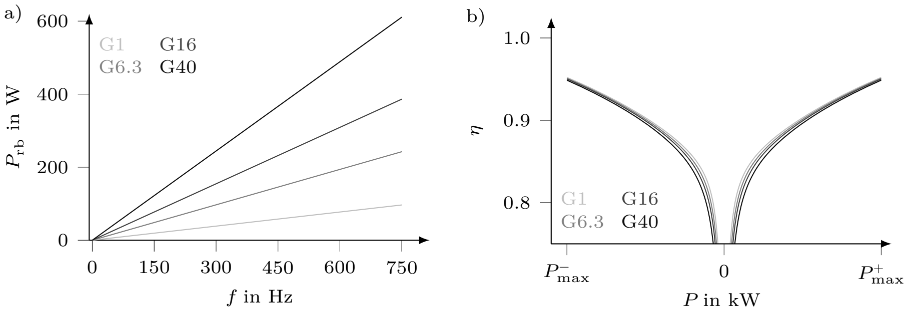

Figure 56: Influence of the unbalance class G_U on radial active bearing losses (a) as well as power the efficiency η of the system (b), visualized in a narrowed efficiency range

4.7.3 Power loss due to gas friction

If an object is moved through a liquid or gaseous medium, the motion is counteracted by a flow resistance force. The resistance increases in proportion to the speed at which the object moves in the fluid. Gas friction occurs when gas molecules hit a moving object. The rotation of the flywheel in the housing generates a friction torque which counteracts the speed of the flywheel. The drag coefficient $\mathrm{c_d}$ is dependent on the Reynolds number Re which describes whether the flow is laminar or turbulent. Reduction of losses due to gas friction is possible by either filling the flywheel housing with gases of lower density such as helium or hydrogen, or by evacuating the housing. Thus, friction is reduced, as the force counteracting the moving object depends on the density of the fluid and the relative velocity between the components. Here the density of the fluid determines the number of molecules that collide with the surface of the object. The number of collisions is approximated using the Maxwell-Boltzmann distribution. In equation (4.9) the losses due to gas friction P_GF

are calculated. As constructive parameters of the flywheel the outer radius r_1 and the height l_r are considered. The gas density ρ_g depends on the gas pressure within the housing p_H, the temperature of the gas ϑ_H and the gas constant R [249, 250, 251].

$$P_{\mathrm{GF}} = \sum_i \mathrm{c_d} \cdot \pi \cdot \rho_{\mathrm{g}} \cdot (2 \cdot \pi \cdot n)^3 \cdot r_1^4 \cdot l_{\mathrm{r}} \tag{4.9}$$

In Figure 57 a the influence of the gas density within the flywheel housing on friction losses is visualized. Gas friction between the inner wall of the hollow cylinder and the gas contained is neglected. It is assumed that the gas within the hollow cylinder rotates at equal speed. In contrast to gas friction between the housing and the outer surface of the flywheel, the velocity gradient is lower.

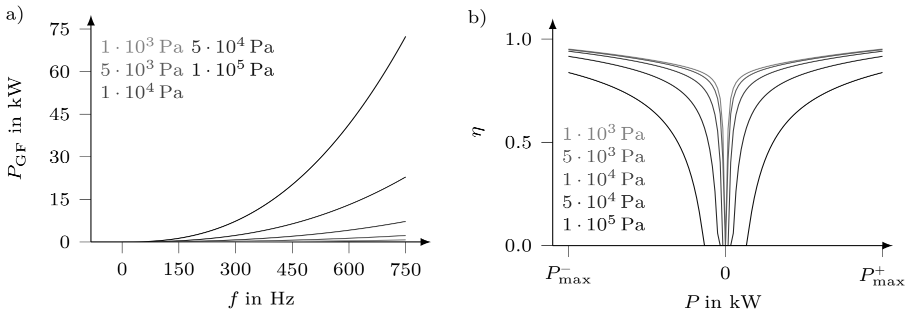

Figure 57: Influence of the gas pressure within the flywheel housing on air friction losses P_{GF} (a) and the efficiency η of the system (b)

As due to gas friction losses the flywheel is decelerated, the ratio of usable output and input of power are affected. Therefore, the influence of the gas friction losses on total efficiency is analyzed in 57 b. For different gas pressures within the flywheel housing, the efficiencies are calculated including all considered loss mechanisms.

4.7.4 Losses for evacuating the flywheel housing

In order to minimize gas friction, as introduced in equation (4.9), it appears desirable to reduce the gas density inside the housing of the flywheel. As ρ_g is associated with the number of gas molecules per volume, a reduction of gas density is possible by transporting gas out of the housing using a vacuum pump. Due to leakages of the housing, a gas flow occurs if there is a pressure difference Δp between the ambient pressure p_a and the internal pressure p_i within the housing. The volume flow $\dot{V}_\mathrm{l}$ of the leakage is estimated as a function of the leakage area A according to the formula below:

$$\dot{V}_\mathrm{l} \quad = \quad A \cdot v \quad = \quad A \cdot \sqrt{\frac{2 \cdot \Delta p}{\rho}} \tag{4.10}$$

As a consequence of the volume flow, gas particles enter the housing, causing the mass contained to increase and the pressure p_i to rise. It is therefore the task of the vacuum pump to counteract the incoming volume flow. Due to comparatively low volume flows, discontinuous operation of the vacuum pump, triggered by violation of the permissible band of gas pressure within the housing is common. Therefore, for a known time span, the vacuum pump is required to transport an average mass, which has entered the housing due to van average pressure difference $\overline{\Delta p}$, out of the housing. In discontinuous operation, the power required for operation of the vacuum pump is not constant over time. Power required for operation is calculated as an average value.

4.7.5 Losses of the electric machine and other auxiliary systems

In high-speed flywheel storages, predominantly permanent magnet synchronous motors (PMSM) are used as they are simple to control and robust [252]. The efficiency of the electric machine, which acts as motor and generator of the flywheel storage, is calculated as a function of torque and power as depicted in Figure 58 a.

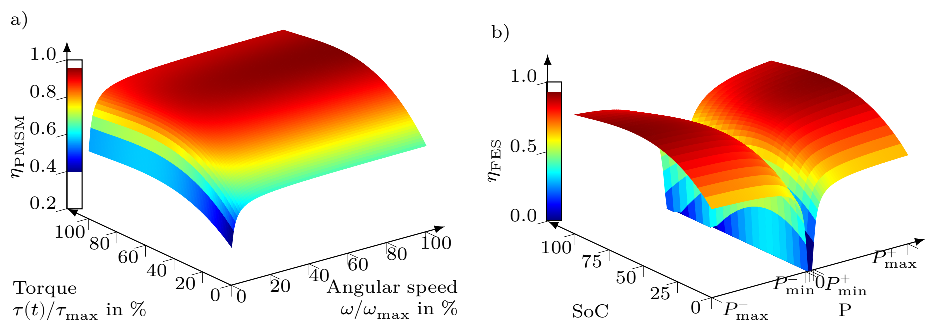

Figure 58: Efficiency map of the electric machine as a function of power and torque (a) as well as efficiency map of a flywheel incorporating all losses for a permissible SoC range between 0 and 100 (b)

Further losses occur in auxiliary devices of the flywheel as in power electronic equipment, wiring or control. Those losses reduce the amount of electric energy supplied to the storage or deducted from it immediately. They are considered based on the efficiencies the converter η_i and denoted with a constant value. [239]

4.7.6 Evaluation of the flywheel model

In order to assess the introduced model of a high-speed flywheel storage, it is implemented in simulation and tested based on typical scenarios [239, 253, 254, 255]. All models are created in Python using NumPy and SciPy. In a first step, design parameters of the flywheel are predefined. The flywheel is considered a hollow cylinder of outer radius of 0.225 m, wall thickness of 0.025 m and height of 0.5 m. As material of the flywheel a carbon fiber compound is used featuring a specific mass of 1600 kg m^{-3}. The air gap between flywheel and housing is 10 mm and air gaps of the magnetic bearings are 1 mm. The unbalance class of the rotor is 0.0063 m s^{-1}. Ambient gas pressure is assumed to be 10^5 Pa and the simulated vacuum pump is capable of reducing the pressure within the housing to 10^2 Pa. In Figure 59 a the losses of the flywheel storage are depicted for a series of successive charging and discharging cycles and in Figure 59 b the corresponding SoC and the total losses P_l as a percentage of the maximum losses $P_{\mathrm{l,max}}$ are provided.

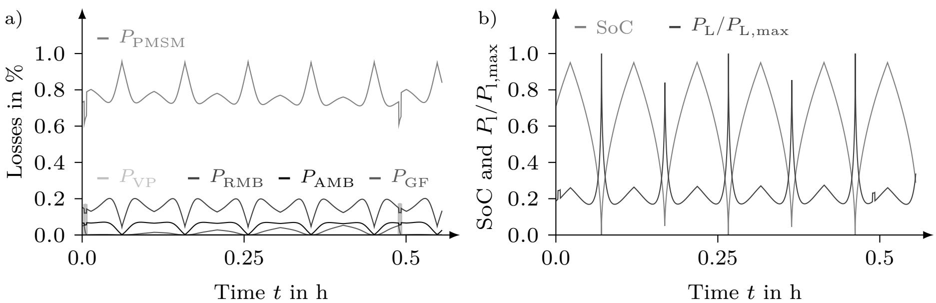

Figure 59: Visualization of losses during charging and discharging the flywheel storage with constant power (a) and of the angular velocity as well as the SoC of the system (b)

As a further result of implementing the introduced functions, the efficiency of arbitrary design configurations is evaluated. Therefore, three-dimensional efficiency maps in dependence of charging or discharging power and state of charge are calculated (Fig. 58 b). Those indicate favorable operation conditions, which are characterized by high efficiency.

4.8 Modeling of the vanadium redox flow battery

Flow batteries are electrochemic storage systems and reversibly convert electricity into chemical energy. Unlike most battery systems, in flow batteries energy conversion and storage occurs separately in different components of the system (Fig. 60). Two different electrolytes, segregated by an ion exchange membrane carry dissolved electro-active species. Charges are transferred to the electrolytes by inert electrodes. Vanadium redox flow batteries (VRFB) use anolytes and catholytes containing dissolved vanadium ions [256]. VRFB systems consist of one or a stack of cells, two tanks for storage of electrolytes and a circulating system of pipes and pumps. [256, 257, 258]

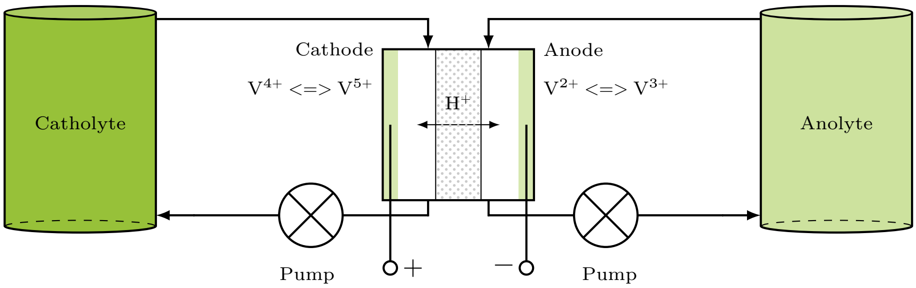

Figure 60: Schematic draft of a VRFB with one cell [259]

The electrolyte of VRFB systems contains vanadium ions of different oxidation states dissolved in sulfuric acid for the positive electrode as well as for the negative electrode. Four different oxidation states of vanadium are utilized for oxidation and reduction on both sides of the membrane. In the positive compartment of the positive electrode vanadium V^{4+} ions are being transferred into vanadium V^{5+} ions and vice versa. Simultaneously in the negative compartment of the negative electrode vanadium V^{3+} ions are being transferred into vanadium V^{2+} ions and vice versa. [260]

$$V^{2+} \underset{\text{discharge}}{\overset{\text{charge}}{\rightleftharpoons}} V^{3+} + e^- \tag{4.11}$$

$$VO_2^+ + 2\,H^+ + e^- \underset{\text{discharge}}{\overset{\text{charge}}{\rightleftharpoons}} VO^{2+} + H_2O \tag{4.12}$$

Both reactions are accompanied by release or absorption of H^+ ions [261]. Furthermore, particular side reactions are concomitant with the principal reaction [262].

$$
\begin{aligned}
2\,H_2O + 2\,e^- &\rightleftharpoons H_2 + 2\,OH^- && (4.13)\\
2\,H_2O &\rightleftharpoons O_2 + 4\,e^- + 4\,H^+ && (4.14)\\
VO^{2+} + 2\,H_2O &\rightleftharpoons HVO_3 + 3\,H^+ + e^- && (4.15)
\end{aligned}
$$

4.8.1 Fundamental principles of vanadium redox flow batteries

In the entire volume V of each of both electrolytic circuits a certain amount of substance n in mol is dissolved. By multiplication with the Avogadro constant N_A the number of elementary entities of the individual substance N can be determined. Molar concentration c of a solute substance is defined as units of moles of solute per units of volume.

$$c = \frac{n}{V} = \frac{N}{V \cdot N_A} \tag{4.16}$$

Corresponding to the main reaction equations (2.8) and (2.9), molar concentrations $c_{V^{2+}}$, $c_{V^{3+}}$, $c_{VO^{2+}}$ and $c_{VO_2^+}$ are relevant for assessment of the state of a VRFB. The concentrations of protons H^+ is represented by c_{H^+}. An important state indicator of a VRFB which is calculated based on the molar concentrations of vanadium ions is the state of charge SoC. The SoC is determined by diving either the concentration of unoxidized vanadium $c_{V^{2+}}$ or the concentration of vanadium oxide $c_{VO_2^+}$ through the total concentration of solute vanadium c_V [263].

$$\mathrm{SoC} = \frac{c_{V^{2+}}}{c_V} = \frac{c_{VO_2^+}}{c_V} \tag{4.17}$$

Given the chambers of the cell, which are separated by the membrane, are filled one with anolyte and the other with catholyte, an open circuit voltage U_{OCV} occurs. The open circuit voltage is considered the highest voltage to be provided by a particular ionic concentration within the VRFB disregarding any losses [263]. The Nernst equation provides the electromotive force as a voltage of a redox pair in dependence of the concentrations of the ions involved [259].

$$U_{\mathrm{OCV}} \quad = \quad E^{\ominus\prime} + \frac{R \cdot T}{F} \cdot \ln\Big\{ \Big(\frac{c_{\mathrm{VO^{2+}}} \cdot c^2_{\mathrm{H^+}}}{c_{\mathrm{VO^2}}} \Big) \cdot \Big(\frac{c_{\mathrm{V^{2+}}}}{c_{\mathrm{V^{3+}}}} \Big) \Big\} \tag{4.18}$$

For constant hydrogen ion concentration c_{H^+} the open circuit cell voltage is calculated based on SoC [264, 265].

$$U_{\mathrm{OCV}} \quad = \quad E^{\ominus\prime} + \frac{R \cdot T}{F} \ln\Big(\frac{\mathrm{SoC}}{1 - \mathrm{SoC}} \Big) \tag{4.19}$$

Aside from information on ion concentrations, physical constants as universal gas constant R and Faraday constant F are part of the equation as well as electrolyte temperature T in Kelvin K and the formal potential $E^{\ominus\prime}$. As an experimental value for $E^{\ominus\prime}$ is not available in many cases, it is substituted by the standard potential $E^{\ominus}$. In electrochemistry the latter represents an ideal state of the VRFB at standard conditions with a fluid temperature T of 25 °C and a concentration of all vanadium species c_V of 1 mol m^{-3} [266]. It is calculated according to the following equation based on the Gibbs free enthalpy $\Delta G^{\ominus}$ using standard reaction enthalpy $H_r^{\ominus}$ and standard reaction entropy $S_r^{\ominus}$ [263].

$$E^{\ominus} \quad = \quad -\frac{\Delta G^{\ominus}}{n \cdot F} \quad = \quad \frac{\Delta H_r^{\ominus} - T \cdot \Delta S_r^{\ominus}}{n \cdot F} \tag{4.20}$$

Both $H_r^{\ominus}$ and $S_r^{\ominus}$ are determined by molar formation enthalpy as well as entropy between the products and reagents of the involved isotopes [266].

$$\Delta H_r^{\ominus} \quad = \quad \sum_{\text{products}} \Delta H^{\ominus}_{\mathrm{f,product}} - \sum_{\text{reagents}} \Delta H^{\ominus}_{\mathrm{f,reagent}} \tag{4.21}$$

$$\Delta S_r^{\ominus} \quad = \quad \sum_{\text{products}} \Delta S^{\ominus}_{\mathrm{f,product}} - \sum_{\text{reagents}} \Delta S^{\ominus}_{\mathrm{f,reagent}} \tag{4.22}$$

4.8.2 Approaches for determining the open circuit voltage

Beyond the method described for determining the open circuit voltage of a redox flow cell, other approaches are known from literature, which are based on different assumptions. A comparison between the cell voltages in dependence of the SoC calculated by different models is provided in Figure 61 a.

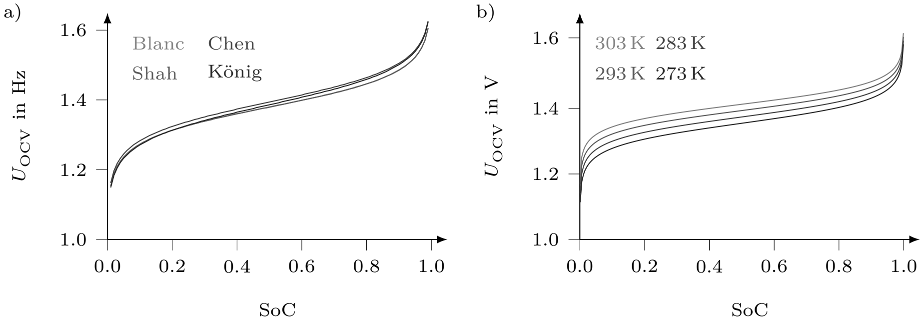

Figure 61: Visualization of the dependence of the cell voltage on the state of charge calculated by several models [256, 258, 265, 267] (a) and on the temperature (b)

As in all equations the temperature of the fluid is incorporated, it is assumed that the ambient temperature exerts an influence on the operation of a redox flow battery. Therefore, Figure 61 b visualizes the cell voltage in dependence of the temperature. In the aforementioned equations, a constant concentration of protons is assumed. However, during charging and discharging operations protons are produced and consumed. Moreover, protons pass the membrane. Within a VRFB, sulphuric acid H_2SO_4 and dissociation of water are considered the most important origins of protons. [256, 265]

In addition to the mathematical formulation, these differ in particular in the factors influencing the determination of the cell voltage. Thus, some models additionally consider the proton concentration and Chen's model furthermore includes the Donnan potential $\Delta\Phi$ in the open circuit voltage calculation. Models that consider the contribution of protons to the open circuit voltage feature a much higher cell voltage and are closer to the actual measured values in comparison to models that neglect proton concentration.

4.8.3 Influences on the terminal voltage of a cell

Processes of energy transfer and energy conversion during charging, discharging and storage within a redox flow cell are lossy. Shunt currents and overpotentials are known as essential loss mechanisms. Overpotentials occur as ohmic overpotentials ζ_Ω at the membrane ζ_m, electrolyte ζ_e and current collector ζ_{cc} as well as concentration overpotentials ζ_c in the cell. [268, 269, 270, 271]

Components of the ohmic overpotential

In a cell the electrolyte perfuses a porous graphite felt located between an electrode and the membrane. Therefore, the conductivity is determined by the interaction of the fluid with the porous surrounding material. The associated overpotential ζ_{e} is determined according to the subsequent equation [267, 272]:

$$\zeta_{\mathrm{e}} = I_c \left(\frac{\delta_{\mathrm{e}}}{\varepsilon^{\frac{3}{2}} \cdot \sigma_{\mathrm{el}}} \right) \tag{4.23}$$

The electrolytic conductivity σ_{el} is calculated on the basis of the measured SoC. Different approaches are available (Fig. 62 a) [258, 265, 267]. Due to non-ideal behavior of the cells, the current causes an increase of the voltage for charging processes and a decrease for discharging processes. The voltage change is proportional to the cell current I_{c} as well as the resistance R_{cc}.

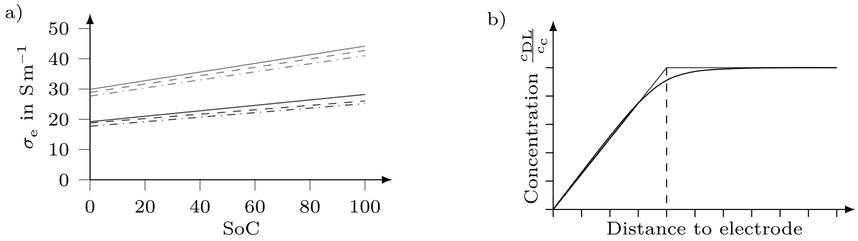

Figure 62: Representation of the conductivity of anolyte (dark gray) and catholyte (gray) according to König (continuous line), Corcuera (dashed) and Bromberger (dashdotted) at a temperature of 298 K (a) and visualization of the concentration gradient in the diffusion layer of the electrode (b)

The latter is derived analytically from the geometry A_{e}, the specific conductivity of the electrode material σ_{e} and the diameter δ_{e} [176, 256, 273]:

$$R_{cc} = \frac{\delta_{\mathrm{e}}}{\sigma_{\mathrm{e}} \cdot A_{\mathrm{e}}} \tag{4.24}$$

$$\zeta_{\mathrm{cc}} = I_{\mathrm{c}} \cdot R_{\mathrm{cc}} \tag{4.25}$$

In order to calculate the resistivities of a redox flow cell, the dimensions and conductivities of the components are required. The conductivity of the current collector σ_{cc} is assumed as $9.1 \cdot 10^{-4}$ S m^{-1} [274]. Calculation of the overpotential of the membrane η_{m} is possible analogous to equation (4.25), where the length of the membrane δ_{m} and the conductivity σ_{m} of the membrane are used. The conductivity of a Nafion membrane depends on the temperature and the water content in the membrane [272].

$$\sigma_{\mathrm{m}} = (0.5139\lambda - 0.326)^{1268\cdot\left(\frac{1}{303}-\frac{1}{T}\right)} \tag{4.26}$$

$$\zeta_{\mathrm{m}} = I_{\mathrm{c}} \cdot \frac{\delta_{\mathrm{m}}}{\sigma_{\mathrm{m}}} \tag{4.27}$$

Values for the specific resistivity $\varrho_{\mathrm{e}} = \sigma_{\mathrm{e}}^{-1}$ of the electrode material σ_{e} are known from literature or specified from manufacturers as surface resistance values and are assumed in an interval between $\varrho_{\mathrm{e}} = 1.5\,\Omega\,\mathrm{cm}^{-2}$ and $\varrho_{\mathrm{e}} = 3.13\,\Omega\,\mathrm{cm}^{-2}$ [256, 258, 275].

Concentration overpotential due to the occurrence of fluid layers

Within the cells, the charge transfer reactions take place at the electrodes. Therefore, a change of the ionic concentrations occurs. During operation of the flow battery the concentration gradient is partially removed by the electrolyte flow transported through the cells. However, due to effects as diffusion, migration or convection the mass transfer towards the electrodes is limited. As a consequence, a gradient of concentrations is sustained, which are considered as layers featuring different concentrations (Fig. 62 b). The concentration overpotential ζ_{c} can be determined based on the NERNST equation [256, 272, 276, 277]:

$$\zeta_{\mathrm{c}} = \frac{R \cdot T}{z \cdot F} \ln\left(\frac{c_c}{c_{DL}}\right) \tag{4.28}$$

In order to be able to incorporate design variables of the redox flow battery, equation (4.28) is reformulated as follows [278].

$$\zeta_{\mathrm{c}} = \frac{R \cdot T}{z \cdot F} \ln\left(1 - \frac{|I| \cdot 10^4}{1.6 \cdot F \cdot c_T \cdot l_{El} \cdot w_{El} \cdot \left(\frac{Q_{HC}}{h_{el} \cdot w_{el}}\right)^{0.4}}\right) \tag{4.29}$$

While the concentration overpotential is added to the cell voltage during charging, the concentration voltage reduces the cell voltage during discharging [258]. The sign of the overpotentials introduced assumes negative values for reductive processes and positive values for oxidative processes [256, 279]. The cell voltage is calculated based on the open circuit voltage and the overpotentials as follows.

$$U_{\mathrm{c}} \quad = \quad E_{\mathrm{OCV}} - \zeta_{\Omega} - \zeta_{\mathrm{c}} \quad = \quad E_{\mathrm{OCV}} - \zeta_{\mathrm{c}} - \zeta_{\mathrm{m}} - \zeta_{\mathrm{cc}} - \zeta_{\mathrm{c}} \qquad (4.30)$$

4.8.4 Shunt currents due to potential differences between cells

In a redox flow battery comprising multiple cells in series or parallel connection, the individual cells are supplied with the electrolytes via common fluid ducts. Accordingly, different electric potentials are connected by the fluid system. As the electrolytes feature high ionic conductivity, ion currents, mainly consisting of protons, across the cells arise. Those ion currents are referred to as shunt currents and lower both battery efficiency as battery life due to material corrosion [280, 281, 282].

For calculation of the shunt current I_{sh} an equivalent circuit diagram of a battery with electrical and hydraulic components is designed (Fig. 63 a). It contains the present electrical resistances of a cell R_{c}, of the lines R_{m}, of cell supply lines R_{ch} and external hydraulic components of the system R_{ext}.

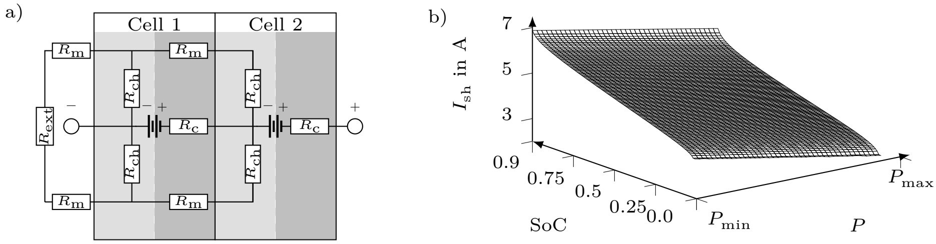

Figure 63: Equivalent circuit model of a battery cell (a) and visualization of shunt currents in dependence of the cell voltage (b)

The shunt current $I_{\mathrm{sh}}^{i,j}$ of two individual cells i and j is calculated according to equation (4.31). To determine the total shunt current of a battery consisting of several cells in several cell stacks I_{sh}, the calculated shunt currents between individual cells are summarized.

$$I_{\mathrm{sh}}^{i,j} \quad = \quad (j-i) \cdot \frac{U_{\mathrm{c}}}{R_{\mathrm{ch}}} \qquad (4.31)$$

4.8.5 Modeling of the hydraulic circuit

During operation of the redox flow battery, electrolyte exchange between the cells and the tanks is essential. This requires the electrolytes to be transported from the fluid tanks to the stacks (Fig. 64 a), from there into the cells (Fig. 64 b) and then back into the tanks. In order to transport the electrolytes through the components of the redox flow battery, power is applied by the fluid pump.

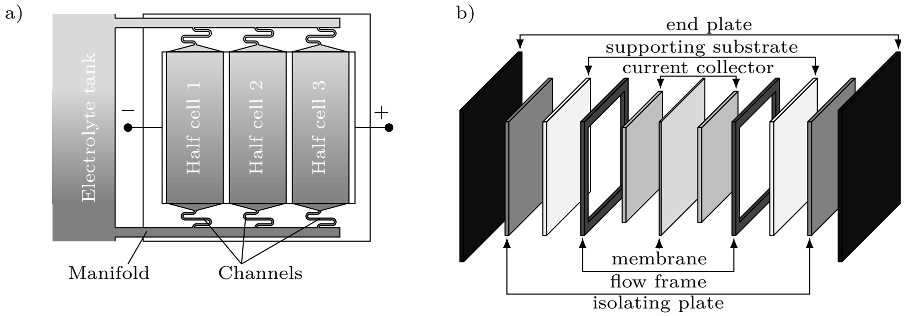

Figure 64: Visualization of the fluid system of a redox flow battery (a) and the components of a redox flow battery cell (b)

This is due to the fact that a volume flow through the battery components has to overcome the flow resistance of the individual system components. The flow resistance is proportional to the volume flow and, like electrical networks, manifests itself in the form of a pressure drop. The total pressure drop of the fluid system includes the pressure drop of the fluid lines, other components of the fluid system and the cells or cell stack. In equivalent circuit diagrams the flow resistances of individual components are determined. The pressure drop in the hydraulic system is calculated afterwards by linking the individual pressure drops in accordance with the KIRCHHOFF laws. Basically, a distinction is made between two approaches for the design of the electrolyte supply of the cells. In series connection, the electrolytes flow through the cells of the stack one after the other. In contrast, in the case of parallel connection, the electrolyte flow supplied is split before the cell stack and partial flows perfuse the individual cells. [258, 259]

Pressure drop of straight fluid pipes

Simplistically, the pressure loss in straight pipes is calculated using the extended Bernoulli equation of energy, which incorporates the friction of the electrolyte on the pipe wall as well as changes in flow direction and velocity. In order to be able to compare different hydraulic potentials, they are usually represented as a comparative quantity designated as hydraulic head h. As there is no difference in elevation in a closed hydraulic circuit, the pressure drop due to friction Δp_{f} is denoted as follows [258, 259, 272]:

$$\Delta p_{\mathrm{f}} = h_{\mathrm{f}} \cdot \rho_{\mathrm{el}} \cdot g \tag{4.32}$$

The determination of the hydraulic head due to friction h_{f} is possible for round and straight pipes with a constant cross-section. Geometric parameters such as length, diameter, friction coefficient and flow velocity are included. Calculation of h_{f} is possible according to equation (4.33) and the total pressure loss due to pipe friction according to equation (4.34) [258, 266].

$$h_{\mathrm{f}} = \lambda_{\mathrm{f}} \cdot \frac{l_{\mathrm{P}} \cdot v_{\mathrm{P}}^2}{d_{\mathrm{P}} \cdot 2 \cdot g} \tag{4.33}$$

$$\Delta p_{\mathrm{P}} = 8 \cdot k_{\mathrm{f}} \cdot \dot{V}_{\mathrm{P}}^2 \cdot \frac{l_{\mathrm{P}} \cdot \rho_{\mathrm{el}}}{d_{\mathrm{P}}^5 \cdot \pi^2} \tag{4.34}$$

The pipe friction coefficient k_{f} is determined as a function of the volume flow $\dot{V}_{\mathrm{P}}$. Here, the method of determining k_{f} depends on whether the flow in the pipe is laminar or turbulent. A measure of this is the Reynolds number Re. Below a value of the Reynolds number of 2300, the flow is laminar. In the range between $2300 \leq \mathrm{Re} \leq 4000$ there is a transition between a laminar flow and a turbulent flow. Above 4000, the flow is turbulent. [258, 259, 283]

Pressure drop of components and lines with geometry change

If the flow direction or the flow velocity of the fluid changes due to a change in geometry, this causes a pressure drop. The loss coefficient k_{l} contained in the equation for calculation of the hydraulic head of the geometry h_{m} has already been determined for numerous structural shapes.

$$h_{\mathrm{m}} = k_{\mathrm{l}} \cdot \frac{v_{\mathrm{f}}^2}{2 \cdot g} \tag{4.35}$$

Pressure drop of cells and cell stack

Cells and the cell stack are considered the most important source of the total pressure drop due to the complex geometry. Due to numerous alterations of the diameter and changes of velocity or direction of the flow, the total flow resistance is comparatively high. For precise determination of the flow resistivity of a cell or a cell stack, finite element simulation is required. Subsequently, a simplistic approach for approximating the pressure drop is outlined. Within a cell, there are elements whose pressure drop increases linearly with the flow velocity, such as the felt. Beyond, elements with quadratic relation between pressure drop and flow rate are present, for example pipe turns. The total pressure drop in a cell is calculated using a quadratic equation. [258, 283]

$$\Delta p_\mathrm{c} = \beta \dot{V}_\mathrm{c} + \gamma \dot{V}_\mathrm{c}^2 \tag{4.36}$$

The parameters β and γ are determined according to the cell geometry.

Relationship between pressure drop and pump power

Transport of the electrolytes is propelled using pumps, whose delivery rate is proportional to the electrical power supplied. The required power P_FP (Fig. 65 a) depends on the desired flow rate $\dot{V}$, the efficiency of the pump η_p and the pressure drop of the hydraulic system Δp. [256, 258]

$$P_\mathrm{FP} = \frac{\dot{V} \cdot \Delta p}{\eta_p} \tag{4.37}$$

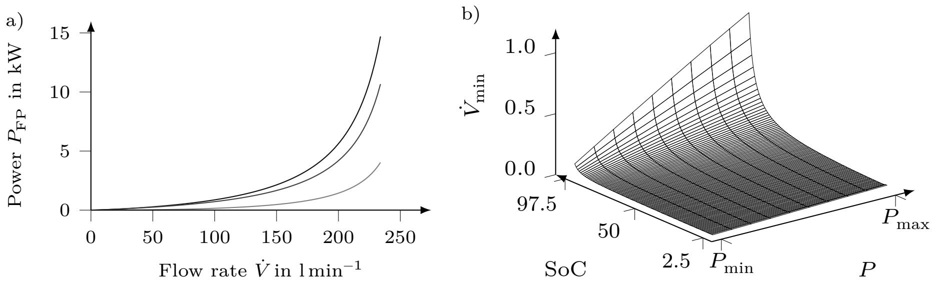

Figure 65: Power required for transporting the electrolytes through the fluid pipes (light gray), the cell stack (gray) and the total system (dark gray) in dependence of the flow rate (a) and depiction of the minimum flow rate $\dot{V}_\mathrm{min}$ in dependence of the SoC and power (b)

4.8.6 Estimation of the required electrolyte flow rate

During charge and discharge, ionic concentrations are changed on both sides of the membrane within the cell. As a result, the ionic concentrations in the cell deviate from the concentrations in the electrolyte tanks. By pumping electrolyte from the tanks through the cells the concentration gradient is compensated. As transport of the liquid is associated with consumption of electrical power, reduction to a minimum or optimum is desired [266]. Determined by the geometry of the cells, the cell stack and all piping, the liquid pumped through the system faces a flow resistance. Concomitant to increasing flow rates, both the resistance and the power for pump operation are rising. Therefore, it is to be investigated, whether performance gains achieved by increased flow rates justify higher power consumption [262]. Minimum flow-rate $\dot{V}_{\mathrm{min}}$ is determined by current $i(t)$, representing the electric charge Q_{el} exchanged over a time t between the electrodes and the electrolytes.

$$\dot{V}_{\mathrm{min}} = \frac{n \cdot N_{\mathrm{cell}} \cdot i(t)}{F(c_{\mathrm{out,min}} - c_{\mathrm{in}}(t))} \qquad (4.38)$$

Accordingly, a suitable amount of ions corresponding to the charge to be exchanged has to be available at the electrodes. The number of ions of a particular species per volume is determined by the molar concentration.

A simplistic approach is defining a fixed flow rate for all possible SoC and power values. Accordingly, the fixed flow rate equals the maximum value of all calculated $\dot{V}_{\mathrm{min}}$ for charging and discharging within the permissible range of operation (Fig. 65 b). Limitation of the fixed flow rate is possible by narrowing the range of possible SoC values for both sides of the spectrum. If a variable flow rate is calculated for variant operating conditions, the minimum flow rate $\dot{V}_{\mathrm{min}}$ is to be respected at all times. Optimization is possible by allowing a flow rate higher in comparison to $\dot{V}_{\mathrm{min}}$, if power for pump operation is lower. Both the efficiency functions of the pump drive and the flow resistance of the fluid system in dependence of $\dot{V}$ are relevant parameters.

4.8.7 Evaluation of the battery model

In order to analyze the presented assumptions, a battery model is investigated in simulation [253, 254, 268, 269, 270, 284]. The model of the redox flow battery consists of three battery stacks, comprising 30 battery cells each. An individual battery cell features a length of 58.095 cm, a width of 25.820 cm and correspondingly an active cell area of 1500 cm². The electrolyte contains 1.6

moles of vanadium ions per liter. Current density is limited to 100 mA cm^{-2}. In order to investigate relevant parameters as cell voltage and required electrolyte flow rate, the battery is repeatedly charged until the maximum SoC is present and subsequently discharged to the minimum SoC. By varying the permissible SoC range (66 a and b), the behavior of the model is analyzed. If the limits of the SoC are shifted towards the maximum values 0 and 1, a significant increase of the required electrolyte flow rate is observed. This is due to the fact that the concentration of ions available for a respective conversion is low. During charging or discharging the battery model with a constant current, the occurrence of overpotentials can be observed in dependence of the permissible range of SoC. Those overpotentials cause a violation of the voltage limitation. As a consequence, for further charging or discharging, it is necessary to reduce the current. As visualized in Figure 66 a, for a SoC range between 0.1 and 0.9 a limitation of the battery current due to overpotentials is not necessary.

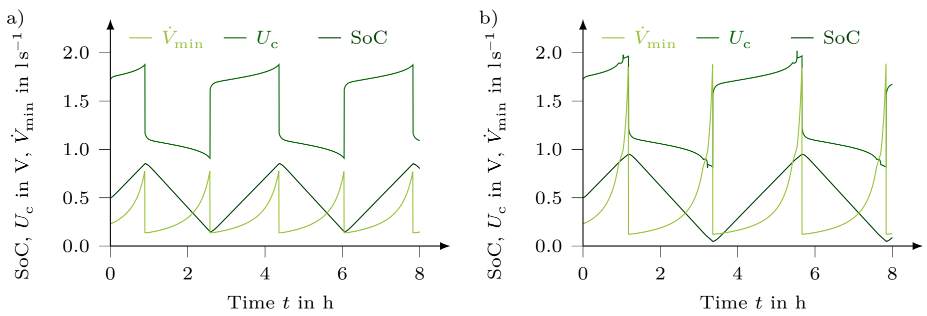

Figure 66: Visualization of the cell voltage, SoC an flow rate for charging and discharging cycles for a SoC range between 0.1 and 0.9 (a) and for a SoC range between 0.05 and 0.95

If the SoC range is extended to the interval between 0.05 and 0.95, harmful overpotentials occur and $\dot{V}_{\mathrm{min}}$ is significantly increased (Fig. 66 b). It is concluded that battery operation is not advantageous in these SoC areas. As a further result three-dimensional efficiency maps for different configurations and environmental parameters are derived. An efficiency η_{RFB} is assigned to each combination of SoC and power as visualized in Figure 89 a and b. The three-dimensional representation indicates in which operating ranges the vanadium redox flow battery features high efficiencies and which ranges are to be avoided due to low efficiencies. For example, it becomes evident that relatively high losses for the electrolyte pump lead to low efficiencies for low power values of both charging and discharging. High electrolyte flow rates, which occur for SoC values close to the limits, are also associated with relatively low efficiencies.

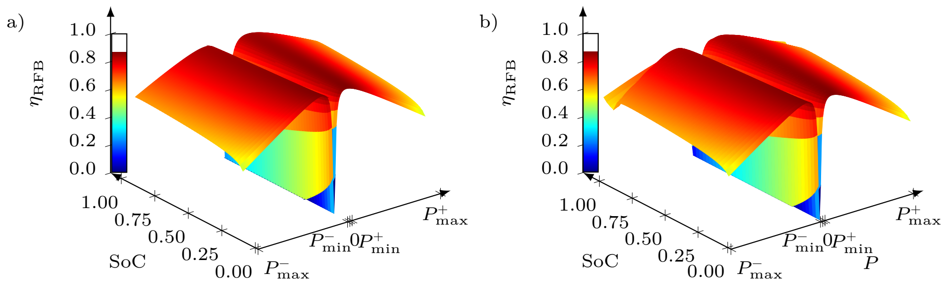

Figure 67: Three-dimensional efficiency map of a redox flow battery incorporating all losses for a SoC range between 0.1 and 0.9 (a) and a SoC range between 0.05 and 0.95 (b)

5 Control of the hybrid compensation system

In order to utilize the introduced setup for provision of system services, a control structure including measurement and determination of present power quality deviations, calculation of control commands and parameterization of the actor is required. Therefore, approaches for interpreting measured analog input signals and calculating deviations of relevant power quality parameters for application in control are developed. Restrictions and the influence of disturbing effects are analyzed. Subsequently, power values associated with the determined deviations are calculated. Aim of this chapter is to present a solution for the distribution of power to various system services according to the demand.

5.1 Methods for power quality assessment

As introduced in chapter two, a broad variety of approaches is available for determination of different attributes of power quality. Evaluation of the methods regarding their application in the control of the plant was subject of the conducted reseach work. In order to evaluate the applicability of selected approaches their accuracy is analyzed for typical magnitudes of the power quality attributes under consideration and relevant scenarios of superposing other deviations. Of particular relevance are variations of the fundamental frequency, which is subject to steady alteration in the range between 49.8 Hz and 50.2 Hz. Statistically, the grid frequency has a small standard deviation from the set point of 50 Hz. A long-term observation from June 2011 to the end of December 2014 showed a standard deviation of f $\sigma\ = 0.0274$ Hz, so that approximately 68 % of the measured network frequency values were in the range between 49.9726 Hz and 50.0274 Hz [285]. Thus, the vast majority of the occurring frequency values are between 49.95 Hz and 50.05 Hz. Frequencies lower than 49.90 Hz or higher than 50.10 Hz rarely occur.

5.1.1 Mean and root mean square value of signals

To observe the instantaneous values of the phase voltages and phase currents, both mean value $\overline{X}$ and root mean square value $\overline{X^2}$ are calculated from the sampled measured values. The calculation is based on known formulas for time-discrete signals. Basis of each calculation is a sample vector containing

N sampled values x_n of the signal under consideration, which have been recorded in equidistant time steps with a fixed sampling frequency. The determination of the mean values of the voltage signals enables identification of any superimposed DC voltage components. For any AC voltage signal without DC voltage component, the mean value is zero. If mean values different to zero occur, the mean value of the signal corresponds to the DC voltage component of the signal. To calculate the RMS values of the signals, the individual values x_n of the time-discrete sampled signal are adjusted by the previously determined mean value, so that only the residual AC voltage component of the signal is evaluated.

$$X_{\mathrm{RMS}} = \sqrt{\frac{1}{N}\sum_{n=0}^{N-1}(x_n - \overline{X})^2} \tag{5.1}$$

For measurement and sampling of the voltage and current signals the input signals have to be scaled into the effective range of measurement of the metering equipment. Before interpretation, the calculated RMS values are inversely transformed into the original value range using a reference value.

5.1.2 Assessment of harmonic content

To determine the harmonic signal components of an analog input signal at a known fundamental frequency, the suitability of fast Fourier transformation (FFT) is evaluated. Target of evaluation is determination of magnitudes of the harmonic contents for deviations of the input signal to ideal conditions. For the ideal case of a fundamental frequency of 50 Hz, the FFT provides precise results of the present, integer harmonic components. If the signal frequency is changed at constant sampling frequency, however, in the area of the present signal components spurious oscillations appear. Accordingly, adaptation of the sampling frequency using PLL is reasonable. With increasing deviation of the signal frequency, both magnitude and bandwidth of the spurious oscillations are increased. Result of the FFT is a complex valued vector, whose length corresponds to the number of elements of the input data vector containing sampled values. As there is a direct connection between discretization in time domain and in frequency domain, it is possible to determine the frequency components of interest directly according to equation (5.2).

$$\Delta t \times \Delta f = \frac{1}{N} \tag{5.2}$$

At the respective position a complex value is present, which contains both amplitude and phase angle of the individual oscillation. Their amplitude corresponds to the absolute value of the complex number and the angle to the argument of the complex number. The actual phase angle is determined by correcting the angle of the complex number by a factor consisting of the length of a sampling time step and the angular velocity of the respective oscillation. The complex values of a fast Fourier transformation, executed on a complete signal period of a three-phase input signal are shown below (Fig. 68 a). According to the phase shift between the signals, the arguments of the complex numbers also differ.

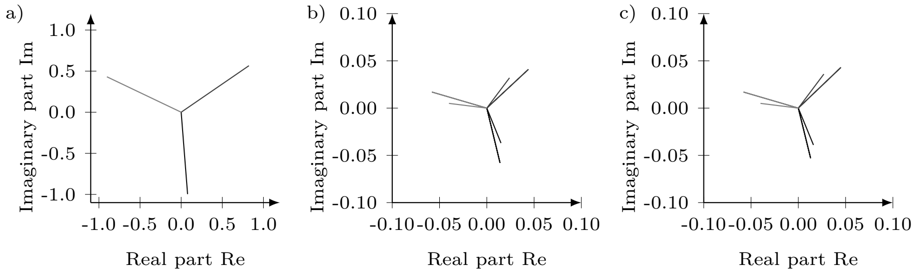

Figure 68: Fundamental oscillation of a symmetrical three-phase system (a) determined by FFT, a symmetrical superposition of the 3rd and 5th harmonics with a proportion of 4 % and 6 % (b) as well as an asymmetrical superposition of the 3rd and 5th harmonic with 5.5 %, 6.25 % and 6 % as well as 4.25 %, 4.5 % and 4 % (c)

Given a suitable time-synchronous, equidistant sampling of the observed signals, which is adapted to observed changes of the fundamental frequency if necessary, the FFT provides an exhaustive description of the signal attributes. Deviations in the signal characteristics are contained in the results of the FFT. For example, if the signal frequency deviates from the design frequency and the sampling frequency, in the spectrum of the FFT, additional oscillation components occur which distort the determined magnitudes of the harmonics. Other deviations, such as the phase shift, are also reproduced.

5.1.3 Determination of line frequency

The frequency of the AC signals is determined based on the sampled values as well. As an alternative to frequency measurement based on counting the zero-crossings, the space phasor is used for frequency determination. Here the circumstance that the space phasor changes its angle φ in dependence of the signal frequency over time serves as basis of the measurement method.

The angular difference $\Delta\varphi$ between the phasors of two sets of sampled values enables frequency determination, provided that the time interval of sampling is known. In general, angular velocity ω is defined as the alteration of angle per time. For a differential time step d and a differential angular difference $\mathrm{d}t$ it is denoted [87]:

$$\omega = \frac{\mathrm{d}\varphi}{\mathrm{d}t} \tag{5.3}$$

The analogous, three-phase input signal is sampled with a known sampling frequency f_s. Accordingly, there is a time span Δt between two sampling times, so that a space phasor $\nu(t)$ at time t and a space phasor $\nu(t+\Delta t)$ at time $t+\Delta t$ is calculated from the sampled quantities. Each space phasor represents a complex number, which can either be regarded as the sum of real part and imaginary part, or defined by its amount and its angle φ to the x-axis. A simple approach for determining the angular difference consist of converting the imaginary parts of the complex phasors into angles using inverse cosine function. Here, however, the problem occurs that the inverse cosine function is not a continuous function over several entire signal periods or integral multiples of $2\,\pi$. To avoid this problem, a method for immediate calculation of the angular difference is used. For real-valued vectors in Cartesian coordinates, the angle between two vectors can be calculated as the ratio of the scalar product or dot product of the two vectors and the product of their length according to the following equation [79].

$$\cos\varphi = \frac{\vec{a} \circ \vec{b}}{\sqrt{\vec{a}^2 \cdot \vec{b}^2}} \tag{5.4}$$

If this calculation scheme is transferred to complex numbers, the result is a complex angle. This is due to the fact that the result of scalar multiplication of complex numbers is a complex value, which is persistent after division by the real-valued product of the complex numbers absolute values [286, 287]. A permissible solution is to convert the complex vectors into non-complex vectors using their real parts and imaginary parts.

$$\cos\varphi = \frac{\mathrm{Re}(\underline{\vec{a}}) \cdot \mathrm{Re}(\underline{\vec{b}}) + \mathrm{Im}(\underline{\vec{a}}) \cdot \mathrm{Im}(\underline{\vec{b}})}{\sqrt{\mathrm{Re}(\underline{\vec{a}})^2 + \mathrm{Im}(\underline{\vec{a}})^2} \cdot \sqrt{\mathrm{Re}(\underline{\vec{b}})^2 + \mathrm{Im}(\underline{\vec{b}})^2}} \tag{5.5}$$

In order to be able to calculate the angle deviation $\Delta\varphi$ between the space phasors $\underline{\nu}(t)$ and $\underline{\nu}(t+\Delta t)$ as a scalar value, equation (5.5) was extended by the complex space phasors. Therefore, the space phasors are represented by their real parts and imaginary parts. As a result, the angular deviation between two space phasors is calculated according to the subsequent equation (5.6).

$$\Delta\varphi = \operatorname{arcos}\left(\frac{\operatorname{Re}(\vec{\underline{\nu}}(t)) \cdot \operatorname{Re}(\vec{\underline{\nu}}(t+\Delta t)) + \operatorname{Im}(\vec{\underline{\nu}}(t)) \cdot \operatorname{Im}(\vec{\underline{\nu}}(t+\Delta t))}{\sqrt{\operatorname{Re}(\vec{\underline{\nu}}(t))^2 + \operatorname{Im}(\vec{\underline{\nu}}(t))^2} \cdot \sqrt{\operatorname{Re}(\vec{\underline{\nu}}(t+\Delta t))^2 + \operatorname{Im}(\vec{\underline{\nu}}(t+\Delta t))^2}}\right) \tag{5.6}$$

The frequency of an analog electric signal f, which is defined as the inverted value of the signal period duration T, corresponds to the angular velocity ω of a coil rotating in a magnetic field. Within T, an entire period of the signal can be observed and thus the angle of the signal phasor is changed by $360\,^\circ$ or $2\,\pi$. Accordingly, angular velocity and frequency are associated by $\omega = 2\,\pi\,f$. By dividing $\Delta\varphi$ by the length of the time step Δt, the angular velocity ω is obtained and the actual signal frequency f is determined:

$$f = \frac{\omega}{2 \cdot \pi} = \frac{\Delta\varphi \cdot f_s}{2 \cdot \pi} \tag{5.7}$$

When considering real analog input signals containing noise or other interference, the analysis of a single pair of space phasors not sufficient for reliable frequency determination. Accordingly, it is recommended to determine the frequency as the average value of several individual angular differences. In Figure 69 it is visualized, how frequency determination is executed for ideal, sinusoidal input signals that are sampled with a low resolution of 6 bits.

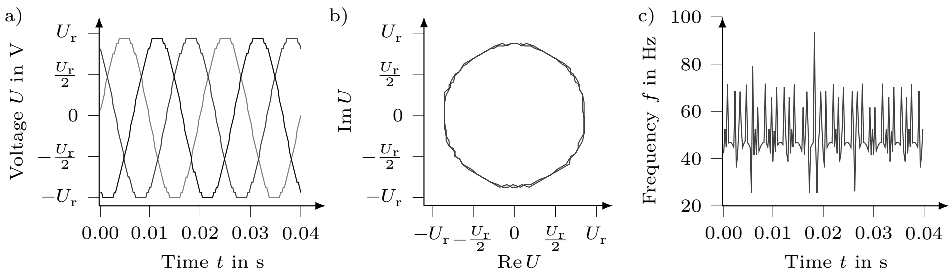

Figure 69: Illustration of determining the frequency of the three-phase system (a) based on the angular differences of of the space vectors (b) for a sampling frequency of 4 kHz, a resolution of 6 bits and a fundamental frequency f of 50 Hz. In (c) the course of the determined frequencies is depicted

For this resolution, only 64 different steps of the digitized signal can be distinguished. The low accuracy of the discrete valued input signals subsequently manifests itself in deviations of the progression of the space phasor from the ideal circular form. Moreover, the complex vectors deviate from the ideal values both in absolute value and argument, so that the angles between two vectors are also affected by an error. Consequently, the frequencies associated with the angular deviation also fluctuate. Nevertheless, a relatively exact reproduction of the frequency is achieved by averaging. For a sampling resolution of 16 bits, the accuracy of the digitized values is sufficient and fluctuations between single frequency values are marginal (Fig. 70).

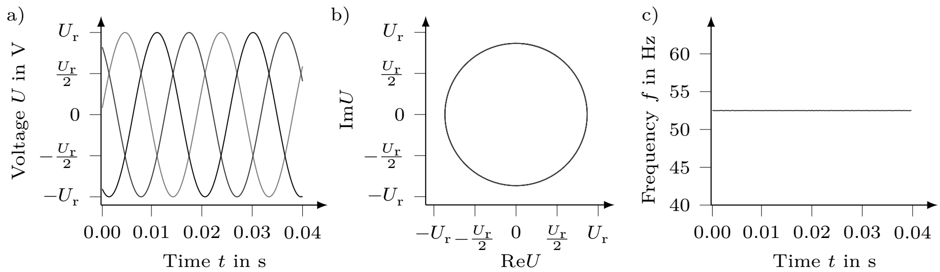

Figure 70: Illustration of determining the frequency of the three-phase system (a) based on the angular differences of of the space vectors (b) for a sampling frequency of 4 kHz, a resolution of 16 bits and a fundamental frequency f of 52.5 Hz. Calculated frequency (c) is 52.50 Hz

The frequency calculations shown were carried out using purely sinusoidal input signals without unbalance or other interference. However, this is often not true for signals in electrical networks. For proper determination of the frequency it is required that disturbances of the input signals do not significantly affect the results. When the method is tested for input signals containing unbalance or superimposed harmonic oscillations (Fig. 71), the disturbances are reflected in the shape of the space vector locus curve.

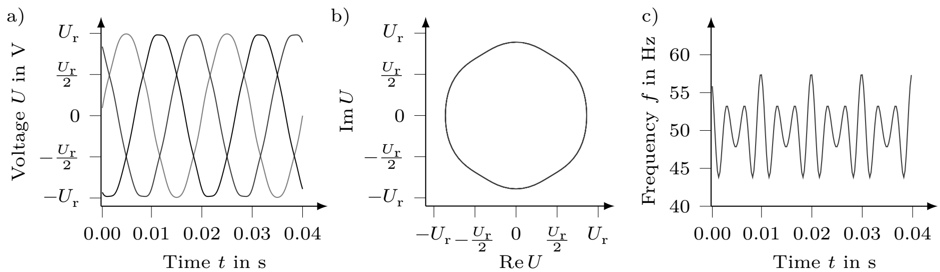

Figure 71: Illustration of determining the frequency of a three-phase system (a) with superimposed harmonics ($h_3 = 0.2\,\%$, $h_5 = 0.8\,\%$, $h_7 = 1.6\,\%$, $h_9 = 0.3\,\%$) based on the angular differences of of the space vectors (b) for a sampling frequency of 4 kHz, a resolution of 16 bits and a fundamental frequency f of 50 Hz. Calculated frequency (c) is 49.954 Hz

Individual frequency values and also the mean values of the frequency deviate from the reference value. The accuracy of the calculated frequency is reduced. For that reason it appears desirable to eliminate interfering signal components by filtering or applying other calculations before executing the frequency determination. A variety of transformations can be applied to the space phasor in order to filter out unwanted signal components [288, 289, 290]. As an alternative, ECKHARDT has demonstrated that a multi-stage FIR-filter, which is tuned to the sampling frequency and the frequencies to be filtered out, reliably eliminates the majority of interfering signal components [87, 291]. Any filter assigns an output value $y(n)$ to an input value or arbitrary excitation $x(n)$ by means of a transfer function $h(n)$ [134].

$$y(n) \quad = \quad h(n) * x(n) \tag{5.8}$$

Filters with finite impulse response (FIR) represent a non-recursive type of digital filters and provide a system response based on the instantaneous input value $x(t)$ as well as a finite, arbitrary selection of earlier input values. However, no previous output values are used. Common FIR filters are designed as averagers, as their transfer function calculates the output values as an average value of the input values [134]. For averaging filters, the transfer function is commonly represented as subsequently presented:

$$\begin{aligned} y(n) &= \frac{1}{N}\left(x[n] + x[n-1] +, \ldots + x[n-(N-1)]\right) \\ &= \frac{1}{N}\sum_{k=0}^{N-1} x[n-k] = \frac{1}{N}\left(N \cdot y(n-1) + x(n) - x(n-N)\right) \end{aligned} \tag{5.9}$$

The use of the term $y(n-1)$ in the formula does not contradict the aforementioned definition of a FIR filter, as it merely represents a simplification for the mathematical notation of the averaging all previous values. It is calculated based on the input values. Initially, parameters of the FIR filter to be used for filtering the space vector are to be defined. The basic order N_b of the filter is calculated in dependence of the lowest harmonic oscillation f_lh to be filtered out of the input signal and the sampling frequency f_s. In Figure 72 a FIR filter of the order N_b is applied to the space phasor.

In this case, the sampling frequency f_s is 4 kHz and the first harmonic to be filtered out h_1 has a frequency f_lh of 100 Hz, which is twice the fundamental frequency of 50 Hz.

$$N_\mathrm{b} \quad = \quad \frac{f_\mathrm{s}}{f_\mathrm{lh}} \tag{5.10}$$

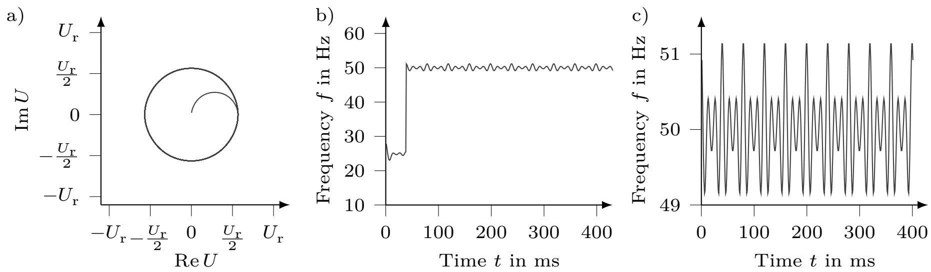

Figure 72: Locus curve of the space phasor in case of filtering using a single-stage FIR filter of 39 th order (a), transient response of the filter (b) and calculated frequencies (c)

If several FIR filters are connected in series, as shown in Figure 73 a, the accuracy increases with each filter stage, but the settling time of the filter is also increased.

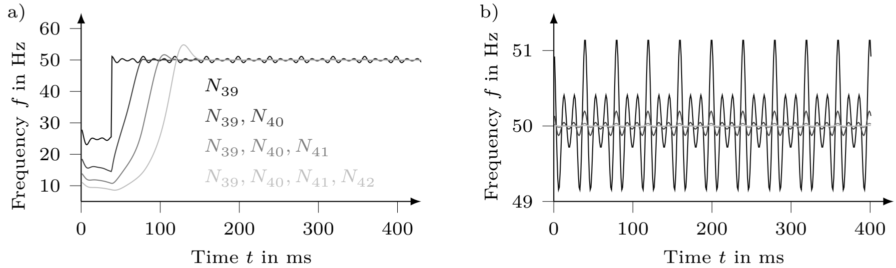

Figure 73: Course of the detected frequencies using one filter stage, two filter stages, three filter stages and four filter stages (a) as well as quantitative analysis of the frequency deviations depending on the filtering (b)

In the case shown, first the basic order N_b of the filter is determined as described and then, starting with a filter of order $N_b - 1$, the filter order is incrementally increased for each subsequent filter. As visualized in Figure 73 b the frequency deviation decreases with increasing number of FIR filters connected in series. The chosen approach has proven to precisely detect the frequency of signals with constant frequency. As frequency permanently fluctuates in electric grids in a small range, but under adverse operating conditions may assume values of 47.5 Hz or 52.5 Hz, the reaction of the procedure to unstable conditions is to be investigated. Therefore, a continuous alteration of frequency is implemented in a common range over some periods of the signal (Fig. 74 a). For that purpose, a fluctuating angular velocity is introduced into the generation of the sinusoidal three-phase test signal. Therefore, a deviation

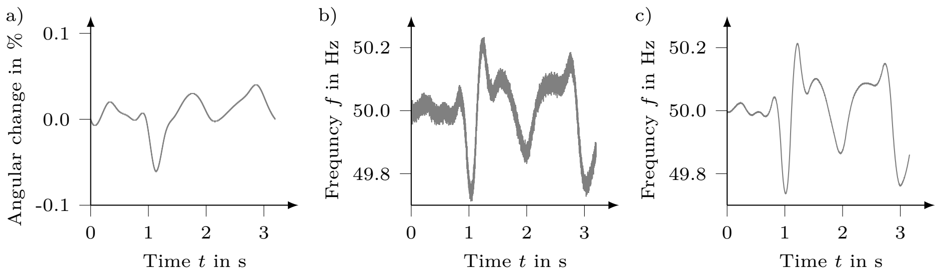

Figure 74: Spline representing the alteration of the angular velocity while calculating the test data for the three-phase system (a) and results of the frequency calculation based on the change of angle of the space phasor without filtering (b) and with a four-stage FIR filter (c)

of the angular frequency is defined for particular time steps. Subsequently, for sampling time steps between those observation time steps the corresponding frequency deviation is approximated. If the frequency curve is calculated on the basis of the introduced deviating angular frequency, it turns out that the angular change and frequency change are not completely analogous to each other (Fig. 74 a and b). This is due to the circumstance that the instantaneous values of the test signal are calculated using trigonometric functions. In summary, both methods for space vector-based frequency calculation are capable of tracking fluctuating frequencies. The course of the determined frequencies without filtering of the space phasor (Fig. 74 b) reveals significantly higher noise in comparison to filtering of the space phasor (Fig. 74 c).

5.1.4 Phase angle determination

For determination of the ratio between transmitted active power and reactive power, for each phase the difference between the phase angles of voltage signal and current signal is to be evaluated. The calculation is based on sampled measured values of the observed continuous time signal as stated in equation (5.11) for a sampling period T_s. For each phase, a data field is set up for the time-discrete current and voltage values of the measurement period. In a first step, the digital sampled values are converted into a complex phasor at a point in time t. The real part of the phasor consists of the digital sampled value $v(t)$ and for the imaginary part the sampled value exactly one quarter of a signal period T_p in the past is used. As for determination of the complex phasors in addition to the instantaneous value of the signal $v(t)$ an earlier measured value is required, it is necessary to obtain measured values from the previous signal period and the observation period. A further condition for the applicability of the method is that only entire periods of the signals may be considered to ensure that starting point and end point of the locus curve coincide in the complex plane. [292]

$$v(t) = v(k \cdot T_\mathrm{s}) \tag{5.11}$$

$$\underline{v}(t) = v(t) + \mathrm{j} \cdot v\left(t - \frac{1}{4} \cdot T_\mathrm{p}\right) \tag{5.12}$$

After a number of n complex current phasors $\underline{i}$ and voltage phasors $\underline{u}$ has been calculated based on a number of n time-synchronous and equidistantly sampled measured values of the current signal and the voltage signal, a set of n complex impedance phasors is generated from these. For undisturbed, perfectly sampled, continuous value signals, where no change in the phase angle occurs during the sampling period, all impedance phasors $\underline{Z}$ assume the same complex value. As this is not possible for real signals, a true impedance value $\overline{\underline{Z}}$ is determined by averaging all impedance phasors $\underline{Z}_i$ of the measurement period. [292]

$$\overline{\underline{Z}} = \frac{1}{N}\sum_{i=1}^{N} \underline{Z}_i = |\overline{\underline{Z}}| \cdot \mathrm{e}^{\mathrm{j}\varphi} \tag{5.13}$$

Now that the method for determining the phase shift between two sampled analog input signals has been introduced, it is evaluated whether the method can also be used for deviations from the ideal conditions. The analog-to-digital converters of the hybrid compensation system scan the analog voltage signals and current signals with a known sampling frequency and transform them into digital signals with a limited value range. Thus, for each instantaneous value of the signals, deviations from the real value caused by the analog-to-digital conversion occur. In addition, the frequency in the electrical network can deviate from the nominal value of 50 Hz, so that the sampled measured values do not correspond to an integer number of periods at an unchanged sampling frequency.

Table 1: Influence of sampling resolution and deviations of the line frequency on the accuracy of the calculation of the phase angle of two input signals phase-shifted by 45.00° at a constant sampling frequency of 4 kHz and a nominal line frequency of 50 Hz

	Grid Frequency:					
ADC Resolution:	47.5 Hz	49.0 Hz	49.8 Hz	50.0 Hz	50.2 Hz	52.5 Hz
2 bit	47.97	43.88	45.31	44.39	45.10	43.55
4 bit	45.39	44.63	45.04	44.97	45.20	44.86
8 bit	45.07	44.96	49.94	45.00	44.96	44.95
16 bit	45.01	44.99	45.00	45.00	45.00	44.86
24 bit	45.01	44.99	45.00	45.00	45.00	44.86

Explanation of the influence of frequency deviations

In the considerations above it has become obvious, that calculations based on Weindl and Freitag phasor are sensitive to frequency deviations. For a known, constant sampling frequency and constant frequency of the signal the phasor calculated using equation (5.12) is based on values which are exactly a quarter of a signal period apart (Fig. 75 a).

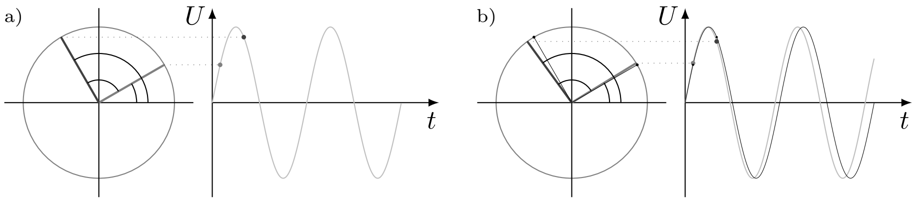

Figure 75: Impact of a frequency deviation on the calculation of the voltage phasor

A complex phasor is then formed from these measured values, where the real part corresponds to the signal amplitude at time t and the imaginary part corresponds to the signal amplitude at time $t - 1/4\,\mathrm{T}$. As for a constant fundamental frequency the signal curve over an entire signal period corresponds to a sinusoidal oscillation over an angle range of 0 to 360 degrees. The voltage phasors belonging to the measured variables used, which are different by a quarter period, enclose a constant angle of 90 degrees. The phasor by Weindl and Freitag results from these voltage phasors by vector addition. If the frequency of the sampled signal changes at constant sampling frequency and the period duration is defined by the number of sampling points, the signal values used to calculate the phasor no longer correspond to a period difference of a quarter period (Fig. 75 b). Accordingly, the angle of the voltage phasor also deviates from 90 degrees. The period T_s of the ideal signal corresponds to a frequency of $f_s = T_s^{-1}$. If the real signal frequency f_r deviates from f_s, a frequency gradient $\Delta f = f_r - f_s$ is present. This frequency gradient is used to determine the frequency-related angular deviation of the voltage phasor. As visualized in Figure 75 there is a time dependent angle deviation $\Delta\varphi$ between the phasor of the signal with ideal frequency f_s and the signal with a different frequency f_r.

Determination of phase angles based on FFT

A further approach of determining the phase angle φ_i between the current and the voltage signal of phase i is comparing the angles of the fundamental components. Therefore, a FFT is executed on a suitable data vector. Then the position of the fundamental component in the spectrum is determined and the argument of the complex number is evaluated. The angle difference between those two angles corresponds to the phase angle. For determination of the phase angles using FFT, however, it is required to analyze a series of signal values. It is not possible to determine alterations of the phase angle within the duration of a signal period. For this case, determination of phase angles based on instantaneous value phasors is better suited.

5.1.5 Calculation of unbalance

There are various methods available for determining the voltage unbalance, which are defined in standards with regard to power quality. However, the calculations differ considerably. Basically, eight different asymmetry cases are distinguished in three-phase AC voltage systems [293].

Table 2: Symmetrical case and all 8 cases of voltage unbalance in three-phase systems [293]

Cases of voltage unbalance		
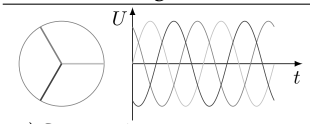 a) Symmetric system	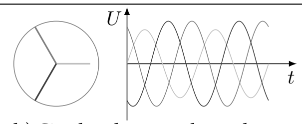 b) Single-phase under-voltage	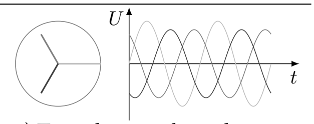 c) Two-phase under-voltage
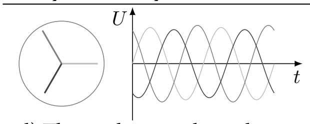 d) Three-phase under-voltage	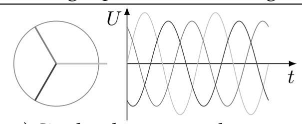 e) Single-phase overvoltage	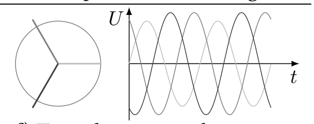 f) Two-phase overvoltage
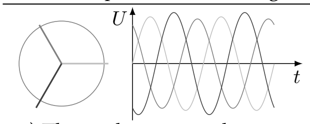 g) Three-phase overvoltage	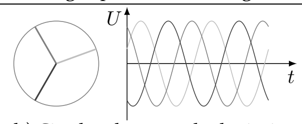 h) Single-phase angle deviation	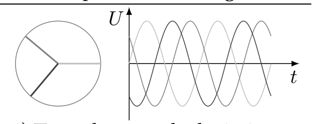 i) Two-phase angle deviation

These are single-phase, two-phase or three-phase under-voltage unbalances, single-phase, two-phase or three-phase overvoltage unbalances as well as single-phase or two-phase deviations of the phase angles. Analogous to the already introduced representation, the IEEE standard 1159 considers unbalance in three-phase systems as the ratio of the magnitude of the negative sequence component to the magnitude of the positive sequence component. For the case that only RMS values of the phase-to-phase voltages are available, calculation is possible disregarding phase angles. [69, 293, 294]

$$\mathrm{VU} = \sqrt{\frac{1-\sqrt{3-6\cdot\beta_{\mathrm{VU}}}}{1+\sqrt{3-6\cdot\beta_{\mathrm{VU}}}}} \tag{5.14}$$

$$\beta_{\mathrm{VU}} = \frac{|V_{12}|^4+|V_{23}|^4+|V_{31}|^4}{(|V_{12}|^2+|V_{23}|^2+|V_{31}|^2)^2} \tag{5.15}$$

If the phase angles are known, the determination by means of the symmetrical components is recommended. According to the principles of calculating the symmetrical components, the voltage imbalance factor VUF is calculated as a quotient of negative sequence component $\mathcal{V}_2$ and positive sequence component $\mathcal{V}_1$. [293, 295, 296, 297]

$$\mathcal{V}_1 = \frac{V_{12}\cdot a^0+V_{23}\cdot a^2+V_{31}\cdot a^1}{3} \tag{5.16}$$

$$\mathcal{V}_2 = \frac{V_{12}\cdot a^0+V_{23}\cdot a^1+V_{31}\cdot a^2}{3} \tag{5.17}$$

$$\mathrm{VUF} = \frac{\mathcal{V}_2}{\mathcal{V}_1} \tag{5.18}$$

For a symmetrical three-phase system (Fig. 76 a) both the voltage phasors of all phases (Fig. 76 b) and the phasors of the positive sequence component and the negative sequence component (Fig. 76 c) form congruent circles.

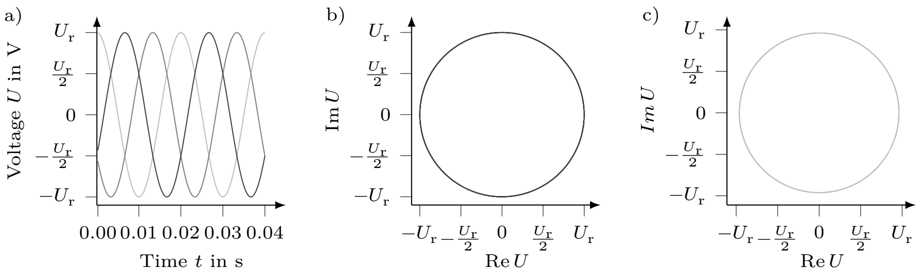

Figure 76: Sampled input signal (a), phase vectors (b) and symmetrical components (c) of a symmetric system for calculation of VUF. VUF $= 0.0\,\%$

Accordingly, the voltage unbalance factor VUF is zero. In unsymmetrical case, for example a single phase overvoltage (Fig. 77 a), the absolute value of one phase voltage phasor differs from the others. As a consequence, the radius of the circular shaped locus curve deviates (Fig. 77 b) and negative sequence component is present (Fig. 77 c).

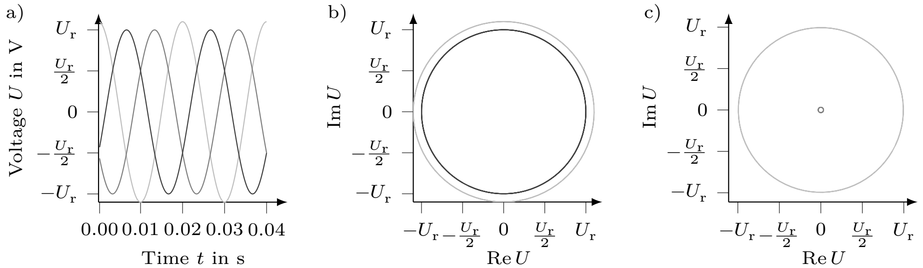

Figure 77: Sampled input signal (a), phase vectors (b) and symmetrical components (c) of a system with one-phase overvoltage of 10 % for calculation of VUF VUF = 3.2 %

If a phase deviation between the voltage signals is present and all phase voltage signals feature the same magnitude (Fig. 78 a), the locus curves of the voltage phasors are congruent (Fig. 78 b). After transformations into symmetrical components, negative sequence component occurs (Fig. 78 c).

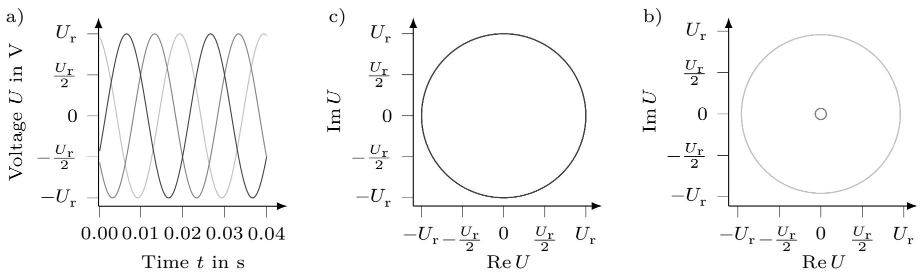

Figure 78: Sampled input signal (a), phase vectors (b) and symmetrical components (c) of a system with a phase shift of phase 3 of 12° for calculation of VUF. VUF = 7.0 %

Both methods have in common that the phase-to-phase voltages are used in the calculation and not the phase-to-neutral voltages. As phase voltages are usually measured as phase-to-neutral voltages, in the apron of unbalance calculation determination of the phase-to-phase voltages is necessary. This is accomplished using the phase angles calculated by FFT or the phasors. Based on the known equation for determination of the voltage phasor, for all three sampled phase-to-neutral voltages the voltage phasors are calculated.

Subsequently, for all individual phase-to-neutral voltage phasors of the observation period, phase-to-phase voltage phasors are provided. Those are then either inserted in computation of the unbalance factor or transformed to symmetrical components.

5.2 Control of the power distribution of the converter

During operation of the hybrid compensation system, power is allocated for provision of system services. Target of superordinate control is to exploit the installed power of the converter at greatest possible benefit regarding power quality. This is executed by allocating the total power output to different system services. In a first step, the total power required for exhaustive compensation of all deviations towards the ideal value of all power quality dimensions under consideration is determined (Fig. 79).

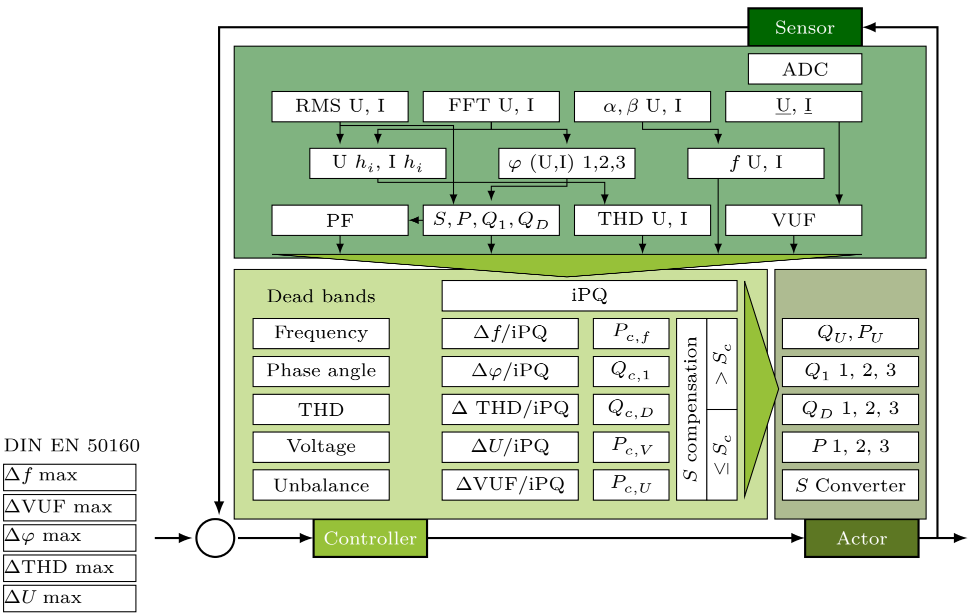

ADC:	Analog-to-digital converter	VUF	Voltage unbalance factor
RMS	Root-mean-square value	THD	Total harmonic distortion index
FFT	Fast-Fourier-Transform	iPQ:	Total power quality indicator
$\varphi(U, I)$	Phase angle between voltage and current signal	P_c	Active power for compensation
α, β	Clarke-transformed voltage and current signals	Q_c	Reactive power for compensation
f	Frequency	S_c	Apparent power of the converter

Figure 79: Visualization of the control loop for determining the parameterization

Before parameterizing the converter, a case distinction is required. If the power required for provision of all system services minus the effective power to be exchanged is less than 100 kW, each system service may be allocated the required power value. Correspondingly, both the required power values for the exchange of active power with the storage system and the power values for provision of the system services are parameterized. If the power required to provide all system services, including the active power to be exchanged, is less than 200 kW, all requirements can be met and the power converter is parameterized in accordance with these power requirements. In the event that the power required to provide the system services minus the active power is less than 200 kW but the active power is greater than the remaining power of the converter, only the remaining power value used for exchange of active power. If the total power required to provide the system services minus the active power exceeds 200 kW, a power distribution according to the procedures outlined above is required.

5.2.1 Calculation of power values

For individual parameters of power quality, the power required for exhaustive compensation is calculated as a function of the measured state variables and known parameters of the network. It is assumed that the power required for compensation equals the power values associated with the present deviations. Based on the fundamental relationships introduced in Section 2.4.11, relevant power values of the network are calculated. It is necessary to transfer the analysis to a three-phase system. In symmetrical three-phase systems, where voltages and currents of the phases feature the same value, the instantaneous active power is constant and equals the sum of all phase power values. In unbalanced three-phase systems, phase voltages and phase currents deviate. [31]

$$P = \frac{1}{T}\int_0^T u_1 \cdot i_1 \,\mathrm{d}t + \frac{1}{T}\int_0^T u_2 \cdot i_2 \,\mathrm{d}t + \frac{1}{T}\int_0^T u_3 \cdot i_3 \,\mathrm{d}t \qquad (5.19)$$

$$= P_1 + P_2 + P_3 \qquad (5.20)$$

Analogously, displacement reactive power Q and the distortion reactive power D in the unbalanced three-phase system are defined as the sum of the phase values. Calculation of power values of a single phase incorporates current values, voltages values and phase angles of all relevant oscillations. [84]

5.2.2 Interpretation of measured values

A first step of controlling the system and subject of the conducted research work is interpretation of measured data and determination of power quality parameters. Those parameters are provided in time steps of 0.1 s seconds by a connected power quality analyzer. Both voltage signals and current signals of the three-phase network are analyzed. The determined deviations are compared to the permissible maximum values of deviation. For validation purposes, the introduced procedures are used to determine the power quality parameters and three-phase test signals for current and voltage are analyzed. The signals are virtually sampled over a period of 100 ms and the calculations of the power quality parameters are executed on these sample vectors. As an example, an effective voltage of the input signals of 20 kV and a current of 300 A per phase is assumed. The system therefore transmits 18 megawatts of power at the time of observation. In Figure 80 input signals of voltage signal (a) and current signal (b) are visualized, represented by a single signal period. The instantaneous amplitudes of the signals are related to the maximum value of the respective signal.

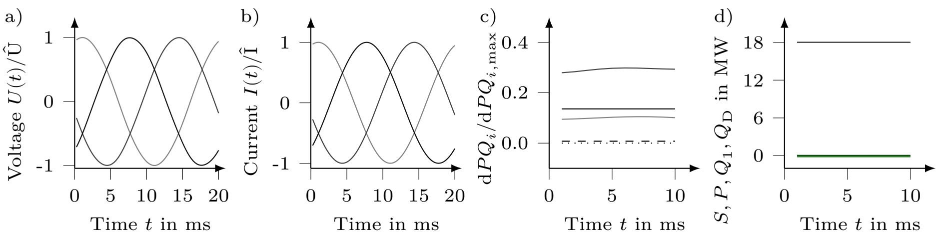

Figure 80: Analysis of voltage (a) and current signals (b) featuring a frequency of 50.02 Hz, a phase angle between voltage signals and current signals present at the phases 1 and 2 of 0.75 ° and superimposed voltage oscillations $h_3 = 0.4\%$ as well as $h_5 = 0.5\%$. Calculation of power quality indicators (c) and associated power values (d)

Figure 80 c visualizes the determined deviations of the power quality parameters in relation to the respective maximum values of deviation. A THD of approximately 0.6 % was determined due to the superimposed harmonic oscillations, which for a maximum permissible THD of 2 % corresponds to a value of 0.3. The determined voltage unbalance factor of 0.4 % results in a value of 0.2 given a maximum permissible unbalance of 2 %. The determined frequency deviation from 50 Hz fluctuates by 0.02 Hz with a few percent deviation. A power factor of 0.00038 was determined and a deviation from the nominal value of the voltage is not present. Corresponding to the low value of the power factor, as shown in Figure 80 d, active power is essentially transported. Both apparent power S and active power P assume a value of 18 MW. A total of 157 kW displacement reactive power is transported and the distortion reactive power is around 50 kW.

In a second example, the phase angle between the voltage signal and the current signal of the phases 1 and 2 is increased to 5 ° as visualized in Figure 81 a and b. Further disturbances are not present.

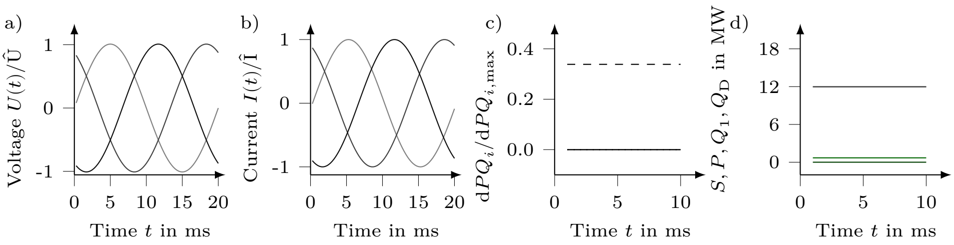

Figure 81: Analysis of voltage (a) and current signals (b) featuring a frequency of 50.00 Hz and a phase angle between voltage signals and current signals present at the phases 1 and 2 of 0.5 °. Calculation of power quality indicators (c) and associated power values (d)

As a consequence, the deviations of the parameters frequency, THD, unbalance and voltage in relation to the permissible maximum values assume the value zero. The power factor, however, is 0.1692, which in comparison to a limit of 0.5 corresponds to a value of 0.34. Correspondingly, here displacement reactive power of 1.05 MW is present. Accordingly, the required power quality parameters are available in the required temporal resolution of 100 ms. Subsequently, average values are calculated over periods of one second each, which are later used to distribute the available converter power to individual system services.

5.2.3 Dead bands for permissible fluctuation ranges

As a reaction to picayune deviations of power quality parameters to their ideal value is not necessarily, dead bands are introduced. Those dead bands define a range, in which fluctuations of the respective power quality parameter are tolerated. If fluctuations of the power quality parameters occur within the tolerated range, the deviation is set to zero. A permissible range for frequency fluctuations is between 49.95 Hz and 50.05 Hz as depicted in Figure 82 a.

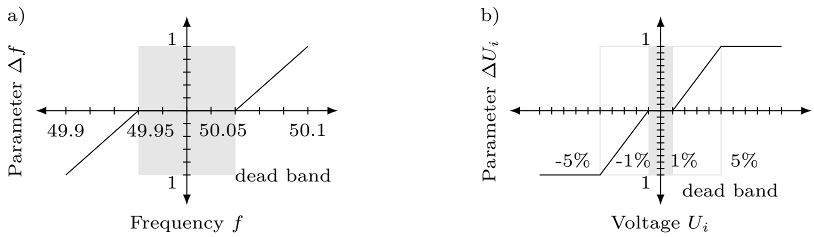

Figure 82: Visualization of dead bands for definition of permissible fluctuation ranges for frequency f (a) and the RMS values of the voltages of all phases U_i (b)

If the metered value of the frequency is outside the defined range, the error signal Δf assumes values different to zero. In cases where the permissible deviation is limited, the error signal assumes a maximum value if the deviation exceeds the limit. Then the error signal assumes a constant maximum value. This is visualized for the voltages U_i of all phases in Figure 82 b.

5.2.4 Calculation of an aggregated index of power quality

As the compensation system is required to distribute its limited value of apparent power to several system services in dependence of the power quality parameters, the permissible fluctuation ranges of individual power quality parameters are converted into comparable, dimension-less indicators Q_i.

$$Q_i = \frac{\mathrm{d}PQ_i}{\mathrm{d}PQ_{i,\max}} \tag{5.21}$$

For those indicators it is defined, that their maximum absolute value is one. If a violation of the permissible fluctuation range occurs, the indicator assumes an absolute value of one disregarding the magnitude of the deviation. The indicators assume a value of zero if no deviation is present or the present deviation is within the dead bands. Based on those indicators, an aggregated index of power quality i_{PQ} is determined. As a result of the conducted research work it is proposed to add up the dimension-less indicators of individual power quality dimensions. With increasing power quality, i_{PQ} is decreasing to a minimum value of zero. According to the calculation of the indicators of individual power quality parameters, the maximum value of i_{PQ} corresponds to the number of included parameters [298].

$$i_{\mathrm{PQ}} = \sum_{i=1}^{n} |Q_i^x| \tag{5.22}$$

The share of each individual power quality deviation is now determined by relating individual dimension-less indicators Q_i to i_{PQ}. In addition to the power quality deviations, a variable index between zero and one representing the urgency of the active power exchange is integrated. By means of this index, the energy exchange with the storage system is controlled.

5.2.5 Allocation of total power output

Based on the calculated share of the deviation of individual power quality parameters, the available power of the converter is distributed. This is executed by relating the relative deviation of each individual reactive power type to the sum of all the reactive power types considered. However, as it is assumed that the demand for action to compensate for an impairment of the power quality becomes disproportionately important with increasing approximation to the permissible limit value, a higher weighting of larger deviations is appropriate. Weighing is achieved by changing the exponent x of the input variables.

$$p_{Q_i} = \frac{Q_i^x}{i_{\mathrm{PQ}}} \tag{5.23}$$

Now that a method for allocating the available power to individual system services has been presented, the available apparent power is distributed. As it is relevant whether the available power is sufficient to exhaustively compensate all present deviations, a case distinction is required. For this reason as a first step, it is necessary to determine the total power required for compensation of all individual phenomena. If the sum of the required power is less than the rated power of the converter, the values determined are parameterized to the converter for compensation. If the required power exceeds the converter power, a distribution according (5.23) is compulsory.

5.2.6 Relation between voltages and currents

As already mentioned, the reaction of the system to detected power quality deviations is feeding compensation currents with suitable signal characteristics into the grid. Known parameters of power quality refer to voltage quantities in the network. In order to eliminate power quality deviations, it is prerequisite that the compensation currents exert an effect on the voltage signals. This is true, as according to ohmic law, a voltage drop occurs when a current passes through a resistor. In electrical AC voltage systems, reactances $\underline{Z}$ are regarded as resistors. As modeling of the real conditions of a distribution network exceeds the scope of this work, the effect of the compensation system is evaluated using a minimalist network model as presented in Fig. 83 a as result of the conducted research work.

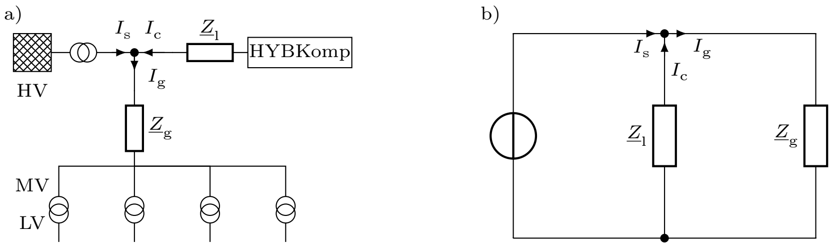

Figure 83: Simplified network model (a) and equivalent circuit diagram to illustrate the branch impedance and the network impedance (b)

A voltage change at the measurement point is proportional to the voltage change due to the compensation current I_c at the reactance of the network branch $\underline{Z}_l$ via which the compensation system is connected to the grid and the change in the load current I_s of the network due to the compensation current at the reactance of the network $\underline{Z}_g$ (Fig. 83 b). Furthermore, the frequency dependence of the reactances is to be taken into account. Accordingly, the voltage drop at the reactances is dependent on the frequency of the current signal in addition to its absolute value. In the frequency range between 50 Hz and 100 kHz, the dependence of the reactance on the frequency is assumed to be linear. The influence of a certain compensation current of the hybrid compensation system on the power quality parameters depends on the reactance of the network under consideration. [299, 300]

An unimpaired voltage signal is provided by the feeding high-voltage network. At the impedances of the network, the equipment, consumers and feeders, induced currents with different, non-ideal time curves are generated by this voltage signal. When passing through impedances of the network, these currents affect the course of the voltage signal. By feeding in compensation currents, the current signal is corrected directly and the voltage signal indirectly. The correction always takes place with regard to the conditions at the reference point. In the case of compensation with reference point at the busbar of the transfer station, current signals and voltage signals are corrected in the direction of the feeding high-voltage network. Load currents of the loads and feeders of the network cannot be compensated. However, the improved voltage signal compensated with regard to the transfer station has a positive effect on the power quality in the network.

5.3 Generation of current signals for compensation

The generation of the supplied current signals is based on the power per system service and on the detected signal attributes. For determining the displacement reactive power Q_1, the amperage at time t is determined as a function of the RMS value of the voltage U_{RMS_i}, the determined phase angle φ_i and Q_1 as visualized in Figure 84 a. As a phase deviation between voltage signal and current signal is present at two phases, compensation currents are provided for two phases only. The detected frequency deviation is within the dead band. Compensation currents are fed in with a phase shift of 180 degrees. The same applies to the calculation of the compensation currents to eliminate harmonics as depicted in Figure 84 b. Their amplitude is determined as a function of the determined amplitude of an individual voltage harmonic in relation to the other amplitudes of the voltage harmonics, the U_{RMS} and the distortion reactive power Q_{D}.

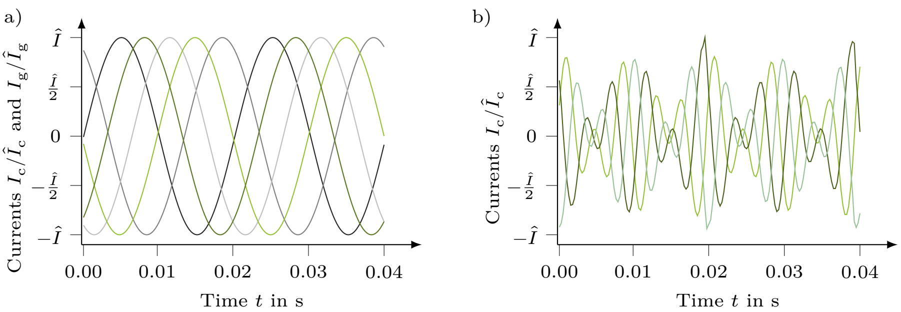

Figure 84: Grid currents and compensation currents for phase 1 (dark gray and green), phase 2 (gray and dark green) and phase 3 (light gray) for the case presented in Figure 81 (a) and of phase 1 (green), phase 2 (dark green) and phase 3 (light green) for the case of Figure 80 (b)

For the provision or withdrawal of active power P, the procedure corresponds to the feeding of displacement reactive power, where the phase angle is zero degrees. For balancing, all powers are distributed proportionally to the phases.

As a result, an integrated approach is available that enables digital processing of the analog input signals, calculation of present power quality deviations as well as their aggregation to power quality indicators. Those indicators are used to distribute the power of the converter to individual system services. In conclusion the obtained information on the observed signals are used to derive the signal progression of the required compensation currents both in waveshape and in magnitude.

6 Power and energy management

It is task of storage control to fulfill several requirements in parallel. Energy management has to plan times and quantities of energy exchange in advance based on forecast variables. Power management is required to control power flows in accordance with optimality criteria and adapted to instantaneous requirements. In order to be able to react to spontaneous performance requirements, storage control aims at enabling flexibility. Energy and power management comprises several stages and is subdivided into a planning phase and a control phase. In planning phase, a quantitative profile of energy exchange is created based on forecast values for load and generation. From this profile, target state of charge values of the storage system are determined for defined intervals. The energy difference of two planned state of charge targets is used as default value in capacity planning. Finally, the amount of energy to be exchanged is translated into target power values using distribution functions. In control phase, the instantaneous power value is distributed to the storage system with the highest possible efficiency. For this purpose, a continuously updated efficiency profile of both storages within the storage system is used, incorporating changes of state of charge as well as environmental parameters. Any deviation between target power value and instantaneous power is tracked. By recalculating the distribution in case of occurring deviations, it is attempted at achieving the planned exchange of energy.

6.1 Energy management

Capacity planning is considered the main task of energy management. Based on prognosis data or empirical values on the temporal structure and the quantity structure of generation surpluses and excess demand, the state of charge of the storage system is determined over a planning period. Target of energy management is to meet external requirements regarding feed-in and storage of energy and to utilize the available capacity of the storage system at best.

6.1.1 Pooling of charging and discharging forecasts to blocks

In a first step, the forecast profile for energy exchange is determined by superimposing generation forecast, load forecast and an individual energy exchange profile (Fig. 85 a).

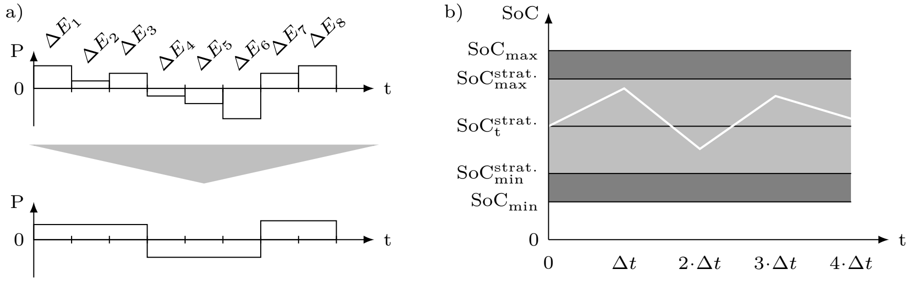

Figure 85: Aggregation of energy quantities from adjacent time periods with the same sign into blocks (a) and exemplary visualization of target state of charge planning over time (b) [234]

The result is an aggregated profile scheduling times of charging as well as discharging and quantifying the amounts of energy to be exchanged between the grid and the storage system. Based on the forecast profile, the state of charge of the storage system is planned over the period under consideration (Fig. 85 b). It appears desirable to charge the storage systems during periods associated with generation surplus, represented by positive values in the forecast profile. Analogously, discharging is supposed to take place in time periods with negative forecast values. In order to ensure distribution of energy during those periods, it is accepted to absorb a quantity of energy exceeding the forecast surplus in the previous time step. Therefore, knowledge of the amounts of energy required in time periods with excess demand is of interest. In a first step adjacent entries with the same sign of the forecast profile are combined and thus transformed into larger blocks. The energy quantity of all elements of the block is added up and each block is defined by its start time and its end time. In the resulting block profile periods with excess demand alternate with time periods of generation surplus.

6.1.2 Subdivision of the capacity of the storage system

In the next step, it is determined which quantities of energy are to be absorbed or released in the time ranges of charging and discharging. The aim is first to determine the target load factors of the storage system for all points in time at the block boundaries. The SoC is a measure of the amount of energy available in a storage at a certain point in time in relation to the capacity of the storage. In the present case of a hybrid storage system, the state of charge of storage system is a composite quantity. Each of the two storages S_1 and S_2 features a certain capacity of C_1 and C_2. With regard to these capacities, each storage i of the storage system may assume a minimum charge level $\mathrm{SoC}^{\mathrm{i}}_{\mathrm{min}}$ and a maximum charge level $\mathrm{SoC}^{\mathrm{i}}_{\mathrm{max}}$ by charging and discharging due to technical restrictions. The storage system therefore has a minimum charge level $\mathrm{SoC}_{\mathrm{min}}$ and a maximum charge level $\mathrm{SoC}_{\mathrm{max}}$. The maximum amount of energy to be absorbed into the storage system or recovered from it by neglecting all loss mechanisms $E^{\mathrm{S}}_{\mathrm{max}}$ is calculated according to the equation (6.1).

$$E^{\mathrm{S}}_{\mathrm{max}} = (\mathrm{SoC}^{1}_{\mathrm{max}} - \mathrm{SoC}^{1}_{\mathrm{min}}) \cdot \mathrm{C}_1 + (\mathrm{SoC}^{2}_{\mathrm{max}} - \mathrm{SoC}^{2}_{\mathrm{min}}) \cdot \mathrm{C}_2 \qquad (6.1)$$

Within the interval of possible storage levels, further limits are introduced for strategic reasons, which are relevant with regard to the behavior of the storage system. First, a maximum strategic state of charge $\mathrm{SoC}^{\mathrm{strat}}_{\mathrm{max}}$ and a minimum strategic state of charge $\mathrm{SoC}^{\mathrm{strat}}_{\mathrm{min}}$ are defined. A reason for this definition is the circumstance that the storage system cannot absorb any further energy when $\mathrm{SoC}^{\mathrm{S}}_{\mathrm{max}}$ is reached and cannot release any energy when $\mathrm{SoC}^{\mathrm{S}}_{\mathrm{min}}$ is reached. In order to maintain a certain level of flexibility, a strategic quantity of energy is kept available in the storage system limiting the discharging to $\mathrm{SoC}^{\mathrm{strat}}_{\mathrm{min}}$. Analogously, in order to be able to absorb a strategic energy quantity, charging is limited to $\mathrm{SoC}^{\mathrm{strat}}_{\mathrm{max}}$. The strategic maximum value or minimum value of the SoC are located at a distance $\Delta E_{\mathrm{strat}}$ from the absolute maximum and minimum values of the SoC. Furthermore, a strategic target value of the state of charge $\mathrm{SoC}^{\mathrm{strat}}_{\mathrm{t}}$ is defined. This value corresponds to the amount of energy which is preferably held available in the storage system, provided that external requirements do not demand other SoC levels.

6.1.3 Planning of the state of charge according to the forecast

The sequence of charging and discharging blocks is analyzed starting with the first element of the period under consideration. If the first element is a discharging block, it is evaluated based on the initial SoC whether the amount of energy available in the storage is sufficient for exhaustively compensating the demand. If this is true, the SoC at the end of the first time interval is determined and the energy quantity ΔE_1 is provided. Otherwise, the SoC at the end of the time interval is $\mathrm{SoC}^{\mathrm{S}}_{\mathrm{min}}$ and only the energy quantity $(\mathrm{SoC}^{\mathrm{S}}_{\mathrm{i}}$

- $\mathrm{SoC}^{\mathrm{S}}_{\mathrm{min}}) \cdot C_{\mathrm{S}}$ is provided. If the first element of the observation period is a charging block or if the SoC at the end of the first discharging block has been determined, now the charging block and the subsequent discharging block are jointly analyzed. Essential input variables are the initial state of charge, the energy quantity to be charged within the charging block ΔE_i and the energy quantity to be discharged during the discharging block ΔE_{i+1}.

If the required amount of energy exceeds the energy difference between $\mathrm{SoC}^{\mathrm{S}}_{\mathrm{max}}$ and $\mathrm{SoC}^{\mathrm{S}}_{\mathrm{min}}$, only this amount of energy is provided by the storage system. Accordingly, the SoC at the beginning of the discharge block is set to $\mathrm{SoC}^{\mathrm{S}}_{\mathrm{max}}$ and to $\mathrm{SoC}^{\mathrm{S}}_{\mathrm{min}}$ at the end of the discharge block. Otherwise, it is possible to provide the required amount of energy and the determination of the SoC depends on further conditions. For example, the amount of energy to be charged is set in a way that the SoC at the end of the discharging period is the optimal charge level. Moreover, if a significant difference between grid load and generation in the grid is predicted, usually impermissible SoC above $\mathrm{SoC}^{\mathrm{strat}}_{\mathrm{max}}$ or below $\mathrm{SoC}^{\mathrm{strat}}_{\mathrm{min}}$ are used. For all transitions between charging periods and discharging periods of the planning period, the target state of charge of the overall system is now fixed and the energy quantities to be exchanged within the blocks between the storage system and the surrounding system are also known. These parameters now serve as planning specifications for short-term power management.

6.2 Energy distribution over time based on functions

For each planning step, duration and amount of energy to be exchanged are known. The energy quantity corresponds to the integral of the function of power exchange over time. In principle, all possible functions for the distribution of power over time are permissible, whose integral features an equal area. However, technical restrictions and other considerations limit the number of possible functions for distribution of power.

6.2.1 Restrictions on power determination

A first limitation of possible power values is given by the specification of the individual storages. Any storage is able to provide power values between a negative maximum value $P^{i,-}_{\mathrm{max}}$ and a negative minimum value $P^{i,-}_{\mathrm{min}}$ as well as between a positive minimum value $P^{i,+}_{\mathrm{min}}$ and a positive maximum value $P^{i,+}_{\mathrm{max}}$. Consequently, the range of power provided by the storage system is divided into a positive range where the storage system provides power to the peripheral system and a negative range where power is fed into the storage. In the negative power range, the minimum negative power $P^{S,-}_{\min}$ corresponds to the lowest of the minimum negative power values of both storages $P^{S,-}_{\min} = \min(P^{1,-}_{\min}, P^{2,-}_{\min})$ and the maximum power value corresponds to the sum of the maximum negative power values $P^{S,-}_{\max} = P^{1,-}_{\max} + P^{2,-}_{\max}$. This applies analogously to the positive power range for the positive power values of the storages by means of $P^{S,+}_{\min} = \min(P^{1,+}_{\min}, P^{2,+}_{\min})$ and $P^{S,+}_{\max} = P^{1,+}_{\max} + P^{2,+}_{\max}$.

As a consequence, a requirement for any permissible function for distribution of power over time is that all power values assumed may not violate the power ranges spanned by the extreme values. Due to technical specifications of the devices, the current is altered in a defined step. For example, current output of the DC-DC-converter of the redox flow battery can be set to integer values only. As the voltage of the DC circuit is regarded relatively constant and power is a product of current and voltage, the possibilities of varying power are limited. Moreover, the size of the time steps $\mathrm{d}t$ is fixed, within which the power values of the storage system are changed. As a consequence, the task of distributing the power provided by the storage system is simplified from the determination of continuous power functions with equal area of the integral in the observation area to the distribution of the total area over a given number of equally large partial areas. The minimum energy exchange during a period of charging or discharging thus corresponds to the minimum permissible power of the storage system $P^{t}_{\min}$ over the duration of a single time step $\mathrm{d}t$. Analogously, the maximum amount of energy exchanged corresponds to the product of the maximum power value of the storage system over all time steps of the charging or discharging period. [161, 301]

6.2.2 Approaches to shaping the power distribution functions

During a period of charging or discharging, the power distribution function may exhibit an arbitrary course (Fig. 86 a) within the limits outlined above. However, the number of permissible functions is reduced to progressions which are deemed advantageous for the following reasons.

It is particularly easy to determine a constant power value (Fig. 86 b), which is provided over the entire charging or discharging period. Advantages of this approach are that the power consumption or power supply is very uniform and, in addition, extreme values of the power intervals are rarely assumed, so that necessary corrections in the event of deviations between nominal and actual values of the power are possible.

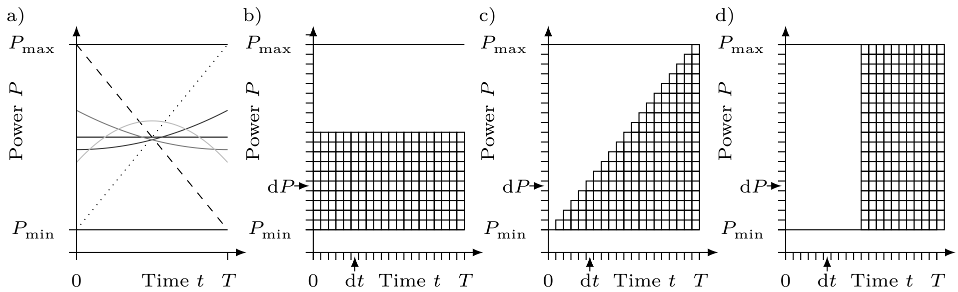

Figure 86: Distribution of a certain amount of energy ΔE by means of different functions (a) and simple strategies for the temporal arrangement of discrete energy blocks in ascending (b), constant (c) or latest possible order (d)

Another approach is based on the fact that stand-by losses of a storage increase with the amount of energy stored and the operation of a storage facility itself is associated with losses. For this reason, efforts are to be made to charge energy into the storage as late as possible within a charging period (Fig. 86 c and d) and to release the energy as quickly as possible within a discharging period. A third approach focuses on considerations regarding network operation. It is assumed that the predicted profiles of the energy demand and the energy supply are a result of continuous functions of the load and the generation. Power values in the transition areas, characterized by a change of the sign, are relatively low. By superposition of those functions, time intervals with generation surplus or demand excess are identified. Therefore, it appears reasonable for the desired distribution function to assume high power values at the middle of a charging or discharging period and low values in the transition areas.

6.2.3 Mathematical problem formulation

In general, the calculation of the power values corresponds to determining parameters of functions. For a certain segment of the functions to be determined the area enclosed with the x-axis is known.

$$E \quad = \quad \int_0^T P(t)\mathrm{d}t \quad = \quad [\,\mathfrak{P}(t) + d]_0^T \tag{6.2}$$

If it is preferred to distribute the majority of energy towards the middle of the time interval, the function conforms with to a downward open parabola as visualized in Figure 87 a. Both start time and end time represent zeros of the function. Therefore, the maximum value of the integral area enclosed by the parabola and the x-axis is determined by the known zeros and the vertex located at the maximum value. The solution of the distribution problem consists in determining the parameters a, b and c of the quadratic function as a function of the zeros, the integral area and the limits 0 and T of the considered interval. As a result of the conducted research work, by acknowledging the zeros of the function at both sides of the time interval T and calculating the antiderivative of a quadratic function the function parameters a, b and c were determined.

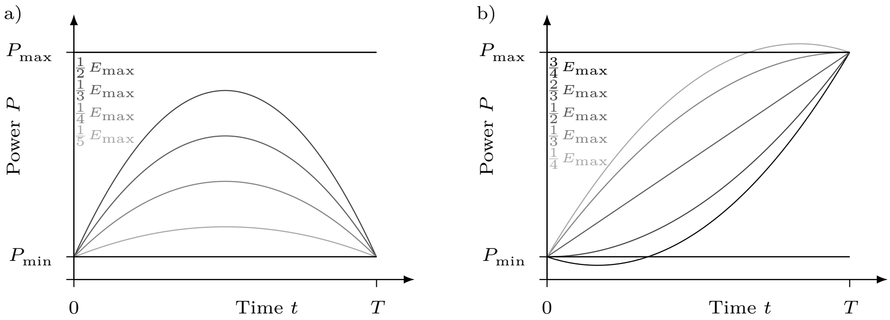

Figure 87: Distribution of energy quantities E over time using quadratic functions with distribution focus at the middle of the time interval (a) or at the end of the time interval (b)

They are represented in dependence of the energy quantity to be distributed E and the length of the time period T in equation (6.3):

$$a = -\frac{6 \cdot E}{T^3}, b = \frac{6 \cdot E}{T^2}, \quad c = 0 \tag{6.3}$$

If the energy quantity is preferably to be distributed as late as possible, the quadratic functions are as follows. The right branch of an upwardly open parabola is to be determined starting at the vertex, provided that the known area is smaller than half of the maximum possible area. Again, for the determination of the quadratic equation, two points as well as the area of the integral within the limits 0 and T are available. For x = 0 the function value 0 is assumed and at point x = T the function value is supposed to be $P_{\max}$. The function parameters a and b were estimated as a function of the boundary conditions T and Pmax:

$$a = -\frac{6 \cdot E}{T^3} + \frac{3 \cdot P_{\max}}{T^2}, b = \frac{6 \cdot E}{T^2} - \frac{2 \cdot P_{\max}}{T}, \quad c = 0 \tag{6.4}$$

Although a family of quadratic function exists, for which the parameters allow a distribution of E, a global application is not possible. This is due to the circumstance that outside a certain interval for E, the functions assume values less than zero or greater than $P_{\max}$ as visualized in Figure 87 b. Permissible combinations are in the range between 1/3 $E_{\max}$ and 2/3 $E_{\max}$. [234]

The power function has a larger area of application with regard to the distribution problem and is defined according to equation (6.5).

$$y \quad = \quad a \cdot x^b \tag{6.5}$$

Again, a zero of the function at x = 0, the value of the function at x = T and the integral area E between the x-axis and the function within the interval between 0 and T are known. Based on $P_{\max}$, T and E the parameters a and b are determined analytically [234].

$$a \quad = \quad P_{\max} \cdot T^{(-\frac{P_{\max}\cdot T}{E}-1)} \quad , \quad b \quad = \quad \frac{P_{\max} \cdot T}{E} - 1, \tag{6.6}$$

Exemplary courses of the power function are shown in Figure 88 a and b.

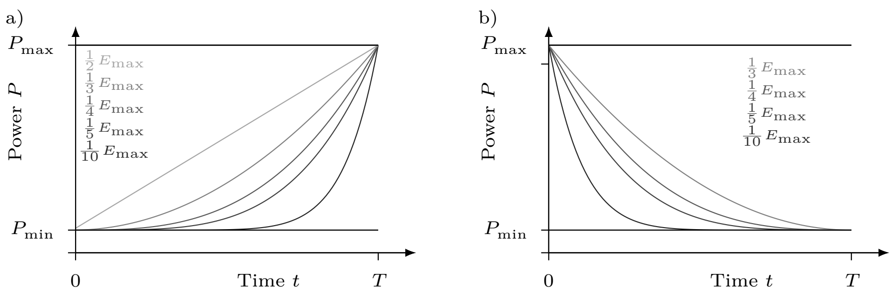

Figure 88: Visualization of power functions for distribution of different amounts of energy for latest distribution (a) and earliest distribution (b)

In theory, the function parameters of the power function are determined for any partial areas of $E_{\max}$. Due to large exponents for very small areas and small exponents for areas close to $E_{\max}$, problems arise in these cases when calculating individual power on implementation in algorithms. In these areas the power target values are calculated as average values.

6.2.4 Conversion into discrete power target values

Now that approaches have been elaborated by means of which energy quantities E are converted into target power values for a certain period between 0 and T, it is now necessary to translate the value-continuous distribution function into time-discrete and discrete-valued power specifications. It is to be taken into account that at time intervals of the length $\mathrm{d}t$ discrete-valued target values can be represented in multiples of the increment $\mathrm{d}P$. In the best case, the discrete power target corresponds to the average value of the values of the distribution function at the interval limits t_{i-1} and t_i. The number power steps $\mathrm{d}P$ is now determined based on the average value, where a rounding is necessary. If the division remainder is greater than 0.5, the next number in greater size of power steps is selected. Finally, it is to be evaluated, whether the number of energy blocks $\mathrm{d}E$ corresponds to the total amount of energy E to be exchanged.

6.3 Efficient power distribution to the storages

As the amounts of energy are to be distributed to two storages, a strategy for operation of the hybrid storage system is required. As a result of the conducted research work, the distribution with highest possible efficiency is investigated using a maximum efficiency point tracking (MEPT) approach.

1. Determination of possible power combinations of the storage system
2. Calculation of the overall efficiencies
3. Derivation of an efficiency profile
4. Determination of the efficiencies of power combinations with identical power value
5. Maximum value determination

Determination of permissible power combinations is executed by altering the power value of each storage in an identical increment ΔP. In a matrix of power combinations, equal power values are located on diagonals, where combinations below the main diagonals are associated with charging and combinations above the diagonal with discharging. For all power combinations stored in the matrix the particular efficiency is calculated. Input variables are the efficiency profiles in dependence of SoC and power. Based on all calculated overall efficiencies of the individual power combinations, efficiency profiles are derived as matrices of the efficiencies for one particular cofiguration of the

SoC values of both storages. The efficiency profile visualizes the efficiency of the entire system as a function of power of both storages. For each efficiency profile, the efficiencies of power combinations with identical value are determined by converting the diagonals into columns. As the maximum value per column corresponds to the best possible efficiency for the power value under consideration, a maximum value determination is carried out as a last step.

6.3.1 Determination of possible power combinations

The relationship between the state of charge of a storage, the power value and the efficiency are known from modeling of the storage technologies. An efficiency characteristic curve is created for any SoC as three-dimensional surface plots (Fig. 89 a).

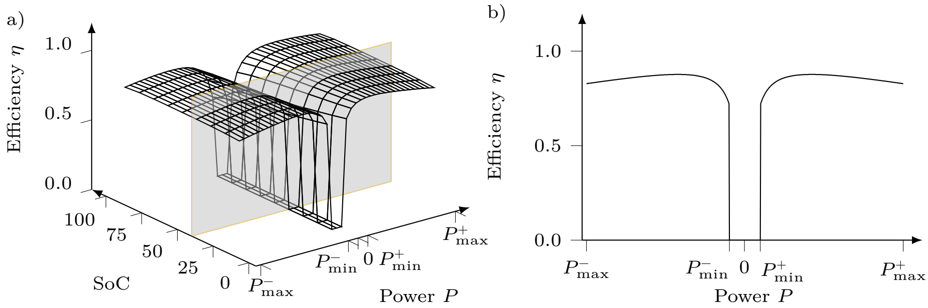

Figure 89: Efficiency profile of an energy storage for all state of charge and both positive and negative power values (a) and isolation of the efficiency curve for a specific SoC (b)

Consequently, for each SoC, the efficiency is a function of power that assigns exactly one efficiency value to each possible power value (Fig. 89 b). Accordingly, for a given SoC, the result of the efficiency function is a vector. The number of elements of which is formed in accordance with the number of possible power values and the elements of which are the efficiencies. For the present storage system, which consists of two energy storages, two efficiency vectors are calculated for a given state of charge of both storages. A solution to determining possible power combinations is altering the power of both storages in equal increment ΔP. Permissible power combinations are visualized in a two-dimensional coordinate plane (Fig. 90 a).

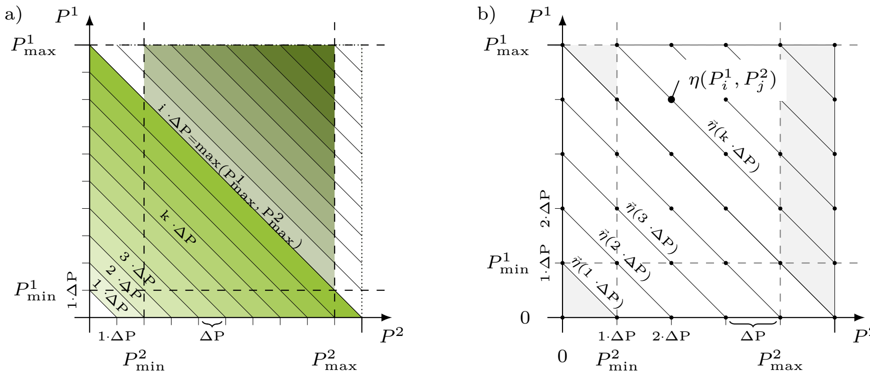

Figure 90: Illustration of the permissible power combinations in the purely positive range and the diagonals of equal power (a) and the corresponding efficiencies (b) [233]

The quantity of possible power combinations of the two storages is formed by two subsets. First, it is possible to operate both storages individually by altering the power value of an individual storage i in equal steps ΔP between the minimum power value P^i_{min} and the maximum power value P^i_{max}. As a second case, both storages are operated simultaneously, where the power of one or both storages is varied in equal steps ΔP. Due to the fact that the storages under consideration may feature different ratings of minimum power value P^i_{min} and the maximum power value P^i_{max}, the numbers of steps differ. Here, storage one assumes M steps and storage 2 N steps. In case that the power value of the power combinations is constant, the alteration of the power value of one storage is accompanied by a corresponding, inverse alteration of power of the other storage. Combinations of equal power are located on diagonals of the matrix, as $\Delta P = \Delta P^1 = \Delta P^2$ (6.7).

$$\underline{P}_{i,j} = \begin{pmatrix} 0 & \Delta P^2 & \dots & N\Delta P^2 \\ \Delta P^1 & \Delta P^1 + \Delta P^2 & \dots & \Delta P^1 + N\Delta P^2 \\ \vdots & \vdots & \ddots & \vdots \\ M\Delta P^1 & M\Delta P^1 + \Delta P^2 & \dots & M\Delta P^1 + N\Delta P^2 \end{pmatrix} \tag{6.7}$$

Knowledge of the position of the power combinations is relevant, as the maximum efficiency power combinations for each power value are to be determined (Fig. 90 b). If a storage system is considered in which both storages provide both positive and negative power values, the area of possible power combinations is divided into four parts by the coordinate axes (Fig. 91 a). The upper right quadrant contains those combinations for which the power output of both storages is positive. The lower left quadrant contains those power combinations, for which both storages provide a negative power, which consequently adds up to a negative overall power. In the other areas, the left upper quadrant and the right lower quadrant, the power output of one storage is positive and that of the other storage is negative. Consequently, these combinations always represent a power exchange between the storages, which in some cases is also accompanied by an external power exchange.

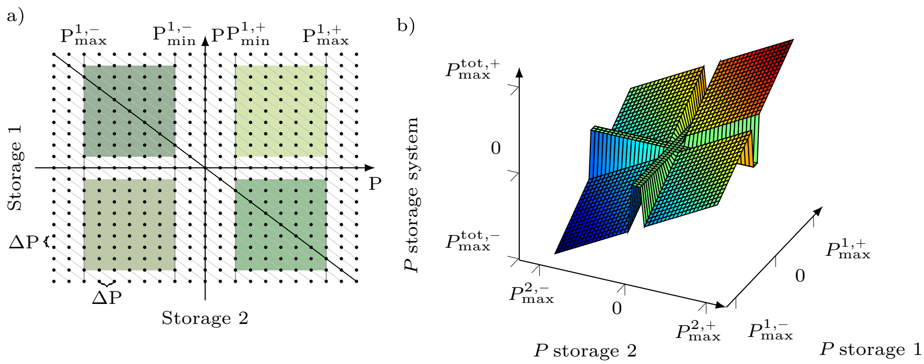

Figure 91: Illustration of possible sub-areas with permissible power combinations (a) and representation of a real power profile (b)

All combinations where power is exchanged between the storages only are located on the main diagonal, representing a power output of zero. On the coordinate axes those power combinations are located, for which the power value of one storage corresponds to the respective axis section and the power value of the other storage is zero. The permissible range of power combinations is limited by specifying a positive maximum value P^{+}_{max}, a positive minimum value P^{+}_{min}, a negative minimum value P^{-}_{min} and a negative maximum value P^{-}_{max} of the power for each storage (Fig. 91 b). These limitations include technical restrictions or operating limits of the storages.

6.3.2 Calculation of the overall efficiencies

With this information it is now possible to determine the efficiencies of different power combinations for a certain SoC of each of the two energy storages. For this purpose, a matrix is introduced whose number of lines corresponds to the elements of the efficiency vector of one storage and whose number of columns results from the number of elements of the efficiency vector of the other storage. The elements of the matrix $\eta_{i,j}$ represent the overall efficiencies of the respective power combinations P_i^1 and P_j^2. For all cases, where the power values of both storages feature an equal sign, the efficiency is determined according to equation (6.8).

$$\eta_{i,j}^{\mathrm{S1,S2}} = \frac{\eta(i \cdot \Delta P^{\mathrm{S1}}) \cdot i \cdot \Delta P^{\mathrm{S1}} + \eta(j \cdot \Delta P^{\mathrm{S2}}) \cdot j \cdot \Delta P^{\mathrm{S2}}}{i \cdot \Delta P^{\mathrm{S1}} + j \cdot \Delta P^{\mathrm{S2}}} \tag{6.8}$$

For those combinations, where the power values of the two storages have a different sign and the absolute values of the power values differ, power is exchanged with the peripheral system and between the storages. The power exchange between the storages equals the smaller value of the two power values of the storages. Calculation of the power exchanged with the peripheral system corresponds to the difference between the power values of the storages. When determining the efficiency, it is to be taken into account that the power exchanged between the two storages is to be multiplied with the efficiency values of both storages and the residual power exchanged with the peripheral system is subject to the efficiency $\eta_{\mathrm{P}_{\max}^{\mathrm{S1,S2}}} = \eta(\max(P^{\mathrm{S1}}, P^{\mathrm{S2}}))$ of the storage with greater value of rated power.

$$\eta_{i,j}^{\mathrm{S1,S2}} = \frac{2 \cdot \min(P^{\mathrm{S1}}, P^{\mathrm{S2}}) \cdot \eta_1 \cdot \eta_2}{\max(P^{\mathrm{S1}}, P^{\mathrm{S2}})} + \frac{(\max(P^{\mathrm{S1}}, P^{\mathrm{S2}}) - \min(P^{\mathrm{S1}}, P^{\mathrm{S2}})) \cdot \eta_{\mathrm{P}_{\max}^{\mathrm{S1,S2}}}}{\max(P^{\mathrm{S1}}, P^{\mathrm{S2}})} \tag{6.9}$$

If power is exchanged between two storages, however, a conversion of the energy form stored in the feeding storage into electrical energy and a further conversion of the electrical energy into the energy form stored in the charged storage is necessary. This results in conversion losses. Since in this case parts of the power are multiplied twice by one efficiency, the overall efficiencies here do not reach the efficiency level of the pure power exchange between the peripheral system and the storage system. Nevertheless, power combinations within the presented range may be beneficial. This is true for cases, where charging or discharging the storage system with a defined power value is associated with poor efficiency, but provision of the same power in combination with exchanging power between the storages is concomitant by a higher efficiency.

Similar to the permissible power combinations, the efficiencies are also converted into a matrix. Thus, the matrix contains the efficiencies of all possible power combinations that are provided by the storage system at a defined SoC.

$$\eta = \begin{pmatrix} 0 & \eta(P^2_1) & \dots & \eta(P^2_N) \\ \eta(P^1_1) & \eta(P^1_1, P^2_1) & & \eta(P^1_1, P^2_N) \\ \vdots & \vdots & & \vdots \\ \eta(P^1_M) & \eta(P^1_M, P^2_1) & & \eta(P^1_M, P^2_N) \end{pmatrix} \tag{6.10}$$

The calculated efficiencies of the power combinations are visualized in Figure 92 a as three-dimensional surface plot and in Figure 92 b as contour plot.

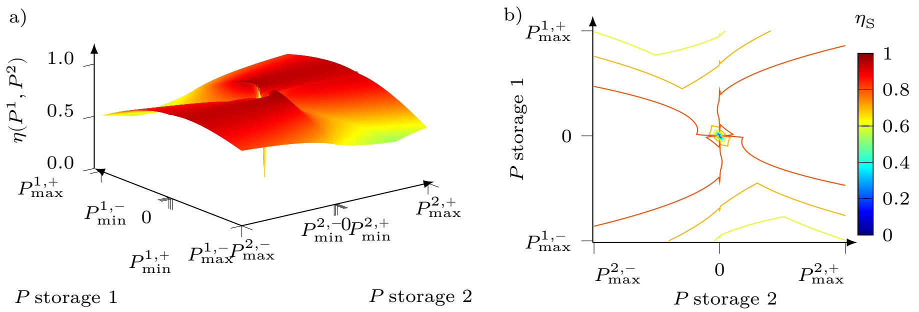

Figure 92: Efficiency profile of a storage system comprising two storages for a given SoC of both storages as three-dimensional efficiency map (a) and as a contour plot of lines with equal efficiency (b)

Based on the efficiencies of all permissible power combinations of the storage system determined, the identification of the maximum efficiency for a certain power value is trivial.

6.3.3 Identification of efficiencies for identical power values

All power combinations on a diagonal are associated with the same value of power. In order to simplify the identification of the power combination with the highest efficiency, the symmetrical efficiency matrix is transformed by a stretching operation (93 a).

In this way, the previous diagonals, on which the efficiencies of combinations of equal power are located, are converted into column vectors. The number of rows of the resulting matrix is equal to the number of rows and columns of the quadratic efficiency matrix as visualized in the Figure 93 b.

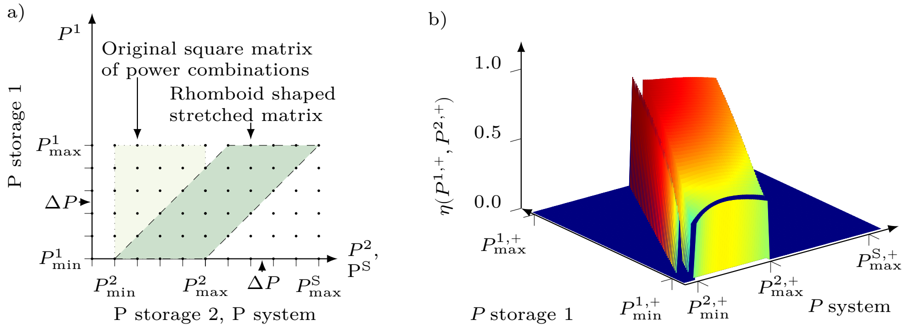

Figure 93: Transformation of the efficiency matrix for positioning the efficiency combinations of equal power in the columns (a) and visualization of a stretched efficiency profile (b)

However, the number of columns n_η is significantly increased. This is due to the circumstance that the number of rows m_η is determined by the maximum value of the power ratings of the individual storages, while the number of columns corresponds to the total power of the storage system.

$$m_\eta = 2 \cdot \max(\max(|P^{1,-}_{\max}|, P^{1,+}_{\max}), \max(|P^{2,-}_{\max}|, P^{2,+}_{\max})) \quad (6.11)$$
$$n_\eta = 2 \cdot (\max(|(P^{1,-}_{\max}|, P^{1,+}_{\max}) + \max(|P^{2,-}_{\max}|, P^{2,+}_{\max})) + 1 \quad (6.12)$$

As a last step, the optimum is identified by determining the maximum efficiency value for each column. The power values to be provided by the individual storages is determined by the position of the optimum value within the column of efficiency values.

6.3.4 Generation of a lookup table

Previous considerations have shown how for a certain power value P, which is to be provided by the storage system, the power combination with the maximum efficiency is determined for a given SoC of the individual storages. An alternative to continuous recalculation in dependence of altered state of charge of the storages is to calculate all power distributions with the highest efficiency once for assumed constant boundary conditions of the storages. Now, the optimal power distribution is selected by simply by calling up the associated list element. If the efficiency-optimal combinations are determined for different power values for all possible state of charge combinations of the two storages and if all other influencing factors are neglected, this results in a three-dimensional matrix. A lookup table calculated for a particular state of system variables and ambient variables comprises power combinations of maximum efficiency for all permissible power values and all defined SoC of both storages. Accordingly, the lookup table is a three-dimensional matrix. The number of elements of the matrix are calculated based on the power range of the storage system between $P^{\mathrm{S},+}_{\max}$ and $P^{\mathrm{S},-}_{\max}$, the step with ΔP in which the power is varied as well as the permissible state of charge range of both storages and the step $\Delta\mathrm{SoC}$ in which the state of charge is altered.

$$n_{\mathrm{lt}} = \frac{(P^{\mathrm{S},+}_{\max} + |P^{\mathrm{S},-}_{\max}|)}{\Delta P} \cdot \frac{(\mathrm{SoC}^1_{\max} - \mathrm{SoC}^1_{\min})}{\Delta\mathrm{SoC}} \cdot \frac{(\mathrm{SoC}^2_{\max} - \mathrm{SoC}^2_{\min})}{\Delta\mathrm{SoC}} \tag{6.13}$$

For all permissible SoC efficiencies regarding the distribution of a particular power value P are contained. By generation of efficiency maps the dependence of the efficiency on the SoC is visualized. In Figure 94 a the efficiency of the storage system is depicted for a power value of -2 kW and in Figure 94 b for a power of 19 kW.

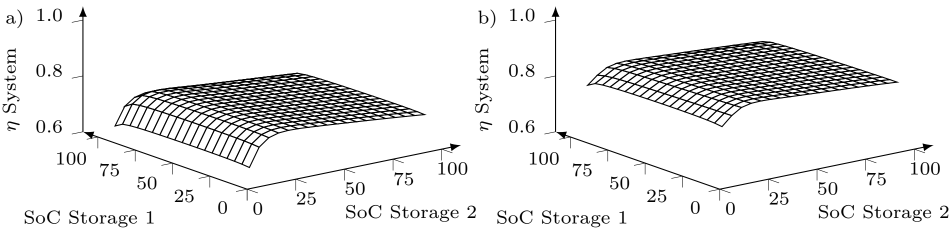

Figure 94: Efficiency at provision of a power of -2 kW (a) and 19 kW (b) for all possible SoC

The shape of the surface plot shows that the efficiency of the storage system is influenced not only by the power value but also by the SoC of the storage system.

How the efficiency of the storage system depends on the SoC of the individual storages is illustrated by generating surface plots of the efficiency by varying the SoC of the storage under consideration and the power exchanged with the storage system. As a result, the allocation of the power to the storages also depends on the SoC. For the power values used in Figure 94, the distribution of power to storage 1 is visualized in Figure 95 a and b.

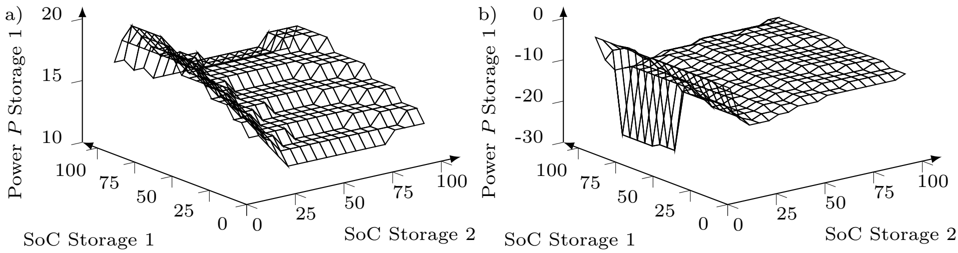

Figure 95: Distribution of a certain power value of -2 kW (a) and 19 kW (b) for all possible SoC of the two storages represented by the power value of storage 1

In the example provided in Figure 96 for the redox flow battery (a) and the flywheel storage (b).

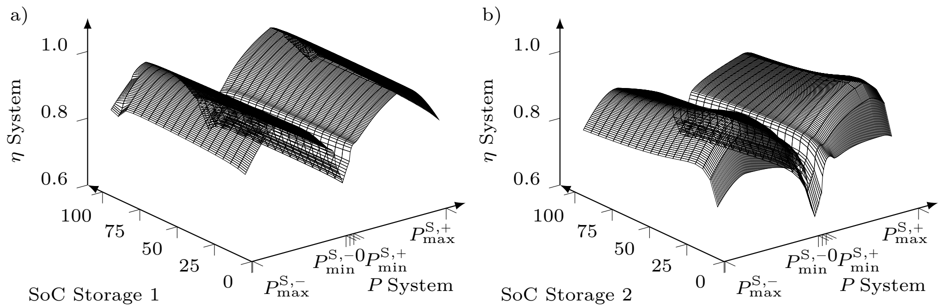

Figure 96: Efficiency of the storage system as a function of power and possible SoC values of storage 1 (a) and storage 2 (b)

Within the presented example, the power of the storage system is altered in an increment of 1 kW. The permissible power range of the redox flow battery is between $\pm$ 10 kW and $\pm$ 40 kW for both positive and negative range of values. For the flywheel, operation is permitted in a power range between $\pm$ 10 kW and $\pm$ 60 kW. Accordingly, the range of operation of the storage system is between 0 kW and $\pm$ 100 kW.

6.3.5 Distribution for a limited power range

For determination of the power target values in planning as well as for each actual power value during the operation of the storage system, distribution to the storages with maximum efficiency is executed. In many cases, however, it is not necessary or permitted to consider all possible power combinations (Fig. 97 a).

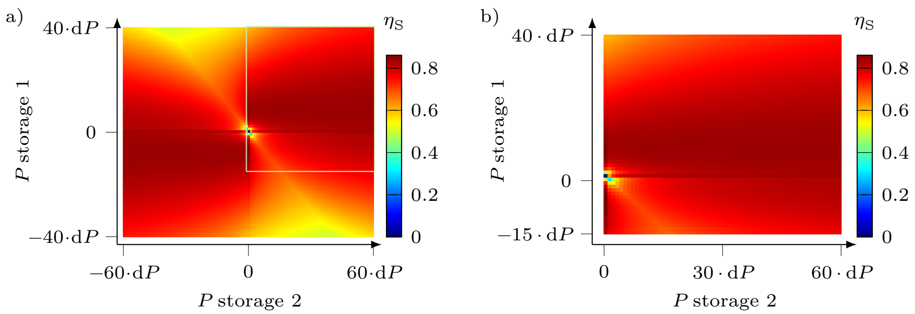

Figure 97: Entire efficiency matrix (a) and cutout with limited power range (b)

Rather, it is required to limit the range of power combinations. If, due to the SoC of at least one storage, the amount of energy to be stored or provided during a time step $\mathrm{d}t$ is smaller than the product of the maximum power value of the storage system and $\mathrm{d}t$, combinations are to be excluded. This applies both to the range of positive power values and of negative power values. For this reason, in each time step a two-dimensional matrix with a reduced value set (Fig. 97 b) is extracted, containing the efficiencies of all permissible power combinations for all SoC. Starting from the matrix element, which corresponds to a power value of zero for both storages, the number of relevant elements is determined in all directions by dividing the absolute value of the respective power values by the power step $\mathrm{d}P$ without remainder. For each dimension, the number of steps corresponds to the sum of the determined steps plus one. The range of matrix elements to be selected is identified using the defined number of steps, starting at the position of the zero element.

6.4 Evaluation of the energy and power management

To assess the developed models for planning of the SoC, calculation of power target values and distribution of power values to the storages, initially a random forecast profile of expected energy quantities is generated (Fig. 98 a).

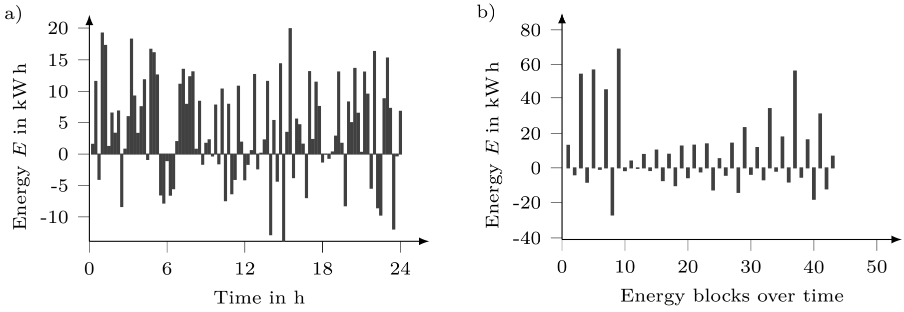

Figure 98: Generated forecast of generation surplus and demand excess for 24 hours in steps of 15 minutes (a) and contraction of adjacent periods with equal sign to energy blocks (b)

Subsequently, the block profile is calculated by adding up adjacent energy quantities with equal sign (Fig. 98 b). By balancing the quantities of energy to be exchanged with the storage system, a general SoC profile is created. The sampling points of the profile represent the planned SoC at the respective transition points of the charging and discharging intervals (Fig. 99 a).

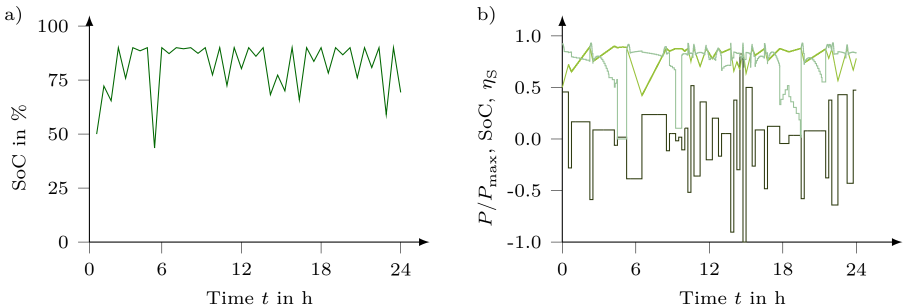

Figure 99: SoC based on the energy blocks (a) and power values (dark green), SoC (green) and efficiency η_S for average value distribution of energy over time (b)

With the energy quantities to be exchanged being known, the calculation of target power values for all sub-time steps $\mathrm{d}t$ with a length of one second is started. In Figure 99 b average values of power are distributed over time and an average efficiency η_S of 82.13 % is achieved.

The course of the SoC over time is similar to the profile generated based on the energy blocks. Distribution of power over time according to a quadratic function with a focus of distribution towards the middle of the distribution periods is depicted in Figure 100 a. An efficiency η_S of 82.42 % is achieved.

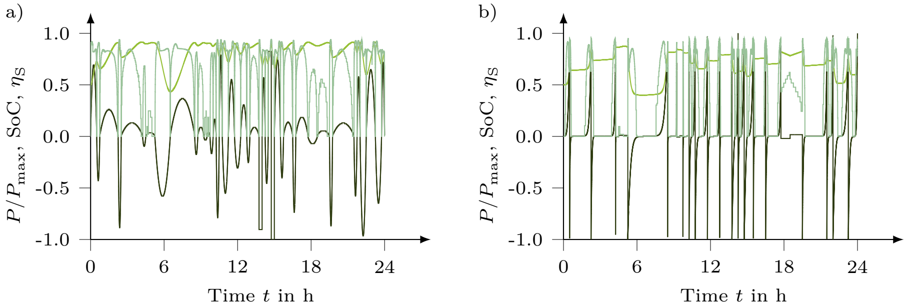

Figure 100: Power values (dark green), SoC (green) and efficiencies η_S (light green) for distributing the predicted energy quantities according to quadratic functions (a) and power functions (b)

For distributing the energy over time using power functions (Fig. 100 b) and thus charging the storage system as late as possible and discharging as soon as possible, an efficiency of 81.40 % was calculated. If the progression of the SoC values of the considered distribution concepts are analyzed (Fig. 101 a), it becomes evident that for distribution using power functions the average values of the SoC are lower and a lower total charge level is present.

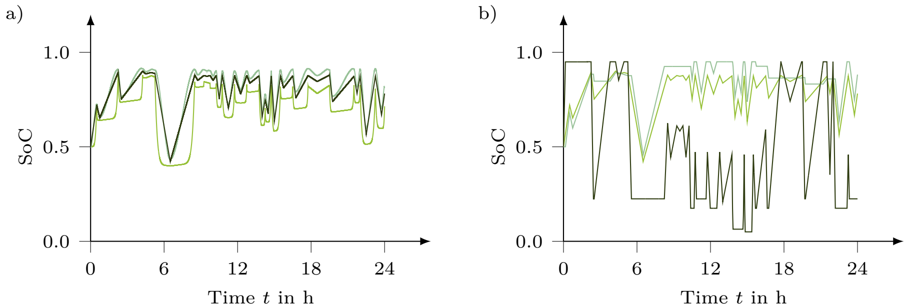

Figure 101: Comparison of the SoC on distributing power as average values (dark green), power functions (green) or quadratic functions (light green) over time (a) and SoC of the flywheel (dark green), the redox flow battery (green) and the storage system (light green) for average distribution (b)

On charging, the highest power target values occur last and the storage is unable to provide the desired power. As the average SoC is lower, stand by losses are expected to be lower, too. With regard to the SoC, power distribution using quadratic functions has little effects regarding lowering average SoC values. In the present example, the average SoC of the storage system is 79.35 % for charging and discharging with average power values, 79.80 %

for distributing power values according to quadratic functions and 70.03 % for power functions. In addition to the SoC of the storage system, the SoC of individual storages are analyzed (Fig. 101 b). Applying different strategies for distributing the power over time is concomitant by a different shape of the SoC profiles (Fig. 102 a and b). The behavior of the storage system is similar for power distribution using power functions and for quadratic functions.

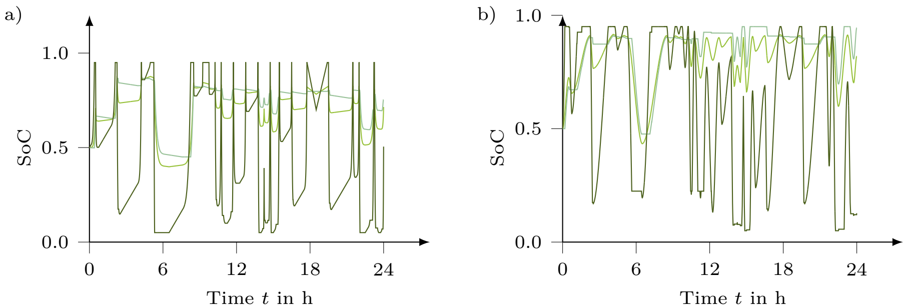

Figure 102: SoC of the flywheel (dark green), the redox flow battery (green) and the storage system (light green) for average distribution for distributing power using power functions (a) and quadratic functions (b)

In total, the developed approach has proven to be stable and is applicable to arbitrary storage systems, if efficiency profiles are available. As the flywheel features a higher efficiency for the majority of possible operating conditions in comparison to the redox flow battery, power is preferably provided to the flywheel. Accordingly, the redox flow battery serves as long-term storage, features higher average SoC values and a lower fluctuation of the SoC. This is furthermore due to the larger capacity of the redox flow battery. Dwelling time of energy in the storage is shortest when the power is distributed using power functions and the lowest average SoC is achieved. With regard to the operation of a hybrid compensation system, this charging strategy is also concomitant to a very unsteady loading of the converter and an irregular provision of system services. Here, the distribution of power on the basis of average values or according to quadratic functions is better suited.

7 Conclusion and Outlook

To motivate the present work, the thesis was formulated that the volatility of generation and the increasing number of power electronic devices pose challenges for power quality and network operation. The analysis of the feed-in profiles of regenerative generation plants, the consideration of the load profiles in the grid, and the consideration of the currents of power electronic consumers as well as feeders confirmed that there is a need for balancing elements such as storages and devices to influence the signal parameters. Deviations from the ideal shape of the signals in electrical networks were described and classified to known deviations of power quality. Subsequently, it was shown how analog signals are processed and interpreted using digital computers. Available system services were presented and it was pointed out that active filters are suitable for providing relevant system services.

Based on the characteristics of known power quality deviations, a selection of system services to be provided by a hybrid compensation system is made. As in particular steady state phenomena, which are present over a longer period of time at varying magnitude, are to be antagonized, compensation of harmonics, of reactive power, of voltage unbalance and of active power due to voltage or frequency deviation are chosen. In order to compensate those phenomena, calculation procedures for proper detection of the deviations are introduced and investigated. Present deviations are detected based on sampled values of voltage and current signals. Power quality indicators are determined on the basis of the relevant standards. In order to make the different power quality deviations comparable, these are related to the maximum values of the tolerated deviation. An aggregated indicator of the total power quality is determined and the share of individual power quality indicators in the aggregated indicator is used for the distribution of power to the system services.

The behavior of common renewable plant types as well as the load of distribution grids with decentralized renewable generation is analyzed. Available storage technologies are characterized using key performance indicators. Based on the indicators, the combination of a redox flow battery and a flywheel storage is chosen for application in an integrated system for compensation of power quality deviations. Both storages feature fast response times and endure high cycle numbers. The redox flow battery is suitable for long term storage with picayune stand by losses and the flywheel features a good efficiency for frequently changing charging and discharging operations. For those storage technologies, models available in literature are extended and tailored to the properties of real storages provided by manufacturers. The models developed are used for both controlling the behavior of the storages and for obtaining information about the efficiencies of charging and discharging power in dependence on the state of charge, the absolute value of power and other boundary conditions.

An algorithm for planning state of charge values based on forecast data and calculation of target power values has been evaluated. For distribution of power to the storages of a hybrid storage system, the efficiencies of all possible power combinations with equal absolute value is calculated and thus the distribution with maximum efficiency is determined. Applicability of different strategies for distributing energy quantities was analyzed based on efficiencies and state of charge values.

In electrical energy systems with increasing share of volatile renewable generation and numerous producers or consumers comprising power electronics, challenges for grid operation arise due to both fluctuations of load or generation and implications on power quality. Therefore, storage of energy is gaining significance and measures for improvement of power quality are demanded within distribution grids. System services to be provided on distribution grid level are power factor correction, compensation of harmonics, voltage stability and compensation of unbalance. Furthermore, support of frequency stability or balancing between generation and demand is possible by feeding in or storing of active power. As storages comprise power electronic converters and those converters are, in addition to drawing or feeding active power, capable of compensating power quality deviations, an integrated approach is developed in the present work. By equipping larger, grid connected energy storages with converters featuring a sufficient clock rate and with measurement as well as communication technology to provide the system services outlined above, it is possible to transfer the developed concepts into application. From a technical point of view, providing the required current signals possible for converters that are available today.

Further research activities are required in order to evaluate the suitability of the hybrid compensation system in terms of compensating disturbances as flicker, voltage fluctuations, transients or noise. In order to be able to compensate for these phenomena, which are partly transient phenomena and feature a higher frequency range, the measurement technology and the clock rate of the converters have to be more advanced. Subject of the investigations carried was the increase in power quality at the transfer point to the feeding high-voltage network. Accordingly, the approach presented is dedicated to supporting the compliance with the power quality limits agreed with the upstream network operator. However, it is not possible to improve the power quality at the consumption points, as load currents can not be influenced. Therefore, it is required to install decentralised compensators at the connection point of consumers or feeders. Accordingly, further research is required to upgrade converters of photovoltaic systems, battery storage systems or other equipment to provide system services. By providing system services using decentralized power converters at the connection points of dirty loads or feeders, the repercussions on the power quality in the overall grid are reduced. Thus, the power quality in the entire grid is improved due to proper current flows between the substations of the grid.

8 Zusammenfassung und Ausblick

Als Motivation zur vorliegenden Arbeit wurde die These formuliert, dass die Volatilität der Erzeugung und die zunehmende Anzahl von leistungselektronischen Einspeisern und Verbrauchern Herausforderungen für die Spannungqualität und den Netzbetrieb darstellen. Eine Analyse der Einspeiseprofile von regenerativen Erzeugungsanlagen, der Lastprofile von Verbrauchern im Netz sowie der Signalform der Ströme leistungselektronischer Verbraucher veranschaulichen, dass ein Bedarf an ausgleichenden Elementen wie Speichern und Geräten zur Beeinflussung der Signalparameter besteht. Wesentliche Abweichungen von der idealen Form der Signale in elektrischen Netzen werden beschrieben und Parametern der Spannungsqualität zugeordnet. Ebenfalls wird gezeigt, wie analoge Signale mit digitalen Rechnern verarbeitet und interpretiert werden. Es werden die verfügbaren Systemdienstleistungen vorgestellt und herausgearbeitet, dass aktive Filter zu deren Bereitstellung geeignet sind.

Basierend auf den Merkmalen bekannter Abweichungen der Spannungsqualität werden einige Systemdienstleistungen ausgewählt, die von einem hybriden Kompensationssystem erbracht werden sollen. Da insbesondere stationäre Phänomene, die über einen längeren Zeitraum in unterschiedlicher Größenordnung beobachtet werden können, durch die Anlage gemindert werden sollen, werden die Kompensation von Oberschwingungen, von Blindleistung, von Unsymmetrie und von Wirkleistung aufgrund von Spannungs- oder Frequenzabweichung selektiert. Um diese Phänomene zu kompensieren, werden Berechnungsverfahren zur korrekten Erkennung der Abweichungen eingeführt und untersucht. Aktuelle Abweichungen werden anhand der Abtastwerte von Spannungs- und Stromsignalen erkannt. Die Indikatoren für die Spannungsqualität werden auf der Grundlage der einschlägigen Normen berechnet. Um die verschiedenen Abweichungen der Spannungsqualität vergleichbar zu machen, werden diese auf die Maximalwerte der tolerierten Abweichung bezogen. Es wird ein aggregierter Indikator für die Spannungsqualität insgesamt bestimmt und der Anteil der einzelnen Parameter am aggregierten Indikator wird für die Verteilung der Leistung auf die Systemdienstleistungen verwendet.

Weiterhin werden verfügbare Speichertechnologien anhand von Key Performance Indicators (KPI) charakterisiert. Basierend auf diesen Indikatoren wird die Kombination aus einer Redox-Flow-Batterie und einem Schwungradspeicher für den Einsatz in einem integrierten System zur Kompensation von Abweichungen der Spannungsqualität ausgewählt. Beide Speicher zeichnen sich durch schnelle Reaktionszeiten und hohe Zyklenzahlen aus. Die Redox-Flow-Batterie ist für die Langzeitspeicherung mit geringen Stand-by-Verlusten geeignet und das Schwungrad zeichnet sich durch einen hohen Wirkungsgrad bei häufigen Lade- und Entladevorgängen aus. Für die genannten Speichertechnologien werden die in der Literatur verfügbaren Modelle entsprechend der Spezifikationen der verwendeten Speicher angepasst. Die entwickelten Modelle werden sowohl für die Steuerung des Verhaltens der Speicher als auch für die Gewinnung von Informationen über die Wirkungsgrade in Abhängigkeit der Lade- und Entladeleistung sowie des Ladezustands und anderen Randbedingungen verwendet.

Ebenfalls wird ein Algorithmus zur Planung der Ladegrade des hybriden Speichersystems auf Basis von Prognosedaten und zur Bestimmung von Soll-Leistungswerten eingeführt. Für die Verteilung der Leistung auf die Speicher des hybriden Speichersystems werden die Wirkungsgrade aller möglicher Leistungskombinationen mit gleichem Absolutwert der Leistung berechnet und hierüber die Kombination mit maximalem Wirkungsgrad bestimmt. Unterschiedliche Strategien zur Verteilung von Energiemengen werden anhand der erreichbaren Wirkungsgrade und Ladezustände analysiert.

Zusammenfassend kann geschlossen werden, dass sich in elektrischen Energiesystemen mit steigendem Anteil an volatiler, regenerativer Erzeugung und zahlreichen leistungselektronischen Einspeisern oder Verbrauchern Herausforderungen für den Netzbetrieb sowohl durch Last- und Erzeugungsschwankungen als auch hinsichtlich der Spannungsqualität ergeben. Daher gewinnt die Speicherung von Energie an Bedeutung und es werden Maßnahmen zur Verbesserung der Spannungsquaität in Verteilnetzen gefordert. Auf Verteilnetzebene zu erbringende Systemleistungen sind die Kompensation von Blindleistung, von Oberschwingungen, die Spannungsstabilität und der Ausgleich von Unsymmetrie. Darüber hinaus ist die Unterstützung der Frequenzstabilität oder der Ausgleich zwischen Erzeugung und Bedarf durch Einspeisung oder Speicherung von Wirkleistung möglich. Da die Speicher leistungselektronische Wandler umfassen und diese neben der Aufnahme oder Einspeisung von Wirkleistung auch in der Lage sind, als aktive Filter Abweichungen der Spannungsqualität zu kompensieren, wird in der vorliegenden Arbeit ein integrierter Ansatz entwickelt. Durch die Ausstattung größerer, netzgekoppelter Energiespeicher mit Umrichtern, die über eine ausreichender Taktrate sowie geeignete Mess- und Kommunikationstechnik zur Erbringung der oben beschriebenen Systemdienstleistungen verfügen, ist es möglich, die entwickelten Konzepte in die Anwendung zu überführen. Technisch gesehen sind heute verfügbare Stromrichter zur Bereitstellung der erforderlichen Kompensationsströme in der Lage.

Weitere Forschungsarbeiten sind erforderlich, um die Eignung des hybriden Systems hinsichtlich der Kompensation von Störungen wie Flickern, Spannungsschwankungen, Transienten oder Rauschen zu bewerten. Um diese Phänomene, die teilweise transiente Phänomene sind und einen höheren Frequenzbereich betreffen, kompensieren zu können, sind die Messtechnik und die Taktrate der Umrichter geeignet weiterzuentwickeln. Gegenstand der durchgeführten Untersuchungen war die Erhöhung der Spannungsqualität an der Übergabestelle zum speisenden Hochspannungsnetz. Dementsprechend widmet sich der vorgestellte Ansatz der Unterstützung der Einhaltung der mit dem vorgelagerten Netzbetreiber vertraglich vereinbarten Grenzwerte der Spannungsqualität. Eine Verbesserung der Spannungsqualität an den Verbrauchsstellen ist jedoch nicht möglich, da die Lastströme nicht beeinflusst werden können. Daher erscheint es vielversprechend, dezentrale Kompensatoren an der Anschlussstelle von Verbrauchern oder Einspeisern zu installieren. Dementsprechend sind weitere Forschungsarbeiten erforderlich, um beispielsweise Stromrichter von Photovoltaikanlagen, Batteriespeichersystemen oder anderen Geräten zur Erbringung von Systemdienstleistungen zu ertüchtigen. Indem die Erbringung von Systemdienstleistungen durch dezentrale Stromrichter an den Anschlussstellen von unsauberen Lasten oder Einspeisern erfolgt, werden deren Auswirkungen auf die Spannungsqualität im Gesamtnetz reduziert.

Bibliography

[1] Epe, C. DistributionCode 2007 - Regeln für den Zugang zu Verteilungsnetzen. Tech. rep. Verband der Netzbetreiber (VDN), 2007.

[2] Berndt, H. TransmissionCode 2007 - Netz- und Systemregeln der deutschen Übertragungsnetzbetreiber. Tech. rep. Verband der Netzbetreiber e. V. (VDN), 2007.

[3] Braun, M. Provision of Ancillary Services by Distributed Generators - Technological and Economic Perspective. Kassel: kassel university press GmbH, 2009.

[4] Stetz, T. and M. Braun. Dezentrale Verfahren zur Spannungshaltung in Niederspannungsnetzen – eine Fallstudie. In: *e & i Elektrotechnik und Informationstechnik* 128.4 (2011-04), pp. 105–109.

[5] Oliveira, J. H. de, J. P. R. Gomes, W. d. C. Boaventura, and V. F. Mendes. Impact of integrating a photovoltaic power plant in a distribution feeder. In: *2016 17th International Conference on Harmonics and Quality of Power (ICHQP)*. 2016-10, pp. 842–847.

[6] Lo, Y., T. Lee, and K. Wu. Grid-Connected Photovoltaic System With Power Factor Correction. In: *IEEE Transactions on Industrial Electronics* 55.5 (2008-05), pp. 2224–2227.

[7] Klaus, T., C. Vollmer, K. Werner, H. Lehmann, and K. Müschen. Energieziel 2050: 100 Prozent Strom aus erneuerbaren Quellen. Tech. rep. Umweltbundesamt, Dessau-Roßlau, 2018.

[8] Bründlinger, T., E. J. König, O. Frank, D. Gründlig, C. Jugel, P. Kraft, O. Krieger, S. Mischinger, P. Prein, H. Seidl, S. Siegemund, C. Stolte, M. Teichmann, J. Wilke, and M. Wolke. dena-Leitstudie Integrierte Energiewende. Tech. rep. Deutsche Energie - Agentur GmbH (dena) – German Energy Agency, 2018.

[9] Burger, B. Öffentliche Nettostromerzeugung in Deutschland im Jahr 2018. URL: http://www.ise.fraunhofer.de/content/dam/ise/de/documents/news/2019/Stromerzeugung_2018_3.pdf (visited on 2019-10-04).

[10] Leonhard, W., F. Crotogino, C. Gatzen, W. Glaunsinger, S. Donadei, M. Kleimaier, M. Koenemund, H. Landinger, T. Lebioda, D. Sauer, H. Weber, A. Wenzel, W. Wolf, W. Woyke, and S. Zunft. VDE-Studie: Energiespeicher in Stromversorgungssystemen mit hohem Anteil erneuerbarer Energieträger. Bedeutung, Stand der Technik, Handlungsbedarf. ETG Task Force Energiespeicher. Ed. by VDE-ETG. 2009-06.

[11] Hemmati, R. and H. Saboori. Emergence of hybrid energy storage systems in renewable energy and transport applications - A review. In: *Renewable and Sustainable Energy Review* 65.7 (2016-07), pp. 11–18.

[12] Li, W. and G. Joos. A Power Electronic Interface for a Battery Supercapacitor Hybrid Energy Storage System for Wind Applications. In: *Power Electronics Specialists conference IEEE*. 2008-08, pp. 1762–1768.

[13] GmbH, T. C. G. P. E. Aktuelle Regelleistungspreise. URL: https://www.teamconsult.net/de/news.php (visited on 2019-10-19).

[14] Stenzel, P. Bereitstellung von Primärregelleistung durch stationäre Großbatteriespeicher. de. Tech. rep. Jülich, DE: Forschungszentrum Jülich, 2016.

[15] Ise, T., M. Kita, and A. Taguchi. Hybrid Energy Storage With a SMES and Secondary Battery. In: *IEEE Transactions on Applied Superconductivity* 15.2 (2005-06), pp. 1915–1918.

[16] Etxeberria, A., I. Vecchiu, H. Camblong, J. M. Vinassa, and H. Camblong. Hybrid Energy Storage Systems for renewable Energy Sources Integration in microgrids: A review. In: *2010 Conference Proceedings IPEC*. 2010-10, pp. 532–537.

[17] Suvire, G., L. J. Ontiveros, and P. E. Mercado. Combined control of a flywheel energy storage system and a vanadium redox flow battery for wind energy applications in microgrids. In: *DYNA* 84 (2017-09), pp. 230–238.

[18] Melzer, H. Die aktuelle Situation der Sternpunktbehandlung in Netzen bis 110 kV (D-A-CH) - eine Bestandsaufnahme mit einer Zusammenfassung der ETG-Umfrage STE 2010, Verfahren der Erdschlusskompensation und selektiven Erdschlusserfassung. Berlin: VDE-Verlag, 2012.

[19] Feng, H. Adaptiver Kompensationsregler für erdschlusskompensierte Hochspannungsnetze; 1. Aufl. PhD thesis. Aachen, 2002.

[20] Stade, D. Erdschlussströme in MS-Netzen mit Resonanzsternpunkterdung. In: *Elektrotechnische Zeitschrift (ETZ)* (2007-11), pp. 1–4.

[21] Dib, D., A. Rezaiguia, and Z. Abada. Improving the Electric Power Quality by UPFC Systems in Electrical Networks. In: *International Journal of Energy* Volume 6 (2012-01), pp. 115–122.

[22] Hatnapure, H. B. and V. K. Chandrakar. Power quality improvement by using UPFC. In: *2017 2nd International Conference for Convergence in Technology (I2CT)*. 2017, pp. 1014–1017.

[23] Yanushkevich, A., Z. Müller, J. Svec, J. Tlustý, and V. Valouch. Power Quality Enhancement using STATCOM with Energy Storage. In: *Renewable Energy and Power Quality Journal* (2014-04), pp. 349–354.

[24] Patel, V. and J. J. Patel. Power quality improvement of grid using solar photovoltaic farm. In: *2017 Innovations in Power and Advanced Computing Technologies (i-PACT)*. 2017, pp. 1–6.

[25] Naik Popavath, L., G. Nagaraju, and K. Naresh. A PV-Statcom for Enhancement of power quality in grid integrated system using Unit Vector Controller. In: *2020 International Conference on Artificial Intelligence and Signal Processing (AISP)*. 2020, pp. 1–6.

[26] Kumar Sinha, A. and S. Mishra. Power quality improvement of grid using PV solar farm by voltage injection method. In: *2017 Recent Developments in Control, Automation Power Engineering (RDCAPE)*. 2017, pp. 297–301.

[27] Patel, A. A. and A. A. Patel. Grid integrated solar photovoltaic system with static compensator. In: *2017 IEEE International Conference on Power, Control, Signals and Instrumentation Engineering (ICPCSI)*. 2017, pp. 2366–2370.

[28] Ismail, N. M. and M. K. Mishra. Control and operation of unified power quality Conditioner with battery-ultracapacitor energy storage system. In: *2014 IEEE International Conference on Power Electronics, Drives and Energy Systems (PEDES)*. 2014, pp. 1–6.

[29] Jeon, J., J. Kim, S. Kim, and J. Kim. Unified compensation control of a hybrid energy storage system for enhancing power quality and operation efficiency in a diesel and wind-turbine based stand-alone microgrid. In: *2012 3rd IEEE International Symposium on Power Electronics for Distributed Generation Systems (PEDG)*. 2012, pp. 264–270.

[30] Geibel, D. Bereitstellung von Zusatzfunktionalitäten durch multifunktionale PV-Batterie-Stromrichtersysteme in Verteilungs- und Industrienetzen. PhD thesis. 2016.

[31] Crastan, V. Elektrische Energieversorgung 1. Springer-Verlag, Berlin Heidelberg, 2007.

[32] Wirtz, F. Zusammenhang von Zuverlässigkeit und Kosten in Mittelspannungsnetzen. PhD thesis. Aachen, 2009.

[33] Hosemann, G. Elektrische Energietechnik: Netze. Klassiker der Technik. Berlin and Heidelberg: Springer, 2001.

[35] Kapetanovic, T., B. M. Buchholz, B. Buchholz, and V. Buehner. Provision of ancillary services by dispersed generation and demand side response – needs, barriers and solutions. In: *e & i Elektrotechnik und Informationstechnik* 125.12 (2008-12), pp. 452–459.

[36] Energie- und Wasserwirtschaft, B. der deutschen. Standardlasprofile Strom. URL: http://www.bdew.de/energie/standardlastprofile-strom (visited on 2019-10-04).

[37] Unterfränkische Überlandzentrale eG. Standardisierte Lastprofile 2018 mit Feiertagskalender Bayern. URL: http://www.uez.de/downloads/SLP_2018.xlsx (visited on 2019-10-04).

[38] Specovius, J. Grundkurs Leistungselektronik - Bauelemente, Schaltungen und Systeme. Vieweg+Teubner Verlag | Springer Fachmedien Wiesbaden GmbH, Wiesbaden, 2011.

[39] Berger, M. and G. Brauner. Zukünftige Tendenzen der Spannungsqualität in elektrischen Verteilnetzen. In: *e & i Elektrotechnik und Informationstechnik* 123.1 (2006-02), pp. 28–33.

[40] Schwab, A. J. Elektromagnetische Verträglichkeit. Springer-Verlag, Berlin Heidelberg, 2007.

[41] Subramaniam, A., A. Sahoo, S. S. Manohar, and S. K. Panda. Voltage and current-harmonics induced ageing in electrical insulation. In: *2017 International Symposium on Electrical Insulating Materials (ISEIM)*. Vol. 1. 2017-09, pp. 403–406.

[42] Montanari, G. C. and D. Fabiani. The effect of nonsinusoidal voltage on intrinsic aging of cable and capacitor insulating materials. In: *IEEE Transactions on Dielectrics and Electrical Insulation* 6.6 (1999-12), pp. 798–802.

[43] Bahadoorsingh, S. and S. M. Rowland. The role of power quality in electrical treeing of epoxy resin. In: *2007 Annual Report - Conference on Electrical Insulation and Dielectric Phenomena*. 2007-10, pp. 221–224.

[44] Deokar, S. A. and L. M. Waghmare. Impact of power system harmonics on insulation failure of distribution transformer and its remedial measures. In: *2011 3rd International Conference on Electronics Computer Technology*. Vol. 3. 2011-04, pp. 136–140.

[45] Gudzius, S., A. Jonaitis, R. Miliune, A. Morkvenas, P. Valatka, and V. Malazinskas. Investigation of influence of short duration overvoltage disturbances on partial discharge characteristics. In: *2017 IEEE 58th International Scientific Conference on Power and Electrical Engineering of Riga Technical University (RTUCON)*. 2017-10, pp. 1–5.

[46] Sones, W. and S. M. Wong. Overview on transient overvoltages and insulation design for a high voltage transmission system. In: *2010 International Conference on High Voltage Engineering and Application*. 2010-10, pp. 12–17.

[47] Heuck, K., K.-D. Dettmann, and D. Schulz. Elektrische Energieversorgung. Vieweg+Teubner, 2007.

[48] Plaßmann, W. and D. Schulz. Handbuch Elektrotechnik. Vieweg+Teubner | GWV Fachverlage GmbH, Wiesbaden, 2009.

[49] Kumar, D., F. Zare, and A. Ghosh. DC Microgrid Technology: System Architectures, AC Grid Interfaces, Grounding Schemes, Power Quality, Communication Networks, Applications, and Standardizations Aspects. In: *IEEE Access* 5 (2017-07), pp. 12230–12256.

[50] Whaite, S., B. Grainger, and A. Kwasinski. Power Quality in DC Power Distribution Systems and Microgrids. In: *Energies* 8.5 (2015-05), pp. 4378–4399.

[51] Tabatabaei, N. M., E. Kabalci, and N. Bizon. Microgrid Architectures, Control and Protection Methods. Springer International Publishing, 2019.

[52] Rajagopalan, S., B. Fortenbery, and D. Symanski. Power quality disturbances within DC data centers. In: *Intelec 2010*. 2010-06, pp. 1–7.

[53] Graham, A. D. The importance of a DC side harmonic study for a DC distribution system. In: *6th IET International Conference on Power Electronics, Machines and Drives (PEMD 2012)*. 2012-03, pp. 1–5.

[54] Asakimori, K., K. Murai, T. Tanaka, and T. Babasaki. Effect of inrush current flowing into EMI filter on the operation of ICT equipment in HVDC system. In: *2014 IEEE 36th International Telecommunications Energy Conference (INTELEC)*. 2014-09, pp. 1–5.

[55] Prabhakaran, P. and V. Agarwal. Mitigation of voltage unbalance in a low voltage bipolar DC microgrid using a boost-SEPIC type interleaved dc-dc compensator. In: *2016 IEEE 2nd Annual Southern Power Electronics Conference (SPEC)*. 2016-12, pp. 1–6.

[56] Mok, K., M. Wang, S. Tan, and S. Y. R. Hui. DC Electric Springs—A Technology for Stabilizing DC Power Distribution Systems. In: *IEEE Transactions on Power Electronics* 32.2 (2017-02), pp. 1088–1105.

[57] IEEE Recommended Practice for Powering and Grounding Electronic Equipment. In: *IEEE Std 1100-2005 (Revision of IEEE Std 1100-1999)* (2006-05), pp. 1–703.

[58] Sankaran, C. Power Quality. Boca Raton, Fla: CRC Press, 2001.

[59] Gustavsson, R., S. Hussain, and A. Saleem. Ancillary services for smart grids - Power quality markets. In: *2013 IEEE Grenoble Conference*. 2013-06, pp. 1–6.

[60] Electromagnetic compatibility (EMC). en. Standard IEC 61000. Geneva, CH: International Electrotechnical Commission (IEC), 2016.

[61] Chattopadhyay, S., M. Mitra, and S. Sengupta. Electric Power Quality. Berlin Heidelberg: Springer Science & Business Media, 2011.

[62] Electromagnetic compatibility (EMC) - Part 1: General. en. Standard IEC 61000-1. Geneva, CH: International Electrotechnical Commission (IEC), 2016.

[63] Electromagnetic compatibility (EMC) - Part 2: Environment. en. Standard IEC 61000-2. Geneva, CH: International Electrotechnical Commission (IEC), 2016.

[64] Electromagnetic compatibility (EMC) - Part 3: Limits. en. Standard IEC 61000-3. Geneva, CH: International Electrotechnical Commission (IEC), 2016.

[65] Electromagnetic compatibility (EMC) - Part 4: Testing and measurement techniques. en. Standard IEC 61000-4. Geneva, CH: International Electrotechnical Commission (IEC), 2016.

[66] Mindykowski, J. Fundamentals of electrical power quality assessment. In: *XVII IMEKO World Congress, Metrology in the 3rd Millennium*. 2003-06.

[67] Electromagnetic compatibility (EMC) - Part 5: Installation and mitigation guidelines. en. Standard IEC 61000-5. Geneva, CH: International Electrotechnical Commission (IEC), 2016.

[68] Electromagnetic compatibility (EMC) - Part 6: Generic Standards. en. Standard IEC 61000-6. Geneva, CH: International Electrotechnical Commission (IEC), 2016.

[69] Smith, J. C., G. Hensley, and L. Ray. IEEE recommended practice for monitoring electric power quality. In: *IEEE Std* (1995), pp. 1159–1995.

[70] Voltage characteristics of electricity supplied by public electricity networks. en. Standard EN50160. Brussels, BE: European Committee for Electrotechnical Standardization (CENELEC), 2015.

[71] Gangl, H. Kann man Spannungsqualität kaufen? In: *e&i Elektrotechnik und Informationstechnik* 118.9 (2001-09), pp. 441–444.

[72] Amornvipas, C. Harmonic Studies and Resonance AAnalyse in Elektrical Power Systems. Shaker Verlag GmbH, Aachen, 2009.

[73] Bollen, M. H. Understanding Power Quality Problems - Voltage Sags and Interruptions. New York: Wiley, 2000.

[74] Ise, T., Y. Hayashi, and K. Tsuji. Definitions of power quality levels and the simplest approach for unbundled power quality services. In: *Ninth International Conference on Harmonics and Quality of Power. Proceedings (Cat. No.00EX441)*. Vol. 2. 2000, pp. 385–390.

[75] Dugan, R. C., M. F. McGranaghan, S. Santoso, and H. W. Beaty. Electrical Power Systems Quality, Third Edition. Madison: McGraw Hill Professional, 2012.

[76] Golkar, M. A. Electric power quality: types and measurements. In: *2004 IEEE International Conference on Electric Utility Deregulation, Restructuring and Power Technologies. Proceedings*. Vol. 1. 2004-04, 317–321 Vol.1.

[77] Gawlik, W. Gegenseitige Beeinflussung zentraler Oberschwingungskompensatoren. PhD thesis. 2004.

[78] Häfner, J. On the Reduction of Harmonics in Power Systems - A New Hybrid Power Filter Approach. PhD thesis. 1999.

[79] Bronstein Ilja Nikolajewitsch Semendjajew, K. A. Taschenbuch der Mathematik. Verlag Harri Deutsch, Thun und Frankfurt am Main, 2001.

[80] Bonner, A., T. Grebe, E. Gunther, L. Hopkins, M. Marz, J. Mahseredjian, N. Miller, T. Ortmeyer, V. Rajagopalan, S. Ranade, P. Ribeiro, B. Spherling, T. Sims, and W. Xu. Modeling and simulation of the propagation of harmonics in electric power networks. I. Concepts, models, and simulation techniques. In: *IEEE Transactions on Power Delivery* 11.1 (1996-01), pp. 452–465.

[81] Negnevitsky, M., K. Debnath, J. Huang, and M. Ringrose. Studies of power quality: disturbance recognition. In: (2000-01).

[82] Heydt, G. T. Electric power quality: a tutorial introduction. In: *IEEE Computer Applications in Power* 11.1 (1998-01), pp. 15–19.

[83] Johnson, D. Issues of Power Quality in Electrical Systems. In: 5 (2016-01), p. 148.

[84] Schlabbach, J., D. Blume, and T. Stephanblome. Voltage Quality in Electrical Power Systems. Stevenage: IET, 2001.

[85] Bakoń, T. Einsatz von Stromrichtern in der Energieversorgung zur Netzstützung und Fehlerstromlöschung. PhD thesis. 2008.

[86] Vukosavic, S. Detection and suppression of parasitic DC voltages in 400V AC grids. In: *Facta universitatis - series: Electronics and Energetics* 28.4 (2015), pp. 527–540.

[87] Eckhardt, V. Drehfeldgerechte dynamische Frequenzmessung in mehrphasigen Energieversorgungsnetzen. In: *Archiv für Elektrotechnik* 70.2 (1987-03), pp. 91–100.

[88] Herbst, P., H. König, J. Reese, D. Siebold, T. Simon, A. Tempelmeier, and B. Walther. Einsatz neuer Technologien zur Blindleistungskompensation in elektrischen Netzen. Tech. rep. Frankfurt am Main: ZVEI - Zentralverband Elektrotechnik- und Elektronikindustrie e. V., Fachverband Starkstromkondensatoren – Fachabteilung Leistungskondensatoren und Spannungsqualität, 2012-12.

[89] Albach, M. Grundlagen der Elektrotechnik 2 - Periodische und nicht periodische Signalformen. Pearson Studium, München, 2005.

[90] Riefenstahl, U. Elektrische Antriebssysteme - Grundlagen, Komponenten, Regelverfahren, Bewegungssteuerung. Wiesbaden: Vieweg+Teubner Verlag, 2010.

[91] Roman, H. Technische Innovationen in Verteilungsnetzen - Vorträge der ETG-Fachtagung vom 1. bis 2. März 2005 in Würzburg. Fellbach: Margret Schneider, 2005.

[92] Union of the Electricity Industry–EURELECTRIC. Ancillary Services: Unbundling Electricity Products - an Emerging Market. 2004.

[93] Pirbazari, A. M. Ancillary services definitions, markets and practices in the world. In: *2010 IEEE/PES Transmission and Distribution Conference and Exposition: Latin America (T D-LA)*. 2010-11, pp. 32–36.

[94] Rebours, Y. G., D. S. Kirschen, M. Trotignon, and S. Rossignol. A Survey of Frequency and Voltage Control Ancillary Services mdash;Part I: Technical Features. In: *IEEE Transactions on Power Systems* 22.1 (2007-02), pp. 350–357.

[95] Schmitt, A. Multikriterielle Optimierung von Systemdienstleistungen für Energieübertragungssysteme. PhD thesis. 2003.

[96] Rehtanz, C. dena Ancillary Services Study 2030 - Security and reliability of a power supply with a high percentage of renewable energy. Tech. rep. Deutsche Energie - Agentur GmbH (dena) – German Energy Agency, 2014.

[97] Ma, Y., S. Lv, X. Zhou, and Z. Gao. Review analysis of voltage stability in power system. In: *2017 IEEE International Conference on Mechatronics and Automation (ICMA)*. 2017-08, pp. 7–12.

[98] Keil, T. Schutzsysteme für elektrische Energieversorgungsnetze mit dezentralen Stromerzeugungsanlagen. Shaker Verlag, Aachen, 2011.

[99] Scherer, M. and W. Schattinger. Test zur Schwarzstart- und Inselbetriebsfähigkeit. Tech. rep. Frick, Switzerland: swissgrid, 2010.

[100] Prillwitz, F. and M. Krüger. Netzwiederaufbau nach Großstörungen. In: (2007-01).

[101] Becker, W., R. Halbauer, and K. Pfeiffer. Ancillary services provided from DSO networks - how to handle volatile dispersed generation combined with highly loaded network equipment. In: *International ETG Congress 2015; Die Energiewende - Blueprints for the new energy age*. 2015-11, pp. 1–6.

[102] Olek, B. Deployment of energy storages for ancillary services. In: *11th International Conference on the European Energy Market (EEM14)*. 2014-05, pp. 1–5.

[103] Triggianese, M., J. Morren, S. W. H. de Haan, and P. Marino. Improved and extended DG capability in voltage regulation by reactive and active power. In: *2007 International Conference on Power Engineering, Energy and Electrical Drives*. 2007-04, pp. 583–588.

[104] Olek, B. and M. Wierzbowski. Ancillary services provided by renewable energy sources. In: *IET Conference on Power in Unity: a Whole System Approach*. 2013-10, pp. 1–7.

[105] Alsokhiry, F. and K. L. Lo. Effect of Distributed Generations based on Renewable Energy on the Transient Fault – Ride through. In: *2013 International Conference on Renewable Energy Research and Applications (ICRERA)*. 2013-10, pp. 1102–1106.

[106] Zipf, M. and D. Möst. Cooperation of TSO and DSO to provide ancillary services. In: *2016 13th International Conference on the European Energy Market (EEM)*. 2016-06, pp. 1–6.

[107] Akagi, H. Active and hybrid filters for power conditioning. In: *ISIE'2000. Proceedings of the 2000 IEEE International Symposium on Industrial Electronics*. Vol. 1. 2000-12, TU26–TU36 vol.1.

[108] Abdusalam, M., P. Poure, and S. Saadate. Hardware implementation of a three-phase active filter system with harmonic isolation based on self-tuning-filter. In: *2008 IEEE Power Electronics Specialists Conference*. 2008-06, pp. 2875–2881.

[110] Vaupel, G. H. Aktive Netzfilter zur Verbesserung der Netzqualität. Tech. rep. Fachhochschule Hamburg, Fachbereich Elektrotechnik und Informatik, 1999.

[111] Dorner, H. and M. Fender. Wissenswertes über Netzrückwirkungen - Grundlagen - Anlagen-Gesamtbetrachtung - Simulation - Normgrenzwerte - Maßnahmen zur Netzverbesserung. Berlin: VDE-Verlag, 2013.

[112] Balzer, G. and C. Neumann. Schalt- und Ausgleichsvorgänge in elektrischen Netzen -. Berlin Heidelberg New York: Springer-Verlag, 2016.

[113] Harrison, J. Elektrische Energieversorgung im Klartext. Pearson Education Deutschland GmbH, 2004.

[114] Oeding, D. and B. R. Oswald. Elektrische Kraftwerke und Netze. Springer-Verlag, Berlin Heidelberg, 2011.

[115] Andersson, G. Modelling an Analysis of Electric Power Systems. EEH - Power Systems Laboratory, ETH Zürich, 2008.

[116] Schwab, A. J. Elektroenergiesysteme. Springer-Verlag, Berlin Heidelberg, 2012.

[117] Paul, R. Elektrotechnik 2 - Netzwerke. Springer-Verlag, Berlin Heidelberg, 1990.

[118] Albach, M. Grundlagen der Elektrotechnik 1 - Erfahrungssätze Bauelemente Gleichstromschaltungen. Pearson Studium, München, 2004.

[119] Zastrow, D. Elektrotechnik - Ein Grundlagenlehrbuch. Vol. 18. Auflage. Vieweg+Teubner Verlag, 2011.

[120] Oswald, B. R. Berechnung von Drehstromnetzen - Berechnung stationärer und nichtstationärer Vorgänge mit Symmetrischen Komponenten und Raumzeigern. Springer Fachmedien, Wiesbaden, 2013.

[121] Weindl, C. Beschreibung und Berechnung von Drehstromsystemen mit leistungselektronischen Anlagen im Zustandsraum. PhD thesis. 2000.

[122] Teigelkötter, J. Energieeffiziente elektrische Antriebe. Vieweg + Teubner | GWV Fachverlage GmbH, Wiesbaden, 2013.

[123] Fortescue, C. L. Method of Symmetrical Co-ordinates Applied to the Solution of Polyphase Networks. In: *A.I.E.E. Trans.* 37 (1918), pp. 1027–1140.

[124] Gehrke, W., M. Winzker, K. Urbanski, and R. Woitowitz. Digitaltechnik - Grundlagen, VHDL, FPGAs, Mikrocontroller. Berlin Heidelberg New York: Springer-Verlag, 2016.

[125] Stranneby, D. Digital Signal Processing and Applications. Amsterdam: Elsevier, 2004.

[126] Lenk, J. D. Simplified Design of Data Converters -. London: Newnes, 1997.

[127] Gevatter, H.-J. and U. Grünhaupt. Handbuch der Mess- und Automatisierungstechnik in der Produktion. Berlin Heidelberg New York: Springer-Verlag, 2013.

[128] Böge, W. Handbuch Elektrotechnik. Berlin Heidelberg New York: Springer-Verlag, 2013.

[129] Hering, E., R. Martin, J. Gutekunst, and J. Kempkes. Elektrotechnik und Elektronik für Maschinenbauer. Berlin Heidelberg New York: Springer-Verlag, 2012.

[130] Geschwinde, H. Einführung in die PLL-Technik -. Berlin Heidelberg New York: Springer-Verlag, 1984.

[131] Weik, M. H. phase-locked loop. In: *Computer Science and Communications Dictionary*. Boston, MA: Springer US, 2001, pp. 1261–1261.

[132] Gardner, F. M. Phaselock Techniques. New York: John Wiley & Sons, 2005.

[133] Brennan, P. V. Phase-Locked Loops - Principles and Practice. Sussex: Macmillan International Higher Education, 1996.

[134] Meyer, M. Signalverarbeitung: Analoge und digitale Signale, Systeme und Filter. Springer Vieweg, 2014.

[135] Shannon, C. Communication in the Presence of Noise. In: *Proceedings of the IRE, Vol. 37, pp. 10-21* (1949).

[136] Gold, B. and C. Rader. Digital Processing of Signals. McGraw-Hill, 1969.

[137] Kammeyer, K.-D. and K. Kroschel. Digitale Signalverarbeitung: Filterung und Spektralanalyse mit MatlabÂ®-Ãœbungen. Vieweg+Teubner, 2009.

[139] Ferizi, A., B. Hoeher, M. Jung, G. Fischer, and A. Koelpin. Design and Implementation of a Fixed-Point Radix-4 FFT Optimized for Local Positioning in Wireless Sensor Networks. In: *9th International Multi-Conference on Systems, Signals and Devices (SSD), IEEE 2012, pp. 1-4*. 2012.

[140] Sun, M., L. Tian, and D. Dai. Radix-8 FFT Processor Design Based on FPGA. In: *5th International Congress on Image and Signal Processing (CISP 2012), IEEE 2012, pp. 1453-1457*. 2012.

[141] Oppenheim, A. and R. Schafer. Digital Signal Processing. Prentice Hall, 1975.

[142] O Serna, J. A. de la. Dynamic Phasor Estimates for Power System Oscillations. In: *IEEE Transactions on Instrumentation and Measurement* 56.5 (2007-10), pp. 1648–1657.

[143] Platas-Garza, M. A. and J. A. de la O Serna. Dynamic Harmonic Analysis Through Taylor-Fourier Transform. In: *IEEE Transactions on Instrumentation and Measurement* 60.3 (2011-03), pp. 804–813.

[144] Kušljević, M. D. and J. J. Tomić. Multiple-Resonator-Based Power System Taylor-Fourier Harmonic Analysis. In: *IEEE Transactions on Instrumentation and Measurement* 64.2 (2015-02), pp. 554–563.

[145] Bernet, S. Selbstgeführte Stromrichter am Gleichspannungszwischenkreis. Springer-Verlag, Berlin Heidelberg, 2012.

[146] Schröder, D. Leistungselektronische Schaltungen. Springer-Verlag, Berlin Heidelberg, 2012.

[147] Komrska, T., Z. Peroutka, and I. Matuljak. A novel least norm-based PWM for a four-leg earth fault compensator. In: *IECON 2014 - 40th Annual Conference of the IEEE Industrial Electronics Society*. 2014-10, pp. 1118–1123.

[148] Kim, J.-H. and S.-K. Sul. A carrier-based PWM method for three-phase four-leg voltage source converters. In: *IEEE Transactions on Power Electronics* 19.1 (2004-01), pp. 66–75.

[149] Kim, J. H., S. K. Sul, and P. N. Enjeti. A Carrier-Based PWM Method With Optimal Switching Sequence for a Multilevel Four-Leg Voltage-Source Inverter. In: *IEEE Transactions on Industry Applications* 44.4 (2008-07), pp. 1239–1248.

[150] Glasberger, T., T. Komrska, and Z. Peroutka. A minimum infinity norm based PWM modulator for four-leg three-phase converters. In: *IECON 2014 - 40th Annual Conference of the IEEE Industrial Electronics Society*. 2014-10, pp. 1053–1059.

[151] Zhong, Q. C., L. Hobson, and M. G. Jayne. Classical control of the neutral point in 4-wire 3-phase DC-AC converters. In: *Electrical Power Quality and Utilisation. Journal* Vol. 11, nr 2 (2005), pp. 73–81.

[152] Zhong, Q. C., J. Liang, G. Weiss, C. M. Feng, and T. C. Green. H^{∞} Control of the Neutral Point in Four-Wire Three-Phase DC–AC Converters. In: *IEEE Transactions on Industrial Electronics* 53.5 (2006-10), pp. 1594–1602.

[153] Mehlmann, G. Grundfrequenzmodulation und Spannungsqualität mehrstufiger Spannungsumrichter. Verlag Dr. Hut, München, 2013.

[154] Dodds, S. J. Feedback Control. Springer London, 2015.

[155] Abramovici, A. and J. Chapsky. Feedback Control Systems. Springer US, 2000.

[156] Wittmers, H. Einführung in die Regelungstechnik. Vieweg+Teubner Verlag, 1965.

[157] Lunze, J. Regelungstechnik 1. Springer Berlin Heidelberg, 2010.

[158] Sierig, J. Photovoltaik und Energiespiecher in elektrischen Energieversorgungssystemen. Verlag der Augustinus Buchhandlung, Aachen, 1993.

[159] Sterner, M. and I. Stadler. Energiespeicher. 2nd ed. Berlin, Heidelberg: Springer-Verlag, 2017.

[163] Völler, S. Optimierte Betriebsführung von Windenergieanlagen durch Energiespeicher. PhD thesis. 2009.

[164] Lachuriya, A. and R. D. Kulkarni. Stationary electrical energy storage technology for global energy sustainability: A review. In: *2017 International Conference on Nascent Technologies in Engineering (ICNTE)*. 2017-01, pp. 1–6.

[165] Chen, H., T. N. Cong, W. Yang, C. Tan, Y. Li, and Y. Ding. Progress in electrical energy storage system: A critical review. In: *Progress in Natural Science* 19.3 (2009), pp. 291–312.

[166] Chatzivasileiadi, A., E. Ampatzi, and I. Knight. Characteristics of electrical energy storage technologies and their applications in buildings. In: *Renewable and Sustainable Energy Reviews* 25 (2013), pp. 814–830.

[167] Georg Fuchs Benedikt Lunz, M. L. and D. U. Sauer. Technology Overview on Electricity Storage. Tech. rep. 2012.

[168] Zhou, L. and Z. ping Qi. Modeling and control of a flywheel energy storage system for uninterruptible power supply. In: *2009 International Conference on Sustainable Power Generation and Supply*. 2009-04, pp. 1–6.

[169] Darrelmann, H. Comparison of high power short time flywheel storage systems. In: *Telecommunication Energy Conference, 1999. INTELEC '99. The 21st International*. 1999-06, p. 492.

[170] Boicea, V. A. Energy Storage Technologies: The Past and the Present. In: *Proceedings of the IEEE* 102.11 (2014-11), pp. 1777–1794.

[171] Ferreira, H. L., R. Garde, G. Fulli, W. Kling, and J. P. Lopes. Characterisation of electrical energy storage technologies. In: *Energy* 53 (2013), pp. 288–298.

[172] San Martín, J., I. Zamora, J. San Martín, V. Aperribay, and P. Eguia. Energy storage technologies for electric applications. In: (2011-05), pp. 593–598.

[173] G, S. M., F. Faraji, A. Majazi, and K. Al-Haddad. A comprehensive review of Flywheel Energy Storage System technology. In: *Renewable and Sustainable Energy Reviews* 67 (2017), pp. 477–490.

[174] Zakeri, B. and S. Syri. Electrical energy storage systems: A comparative life cycle cost analysis. In: *Renewable and Sustainable Energy Reviews* 42 (2015), pp. 569–596.

[175] Rummich, E. Energiespeicher: Grundlagen, Komponenten, Systeme und Anwendungen. 2., Auflage. Renningen: expert Verlag, 2015.

[176] Noack, J., N. Roznyatovskaya, T. Herr, and P. Fischer. Die Chemie der Redox-Flow-Batterien. In: *Angewandte Chemie* 127.34 (2015), pp. 9912–9947.

[177] Kurzweil, P. and O. K. Dietlmeier. Elektrochemische Speicher: Superkondensatoren, Batterien, Elektrolyse-Wasserstoff, Rechtliche Grundlagen. Wiesbaden: Springer Vieweg, 2018.

[178] Oertel, D. Energiespeicher – Stand und Perspektiven. In: 123 (2008).

[179] Hannig, F., T. Smolinka, P. Bretschneider, S. Nicolai, S. Krüger, F. Meißner, and M. Voigt. Stand und Entwicklungspotenzial der Speichertechniken für Elektroenergie–Ableitung von Anforderungen an und Auswirkungen auf die Investitionsgüterindustrie. In: *Abschlussbericht, BMWi-Auftragsstudie* 8 (2009), p. 28.

[180] Korthauer, R. Handbuch Lithium-Ionen-Batterien. Berlin Heidelberg: Springer Vieweg, 2013.

[181] Liu, C., Z. G. Neale, and G. Cao. Understanding electrochemical potentials of cathode materials in rechargeable batteries. In: *Materials Today* 19.2 (2016), pp. 109–123.

[182] Buchmann, I. Will Lithium-Ion batteries power the new millennium. In: *Cadex Electronics Inc., Richmond, BC* (2001).

[183] Ender, M. Mikrostrukturelle Charakterisierung, Modellentwicklung und Simulation poröser Elektroden für Lithiumionenzellen. PhD thesis. 2014.

[184] Luo, X., J. Wang, M. Dooner, and J. Clarke. Overview of current development in electrical energy storage technologies and the application potential in power system operation. In: *Applied Energy* 137 (2015).

[185] Hadjipaschalis, I., A. Poullikkas, and V. Efthimiou. Overview of current and future energy storage technologies for electric power applications. In: *Renewable and Sustainable Energy Reviews* 13.6 (2009), pp. 1513–1522.

[186] Neupert, U., T. Euting, T. Kretschmer, C. Notthoff, K. Ruhlig, and B. Weimert. Energiespeicher - Technische Grundlagen und energiewirtschaftliches Potenzial. 2009-01-01.

[187] Stiny, L. Passive elektronische Bauelemente: Aufbau, Funktion, Eigenschaften, Dimensionierung und Anwendung. 2., überarbeitete und erweiterte Auflage. Wiesbaden: Springer Vieweg, 2015.

[188] Kowal, J., J. Drillkens, and D. U. Sauer. 9. Superkondensatoren elektrochemische Doppelschichtkondensatoren. In: *MTZ - Motortechnische Zeitschrift* 74.2 (2013-02), pp. 158–163.

[189] Alberici, S., S. Boeve, P. van Breevort, Y. Deng, S. Förster, A. Gardiner, V. van Gastel, K. Grave, H. Groenenberg, D. de Jager, E. Klassen, W. Pouwels, M. Smith, E. de Visser, T. Winkel, and K. Wouters. Subsidies and costs of EU energy. Tech. rep. European Commission, 2014-11.

[190] Hall, P. J. and E. J. Bain. Energy-storage technologies and electricity generation. In: *Energy Policy* 36.12 (2008).

[191] Winter, M. and J. O. Besenhard. Wiederaufladbare Batterien. In: *Chemie in unserer Zeit* 33.6 (2004), pp. 320–332.

[192] Chen, H., X. Zhang, J. Liu, and C. Tan. Compressed Air Energy Storage. In: *Energy Storage*. Ed. by A. F. Zobaa. Rijeka: IntechOpen, 2013. Chap. 4.

[193] M. Wietschel and S. J. Ullrich, eds. Energietechnologien der Zukunft: Erzeugung, Speicherung, Effizienz und Netze. Lehrbuch. Wiesbaden: Springer Vieweg, 2015.

[194] Rebhan, E. Energiehandbuch: Gewinnung, Wandlung und Nutzung von Energie. Softcover reprint of the original 1st ed. 2002. Vol. Gewinnung, Wandlung und Nutzung von Energie. VDI-Buch. Berlin: Springer Berlin, 2014.

[195] Guney, M. S. and Y. Tepe. Classification and assessment of energy storage systems. In: *Renewable and Sustainable Energy Reviews* 75.C (2017), pp. 1187–1197.

[196] Zhou, X., Y. Lin, and Y. Ma. The overview of energy storage technology. In: *2015 IEEE International Conference on Mechatronics and Automation (ICMA)*. 2015-08, pp. 43–48.

[197] Carnegie, R., D. Gotham, D. Nderitu, and P. V. Preckel. Utility scale energy storage systems. In: *State Utility Forecasting Group. Purdue University* 1 (2013).

[198] Thielmann, A., A. Sauer, R. Isenmann, and M. Wietschel. Technology Roadmap Energy Storage for Electric Mobility 2030. In: *Fraunhofer Institute for Systems and Innovation Research* (2013).

[199] Ibrahim, H., A. Ilinca, and J. Perron. Energy storage systems - Characteristics and comparisons. In: *Renewable and Sustainable Energy Reviews* 12.5 (2008), pp. 1221–1250.

[200] Zakeri, B., S. Syri, and F. Wagner. Economics of energy storage in the German electricity and reserve markets. In: *2017 14th International Conference on the European Energy Market (EEM)*. 2017-06, pp. 1–6.

[201] Naumann, M., C. N. Truong, R. C. Karl, and A. Jossen. Betriebsabhängige Kostenberechnung von Energiespeichern. In: *EnInnov*. 2014.

[202] Haas, R. and A. Ajanovic. Wirtschaftliche und energetische Aspekte von Langzeitspeichern. In: *e & i Elektrotechnik und Informationstechnik* 130.6 (2013), pp. 169–176.

[203] Guerrero, M. A., E. Romero, F. Barrero, M. I. Milanes, and E. Gonzalez. Overview of medium scale energy storage systems. In: *2009 Compatibility and Power Electronics*. 2009-05, pp. 93–100.

[204] Sauer, D. U. Optionen zur Speicherung elektrischer Energie in Energieversorgungssystemen mit regenerativer Stromerzeugung. In: *Solarzeitalter* 4.2006 (2006), pp. 12–34.

[205] Stahl, H., D. Bauknecht, A. Hermann, W. Jenseit, A. R. Köhler, C. Merz, M. Möller, and D. Schüller. Ableitung von Recycling- und Umweltanforderungen und Strategien zur Vermeidung von Versorgungsrisiken bei innovativen Energiespeichern. Tech. rep. Öko-Institut e. V., Freiburg, 2016.

[207] Koch, D., F. Hannig, and D. Ziener. FPGAs for Software Programmers. Berlin, Heidelberg: Springer, 2016.

[208] Meyer-Baese, U. Digital Signal Processing with Field Programmable Gate Arrays -. Berlin Heidelberg: Springer Science & Business Media, 2013.

[209] Abdul Rahman, N., M. Mohd Radzi, A. Che Soh, N. Mariun, and N. Abd Rahim. Significant insights into the operation of DC-link voltage control of a shunt active power filter using different control algorithms: A comparative study. In: *Turkish Journal of Electrical Engineering and Computer Sciences* 25.3 (2017), pp. 2033–2043.

[210] Mullane, A., G. Lightbody, and R. Yacamini. Comparison of a Cascade and Feedback Linearisation Scheme for DC Link Voltage Control in a Grid Connected Wind Turbine. In: *Rev. Energ. Ren. : Power Engineering* (2001), pp. 29–38.

[211] GRIDCON® Power Conversion System 4-Wire. Maschinenfabrik Reinhausen GmbH. 2017-11.

[213] TruConvert DC 1008, TruConvert System Control. TRUMPF Hüttinger GmbH + Co. KG. 2018-07.

[214] Kim, S.-C., T. H. Nguyen, D.-C. Lee, K.-B. Lee, and J.-M. Kim. Fault Tolerant Control of DC-Link Voltage Sensor for Three-Phase AC/DC/AC PWM Converters. In: *Journal of Power Electronics* 14.4 (2014-07), pp. 695–703.

[215] Kim, Y., S. Park, N. Chang, Q. Xie, Y. Wang, and M. Pedram. Networked architecture for hybrid electrical energy storage systems. In: *DAC Design Automation Conference 2012*. 2012-06, pp. 522–528.

[216] Yue, S., D. Zhu, Y. Wang, M. Pedram, Y. Kim, and N. Chang. SIMES: A simulator for hybrid electrical energy storage systems. In: *International Symposium on Low Power Electronics and Design (ISLPED)*. 2013-09, pp. 33–38.

[217] Xie, Q., Y. Kim, D. Baek, Y. Wang, M. Pedram, and N. Chang. Efficiency-driven design time optimization of a hybrid energy storage system with networked charge transfer interconnect. In: *2015 Design, Automation Test in Europe Conference Exhibition (DATE)*. 2015-03, pp. 1607–1610.

[220] Choi, M. E., S. W. Kim, and S. W. Seo. Energy Management Optimization in a Battery/Supercapacitor Hybrid Energy Storage System. In: *IEEE Transactions on Smart Grid* 3.1 (2012-03), pp. 463–472.

[221] Shen, J., S. Dusmez, and A. Khaligh. Optimization of Sizing and Battery Cycle Life in Battery/Ultracapacitor Hybrid Energy Storage Systems for Electric Vehicle Applications. In: *IEEE Transactions on Industrial Informatics* 10.4 (2014-11), pp. 2112–2121.

[224] Ertel, W. Grundkurs Künstliche Intelligenz: Eine praxisorientierte Einführung. 4., überarbeitete Auflage. Computational Intelligence. Wiesbaden: Springer Vieweg, 2016.

[225] Handreg, M. Entwurf von Künstlichen Neuronalen Netzen zur Regelung von Prozessgrösen in einer Schmelzwanne für Flachglas. doctoralthesis. 2016.

[226] Saidur, R., N. Rahim, and M. Hasanuzzaman. A review on compressed-air energy use and energy savings. In: *Renewable and Sustainable Energy Reviews* 14.4 (2010), pp. 1135–1153.

[227] Bellman, R. The theory of dynamic programming. In: *Bull. Amer. Math. Soc.* 60.6 (1954-11), pp. 503–515.

[228] Bertsekas, D. P. Dynamic Programming and Stochastic Control. Amsterdam, Boston: Academic Press, 1976.

[229] Romaus, C., K. Gathmann, and J. Böcker. Optimal energy management for a hybrid energy storage system for electric vehicles based on Stochastic Dynamic Programming. In: *2010 IEEE Vehicle Power and Propulsion Conference*. 2010-09, pp. 1–6.

[230] Abu-qahouq, J. A., H. Mao, H. J. Al-atrash, and I. Batarseh. Maximum Efficiency Point Tracking (MEPT) Method and Digital Dead Time Control Implementation. In: *IEEE Transactions on Power Electronics* 21.5 (2006-09), pp. 1273–1281.

[231] Borkowski, D. Maximum Efficiency Point Tracking (MEPT) for Variable Speed Small Hydropower Plant With Neural Network Based Estimation of Turbine Discharge. In: *IEEE Transactions on Energy Conversion* 32.3 (2017-09), pp. 1090–1098.

[232] Lemofouet, S. and A. Rufer. A Hybrid Energy Storage System Based on Compressed Air and Supercapacitors With Maximum Efficiency Point Tracking (MEPT). In: *IEEE Transactions on Industrial Electronics* 53.4 (2006-06), pp. 1105–1115.

[235] Chapelsky, C., J. Salmon, and A. Knight. Control of a High-Inertia Flywheel As Part of a High Capacity Energy Storage System. In: *2007 Canadian Conference on Electrical and Computer Engineering*. 2007-04, pp. 1437–1440.

[236] Siostrzonek, T., A. Penczek, and S. Pirog. The control and structure of the power electronic system supplying the Flywheel Energy Storage (FES). In: *Power Electronics and Applications, 2007 European Conference on*. 2007-09, pp. 1–8.

[237] Lashway, C. R., A. T. Elsayed, and O. A. Mohammed. DC voltage ripple quantification for a flywheel-battery based Hybrid Energy Storage System. In: *2016 IEEE Applied Power Electronics Conference and Exposition (APEC)*. 2016-03, pp. 1267–1272.

[238] Suvire, G. O. and P. E. Mercado. Improvement of power quality in wind energy applications using a DSTATCOM coupled with a Flywheel Energy Storage System. In: *2009 Brazilian Power Electronics Conference*. 2009-09, pp. 58–64.

[240] Schweitzer, G., A. Traxler, and H. Bleuler. Magnetlager: Grundlagen, Eigenschaften und Anwendungen berührungsfreier, elektromagnetischer Lager. 1. Auflage. Berlin Heidelberg: Springer Verlag, 1993.

[241] Bartz, W. J. Luftlagerungen und Magnetlager: Grundlagen und Anwendungen : mit 17 Tabellen. 3., völlig neu bearbeitete Auflage. Vol. Band 14. Handbuch der Tribologie und Schmierungstechnik. Renningen: expert verlag, 2014.

[242] Kolk, M. Ein Schwungrad-Energiespeicher mit permanentmagnetischer Lagerung -. Jülich: Forschungszentrum, Zentralbibliothek, 1997.

[243] Halbach, K. Design of permanent multipole magnets with oriented rare earth cobalt material. In: *Nuclear Instrum. Methods* 169.1 (1980-08), pp. 1–10.

[244] Toh, C.-S. and S.-L. Chen. Design, Modeling and Control of Magnetic Bearings for a Ring-Type Flywheel Energy Storage System. In: *Energies* 9.1051 (2016-12), pp. 1–19.

[245] Delamare, J., E. Rulliere, and J. P. Yonnet. Classification and Synthesis of Permanent Magnet Bearing Configurations. In: *IEEE Transactions on Magnetics* 31.6 (1995-11), pp. 4190–4192.

[246] Sotelo, G., A. C. Ferreira, and J. R. de Andrade. Halbach Array Superconducting Magnetic Bearing for a Flywheel Energy Storage System. In: *IEEE Transactions on applied superconductivity* 15.2 (2005-06), pp. 2253–2256.

[247] Kallenbach, E., R. Eick, P. Quendt, T. Ströhla, K. Feindt, M. Kallenbach, and O. Radler. Elektromagnete. Vieweg+Teubner Verlag, 2012.

[248] Mechanical vibration – Balance quality requirements for rotors in a constant (rigid) state – Part 1: Specification and verification of balance tolerances. en. Standard ISO 1940-1:2003. Geneva, CH: International Organization for Standardization (ISO), 2003.

[249] Binder, A., M. Klohr, and T. Schneider. Losses in high speed permanent magnet motor with magnetic levitation for 40000/min, 40 kW. In: 16. International Conference on Electrical Machines, 2004, Krakow. Lodz: Univ., 2004-01.

[250] Saari, J. Thermal analysis of high-speed induction machines. en. 1998.

[251] Stierstadt, K. Thermodynamik. Springer Berlin Heidelberg, 2010.

[252] Wang, Q., H. Yuan, X. Jiang, and X. Xing. A simple sensorless control strategy for IPMSM in 1 MW flywheel energy storage system. In: *2016 IEEE 8th International Power Electronics and Motion Control Conference (IPEMC-ECCE Asia)*. 2016-05, pp. 1923–1928.

[256] Blanc, C. and A. Rufer. Optimization of the operating point of a vanadium redox flow battery. In: *2009 IEEE Energy Conversion Congress and Exposition*. 2009-09, pp. 2600–2605.

[257] Baccino, F., S. Grillo, M. Marinelli, S. Massucco, and F. Silvestro. Power and energy control strategies for a Vanadium Redox Flow Battery and wind farm combined system. In: *Innovative Smart Grid Technologies (ISGT Europe), 2011 2nd IEEE PES International Conference and Exhibition on*. 2011-12, pp. 1–8.

[258] König, S. Model-based Design and Optimization of Vanadium Redox Flow Batteries. PhD thesis. 2017.

[259] Blanc, C. and A. Rufer. Multiphysics and energetic modeling of a vanadium redox flow battery. In: *2008 IEEE International Conference on Sustainable Energy Technologies*. 2008-11, pp. 696–701.

[260] Merei, G., S. Adler, D. Magnor, M. Leuthold, and D. U. Sauer. Multi-physics Model for a Vanadium Redox Flow Battery. In: *Energy Procedia* 46.Supplement C (2014), pp. 194–203.

[261] Averbukh, M., D. Faiman, and K. Batat. Modeling of dynamic behavior of vanadium redox batteries (VRB) with contamination properties of proton exchange membrane. In: *2012 IEEE 27th Convention of Electrical and Electronics Engineers in Israel*. 2012-11, pp. 1–5.

[262] Shah, A., M. Watt-Smith, and F. Walsh. A dynamic performance model for redox-flow batteries involving soluble species. In: *Electrochimica Acta* 53.27 (2008), pp. 8087–8100.

[263] Nguyen, T. A., X. Qiu, J. D. G. II, M. L. Crow, and A. C. Elmore. Performance Characterization for Photovoltaic-Vanadium Redox Battery Microgrid Systems. In: *IEEE Transactions on Sustainable Energy* 5.4 (2014-10), pp. 1379–1388.

[264] König, S., M. R. Suriyah, and T. Leibfried. Volumetric electrolyte flow rate control in vanadium redox flow batteries using a variable flow factor. In: *IREC2015 The Sixth International Renewable Energy Congress*. 2015-03, pp. 1–6.

[265] Corcuera, S. and M. Skyllas-Kazacos. State-of-Charge Monitoring and Electrolyte Rebalancing Methods for the Vanadium Redox Flow Battery. In: *Eur. Chem. Bull.* 12.1 (2012-01), pp. 511–519.

[266] Blanc, C. and A. Rufer. Understanding the Vanadium Redox Flow Batteries. INTECH Open Access Publisher, 2010.

[267] Bromberger, K., J. Kaunert, and T. Smolinka. A Model for All-Vanadium Redox Flow Batteries: Introducing Electrode-Compression Effects on Voltage Losses and Hydraulics. In: *Energy Technology* 2.1 (2014), pp. 64–76.

[272] Badrinarayanan, R., K. J. Tseng, B. H. Soong, and Z. Wei. Modelling and control of vanadium redox flow battery for profile based charging applications. In: *Energy* 141 (2017), pp. 1479–1488.

[273] Noack, J., L. Wietschel, N. Roznyatovskaya, K. Pinkwart, and J. Tübke. Techno-Economic Modeling and Analysis of Redox Flow Battery Systems. In: *Energies* 9.8 (2016).

[274] Shah, A. A., R. Tangirala, R. Singh, R. G. A. Wills, and F. C. Walsh. A Dynamic Unit Cell Model for the All-Vanadium Flow Battery. In: *Journal of The Electrochemical Society* 158.6 (2011), A671–A677.

[275] Tang, A., J. Bao, and M. Skyllas-Kazacos. Studies on pressure losses and flow rate optimization in vanadium redox flow battery. In: *Journal of Power Sources* 248 (2014), pp. 154–162.

[276] Baehr, H. D. and K. Stephan. Wärme- und Stoffübertragung. 9., aktualisierte Auflage. Berlin and Heidelberg: Springer Vieweg, 2016.

[277] Yamamura, T., N. Watanabe, T. Yano, and Y. Shiokawa. Electron-Transfer Kinetics of Np^{3+}/Np^{4+}, NpO_2^{+}/NpO_2^{2+}, V^{2+}/V^{3+} and VO_2^{+}/VO_2^{2+} at Carbon Electrodes. In: *Journal of The Electrochemical Society* 152.4 (2005), A830–A836.

[278] König, S., M. Suriyah, and T. Leibfried. Innovative model-based flow rate optimization for vanadium redox flow batteries. In: *Journal of Power Sources* 333 (2016), pp. 134–144.

[279] He, G., Q. Chen, C. Kang, and Q. Xia. Optimal operating strategy and revenue estimates for the arbitrage of a vanadium redox flow battery considering dynamic efficiencies and capacity loss. In: *IET Generation, Transmission Distribution* 10.5 (2016), pp. 1278–1285.

[280] Xing, F., H. Zhang, and X. Ma. Shunt current loss of the vanadium redox flow battery. In: *Journal of Power Sources* 196.24 (2011), pp. 10753–10757.

[281] Tang, A., J. McCann, J. Bao, and M. Skyllas-Kazacos. Investigation of the effect of shunt current on battery efficiency and stack temperature in vanadium redox flow battery. In: *Journal of Power Sources* 242 (2013), pp. 349–356.

[282] Skyllas-Kazacos, M., J. McCann, Y. Li, J. Bao, and A. Tang. The Mechanism and Modelling of Shunt Current in the Vanadium Redox Flow Battery. In: *ChemistrySelect* 1.10 (), pp. 2249–2256.

[283] Zhang, Y., J. Zhao, P. Wang, M. Skyllas-Kazacos, B. Xiong, and R. Badrinarayanan. A comprehensive equivalent circuit model of all-vanadium redox flow battery for power system analysis. In: *Journal of Power Sources* 290 (2015), pp. 14–24.

[285] Jaschinsky, M. Netzfrequenz.info - Netzfrequenz Häufigkeitsverteilung. URL: https://www.netzfrequenz.info/histogramm-vortag (visited on 2018-10-22).

[286] Scharnhorst, K. Angles in Complex Vector Spaces. In: *Acta Applicandae Mathematica* 69.1 (2001-10), pp. 95–103.

[288] Bradaschia, F., J. P. Arruda, H. E. P. Souza, G. M. S. Azevedo, F. A. S. Neves, and M. C. Cavalcanti. A method for extracting the fundamental frequency positive-sequence voltage vector based on simple mathematical transformations. In: *2008 IEEE Power Electronics Specialists Conference*. 2008-06, pp. 1115–1121.

[289] Souza, H. E. P. de, F. Bradaschia, F. A. S. Neves, M. C. Cavalcanti, G. M. S. Azevedo, and J. P. de Arruda. A Method for Extracting the Fundamental-Frequency Positive-Sequence Voltage Vector Based on Simple Mathematical Transformations. In: *IEEE Transactions on Industrial Electronics* 56.5 (2009-05), pp. 1539–1547.

[290] Meena, P., K. UmaRao, and R. Deekshit. Frequency Measurement and Tracking Algorithm for Integrated Grids. In: *Electrical Power Systems and Computers*. Ed. by X. Wan. Berlin, Heidelberg: Springer Berlin Heidelberg, 2011, pp. 201–212.

[291] Eckhardt, V., P. Hippe, and G. Hosemann. Dynamic measuring of frequency and frequency oscillations in multiphase power systems. In: *IEEE Transactions on Power Delivery* 4.1 (1989-01), pp. 95–102.

[292] Freitag, C. Entwicklung und Untersuchung messtechnischer Verfahren zur Bestimmung des Zustands von Betriebsmitteln der elektrischen Energieversorgung. PhD thesis. 2013.

[293] Rodriguez, A. D., F. M. Fuentes, and A. J. Matta. Comparative analysis between voltage unbalance definitions. In: *2015 Workshop on Engineering Applications - International Congress on Engineering (WEA)*. 2015-10, pp. 1–7.

[294] Singh, A. K., G. K. Singh, and R. Mitra. Some Observations on Definitions of Voltage Unbalance. In: *2007 39th North American Power Symposium*. 2007-09, pp. 473–479.

[295] Olczykowski, Z. and A. Wąsowski. Methods of voltage unbalance estimation in electric power networks. In: *Electrical Power Quality and Utilisation. Journal* Vol. 12, nr 2 (2006), pp. 71–76.

[296] Pillay, P. and M. Manyage. Definitions of Voltage Unbalance. In: *IEEE Power Engineering Review* 21.5 (2001-05), pp. 49–51.

[297] Woolley, N. C. and J. V. Milanović. Estimating the voltage unbalance factor using distribution system state estimation. In: *2010 IEEE PES Innovative Smart Grid Technologies Conference Europe (ISGT Europe)*. 2010-10, pp. 1–7.

[299] Shakra Dr.-Ing., I. Entwicklung eines Regelverfahrens zur selektiven Dämpfung von ausgewählten Oberschwingungen unter Berücksichtigung von zulässigen Grenzwerten für Elektroenergiequalitätsparameter. PhD thesis. 2014.

[300] Foulquier, J. Compensation of harmonics of the mains voltage with a smart charging station for hybrid and electric vehicle. PhD thesis. 2018.

Own publications referring to this work

[34] Böhm, R., R. M. Schaidhauf, B. Wytopil, and J. Franke. Analyse der Marktaussichten von Biogasanlagen. In: *Zeitschrift für Energiewirtschaft* 42.2 (2018-06), pp. 167–176.

[206] Böhm, R., C. Rehtanz, and J. Franke. Inverter-based hybrid compensation systems contributing to grid stabilization in medium voltage distribution networks with decentralized, renewable generation. In: *Electrical Engineering* 98.4 (2016), pp. 355–362.

[212] Böhm, R., M. Steglich, B. Bauernschmitt, C. Rehtanz, and J. Franke. A hybrid compensation system for provision of ancillary services in medium voltage grids. In: *2018 International Conference on Diagnostics in Electrical Engineering (Diagnostika)*. 2018-09, pp. 1–4.

[233] Böhm, R., C. Weindl, and J. Franke. Control of a hybrid storage system (HSS) comprising a RedOx-Flow Battery and a High Speed Flywheel for a hybrid compensation system. In: *2018 IEEE PES Innovative Smart Grid Technologies Conference Europe (ISGT-Europe)*. 2018-10, pp. 1–6.

[234] Böhm, R., M. Steglich, C. Rehtanz, M. Paulsburg, S. Datsevic, B. Brunner, and J. Franke. Control of a Hybrid Energy Storage System for a Hybrid Compensation System. In: *Chem. Eng. Technol.* 42 (2019-05), pp. 1879–1885.

[298] Merkl, R., M. Steglich, M. Paulsburg, C. Rehtanz, and J. Franke. Aggregated Power Quality Indicator for Controlling a Hybrid Compensation System Providing System Services. In: *2020 IEEE PES Innovative Smart Grid Technologies Europe (ISGT-Europe)*. 2020, pp. 700–704.

Students' theses referring to this work

The 2nd (3rd) author names the supervisor; the last author is head of the institute

[109] Paulsburg, M., R. Böhm, and J. Franke. Entwicklung einer Kompensatorschaltung für die Elimination von Signalverzerrungen. bachelor thesis. 2016.

[138] Hamann, T., R. Böhm, and J. Franke. Implementation study for the utilization of digital signal processing methods on prototyping microcontroller boards. master thesis. 2017.

[160] Westhoff, S., R. Böhm, and J. Franke. Entwicklung eines Kennzahlensystems zur Beurteilung und Analyse von Energiespeichertechnologien. project thesis. 2018.

[161] Yu, W., R. Böhm, and J. Franke. Characterization of energy storage technologies. project thesis. 2018.

[162] Nowack, A., R. Böhm, and J. Franke. Energiespeicher – Kennzahlen und aktuelle Entwicklungen. project thesis. 2018.

[218] Sich, O., R. Böhm, and J. Franke. Entwicklung einer optimierten Steuerung des hybriden Speicher-systems aus Schwungmassenspeicher und RedOx-Flow Batterie. master thesis. 2018.

[219] Pierling, S. M., R. Böhm, and J. Franke. Optimierung der Steuerung eines hybriden Speichersystems hinsichtlich Wirkungsgrad und Energiemanagement. project thesis. 2018.

[222] Albert, T., R. Böhm, and J. Franke. Modellierung neuronaler Netze zur Steuerung industrieller Druckluftsysteme und Evaluation der Potentiale. bachelor thesis. 2017.

[223] Nitsche, A., R. Böhm, and J. Franke. Energieeffiziente Steuerung von industriellen Druckluftsystemen durch künstliche neuronale Netzwerke. project thesis. 2017.

[239] Honig, J., R. Böhm, and J. Franke. Modellierung eines Highspeed-Flywheel Speichers für den Einsatz in einem hybriden Speichersystem. master thesis. 2018.

[253] Buchmüller, T., R. Böhm, and J. Franke. Modellierung und Analyse zweier Energiespeicher für die Anwendung in einem hybriden Speichersystem. master thesis. 2017.

[254] Eckstein, T. L., R. Böhm, and J. Franke. Modellierung eines Schwungmassenspeichers sowie einer Redox-Flow-Batterie für den Einsatz in einem hybriden Energiespeichersystem mittels LabVIEW. project thesis. 2018.

[255] Pollack, S., R. Böhm, and J. Franke. Entwicklung und Analyse eines hybriden Energiespeichersystems anhand einer modellhaften Betrachtung. master thesis. 2017.

[268] Knöll, S., R. Böhm, and J. Franke. Charakterisierung eines hybriden Energiespeichersystems aus RedOx-Flow Batterie und Schwungmassenspeicher anhand einfacher Modellbetrachtungen. project thesis. 2017.

[269] Schindler, J., R. Böhm, and J. Franke. Modellierung hybriden Speichersystems aus RedOx-Flow Batterie und Schwungmassenspeicher sowie einer Steuerung auf Basis neuronaler Netze. master thesis. 2018.

[270] Peter, D., R. Böhm, and J. Franke. Modellierung eines hybriden Energiespeichersystems aus Schwungmassen- und Redox-Flow-Speicher und Entwicklung von optimierten Steuerungsstrategien. master thesis. 2018.

[271] Meyer, T., R. Böhm, and J. Franke. Modeling of Redox-Flow Batteries and Flywheels for the application in hybrid storage systems. master thesis. 2017.

[284] Neudert, M., R. Böhm, and J. Franke. Hybride Systeme für die Speicherung von elektrischer Energie – Modellierung eines Systems aus Schwungmassen- und Redox-Flow Speicher durch analytische und simulative Ansätze. master thesis. 2017.

[287] Corona, M., R. Böhm, and J. Franke. Implementierung von Methoden der Signalanalyse zur Verbesserung der Spannungsqualität. bachelor thesis. 2018.

[301] Beile, F., R. Böhm, and J. Franke. Optimierung eines hybriden Energiespeichersystems hinsichtlich der Ladestrategie. bachelor thesis. 2018.

Reihenübersicht

Koordination der Reihe (Stand 2021):
Geschäftsstelle Maschinenbau, Dr.-Ing. Oliver Kreis, www.mb.fau.de/diss/

Im Rahmen der Reihe sind bisher die nachfolgenden Bände erschienen.

Band 1 – 52
Fertigungstechnik – Erlangen
ISSN 1431-6226
Carl Hanser Verlag, München

Band 53 – 307
Fertigungstechnik – Erlangen
ISSN 1431-6226
Meisenbach Verlag, Bamberg

ab Band 308
FAU Studien aus dem Maschinenbau
ISSN 2625-9974
FAU University Press, Erlangen

Die Zugehörigkeit zu den jeweiligen Lehrstühlen ist wie folgt gekennzeichnet:

Lehrstühle:

FAPS	Lehrstuhl für Fertigungsautomatisierung und Produktionssystematik
KTmfk	Lehrstuhl für Konstruktionstechnik
LFT	Lehrstuhl für Fertigungstechnologie
LPT	Lehrstuhl für Photonische Technologien

Band 1: Andreas Hemberger
Innovationspotentiale in der rechnerintegrierten Produktion durch wissensbasierte Systeme
FAPS, 208 Seiten, 107 Bilder. 1988.
ISBN 3-446-15234-2.

Band 2: Detlef Classe
Beitrag zur Steigerung der Flexibilität automatisierter Montagesysteme durch Sensorintegration und erweiterte Steuerungskonzepte
FAPS, 194 Seiten, 70 Bilder. 1988.
ISBN 3-446-15529-5.

Band 3: Friedrich-Wilhelm Nolting
Projektierung von Montagesystemen
FAPS, 201 Seiten, 107 Bilder, 1 Tab. 1989.
ISBN 3-446-15541-4.

Band 4: Karsten Schlüter
Nutzungsgradsteigerung von Montagesystemen durch den Einsatz der Simulationstechnik
FAPS, 177 Seiten, 97 Bilder. 1989.
ISBN 3-446-15542-2.

Band 5: Shir-Kuan Lin
Aufbau von Modellen zur Lageregelung von Industrierobotern
FAPS, 168 Seiten, 46 Bilder. 1989.
ISBN 3-446-15546-5.

Band 6: Rudolf Nuss
Untersuchungen zur Bearbeitungsqualität im Fertigungssystem Laserstrahlschneiden
LFT, 206 Seiten, 115 Bilder, 6 Tab. 1989.
ISBN 3-446-15783-2.

Band 7: Wolfgang Scholz
Modell zur datenbankgestützten Planung automatisierter Montageanlagen
FAPS, 194 Seiten, 89 Bilder. 1989.
ISBN 3-446-15825-1.

Band 8: Hans-Jürgen Wißmeier
Beitrag zur Beurteilung des Bruchverhaltens von Hartmetall-Fließpreßmatrizen
LFT, 179 Seiten, 99 Bilder, 9 Tab. 1989.
ISBN 3-446-15921-5.

Band 9: Rainer Eisele
Konzeption und Wirtschaftlichkeit von Planungssystemen in der Produktion
FAPS, 183 Seiten, 86 Bilder. 1990.
ISBN 3-446-16107-4.

Band 10: Rolf Pfeiffer
Technologisch orientierte Montageplanung am Beispiel der Schraubtechnik
FAPS, 216 Seiten, 102 Bilder, 16 Tab. 1990.
ISBN 3-446-16161-9.

Band 11: Herbert Fischer
Verteilte Planungssysteme zur Flexibilitätssteigerung der rechnerintegrierten Teilefertigung
FAPS, 201 Seiten, 82 Bilder. 1990.
ISBN 3-446-16105-8.

Band 12: Gerhard Kleineidam
CAD/CAP: Rechnergestützte Montagefeinplanung
FAPS, 203 Seiten, 107 Bilder. 1990.
ISBN 3-446-16112-0.

Band 13: Frank Vollertsen
Pulvermetallurgische Verarbeitung eines übereutektoiden verschleißfesten Stahls
LFT, XIII u. 217 Seiten, 67 Bilder, 34 Tab. 1990. ISBN 3-446-16133-3.

Band 14: Stephan Biermann
Untersuchungen zur Anlagen- und Prozeßdiagnostik für das Schneiden mit CO2-Hochleistungslasern
LFT, VIII u. 170 Seiten, 93 Bilder, 4 Tab. 1991. ISBN 3-446-16269-0.

Band 15: Uwe Geißler
Material- und Datenfluß in einer flexiblen Blechbearbeitungszelle
LFT, 124 Seiten, 41 Bilder, 7 Tab. 1991. ISBN 3-446-16358-1.

Band 16: Frank Oswald Hake
Entwicklung eines rechnergestützten Diagnosesystems für automatisierte Montagezellen
FAPS, XIV u. 166 Seiten, 77 Bilder. 1991. ISBN 3-446-16428-6.

Band 17: Herbert Reichel
Optimierung der Werkzeugbereitstellung durch rechnergestützte Arbeitsfolgenbestimmung
FAPS, 198 Seiten, 73 Bilder, 2 Tab. 1991. ISBN 3-446-16453-7.

Band 18: Josef Scheller
Modellierung und Einsatz von Softwaresystemen für rechnergeführte Montagezellen
FAPS, 198 Seiten, 65 Bilder. 1991. ISBN 3-446-16454-5.

Band 19: Arnold vom Ende
Untersuchungen zum Biegeumforme mit elastischer Matrize
LFT, 166 Seiten, 55 Bilder, 13 Tab. 1991. ISBN 3-446-16493-6.

Band 20: Joachim Schmid
Beitrag zum automatisierten Bearbeiten von Keramikguß mit Industrierobotern
FAPS, XIV u. 176 Seiten, 111 Bilder, 6 Tab. 1991. ISBN 3-446-16560-6.

Band 21: Egon Sommer
Multiprozessorsteuerung für kooperierende Industrieroboter in Montagezellen
FAPS, 188 Seiten, 102 Bilder. 1991. ISBN 3-446-17062-6.

Band 22: Georg Geyer
Entwicklung problemspezifischer Verfahrensketten in der Montage
FAPS, 192 Seiten, 112 Bilder. 1991. ISBN 3-446-16552-5.

Band 23: Rainer Flohr
Beitrag zur optimalen Verbindungstechnik in der Oberflächenmontage (SMT)
FAPS, 186 Seiten, 79 Bilder. 1991. ISBN 3-446-16568-1.

Band 24: Alfons Rief
Untersuchungen zur Verfahrensfolge Laserstrahlschneiden und -schweißen in der Rohkarosseriefertigung
LFT, VI u. 145 Seiten, 58 Bilder, 5 Tab. 1991. ISBN 3-446-16593-2.

Band 25: Christoph Thim
Rechnerunterstützte Optimierung
von Materialflußstrukturen in der
Elektronikmontage durch Simulation
FAPS, 188 Seiten, 74 Bilder. 1992.
ISBN 3-446-17118-5.

Band 26: Roland Müller
CO_2 -Laserstrahlschneiden von
kurzglasverstärkten Verbundwerkstoffen
LFT, 141 Seiten, 107 Bilder, 4 Tab. 1992.
ISBN 3-446-17104-5.

Band 27: Günther Schäfer
Integrierte Informationsverarbeitung
bei der Montageplanung
FAPS, 195 Seiten, 76 Bilder. 1992.
ISBN 3-446-17117-7.

Band 28: Martin Hoffmann
Entwicklung einer
CAD/CAM-Prozeßkette für die
Herstellung von Blechbiegeteilen
LFT, 149 Seiten, 89 Bilder. 1992.
ISBN 3-446-17154-1.

Band 29: Peter Hoffmann
Verfahrensfolge Laserstrahlschneiden
und –schweißen: Prozeßführung und
Systemtechnik in der 3D-Laserstrahlbearbeitung von Blechformteilen
LFT, 186 Seiten, 92 Bilder, 10 Tab. 1992.
ISBN 3-446-17153-3.

Band 30: Olaf Schrödel
Flexible Werkstattsteuerung mit
objektorientierten Softwarestrukturen
FAPS, 180 Seiten, 84 Bilder. 1992.
ISBN 3-446-17242-4.

Band 31: Hubert Reinisch
Planungs- und Steuerungswerkzeuge
zur impliziten Geräteprogrammierung
in Roboterzellen
FAPS, XI u. 212 Seiten, 112 Bilder. 1992.
ISBN 3-446-17380-3.

Band 32: Brigitte Bärnreuther
Ein Beitrag zur Bewertung des Kommunikationsverhaltens von Automatisierungsgeräten in flexiblen Produktionszellen
FAPS, XI u. 179 Seiten, 71 Bilder. 1992.
ISBN 3-446-17451-6.

Band 33: Joachim Hutfless
Laserstrahlregelung und Optikdiagnostik
in der Strahlführung einer
CO_2-Hochleistungslaseranlage
LFT, 175 Seiten, 70 Bilder, 17 Tab. 1993.
ISBN 3-446-17532-6.

Band 34: Uwe Günzel
Entwicklung und Einsatz eines Simulationsverfahrens für operative und
strategische Probleme der
Produktionsplanung und –steuerung
FAPS, XIV u. 170 Seiten, 66 Bilder, 5 Tab.
1993. ISBN 3-446-17604-7.

Band 35: Bertram Ehmann
Operatives Fertigungscontrolling durch
Optimierung auftragsbezogener Bearbeitungsabläufe in der Elektronikfertigung
FAPS, XV u. 167 Seiten, 114 Bilder. 1993.
ISBN 3-446-17658-6.

Band 36: Harald Kolléra
Entwicklung eines benutzerorientierten
Werkstattprogrammiersystems für das
Laserstrahlschneiden
LFT, 129 Seiten, 66 Bilder, 1 Tab. 1993.
ISBN 3-446-17719-1.

Band 37: Stephanie Abels
Modellierung und Optimierung von Montageanlagen in einem integrierten Simulationssystem
FAPS, 188 Seiten, 88 Bilder. 1993.
ISBN 3-446-17731-0.

Band 38: Robert Schmidt-Hebbel
Laserstrahlbohren durchflußbestimmender Durchgangslöcher
LFT, 145 Seiten, 63 Bilder, 11 Tab. 1993.
ISBN 3-446-17778-7.

Band 39: Norbert Lutz
Oberflächenfeinbearbeitung keramischer Werkstoffe mit XeCl-Excimerlaserstrahlung
LFT, 187 Seiten, 98 Bilder, 29 Tab. 1994.
ISBN 3-446-17970-4.

Band 40: Konrad Grampp
Rechnerunterstützung bei Test und Schulung an Steuerungssoftware von SMD-Bestücklinien
FAPS, 178 Seiten, 88 Bilder. 1995.
ISBN 3-446-18173-3.

Band 41: Martin Koch
Wissensbasierte Unterstützung der Angebotsbearbeitung in der Investitionsgüterindustrie
FAPS, 169 Seiten, 68 Bilder. 1995.
ISBN 3-446-18174-1.

Band 42: Armin Gropp
Anlagen- und Prozeßdiagnostik beim Schneiden mit einem gepulsten Nd:YAG-Laser
LFT, 160 Seiten, 88 Bilder, 7 Tab. 1995.
ISBN 3-446-18241-1.

Band 43: Werner Heckel
Optische 3D-Konturerfassung und on-line Biegewinkelmessung mit dem Lichtschnittverfahren
LFT, 149 Seiten, 43 Bilder, 11 Tab. 1995.
ISBN 3-446-18243-8.

Band 44: Armin Rothhaupt
Modulares Planungssystem zur Optimierung der Elektronikfertigung
FAPS, 180 Seiten, 101 Bilder. 1995.
ISBN 3-446-18307-8.

Band 45: Bernd Zöllner
Adaptive Diagnose in der Elektronikproduktion
FAPS, 195 Seiten, 74 Bilder, 3 Tab. 1995.
ISBN 3-446-18308-6.

Band 46: Bodo Vormann
Beitrag zur automatisierten Handhabungsplanung komplexer Blechbiegeteile
LFT, 126 Seiten, 89 Bilder, 3 Tab. 1995.
ISBN 3-446-18345-0.

Band 47: Peter Schnepf
Zielkostenorientierte Montageplanung
FAPS, 144 Seiten, 75 Bilder. 1995.
ISBN 3-446-18397-3.

Band 48: Rainer Klotzbücher
Konzept zur rechnerintegrierten Materialversorgung in flexiblen Fertigungssystemen
FAPS, 156 Seiten, 62 Bilder. 1995.
ISBN 3-446-18412-0.

Band 49: Wolfgang Greska
Wissensbasierte Analyse und Klassifizierung von Blechteilen
LFT, 144 Seiten, 96 Bilder. 1995.
ISBN 3-446-18462-7.

Band 50: Jörg Franke
Integrierte Entwicklung neuer Produkt- und Produktionstechnologien für räumliche spritzgegossene Schaltungsträger (3-D MID)
FAPS, 196 Seiten, 86 Bilder, 4 Tab. 1995.
ISBN 3-446-18448-1.

Band 51: Franz-Josef Zeller
Sensorplanung und schnelle Sensorregelung für Industrieroboter
FAPS, 190 Seiten, 102 Bilder, 9 Tab. 1995.
ISBN 3-446-18601-8.

Band 52: Michael Solvie
Zeitbehandlung und Multimedia-Unterstützung in Feldkommunikationssystemen
FAPS, 200 Seiten, 87 Bilder, 35 Tab. 1996.
ISBN 3-446-18607-7.

Band 53: Robert Hopperdietzel
Reengineering in der Elektro- und Elektronikindustrie
FAPS, 180 Seiten, 109 Bilder, 1 Tab. 1996.
ISBN 3-87525-070-2.

Band 54: Thomas Rebhahn
Beitrag zur Mikromaterialbearbeitung mit Excimerlasern - Systemkomponenten und Verfahrensoptimierungen
LFT, 148 Seiten, 61 Bilder, 10 Tab. 1996.
ISBN 3-87525-075-3.

Band 55: Henning Hanebuth
Laserstrahlhartlöten mit Zweistrahltechnik
LFT, 157 Seiten, 58 Bilder, 11 Tab. 1996.
ISBN 3-87525-074-5.

Band 56: Uwe Schönherr
Steuerung und Sensordatenintegration für flexible Fertigungszellen mit kooperierenden Robotern
FAPS, 188 Seiten, 116 Bilder, 3 Tab. 1996.
ISBN 3-87525-076-1.

Band 57: Stefan Holzer
Berührungslose Formgebung mit Laserstrahlung
LFT, 162 Seiten, 69 Bilder, 11 Tab. 1996.
ISBN 3-87525-079-6.

Band 58: Markus Schultz
Fertigungsqualität beim 3D-Laserstrahlschweißen von Blechformteilen
LFT, 165 Seiten, 88 Bilder, 9 Tab. 1997.
ISBN 3-87525-080-X.

Band 59: Thomas Krebs
Integration elektromechanischer CA-Anwendungen über einem STEP-Produktmodell
FAPS, 198 Seiten, 58 Bilder, 8 Tab. 1997.
ISBN 3-87525-081-8.

Band 60: Jürgen Sturm
Prozeßintegrierte Qualitätssicherung in der Elektronikproduktion
FAPS, 167 Seiten, 112 Bilder, 5 Tab. 1997.
ISBN 3-87525-082-6.

Band 61: Andreas Brand
Prozesse und Systeme zur Bestückung räumlicher elektronischer Baugruppen (3D-MID)
FAPS, 182 Seiten, 100 Bilder. 1997.
ISBN 3-87525-087-7.

Band 62: Michael Kauf
Regelung der Laserstrahlleistung und der Fokusparameter einer CO_2-Hochleistungslaseranlage
LFT, 140 Seiten, 70 Bilder, 5 Tab. 1997.
ISBN 3-87525-083-4.

Band 63: Peter Steinwasser
Modulares Informationsmanagement in der integrierten Produkt- und Prozeßplanung
FAPS, 190 Seiten, 87 Bilder. 1997.
ISBN 3-87525-084-2.

Band 64: Georg Liedl
Integriertes Automatisierungskonzept für den flexiblen Materialfluß in der Elektronikproduktion
FAPS, 196 Seiten, 96 Bilder, 3 Tab. 1997.
ISBN 3-87525-086-9.

Band 65: Andreas Otto
Transiente Prozesse beim Laserstrahlschweißen
LFT, 132 Seiten, 62 Bilder, 1 Tab. 1997.
ISBN 3-87525-089-3.

Band 66: Wolfgang Blöchl
Erweiterte Informationsbereitstellung an offenen CNC-Steuerungen zur Prozeß- und Programmoptimierung
FAPS, 168 Seiten, 96 Bilder. 1997.
ISBN 3-87525-091-5.

Band 67: Klaus-Uwe Wolf
Verbesserte Prozeßführung und Prozeßplanung zur Leistungs- und Qualitätssteigerung beim Spulenwickeln
FAPS, 186 Seiten, 125 Bilder. 1997.
ISBN 3-87525-092-3.

Band 68: Frank Backes
Technologieorientierte Bahnplanung für die 3D-Laserstrahlbearbeitung
LFT, 138 Seiten, 71 Bilder, 2 Tab. 1997.
ISBN 3-87525-093-1.

Band 69: Jürgen Kraus
Laserstrahlumformen von Profilen
LFT, 137 Seiten, 72 Bilder, 8 Tab. 1997.
ISBN 3-87525-094-X.

Band 70: Norbert Neubauer
Adaptive Strahlführungen für CO_2-Laseranlagen
LFT, 120 Seiten, 50 Bilder, 3 Tab. 1997.
ISBN 3-87525-095-8.

Band 71: Michael Steber
Prozeßoptimierter Betrieb flexibler Schraubstationen in der automatisierten Montage
FAPS, 168 Seiten, 78 Bilder, 3 Tab. 1997.
ISBN 3-87525-096-6.

Band 72: Markus Pfestorf
Funktionale 3D-Oberflächenkenngrößen in der Umformtechnik
LFT, 162 Seiten, 84 Bilder, 15 Tab. 1997.
ISBN 3-87525-097-4.

Band 73: Volker Franke
Integrierte Planung und Konstruktion von Werkzeugen für die Biegebearbeitung
LFT, 143 Seiten, 81 Bilder. 1998.
ISBN 3-87525-098-2.

Band 74: Herbert Scheller
Automatisierte Demontagesysteme und recyclinggerechte Produktgestaltung elektronischer Baugruppen
FAPS, 184 Seiten, 104 Bilder, 17 Tab. 1998.
ISBN 3-87525-099-0.

Band 75: Arthur Meßner
Kaltmassivumformung metallischer Kleinstteile - Werkstoffverhalten, Wirkflächenreibung, Prozeßauslegung
LFT, 164 Seiten, 92 Bilder, 14 Tab. 1998.
ISBN 3-87525-100-8.

Band 76: Mathias Glasmacher
Prozeß- und Systemtechnik zum Laserstrahl-Mikroschweißen
LFT, 184 Seiten, 104 Bilder, 12 Tab. 1998.
ISBN 3-87525-101-6.

Band 77: Michael Schwind
Zerstörungsfreie Ermittlung mechanischer Eigenschaften von Feinblechen mit dem Wirbelstromverfahren
LFT, 124 Seiten, 68 Bilder, 8 Tab. 1998.
ISBN 3-87525-102-4.

Band 78: Manfred Gerhard
Qualitätssteigerung in der Elektronikproduktion durch Optimierung der Prozeßführung beim Löten komplexer Baugruppen
FAPS, 179 Seiten, 113 Bilder, 7 Tab. 1998.
ISBN 3-87525-103-2.

Band 79: Elke Rauh
Methodische Einbindung der Simulation in die betrieblichen Planungs- und Entscheidungsabläufe
FAPS, 192 Seiten, 114 Bilder, 4 Tab. 1998.
ISBN 3-87525-104-0.

Band 80: Sorin Niederkorn
Meßeinrichtung zur Untersuchung der Wirkflächenreibung bei umformtechnischen Prozessen
LFT, 99 Seiten, 46 Bilder, 6 Tab. 1998.
ISBN 3-87525-105-9.

Band 81: Stefan Schuberth
Regelung der Fokuslage beim Schweißen mit CO_2-Hochleistungslasern unter Einsatz von adaptiven Optiken
LFT, 140 Seiten, 64 Bilder, 3 Tab. 1998.
ISBN 3-87525-106-7.

Band 82: Armando Walter Colombo
Development and Implementation of Hierarchical Control Structures of Flexible Production Systems Using High Level Petri Nets
FAPS, 216 Seiten, 86 Bilder. 1998.
ISBN 3-87525-109-1.

Band 83: Otto Meedt
Effizienzsteigerung bei Demontage und Recycling durch flexible Demontagetechnologien und optimierte Produktgestaltung
FAPS, 186 Seiten, 103 Bilder. 1998.
ISBN 3-87525-108-3.

Band 84: Knuth Götz
Modelle und effiziente Modellbildung zur Qualitätssicherung in der Elektronikproduktion
FAPS, 212 Seiten, 129 Bilder, 24 Tab. 1998.
ISBN 3-87525-112-1.

Band 85: Ralf Luchs
Einsatzmöglichkeiten leitender Klebstoffe zur zuverlässigen Kontaktierung elektronischer Bauelemente in der SMT
FAPS, 176 Seiten, 126 Bilder, 30 Tab. 1998.
ISBN 3-87525-113-7.

Band 86: Frank Pöhlau
Entscheidungsgrundlagen zur Einführung räumlicher spritzgegossener Schaltungsträger (3-D MID)
FAPS, 144 Seiten, 99 Bilder. 1999.
ISBN 3-87525-114-8.

Band 87: Roland T. A. Kals
Fundamentals on the miniaturization of sheet metal working processes
LFT, 128 Seiten, 58 Bilder, 11 Tab. 1999.
ISBN 3-87525-115-6.

Band 88: Gerhard Luhn
Implizites Wissen und technisches Handeln am Beispiel der Elektronikproduktion
FAPS, 252 Seiten, 61 Bilder, 1 Tab. 1999.
ISBN 3-87525-116-4.

Band 89: Axel Sprenger
Adaptives Streckbiegen von Aluminium-Strangpreßprofilen
LFT, 114 Seiten, 63 Bilder, 4 Tab. 1999.
ISBN 3-87525-117-2.

Band 90: Hans-Jörg Pucher
Untersuchungen zur Prozeßfolge Umformen, Bestücken und Laserstrahllöten von Mikrokontakten
LFT, 158 Seiten, 69 Bilder, 9 Tab. 1999.
ISBN 3-87525-119-9.

Band 91: Horst Arnet
Profilbiegen mit kinematischer Gestalterzeugung
LFT, 128 Seiten, 67 Bilder, 7 Tab. 1999.
ISBN 3-87525-120-2.

Band 92: Doris Schubart
Prozeßmodellierung und Technologieentwicklung beim Abtragen mit CO_2-Laserstrahlung
LFT, 133 Seiten, 57 Bilder, 13 Tab. 1999.
ISBN 3-87525-122-9.

Band 93: Adrianus L. P. Coremans
Laserstrahlsintern von Metallpulver - Prozeßmodellierung, Systemtechnik, Eigenschaften laserstrahlgesinterter Metallkörper
LFT, 184 Seiten, 108 Bilder, 12 Tab. 1999.
ISBN 3-87525-124-5.

Band 94: Hans-Martin Biehler
Optimierungskonzepte für Qualitätsdatenverarbeitung und Informationsbereitstellung in der Elektronikfertigung
FAPS, 194 Seiten, 105 Bilder. 1999.
ISBN 3-87525-126-1.

Band 95: Wolfgang Becker
Oberflächenausbildung und tribologische Eigenschaften excimerlaserstrahlbearbeiteter Hochleistungskeramiken
LFT, 175 Seiten, 71 Bilder, 3 Tab. 1999.
ISBN 3-87525-127-X.

Band 96: Philipp Hein
Innenhochdruck-Umformen von Blechpaaren: Modellierung, Prozeßauslegung und Prozeßführung
LFT, 129 Seiten, 57 Bilder, 7 Tab. 1999.
ISBN 3-87525-128-8.

Band 97: Gunter Beitinger
Herstellungs- und Prüfverfahren für thermoplastische Schaltungsträger
FAPS, 169 Seiten, 92 Bilder, 20 Tab. 1999.
ISBN 3-87525-129-6.

Band 98: Jürgen Knoblach
Beitrag zur rechnerunterstützten verursachungsgerechten Angebotskalkulation von Blechteilen mit Hilfe wissensbasierter Methoden
LFT, 155 Seiten, 53 Bilder, 26 Tab. 1999.
ISBN 3-87525-130-X.

Band 99: Frank Breitenbach
Bildverarbeitungssystem zur Erfassung der Anschlußgeometrie elektronischer SMT-Bauelemente
LFT, 147 Seiten, 92 Bilder, 12 Tab. 2000.
ISBN 3-87525-131-8.

Band 100: Bernd Falk
Simulationsbasierte Lebensdauervorhersage für Werkzeuge der Kaltmassivumformung
LFT, 134 Seiten, 44 Bilder, 15 Tab. 2000.
ISBN 3-87525-136-9.

Band 101: Wolfgang Schlögl
Integriertes Simulationsdaten-Management für Maschinenentwicklung und Anlagenplanung
FAPS, 169 Seiten, 101 Bilder, 20 Tab. 2000.
ISBN 3-87525-137-7.

Band 102: Christian Hinsel
Ermüdungsbruchversagen hartstoffbeschichteter Werkzeugstähle in der Kaltmassivumformung
LFT, 130 Seiten, 80 Bilder, 14 Tab. 2000.
ISBN 3-87525-138-5.

Band 103: Stefan Bobbert
Simulationsgestützte Prozessauslegung für das Innenhochdruck-Umformen von Blechpaaren
LFT, 123 Seiten, 77 Bilder. 2000.
ISBN 3-87525-145-8.

Band 104: Harald Rottbauer
Modulares Planungswerkzeug zum Produktionsmanagement in der Elektronikproduktion
FAPS, 166 Seiten, 106 Bilder. 2001.
ISBN 3-87525-139-3.

Band 105: Thomas Hennige
Flexible Formgebung von Blechen durch Laserstrahlumformen
LFT, 119 Seiten, 50 Bilder. 2001.
ISBN 3-87525-140-7.

Band 106: Thomas Menzel
Wissensbasierte Methoden für die rechnergestützte Charakterisierung und Bewertung innovativer Fertigungsprozesse
LFT, 152 Seiten, 71 Bilder. 2001.
ISBN 3-87525-142-3.

Band 107: Thomas Stöckel
Kommunikationstechnische Integration der Prozeßebene in Produktionssysteme durch Middleware-Frameworks
FAPS, 147 Seiten, 65 Bilder, 5 Tab. 2001.
ISBN 3-87525-143-1.

Band 108: Frank Pitter
Verfügbarkeitssteigerung von Werkzeugmaschinen durch Einsatz mechatronischer Sensorlösungen
FAPS, 158 Seiten, 131 Bilder, 8 Tab. 2001.
ISBN 3-87525-144-X.

Band 109: Markus Korneli
Integration lokaler CAP-Systeme in einen globalen Fertigungsdatenverbund
FAPS, 121 Seiten, 53 Bilder, 11 Tab. 2001.
ISBN 3-87525-146-6.

Band 110: Burkhard Müller
Laserstrahljustieren mit Excimer-Lasern - Prozeßparameter und Modelle zur Aktorkonstruktion
LFT, 128 Seiten, 36 Bilder, 9 Tab. 2001.
ISBN 3-87525-159-8.

Band 111: Jürgen Göhringer
Integrierte Telediagnose via Internet zum effizienten Service von Produktionssystemen
FAPS, 178 Seiten, 98 Bilder, 5 Tab. 2001.
ISBN 3-87525-147-4.

Band 112: Robert Feuerstein
Qualitäts- und kosteneffiziente Integration neuer Bauelementetechnologien in die Flachbaugruppenfertigung
FAPS, 161 Seiten, 99 Bilder, 10 Tab. 2001.
ISBN 3-87525-151-2.

Band 113: Marcus Reichenberger
Eigenschaften und Einsatzmöglichkeiten alternativer Elektroniklote in der Oberflächenmontage (SMT)
FAPS, 165 Seiten, 97 Bilder, 18 Tab. 2001.
ISBN 3-87525-152-0.

Band 114: Alexander Huber
Justieren vormontierter Systeme mit dem Nd:YAG-Laser unter Einsatz von Aktoren
LFT, 122 Seiten, 58 Bilder, 5 Tab. 2001.
ISBN 3-87525-153-9.

Band 115: Sami Krimi
Analyse und Optimierung von Montagesystemen in der Elektronikproduktion
FAPS, 155 Seiten, 88 Bilder, 3 Tab. 2001.
ISBN 3-87525-157-1.

Band 116: Marion Merklein
Laserstrahlumformen von Aluminiumwerkstoffen - Beeinflussung der Mikrostruktur und der mechanischen Eigenschaften
LFT, 122 Seiten, 65 Bilder, 15 Tab. 2001.
ISBN 3-87525-156-3.

Band 117: Thomas Collisi
Ein informationslogistisches Architekturkonzept zur Akquisition simulationsrelevanter Daten
FAPS, 181 Seiten, 105 Bilder, 7 Tab. 2002.
ISBN 3-87525-164-4.

Band 118: Markus Koch
Rationalisierung und ergonomische Optimierung im Innenausbau durch den Einsatz moderner Automatisierungstechnik
FAPS, 176 Seiten, 98 Bilder, 9 Tab. 2002.
ISBN 3-87525-165-2.

Band 119: Michael Schmidt
Prozeßregelung für das Laserstrahl-Punktschweißen in der Elektronikproduktion
LFT, 152 Seiten, 71 Bilder, 3 Tab. 2002.
ISBN 3-87525-166-0.

Band 120: Nicolas Tiesler
Grundlegende Untersuchungen zum Fließpressen metallischer Kleinstteile
LFT, 126 Seiten, 78 Bilder, 12 Tab. 2002.
ISBN 3-87525-175-X.

Band 121: Lars Pursche
Methoden zur technologieorientierten Programmierung für die 3D-Lasermikrobearbeitung
LFT, 111 Seiten, 39 Bilder, 0 Tab. 2002.
ISBN 3-87525-183-0.

Band 122: Jan-Oliver Brassel
Prozeßkontrolle beim Laserstrahl-Mikroschweißen
LFT, 148 Seiten, 72 Bilder, 12 Tab. 2002.
ISBN 3-87525-181-4.

Band 123: Mark Geisel
Prozeßkontrolle und -steuerung beim Laserstrahlschweißen mit den Methoden der nichtlinearen Dynamik
LFT, 135 Seiten, 46 Bilder, 2 Tab. 2002.
ISBN 3-87525-180-6.

Band 124: Gerd Eßer
Laserstrahlunterstützte Erzeugung metallischer Leiterstrukturen auf Thermoplastsubstraten für die MID-Technik
LFT, 148 Seiten, 60 Bilder, 6 Tab. 2002.
ISBN 3-87525-171-7.

Band 125: Marc Fleckenstein
Qualität laserstrahl-gefügter Mikroverbindungen elektronischer Kontakte
LFT, 159 Seiten, 77 Bilder, 7 Tab. 2002.
ISBN 3-87525-170-9.

Band 126: Stefan Kaufmann
Grundlegende Untersuchungen zum Nd:YAG- Laserstrahlfügen von Silizium für Komponenten der Optoelektronik
LFT, 159 Seiten, 100 Bilder, 6 Tab. 2002.
ISBN 3-87525-172-5.

Band 127: Thomas Fröhlich
Simultanes Löten von Anschlußkontakten elektronischer Bauelemente mit Diodenlaserstrahlung
LFT, 143 Seiten, 75 Bilder, 6 Tab. 2002.
ISBN 3-87525-186-5.

Band 128: Achim Hofmann
Erweiterung der Formgebungsgrenzen beim Umformen von Aluminiumwerkstoffen durch den Einsatz prozessangepasster Platinen
LFT, 113 Seiten, 58 Bilder, 4 Tab. 2002.
ISBN 3-87525-182-2.

Band 129: Ingo Kriebitzsch
3 - D MID Technologie in der Automobilelektronik
FAPS, 129 Seiten, 102 Bilder, 10 Tab. 2002.
ISBN 3-87525-169-5.

Band 130: Thomas Pohl
Fertigungsqualität und Umformbarkeit laserstrahlgeschweißter Formplatinen aus Aluminiumlegierungen
LFT, 133 Seiten, 93 Bilder, 12 Tab. 2002.
ISBN 3-87525-173-3.

Band 131: Matthias Wenk
Entwicklung eines konfigurierbaren Steuerungssystems für die flexible Sensorführung von Industrierobotern
FAPS, 167 Seiten, 85 Bilder, 1 Tab. 2002.
ISBN 3-87525-174-1.

Band 132: Matthias Negendanck
Neue Sensorik und Aktorik für Bearbeitungsköpfe zum Laserstrahlschweißen
LFT, 116 Seiten, 60 Bilder, 14 Tab. 2002.
ISBN 3-87525-184-9.

Band 133: Oliver Kreis
Integrierte Fertigung - Verfahrensintegration durch Innenhochdruck-Umformen, Trennen und Laserstrahlschweißen in einem Werkzeug sowie ihre tele- und multimediale Präsentation
LFT, 167 Seiten, 90 Bilder, 43 Tab. 2002.
ISBN 3-87525-176-8.

Band 134: Stefan Trautner
Technische Umsetzung produktbezogener Instrumente der Umweltpolitik bei Elektro- und Elektronikgeräten
FAPS, 179 Seiten, 92 Bilder, 11 Tab. 2002.
ISBN 3-87525-177-6.

Band 135: Roland Meier
Strategien für einen produktorientierten Einsatz räumlicher spritzgegossener Schaltungsträger (3-D MID)
FAPS, 155 Seiten, 88 Bilder, 14 Tab. 2002.
ISBN 3-87525-178-4.

Band 136: Jürgen Wunderlich
Kostensimulation - Simulationsbasierte Wirtschaftlichkeitsregelung komplexer Produktionssysteme
FAPS, 202 Seiten, 119 Bilder, 17 Tab. 2002.
ISBN 3-87525-179-2.

Band 137: Stefan Novotny
Innenhochdruck-Umformen von Blechen aus Aluminium- und Magnesiumlegierungen bei erhöhter Temperatur
LFT, 132 Seiten, 82 Bilder, 6 Tab. 2002.
ISBN 3-87525-185-7.

Band 138: Andreas Licha
Flexible Montageautomatisierung zur Komplettmontage flächenhafter Produktstrukturen durch kooperierende Industrieroboter
FAPS, 158 Seiten, 87 Bilder, 8 Tab. 2003.
ISBN 3-87525-189-X.

Band 139: Michael Eisenbarth
Beitrag zur Optimierung der Aufbau- und Verbindungstechnik für mechatronische Baugruppen
FAPS, 207 Seiten, 141 Bilder, 9 Tab. 2003.
ISBN 3-87525-190-3.

Band 140: Frank Christoph
Durchgängige simulationsgestützte Planung von Fertigungseinrichtungen der Elektronikproduktion
FAPS, 187 Seiten, 107 Bilder, 9 Tab. 2003.
ISBN 3-87525-191-1.

Band 141: Hinnerk Hagenah
Simulationsbasierte Bestimmung der zu erwartenden Maßhaltigkeit für das Blechbiegen
LFT, 131 Seiten, 36 Bilder, 26 Tab. 2003.
ISBN 3-87525-192-X.

Band 142: Ralf Eckstein
Scherschneiden und Biegen metallischer Kleinstteile - Materialeinfluss und Materialverhalten
LFT, 148 Seiten, 71 Bilder, 19 Tab. 2003.
ISBN 3-87525-193-8.

Band 143: Frank H. Meyer-Pittroff
Excimerlaserstrahlbiegen dünner metallischer Folien mit homogener Lichtlinie
LFT, 138 Seiten, 60 Bilder, 16 Tab. 2003.
ISBN 3-87525-196-2.

Band 144: Andreas Kach
Rechnergestützte Anpassung von Laserstrahlschneidbahnen an Bauteilabweichungen
LFT, 139 Seiten, 69 Bilder, 11 Tab. 2004.
ISBN 3-87525-197-0.

Band 145: Stefan Hierl
System- und Prozeßtechnik für das simultane Löten mit Diodenlaserstrahlung von elektronischen Bauelementen
LFT, 124 Seiten, 66 Bilder, 4 Tab. 2004.
ISBN 3-87525-198-9.

Band 146: Thomas Neudecker
Tribologische Eigenschaften keramischer Blechumformwerkzeuge- Einfluss einer Oberflächenendbearbeitung mittels Excimerlaserstrahlung
LFT, 166 Seiten, 75 Bilder, 26 Tab. 2004.
ISBN 3-87525-200-4.

Band 147: Ulrich Wenger
Prozessoptimierung in der Wickeltechnik durch innovative maschinenbauliche und regelungstechnische Ansätze
FAPS, 132 Seiten, 88 Bilder, 0 Tab. 2004.
ISBN 3-87525-203-9.

Band 148: Stefan Slama
Effizienzsteigerung in der Montage durch marktorientierte Montagestrukturen und erweiterte Mitarbeiterkompetenz
FAPS, 188 Seiten, 125 Bilder, 0 Tab. 2004.
ISBN 3-87525-204-7.

Band 149: Thomas Wurm
Laserstrahljustieren mittels Aktoren-Entwicklung von Konzepten und Methoden für die rechnerunterstützte Modellierung und Optimierung von komplexen Aktorsystemen in der Mikrotechnik
LFT, 122 Seiten, 51 Bilder, 9 Tab. 2004.
ISBN 3-87525-206-3.

Band 150: Martino Celeghini
Wirkmedienbasierte Blechumformung: Grundlagenuntersuchungen zum Einfluss von Werkstoff und Bauteilgeometrie
LFT, 146 Seiten, 77 Bilder, 6 Tab. 2004.
ISBN 3-87525-207-1.

Band 151: Ralph Hohenstein
Entwurf hochdynamischer Sensor- und Regelsysteme für die adaptive Laserbearbeitung
LFT, 282 Seiten, 63 Bilder, 16 Tab. 2004.
ISBN 3-87525-210-1.

Band 152: Angelika Hutterer
Entwicklung prozessüberwachender Regelkreise für flexible Formgebungsprozesse
LFT, 149 Seiten, 57 Bilder, 2 Tab. 2005.
ISBN 3-87525-212-8.

Band 153: Emil Egerer
Massivumformen metallischer Kleinstteile bei erhöhter Prozesstemperatur
LFT, 158 Seiten, 87 Bilder, 10 Tab. 2005.
ISBN 3-87525-213-6.

Band 154: Rüdiger Holzmann
Strategien zur nachhaltigen Optimierung von Qualität und Zuverlässigkeit in der Fertigung hochintegrierter Flachbaugruppen
FAPS, 186 Seiten, 99 Bilder, 19 Tab. 2005.
ISBN 3-87525-217-9.

Band 155: Marco Nock
Biegeumformen mit Elastomerwerkzeugen Modellierung, Prozessauslegung und Abgrenzung des Verfahrens am Beispiel des Rohrbiegens
LFT, 164 Seiten, 85 Bilder, 13 Tab. 2005.
ISBN 3-87525-218-7.

Band 156: Frank Niebling
Qualifizierung einer Prozesskette zum Laserstrahlsintern metallischer Bauteile
LFT, 148 Seiten, 89 Bilder, 3 Tab. 2005.
ISBN 3-87525-219-5.

Band 157: Markus Meiler
Großserientauglichkeit trockenschmierstoffbeschichteter Aluminiumbleche im Presswerk Grundlegende Untersuchungen zur Tribologie, zum Umformverhalten und Bauteilversuche
LFT, 104 Seiten, 57 Bilder, 21 Tab. 2005.
ISBN 3-87525-221-7.

Band 158: Agus Sutanto
Solution Approaches for Planning of Assembly Systems in Three-Dimensional Virtual Environments
FAPS, 169 Seiten, 98 Bilder, 3 Tab. 2005.
ISBN 3-87525-220-9.

Band 159: Matthias Boiger
Hochleistungssysteme für die Fertigung elektronischer Baugruppen auf der Basis flexibler Schaltungsträger
FAPS, 175 Seiten, 111 Bilder, 8 Tab. 2005.
ISBN 3-87525-222-5.

Band 160: Matthias Pitz
Laserunterstütztes Biegen höchstfester Mehrphasenstähle
LFT, 120 Seiten, 73 Bilder, 11 Tab. 2005.
ISBN 3-87525-223-3.

Band 161: Meik Vahl
Beitrag zur gezielten Beeinflussung des Werkstoffflusses beim Innenhochdruck-Umformen von Blechen
LFT, 165 Seiten, 94 Bilder, 15 Tab. 2005.
ISBN 3-87525-224-1.

Band 162: Peter K. Kraus
Plattformstrategien - Realisierung einer varianz- und kostenoptimierten Wertschöpfung
FAPS, 181 Seiten, 95 Bilder, 0 Tab. 2005.
ISBN 3-87525-226-8.

Band 163: Adrienn Cser
Laserstrahlschmelzabtrag - Prozessanalyse und -modellierung
LFT, 146 Seiten, 79 Bilder, 3 Tab. 2005.
ISBN 3-87525-227-6.

Band 164: Markus C. Hahn
Grundlegende Untersuchungen zur Herstellung von Leichtbauverbundstrukturen mit Aluminiumschaumkern
LFT, 143 Seiten, 60 Bilder, 16 Tab. 2005.
ISBN 3-87525-228-4.

Band 165: Gordana Michos
Mechatronische Ansätze zur Optimierung von Vorschubachsen
FAPS, 146 Seiten, 87 Bilder, 17 Tab. 2005.
ISBN 3-87525-230-6.

Band 166: Markus Stark
Auslegung und Fertigung hochpräziser Faser-Kollimator-Arrays
LFT, 158 Seiten, 115 Bilder, 11 Tab. 2005.
ISBN 3-87525-231-4.

Band 167: Yurong Zhou
Kollaboratives Engineering Management in der integrierten virtuellen Entwicklung der Anlagen für die Elektronikproduktion
FAPS, 156 Seiten, 84 Bilder, 6 Tab. 2005.
ISBN 3-87525-232-2.

Band 168: Werner Enser
Neue Formen permanenter und lösbarer elektrischer Kontaktierungen für mechatronische Baugruppen
FAPS, 190 Seiten, 112 Bilder, 5 Tab. 2005.
ISBN 3-87525-233-0.

Band 169: Katrin Melzer
Integrierte Produktpolitik bei elektrischen und elektronischen Geräten zur Optimierung des Product-Life-Cycle
FAPS, 155 Seiten, 91 Bilder, 17 Tab. 2005.
ISBN 3-87525-234-9.

Band 170: Alexander Putz
Grundlegende Untersuchungen zur Erfassung der realen Vorspannung von armierten Kaltfließpresswerkzeugen mittels Ultraschall
LFT, 137 Seiten, 71 Bilder, 15 Tab. 2006.
ISBN 3-87525-237-3.

Band 171: Martin Prechtl
Automatisiertes Schichtverfahren für metallische Folien - System- und Prozesstechnik
LFT, 154 Seiten, 45 Bilder, 7 Tab. 2006.
ISBN 3-87525-238-1.

Band 172: Markus Meidert
Beitrag zur deterministischen Lebensdauerabschätzung von Werkzeugen der Kaltmassivumformung
LFT, 131 Seiten, 78 Bilder, 9 Tab. 2006.
ISBN 3-87525-239-X.

Band 173: Bernd Müller
Robuste, automatisierte Montagesysteme durch adaptive Prozessführung und montageübergreifende Fehlerprävention am Beispiel flächiger Leichtbauteile
FAPS, 147 Seiten, 77 Bilder, 0 Tab. 2006.
ISBN 3-87525-240-3.

Band 174: Alexander Hofmann
Hybrides Laserdurchstrahlschweißen von Kunststoffen
LFT, 136 Seiten, 72 Bilder, 4 Tab. 2006.
ISBN 978-3-87525-243-9.

Band 175: Peter Wölflick
Innovative Substrate und Prozesse mit feinsten Strukturen für bleifreie Mechatronik-Anwendungen
FAPS, 177 Seiten, 148 Bilder, 24 Tab. 2006.
ISBN 978-3-87525-246-0.

Band 176: Attila Komlodi
Detection and Prevention of Hot Cracks during Laser Welding of Aluminium Alloys Using Advanced Simulation Methods
LFT, 155 Seiten, 89 Bilder, 14 Tab. 2006.
ISBN 978-3-87525-248-4.

Band 177: Uwe Popp
Grundlegende Untersuchungen zum Laserstrahlstrukturieren von Kaltmassivumformwerkzeugen
LFT, 140 Seiten, 67 Bilder, 16 Tab. 2006.
ISBN 978-3-87525-249-1.

Band 178: Veit Rückel
Rechnergestützte Ablaufplanung und Bahngenerierung Für kooperierende Industrieroboter
FAPS, 148 Seiten, 75 Bilder, 7 Tab. 2006.
ISBN 978-3-87525-250-7.

Band 179: Manfred Dirscherl
Nicht-thermische Mikrojustiertechnik mittels ultrakurzer Laserpulse
LFT, 154 Seiten, 69 Bilder, 10 Tab. 2007.
ISBN 978-3-87525-251-4.

Band 180: Yong Zhuo
Entwurf eines rechnergestützten integrierten Systems für Konstruktion und Fertigungsplanung räumlicher spritzgegossener Schaltungsträger (3D-MID)
FAPS, 181 Seiten, 95 Bilder, 5 Tab. 2007.
ISBN 978-3-87525-253-8.

Band 181: Stefan Lang
Durchgängige Mitarbeiterinformation zur Steigerung von Effizienz und Prozesssicherheit in der Produktion
FAPS, 172 Seiten, 93 Bilder. 2007.
ISBN 978-3-87525-257-6.

Band 182: Hans-Joachim Krauß
Laserstrahlinduzierte Pyrolyse präkeramischer Polymere
LFT, 171 Seiten, 100 Bilder. 2007.
ISBN 978-3-87525-258-3.

Band 183: Stefan Junker
Technologien und Systemlösungen für die flexibel automatisierte Bestückung permanent erregter Läufer mit oberflächenmontierten Dauermagneten
FAPS, 173 Seiten, 75 Bilder. 2007.
ISBN 978-3-87525-259-0.

Band 184: Rainer Kohlbauer
Wissensbasierte Methoden für die simulationsgestützte Auslegung wirkmedienbasierter Blechumformprozesse
LFT, 135 Seiten, 50 Bilder. 2007.
ISBN 978-3-87525-260-6.

Band 185: Klaus Lamprecht
Wirkmedienbasierte Umformung tiefgezogener Vorformen unter besonderer Berücksichtigung maßgeschneiderter Halbzeuge
LFT, 137 Seiten, 81 Bilder. 2007.
ISBN 978-3-87525-265-1.

Band 186: Bernd Zolleiß
Optimierte Prozesse und Systeme für die Bestückung mechatronischer Baugruppen
FAPS, 180 Seiten, 117 Bilder. 2007.
ISBN 978-3-87525-266-8.

Band 187: Michael Kerausch
Simulationsgestützte Prozessauslegung für das Umformen lokal wärmebehandelter Aluminiumplatinen
LFT, 146 Seiten, 76 Bilder, 7 Tab. 2007.
ISBN 978-3-87525-267-5.

Band 188: Matthias Weber
Unterstützung der Wandlungsfähigkeit von Produktionsanlagen durch innovative Softwaresysteme
FAPS, 183 Seiten, 122 Bilder, 3 Tab. 2007.
ISBN 978-3-87525-269-9.

Band 189: Thomas Frick
Untersuchung der prozessbestimmenden Strahl-Stoff-Wechselwirkungen beim Laserstrahlschweißen von Kunststoffen
LFT, 104 Seiten, 62 Bilder, 8 Tab. 2007.
ISBN 978-3-87525-268-2.

Band 190: Joachim Hecht
Werkstoffcharakterisierung und Prozessauslegung für die wirkmedienbasierte Doppelblech-Umformung von Magnesiumlegierungen
LFT, 107 Seiten, 91 Bilder, 2 Tab. 2007.
ISBN 978-3-87525-270-5.

Band 191: Ralf Völkl
Stochastische Simulation zur Werkzeuglebensdaueroptimierung und Präzisionsfertigung in der Kaltmassivumformung
LFT, 178 Seiten, 75 Bilder, 12 Tab. 2008.
ISBN 978-3-87525-272-9.

Band 192: Massimo Tolazzi
Innenhochdruck-Umformen verstärkter Blech-Rahmenstrukturen
LFT, 164 Seiten, 85 Bilder, 7 Tab. 2008.
ISBN 978-3-87525-273-6.

Band 193: Cornelia Hoff
Untersuchung der Prozesseinflussgrößen beim Presshärten des höchstfesten Vergütungsstahls 22MnB5
LFT, 133 Seiten, 92 Bilder, 5 Tab. 2008.
ISBN 978-3-87525-275-0.

Band 194: Christian Alvarez
Simulationsgestützte Methoden zur effizienten Gestaltung von Lötprozessen in der Elektronikproduktion
FAPS, 149 Seiten, 86 Bilder, 8 Tab. 2008.
ISBN 978-3-87525-277-4.

Band 195: Andreas Kunze
Automatisierte Montage von makromechatronischen Modulen zur flexiblen Integration in hybride Pkw-Bordnetzsysteme
FAPS, 160 Seiten, 90 Bilder, 14 Tab. 2008.
ISBN 978-3-87525-278-1.

Band 196: Wolfgang Hußnätter
Grundlegende Untersuchungen zur experimentellen Ermittlung und zur Modellierung von Fließortkurven bei erhöhten Temperaturen
LFT, 152 Seiten, 73 Bilder, 21 Tab. 2008.
ISBN 978-3-87525-279-8.

Band 197: Thomas Bigl
Entwicklung, angepasste Herstellungsverfahren und erweiterte Qualitätssicherung von einsatzgerechten elektronischen Baugruppen
FAPS, 175 Seiten, 107 Bilder, 14 Tab. 2008.
ISBN 978-3-87525-280-4.

Band 198: Stephan Roth
Grundlegende Untersuchungen zum Excimerlaserstrahl-Abtragen unter Flüssigkeitsfilmen
LFT, 113 Seiten, 47 Bilder, 14 Tab. 2008.
ISBN 978-3-87525-281-1.

Band 199: Artur Giera
Prozesstechnische Untersuchungen zum Rührreibschweißen metallischer Werkstoffe
LFT, 179 Seiten, 104 Bilder, 36 Tab. 2008.
ISBN 978-3-87525-282-8.

Band 200: Jürgen Lechler
Beschreibung und Modellierung des Werkstoffverhaltens von presshärtbaren Bor-Manganstählen
LFT, 154 Seiten, 75 Bilder, 12 Tab. 2009.
ISBN 978-3-87525-286-6.

Band 201: Andreas Blankl
Untersuchungen zur Erhöhung der Prozessrobustheit bei der Innenhochdruck-Umformung von flächigen Halbzeugen mit vor- bzw. nachgeschalteten Laserstrahlfügeoperationen
LFT, 120 Seiten, 68 Bilder, 9 Tab. 2009.
ISBN 978-3-87525-287-3.

Band 202: Andreas Schaller
Modellierung eines nachfrageorientierten Produktionskonzeptes für mobile Telekommunikationsgeräte
FAPS, 120 Seiten, 79 Bilder, 0 Tab. 2009.
ISBN 978-3-87525-289-7.

Band 203: Claudius Schimpf
Optimierung von Zuverlässigkeitsuntersuchungen, Prüfabläufen und Nacharbeitsprozessen in der Elektronikproduktion
FAPS, 162 Seiten, 90 Bilder, 14 Tab. 2009.
ISBN 978-3-87525-290-3.

Band 204: Simon Dietrich
Sensoriken zur Schwerpunktslagebestimmung der optischen Prozessemissionen beim Laserstrahltiefschweißen
LFT, 138 Seiten, 70 Bilder, 5 Tab. 2009.
ISBN 978-3-87525-292-7.

Band 205: Wolfgang Wolf
Entwicklung eines agentenbasierten Steuerungssystems zur Materialflussorganisation im wandelbaren Produktionsumfeld
FAPS, 167 Seiten, 98 Bilder. 2009.
ISBN 978-3-87525-293-4.

Band 206: Steffen Polster
Laserdurchstrahlschweißen transparenter Polymerbauteile
LFT, 160 Seiten, 92 Bilder, 13 Tab. 2009.
ISBN 978-3-87525-294-1.

Band 207: Stephan Manuel Dörfler
Rührreibschweißen von walzplattiertem Halbzeug und Aluminiumblech zur Herstellung flächiger Aluminiumschaum-Sandwich-Verbundstrukturen
LFT, 190 Seiten, 98 Bilder, 5 Tab. 2009.
ISBN 978-3-87525-295-8.

Band 208: Uwe Vogt
Seriennahe Auslegung von Aluminium Tailored Heat Treated Blanks
LFT, 151 Seiten, 68 Bilder, 26 Tab. 2009.
ISBN 978-3-87525-296-5.

Band 209: Till Laumann
Qualitative und quantitative Bewertung der Crashtauglichkeit von höchstfesten Stählen
LFT, 117 Seiten, 69 Bilder, 7 Tab. 2009.
ISBN 978-3-87525-299-6.

Band 210: Alexander Diehl
Größeneffekte bei Biegeprozessen- Entwicklung einer Methodik zur Identifikation und Quantifizierung
LFT, 180 Seiten, 92 Bilder, 12 Tab. 2010.
ISBN 978-3-87525-302-3.

Band 211: Detlev Staud
Effiziente Prozesskettenauslegung für das Umformen lokal wärmebehandelter und geschweißter Aluminiumbleche
LFT, 164 Seiten, 72 Bilder, 12 Tab. 2010.
ISBN 978-3-87525-303-0.

Band 212: Jens Ackermann
Prozesssicherung beim Laserdurchstrahlschweißen thermoplastischer Kunststoffe
LPT, 129 Seiten, 74 Bilder, 13 Tab. 2010.
ISBN 978-3-87525-305-4.

Band 213: Stephan Weidel
Grundlegende Untersuchungen zum Kontaktzustand zwischen Werkstück und Werkzeug bei umformtechnischen Prozessen unter tribologischen Gesichtspunkten
LFT, 144 Seiten, 67 Bilder, 11 Tab. 2010.
ISBN 978-3-87525-307-8.

Band 214: Stefan Geißdörfer
Entwicklung eines mesoskopischen Modells zur Abbildung von Größeneffekten in der Kaltmassivumformung mit Methoden der FE-Simulation
LFT, 133 Seiten, 83 Bilder, 11 Tab. 2010.
ISBN 978-3-87525-308-5.

Band 215: Christian Matzner
Konzeption produktspezifischer Lösungen zur Robustheitssteigerung elektronischer Systeme gegen die Einwirkung von Betauung im Automobil
FAPS, 165 Seiten, 93 Bilder, 14 Tab. 2010.
ISBN 978-3-87525-309-2.

Band 216: Florian Schüßler
Verbindungs- und Systemtechnik für thermisch hochbeanspruchte und miniaturisierte elektronische Baugruppen
FAPS, 184 Seiten, 93 Bilder, 18 Tab. 2010.
ISBN 978-3-87525-310-8.

Band 217: Massimo Cojutti
Strategien zur Erweiterung der Prozessgrenzen bei der Innhochdruck-Umformung von Rohren und Blechpaaren
LFT, 125 Seiten, 56 Bilder, 9 Tab. 2010.
ISBN 978-3-87525-312-2.

Band 218: Raoul Plettke
Mehrkriterielle Optimierung komplexer Aktorsysteme für das Laserstrahljustieren
LFT, 152 Seiten, 25 Bilder, 3 Tab. 2010.
ISBN 978-3-87525-315-3.

Band 219: Andreas Dobroschke
Flexible Automatisierungslösungen für die Fertigung wickeltechnischer Produkte
FAPS, 184 Seiten, 109 Bilder, 18 Tab. 2011.
ISBN 978-3-87525-317-7.

Band 220: Azhar Zam
Optical Tissue Differentiation for Sensor-Controlled Tissue-Specific Laser Surgery
LPT, 99 Seiten, 45 Bilder, 8 Tab. 2011.
ISBN 978-3-87525-318-4.

Band 221: Michael Rösch
Potenziale und Strategien zur Optimierung des Schablonendruckprozesses in der Elektronikproduktion
FAPS, 192 Seiten, 127 Bilder, 19 Tab. 2011.
ISBN 978-3-87525-319-1.

Band 222: Thomas Rechtenwald
Quasi-isothermes Laserstrahlsintern von Hochtemperatur-Thermoplasten - Eine Betrachtung werkstoff-prozessspezifischer Aspekte am Beispiel PEEK
LPT, 150 Seiten, 62 Bilder, 8 Tab. 2011.
ISBN 978-3-87525-320-7.

Band 223: Daniel Craiovan
Prozesse und Systemlösungen für die SMT-Montage optischer Bauelemente auf Substrate mit integrierten Lichtwellenleitern
FAPS, 165 Seiten, 85 Bilder, 8 Tab. 2011.
ISBN 978-3-87525-324-5.

Band 224: Kay Wagner
Beanspruchungsangepasste Kaltmassivumformwerkzeuge durch lokal optimierte Werkzeugoberflächen
LFT, 147 Seiten, 103 Bilder, 17 Tab. 2011.
ISBN 978-3-87525-325-2.

Band 225: Martin Brandhuber
Verbesserung der Prognosegüte des Versagens von Punktschweißverbindungen bei höchstfesten Stahlgüten
LFT, 155 Seiten, 91 Bilder, 19 Tab. 2011.
ISBN 978-3-87525-327-6.

Band 226: Peter Sebastian Feuser
Ein Ansatz zur Herstellung von pressgehärteten Karosseriekomponenten mit maßgeschneiderten mechanischen Eigenschaften: Temperierte Umformwerkzeuge. Prozessfenster, Prozesssimulation und funktionale Untersuchung
LFT, 195 Seiten, 97 Bilder, 60 Tab. 2012.
ISBN 978-3-87525-328-3.

Band 227: Murat Arbak
Material Adapted Design of Cold Forging Tools Exemplified by Powder Metallurgical Tool Steels and Ceramics
LFT, 109 Seiten, 56 Bilder, 8 Tab. 2012.
ISBN 978-3-87525-330-6.

Band 228: Indra Pitz
Beschleunigte Simulation des Laserstrahlumformens von Aluminiumblechen
LPT, 137 Seiten, 45 Bilder, 27 Tab. 2012.
ISBN 978-3-87525-333-7.

Band 229: Alexander Grimm
Prozessanalyse und -überwachung des Laserstrahlhartlötens mittels optischer Sensorik
LPT, 125 Seiten, 61 Bilder, 5 Tab. 2012.
ISBN 978-3-87525-334-4.

Band 230: Markus Kaupper
Biegen von höhenfesten Stahlblechwerkstoffen - Umformverhalten und Grenzen der Biegbarkeit
LFT, 160 Seiten, 57 Bilder, 10 Tab. 2012.
ISBN 978-3-87525-339-9.

Band 231: Thomas Kroiß
Modellbasierte Prozessauslegung für die Kaltmassivumformung unter Brücksichtigung der Werkzeug- und Pressenauffederung
LFT, 169 Seiten, 50 Bilder, 19 Tab. 2012.
ISBN 978-3-87525-341-2.

Band 232: Christian Goth
Analyse und Optimierung der Entwicklung und Zuverlässigkeit räumlicher Schaltungsträger (3D-MID)
FAPS, 176 Seiten, 102 Bilder, 22 Tab. 2012.
ISBN 978-3-87525-340-5.

Band 233: Christian Ziegler
Ganzheitliche Automatisierung mechatronischer Systeme in der Medizin am Beispiel Strahlentherapie
FAPS, 170 Seiten, 71 Bilder, 19 Tab. 2012.
ISBN 978-3-87525-342-9.

Band 234: Florian Albert
Automatisiertes Laserstrahllöten und -reparaturlöten elektronischer Baugruppen
LPT, 127 Seiten, 78 Bilder, 11 Tab. 2012.
ISBN 978-3-87525-344-3.

Band 235: Thomas Stöhr
Analyse und Beschreibung des mechanischen Werkstoffverhaltens von presshärtbaren Bor-Manganstählen
LFT, 118 Seiten, 74 Bilder, 18 Tab. 2013.
ISBN 978-3-87525-346-7.

Band 236: Christian Kägeler
Prozessdynamik beim Laserstrahlschweißen verzinkter Stahlbleche im Überlappstoß
LPT, 145 Seiten, 80 Bilder, 3 Tab. 2013.
ISBN 978-3-87525-347-4.

Band 237: Andreas Sulzberger
Seriennahe Auslegung der Prozesskette zur wärmeunterstützten Umformung von Aluminiumblechwerkstoffen
LFT, 153 Seiten, 87 Bilder, 17 Tab. 2013.
ISBN 978-3-87525-349-8.

Band 238: Simon Opel
Herstellung prozessangepasster Halbzeuge mit variabler Blechdicke durch die Anwendung von Verfahren der Blechmassivumformung
LFT, 165 Seiten, 108 Bilder, 27 Tab. 2013.
ISBN 978-3-87525-350-4.

Band 239: Rajesh Kanawade
In-vivo Monitoring of Epithelium Vessel and Capillary Density for the Application of Detection of Clinical Shock and Early Signs of Cancer Development
LPT, 124 Seiten, 58 Bilder, 15 Tab. 2013.
ISBN 978-3-87525-351-1.

Band 240: Stephan Busse
Entwicklung und Qualifizierung eines Schneidclinchverfahrens
LFT, 119 Seiten, 86 Bilder, 20 Tab. 2013.
ISBN 978-3-87525-352-8.

Band 241: Karl-Heinz Leitz
Mikro- und Nanostrukturierung mit kurz und ultrakurz gepulster Laserstrahlung
LPT, 154 Seiten, 71 Bilder, 9 Tab. 2013.
ISBN 978-3-87525-355-9.

Band 242: Markus Michl
Webbasierte Ansätze zur ganzheitlichen technischen Diagnose
FAPS, 182 Seiten, 62 Bilder, 20 Tab. 2013.
ISBN 978-3-87525-356-6.

Band 243: Vera Sturm
Einfluss von Chargenschwankungen auf die Verarbeitungsgrenzen von Stahlwerkstoffen
LFT, 113 Seiten, 58 Bilder, 9 Tab. 2013.
ISBN 978-3-87525-357-3.

Band 244: Christian Neudel
Mikrostrukturelle und mechanisch-technologische Eigenschaften widerstandspunktgeschweißter Aluminium-Stahl-Verbindungen für den Fahrzeugbau
LFT, 178 Seiten, 171 Bilder, 31 Tab. 2014.
ISBN 978-3-87525-358-0.

Band 245: Anja Neumann
Konzept zur Beherrschung der Prozessschwankungen im Presswerk
LFT, 162 Seiten, 68 Bilder, 15 Tab. 2014.
ISBN 978-3-87525-360-3.

Band 246: Ulf-Hermann Quentin
Laserbasierte Nanostrukturierung mit optisch positionierten Mikrolinsen
LPT, 137 Seiten, 89 Bilder, 6 Tab. 2014.
ISBN 978-3-87525-361-0.

Band 247: Erik Lamprecht
Der Einfluss der Fertigungsverfahren auf die Wirbelstromverluste von Stator-Einzelzahnblechpaketen für den Einsatz in Hybrid- und Elektrofahrzeugen
FAPS, 148 Seiten, 138 Bilder, 4 Tab. 2014.
ISBN 978-3-87525-362-7.

Band 248: Sebastian Rösel
Wirkmedienbasierte Umformung von Blechhalbzeugen unter Anwendung magnetorheologischer Flüssigkeiten als kombiniertes Wirk- und Dichtmedium
LFT, 148 Seiten, 61 Bilder, 12 Tab. 2014.
ISBN 978-3-87525-363-4.

Band 249: Paul Hippchen
Simulative Prognose der Geometrie indirekt pressgehärteter Karosseriebauteile für die industrielle Anwendung
LFT, 163 Seiten, 89 Bilder, 12 Tab. 2014.
ISBN 978-3-87525-364-1.

Band 250: Martin Zubeil
Versagensprognose bei der Prozesssimulation von Biegeumform- und Falzverfahren
LFT, 171 Seiten, 90 Bilder, 5 Tab. 2014.
ISBN 978-3-87525-365-8.

Band 251: Alexander Kühl
Flexible Automatisierung der Statorenmontage mit Hilfe einer universellen ambidexteren Kinematik
FAPS, 142 Seiten, 60 Bilder, 26 Tab. 2014.
ISBN 978-3-87525-367-2.

Band 252: Thomas Albrecht
Optimierte Fertigungstechnologien für Rotoren getriebeintegrierter PM-Synchronmotoren von Hybridfahrzeugen
FAPS, 198 Seiten, 130 Bilder, 38 Tab. 2014.
ISBN 978-3-87525-368-9.

Band 253: Florian Risch
Planning and Production Concepts for Contactless Power Transfer Systems for Electric Vehicles
FAPS, 185 Seiten, 125 Bilder, 13 Tab. 2014.
ISBN 978-3-87525-369-6.

Band 254: Markus Weigl
Laserstrahlschweißen von Mischverbindungen aus austenitischen und ferritischen korrosionsbeständigen Stahlwerkstoffen
LPT, 184 Seiten, 110 Bilder, 6 Tab. 2014.
ISBN 978-3-87525-370-2.

Band 255: Johannes Noneder
Beanspruchungserfassung für die Validierung von FE-Modellen zur Auslegung von Massivumformwerkzeugen
LFT, 161 Seiten, 65 Bilder, 14 Tab. 2014.
ISBN 978-3-87525-371-9.

Band 256: Andreas Reinhardt
Ressourceneffiziente Prozess- und Produktionstechnologie für flexible Schaltungsträger
FAPS, 123 Seiten, 69 Bilder, 19 Tab. 2014.
ISBN 978-3-87525-373-3.

Band 257: Tobias Schmuck
Ein Beitrag zur effizienten Gestaltung globaler Produktions- und Logistiknetzwerke mittels Simulation
FAPS, 151 Seiten, 74 Bilder. 2014.
ISBN 978-3-87525-374-0.

Band 258: Bernd Eichenhüller
Untersuchungen der Effekte und Wechselwirkungen charakteristischer Einflussgrößen auf das Umformverhalten bei Mikroumformprozessen
LFT, 127 Seiten, 29 Bilder, 9 Tab. 2014.
ISBN 978-3-87525-375-7.

Band 259: Felix Lütteke
Vielseitiges autonomes Transportsystem basierend auf Weltmodellerstellung mittels Datenfusion von Deckenkameras und Fahrzeugsensoren
FAPS, 152 Seiten, 54 Bilder, 20 Tab. 2014.
ISBN 978-3-87525-376-4.

Band 260: Martin Grüner
Hochdruck-Blechumformung mit formlos festen Stoffen als Wirkmedium
LFT, 144 Seiten, 66 Bilder, 29 Tab. 2014.
ISBN 978-3-87525-379-5.

Band 261: Christian Brock
Analyse und Regelung des Laserstrahltiefschweißprozesses durch Detektion der Metalldampffackelposition
LPT, 126 Seiten, 65 Bilder, 3 Tab. 2015.
ISBN 978-3-87525-380-1.

Band 262: Peter Vatter
Sensitivitätsanalyse des 3-Rollen-Schubbiegens auf Basis der Finite Elemente Methode
LFT, 145 Seiten, 57 Bilder, 26 Tab. 2015.
ISBN 978-3-87525-381-8.

Band 263: Florian Klämpfl
Planung von Laserbestrahlungen durch simulationsbasierte Optimierung
LPT, 169 Seiten, 78 Bilder, 32 Tab. 2015.
ISBN 978-3-87525-384-9.

Band 264: Matthias Domke
Transiente physikalische Mechanismen bei der Laserablation von dünnen Metallschichten
LPT, 133 Seiten, 43 Bilder, 3 Tab. 2015.
ISBN 978-3-87525-385-6.

Band 265: Johannes Götz
Community-basierte Optimierung des Anlagenengineerings
FAPS, 177 Seiten, 80 Bilder, 30 Tab. 2015.
ISBN 978-3-87525-386-3.

Band 266: Hung Nguyen
Qualifizierung des Potentials von Verfestigungseffekten zur Erweiterung des Umformvermögens aushärtbarer Aluminiumlegierungen
LFT, 137 Seiten, 57 Bilder, 16 Tab. 2015.
ISBN 978-3-87525-387-0.

Band 267: Andreas Kuppert
Erweiterung und Verbesserung von Versuchs- und Auswertetechniken für die Bestimmung von Grenzformänderungskurven
LFT, 138 Seiten, 82 Bilder, 2 Tab. 2015.
ISBN 978-3-87525-388-7.

Band 268: Kathleen Klaus
Erstellung eines Werkstofforientierten Fertigungsprozessfensters zur Steigerung des Formgebungsvermögens von Aluminiumlegierungen unter Anwendung einer zwischengeschalteten Wärmebehandlung
LFT, 154 Seiten, 70 Bilder, 8 Tab. 2015.
ISBN 978-3-87525-391-7.

Band 269: Thomas Svec
Untersuchungen zur Herstellung von funktionsoptimierten Bauteilen im partiellen Presshärtprozess mittels lokal unterschiedlich temperierter Werkzeuge
LFT, 166 Seiten, 87 Bilder, 15 Tab. 2015.
ISBN 978-3-87525-392-4.

Band 270: Tobias Schrader
Grundlegende Untersuchungen zur Verschleißcharakterisierung beschichteter Kaltmassivumformwerkzeuge
LFT, 164 Seiten, 55 Bilder, 11 Tab. 2015.
ISBN 978-3-87525-393-1.

Band 271: Matthäus Brela
Untersuchung von Magnetfeld-Messmethoden zur ganzheitlichen Wertschöpfungsoptimierung und Fehlerdetektion an magnetischen Aktoren
FAPS, 170 Seiten, 97 Bilder, 4 Tab. 2015.
ISBN 978-3-87525-394-8.

Band 272: Michael Wieland
Entwicklung einer Methode zur Prognose adhäsiven Verschleißes an Werkzeugen für das direkte Presshärten
LFT, 156 Seiten, 84 Bilder, 9 Tab. 2015.
ISBN 978-3-87525-395-5.

Band 273: René Schramm
Strukturierte additive Metallisierung durch kaltaktives Atmosphärendruckplasma
FAPS, 136 Seiten, 62 Bilder, 15 Tab. 2015.
ISBN 978-3-87525-396-2.

Band 274: Michael Lechner
Herstellung beanspruchungsangepasster Aluminiumblechhalbzeuge durch eine maßgeschneiderte Variation der Abkühlgeschwindigkeit nach Lösungsglühen
LFT, 136 Seiten, 62 Bilder, 15 Tab. 2015.
ISBN 978-3-87525-397-9.

Band 275: Kolja Andreas
Einfluss der Oberflächenbeschaffenheit auf das Werkzeugeinsatzverhalten beim Kaltfließpressen
LFT, 169 Seiten, 76 Bilder, 4 Tab. 2015.
ISBN 978-3-87525-398-6.

Band 276: Marcus Baum
Laser Consolidation of ITO Nanoparticles for the Generation of Thin Conductive Layers on Transparent Substrates
LPT, 158 Seiten, 75 Bilder, 3 Tab. 2015.
ISBN 978-3-87525-399-3.

Band 277: Thomas Schneider
Umformtechnische Herstellung dünnwandiger Funktionsbauteile aus Feinblech durch Verfahren der Blechmassivumformung
LFT, 188 Seiten, 95 Bilder, 7 Tab. 2015.
ISBN 978-3-87525-401-3.

Band 278: Jochen Merhof
Sematische Modellierung automatisierter Produktionssysteme zur Verbesserung der IT-Integration zwischen Anlagen-Engineering und Steuerungsebene
FAPS, 157 Seiten, 88 Bilder, 8 Tab. 2015.
ISBN 978-3-87525-402-0.

Band 279: Fabian Zöller
Erarbeitung von Grundlagen zur Abbildung des tribologischen Systems in der Umformsimulation
LFT, 126 Seiten, 51 Bilder, 3 Tab. 2016.
ISBN 978-3-87525-403-7.

Band 280: Christian Hezler
Einsatz technologischer Versuche zur Erweiterung der Versagensvorhersage bei Karosseriebauteilen aus höchstfesten Stählen
LFT, 147 Seiten, 63 Bilder, 44 Tab. 2016.
ISBN 978-3-87525-404-4.

Band 281: Jochen Bönig
Integration des Systemverhaltens von Automobil-Hochvoltleitungen in die virtuelle Absicherung durch strukturmechanische Simulation
FAPS, 177 Seiten, 107 Bilder, 17 Tab. 2016.
ISBN 978-3-87525-405-1.

Band 282: Johannes Kohl
Automatisierte Datenerfassung für diskret ereignisorientierte Simulationen in der energieflexibelen Fabrik
FAPS, 160 Seiten, 80 Bilder, 27 Tab. 2016.
ISBN 978-3-87525-406-8.

Band 283: Peter Bechtold
Mikroschockwellenumformung mittels ultrakurzer Laserpulse
LPT, 155 Seiten, 59 Bilder, 10 Tab. 2016.
ISBN 978-3-87525-407-5.

Band 284: Stefan Berger
Laserstrahlschweißen thermoplastischer Kohlenstofffaserverbundwerkstoffe mit spezifischem Zusatzdraht
LPT, 118 Seiten, 68 Bilder, 9 Tab. 2016.
ISBN 978-3-87525-408-2.

Band 285: Martin Bornschlegl
Methods-Energy Measurement - Eine Methode zur Energieplanung für Fügeverfahren im Karosseriebau
FAPS, 136 Seiten, 72 Bilder, 46 Tab. 2016.
ISBN 978-3-87525-409-9.

Band 286: Tobias Rackow
Erweiterung des Unternehmenscontrollings um die Dimension Energie
FAPS, 164 Seiten, 82 Bilder, 29 Tab. 2016.
ISBN 978-3-87525-410-5.

Band 287: Johannes Koch
Grundlegende Untersuchungen zur Herstellung zyklisch-symmetrischer Bauteile mit Nebenformelementen durch Blechmassivumformung
LFT, 125 Seiten, 49 Bilder, 17 Tab. 2016.
ISBN 978-3-87525-411-2.

Band 288: Hans Ulrich Vierzigmann
Beitrag zur Untersuchung der tribologischen Bedingungen in der Blechmassivumformung - Bereitstellung von tribologischen Modellversuchen und Realisierung von Tailored Surfaces
LFT, 174 Seiten, 102 Bilder, 34 Tab. 2016.
ISBN 978-3-87525-412-9.

Band 289: Thomas Senner
Methodik zur virtuellen Absicherung der formgebenden Operation des Nasspressprozesses von Gelege-Mehrschichtverbunden
LFT, 156 Seiten, 96 Bilder, 21 Tab. 2016.
ISBN 978-3-87525-414-3.

Band 290: Sven Kreitlein
Der grundoperationsspezifische Mindestenergiebedarf als Referenzwert zur Bewertung der Energieeffizienz in der Produktion
FAPS, 185 Seiten, 64 Bilder, 30 Tab. 2016.
ISBN 978-3-87525-415-0.

Band 291: Christian Roos
Remote-Laserstrahlschweißen verzinkter Stahlbleche in Kehlnahtgeometrie
LPT, 123 Seiten, 52 Bilder, 0 Tab. 2016.
ISBN 978-3-87525-416-7.

Band 292: Alexander Kahrimanidis
Thermisch unterstützte Umformung von Aluminiumblechen
LFT, 165 Seiten, 103 Bilder, 18 Tab. 2016.
ISBN 978-3-87525-417-4.

Band 293: Jan Tremel
Flexible Systems for Permanent Magnet Assembly and Magnetic Rotor Measurement / Flexible Systeme zur Montage von Permanentmagneten und zur Messung magnetischer Rotoren
FAPS, 152 Seiten, 91 Bilder, 12 Tab. 2016.
ISBN 978-3-87525-419-8.

Band 294: Ioannis Tsoupis
Schädigungs- und Versagensverhalten hochfester Leichtbauwerkstoffe unter Biegebeanspruchung
LFT, 176 Seiten, 51 Bilder, 6 Tab. 2017.
ISBN 978-3-87525-420-4.

Band 295: Sven Hildering
Grundlegende Untersuchungen zum Prozessverhalten von Silizium als Werkzeugwerkstoff für das Mikroscherschneiden metallischer Folien
LFT, 177 Seiten, 74 Bilder, 17 Tab. 2017.
ISBN 978-3-87525-422-8.

Band 296: Sasia Mareike Hertweck
Zeitliche Pulsformung in der Lasermikromaterialbearbeitung – Grundlegende Untersuchungen und Anwendungen
LPT, 146 Seiten, 67 Bilder, 5 Tab. 2017.
ISBN 978-3-87525-423-5.

Band 297: Paryanto
Mechatronic Simulation Approach for the Process Planning of Energy-Efficient Handling Systems
FAPS, 162 Seiten, 86 Bilder, 13 Tab. 2017.
ISBN 978-3-87525-424-2.

Band 298: Peer Stenzel
Großserientaugliche Nadelwickeltechnik für verteilte Wicklungen im Anwendungsfall der E-Traktionsantriebe
FAPS, 239 Seiten, 147 Bilder, 20 Tab. 2017.
ISBN 978-3-87525-425-9.

Band 299: Mario Lušić
Ein Vorgehensmodell zur Erstellung montageführender Werkerinformationssysteme simultan zum Produktentstehungsprozess
FAPS, 174 Seiten, 79 Bilder, 22 Tab. 2017.
ISBN 978-3-87525-426-6.

Band 300: Arnd Buschhaus
Hochpräzise adaptive Steuerung und Regelung robotergeführter Prozesse
FAPS, 202 Seiten, 96 Bilder, 4 Tab. 2017.
ISBN 978-3-87525-427-3.

Band 301: Tobias Laumer
Erzeugung von thermoplastischen Werkstoffverbunden mittels simultanem, intensitätsselektivem Laserstrahlschmelzen
LPT, 140 Seiten, 82 Bilder, 0 Tab. 2017.
ISBN 978-3-87525-428-0.

Band 302: Nora Unger
Untersuchung einer thermisch unterstützten Fertigungskette zur Herstellung umgeformter Bauteile aus der höherfesten Aluminiumlegierung EN AW-7020
LFT, 142 Seiten, 53 Bilder, 8 Tab. 2017.
ISBN 978-3-87525-429-7.

Band 303: Tommaso Stellin
Design of Manufacturing Processes for the Cold Bulk Forming of Small Metal Components from Metal Strip
LFT, 146 Seiten, 67 Bilder, 7 Tab. 2017.
ISBN 978-3-87525-430-3.

Band 304: Bassim Bachy
Experimental Investigation, Modeling, Simulation and Optimization of Molded Interconnect Devices (MID) Based on Laser Direct Structuring (LDS) / Experimentelle Untersuchung, Modellierung, Simulation und Optimierung von Molded Interconnect Devices (MID) basierend auf Laser Direktstrukturierung (LDS)
FAPS, 168 Seiten, 120 Bilder, 26 Tab. 2017.
ISBN 978-3-87525-431-0.

Band 305: Michael Spahr
Automatisierte Kontaktierungsverfahren für flachleiterbasierte Pkw-Bordnetzsysteme
FAPS, 197 Seiten, 98 Bilder, 17 Tab. 2017.
ISBN 978-3-87525-432-7.

Band 306: Sebastian Suttner
Charakterisierung und Modellierung des spannungszustandsabhängigen Werkstoffverhaltens der Magnesiumlegierung AZ31B für die numerische Prozessauslegung
LFT, 150 Seiten, 84 Bilder, 19 Tab. 2017.
ISBN 978-3-87525-433-4.

Band 307: Bhargav Potdar
A reliable methodology to deduce thermo-mechanical flow behaviour of hot stamping steels
LFT, 203 Seiten, 98 Bilder, 27 Tab. 2017.
ISBN 978-3-87525-436-5.

Band 308: Maria Löffler
Steuerung von Blechmassivumformprozessen durch maßgeschneiderte tribologische Systeme
LFT, viii u. 166 Seiten, 90 Bilder, 5 Tab.
2018. ISBN 978-3-96147-133-1.

Band 309: Martin Müller
Untersuchung des kombinierten Trenn- und Umformprozesses beim Fügen artungleicher Werkstoffe mittels Schneidclinchverfahren
LFT, xi u. 149 Seiten, 89 Bilder, 6 Tab.
2018. ISBN: 978-3-96147-135-5.

Band 310: Christopher Kästle
Qualifizierung der Kupfer-Drahtbondtechnologie für integrierte Leistungsmodule in harschen Umgebungsbedingungen
FAPS, xii u. 167 Seiten, 70 Bilder, 18 Tab.
2018. ISBN 978-3-96147-145-4.

Band 311: Daniel Vipavc
Eine Simulationsmethode für das 3-Rollen-Schubbiegen
LFT, xiii u. 121 Seiten, 56 Bilder, 17 Tab.
2018. ISBN 978-3-96147-147-8.

Band 312: Christina Ramer
Arbeitsraumüberwachung und autonome Bahnplanung für ein sicheres und flexibles Roboter-Assistenzsystem in der Fertigung
FAPS, xiv u. 188 Seiten, 57 Bilder, 9 Tab.
2018. ISBN 978-3-96147-153-9.

Band 313: Miriam Rauer
Der Einfluss von Poren auf die Zuverlässigkeit der Lötverbindungen von Hochleistungs-Leuchtdioden
FAPS, xii u. 209 Seiten, 108 Bilder, 21 Tab.
2018. ISBN 978-3-96147-157-7.

Band 314: Felix Tenner
Kamerabasierte Untersuchungen der Schmelze und Gasströmungen beim Laserstrahlschweißen verzinkter Stahlbleche
LPT, xxiii u. 184 Seiten, 94 Bilder, 7 Tab. 2018. ISBN 978-3-96147-160-7.

Band 315: Aarief Syed-Khaja
Diffusion Soldering for High-temperature Packaging of Power Electronics
FAPS, x u. 202 Seiten, 144 Bilder, 32 Tab. 2018. ISBN 978-3-87525-162-1.

Band 316: Adam Schaub
Grundlagenwissenschaftliche Untersuchung der kombinierten Prozesskette aus Umformen und Additive Fertigung
LFT, xi u. 192 Seiten, 72 Bilder, 27 Tab. 2019. ISBN 978-3-96147-166-9.

Band 317: Daniel Gröbel
Herstellung von Nebenformelementen unterschiedlicher Geometrie an Blechen mittels Fließpressverfahren der Blechmassivumformung
LFT, x u. 165 Seiten, 96 Bilder, 13 Tab. 2019. ISBN 978-3-96147-168-3.

Band 318: Philipp Hildenbrand
Entwicklung einer Methodik zur Herstellung von Tailored Blanks mit definierten Halbzeugeigenschaften durch einen Taumelprozess
LFT, ix u. 153 Seiten, 77 Bilder, 4 Tab. 2019. ISBN 978-3-96147-174-4.

Band 319: Tobias Konrad
Simulative Auslegung der Spann- und Fixierkonzepte im Karosserierohbau: Bewertung der Baugruppenmaßhaltigkeit unter Berücksichtigung schwankender Einflussgrößen
LFT, x u. 203 Seiten, 134 Bilder, 32 Tab. 2019. ISBN 978-3-96147-176-8.

Band 320: David Meinel
Architektur applikationsspezifischer Multi-Physics-Simulationskonfiguratoren am Beispiel modularer Triebzüge
FAPS, xii u. 166 Seiten, 82 Bilder, 25 Tab. 2019. ISBN 978-3-96147-184-3.

Band 321: Andrea Zimmermann
Grundlegende Untersuchungen zum Einfluss fertigungsbedingter Eigenschaften auf die Ermüdungsfestigkeit kaltmassivumgeformter Bauteile
LFT, ix u. 160 Seiten, 66 Bilder, 5 Tab. 2019. ISBN 978-3-96147-190-4.

Band 322: Christoph Amann
Simulative Prognose der Geometrie nassgepresster Karosseriebauteile aus Gelege-Mehrschichtverbunden
LFT, xvi u. 169 Seiten, 80 Bilder, 13 Tab. 2019. ISBN 978-3-96147-194-2.

Band 323: Jennifer Tenner
Realisierung schmierstofffreier Tiefziehprozesse durch maßgeschneiderte Werkzeugoberflächen
LFT, x u. 187 Seiten, 68 Bilder, 13 Tab. 2019. ISBN 978-3-96147-196-6.

Band 324: Susan Zöller
Mapping Individual Subjective Values to Product Design
KTmfk, xi u. 223 Seiten, 81 Bilder, 25 Tab. 2019. ISBN 978-3-96147-202-4.

Band 325: Stefan Lutz
Erarbeitung einer Methodik zur semiempirischen Ermittlung der Umwandlungskinetik durchhärtender Wälzlagerstähle für die Wärmebehandlungssimulation
LFT, xiv u. 189 Seiten, 75 Bilder, 32 Tab. 2019. ISBN 978-3-96147-209-3.

Band 326: Tobias Gnibl
Modellbasierte Prozesskettenabbildung rührreibgeschweißter Aluminiumhalbzeuge zur umformtechnischen Herstellung höchstfester Leichtbaustrukturteile
LFT, xii u. 167 Seiten, 68 Bilder, 17 Tab. 2019. ISBN 978-3-96147-217-8.

Band 327: Johannes Bürner
Technisch-wirtschaftliche Optionen zur Lastflexibilisierung durch intelligente elektrische Wärmespeicher
FAPS, xiv u. 233 Seiten, 89 Bilder, 27 Tab. 2019. ISBN 978-3-96147-219-2.

Band 328: Wolfgang Böhm
Verbesserung des Umformverhaltens von mehrlagigen Aluminiumblechwerkstoffen mit ultrafeinkörnigem Gefüge
LFT, ix u. 160 Seiten, 88 Bilder, 14 Tab. 2019. ISBN 978-3-96147-227-7.

Band 329: Stefan Landkammer
Grundsatzuntersuchungen, mathematische Modellierung und Ableitung einer Auslegungsmethodik für Gelenkantriebe nach dem Spinnenbeinprinzip
LFT, xii u. 200 Seiten, 83 Bilder, 13 Tab. 2019. ISBN 978-3-96147-229-1.

Band 330: Stephan Rapp
Pump-Probe-Ellipsometrie zur Messung transienter optischer Materialeigenschaften bei der Ultrakurzpuls-Lasermaterialbearbeitung
LPT, xi u. 143 Seiten, 49 Bilder, 2 Tab. 2019. ISBN 978-3-96147-235-2.

Band 331: Michael Scholz
Intralogistics Execution System mit integrierten autonomen, servicebasierten Transportentitäten
FAPS, xi u. 195 Seiten, 55 Bilder, 11 Tab. 2019. ISBN 978-3-96147-237-6.

Band 332: Eva Bogner
Strategien der Produktindividualisierung in der produzierenden Industrie im Kontext der Digitalisierung
FAPS, ix u. 201 Seiten, 55 Bilder, 28 Tab. 2019. ISBN 978-3-96147-246-8.

Band 333: Daniel Benjamin Krüger
Ein Ansatz zur CAD-integrierten muskuloskelettalen Analyse der Mensch-Maschine-Interaktion
KTmfk, x u. 217 Seiten, 102 Bilder, 7 Tab. 2019. ISBN 978-3-96147-250-5.

Band 334: Thomas Kuhn
Qualität und Zuverlässigkeit laserdirektstrukturierter mechatronisch integrierter Baugruppen (LDS-MID)
FAPS, ix u. 152 Seiten, 69 Bilder, 12 Tab. 2019. ISBN: 978-3-96147-252-9.

Band 335: Hans Fleischmann
Modellbasierte Zustands- und Prozessüberwachung auf Basis sozio-cyber-physischer Systeme
FAPS, xi u. 214 Seiten, 111 Bilder, 18 Tab.
2019. ISBN: 978-3-96147-256-7.

Band 336: Markus Michalski
Grundlegende Untersuchungen zum Prozess- und Werkstoffverhalten bei schwingungsüberlagerter Umformung
LFT, xii u. 197 Seiten, 93 Bilder, 11 Tab.
2019. ISBN: 978-3-96147-270-3.

Band 337: Markus Brandmeier
Ganzheitliches ontologiebasiertes Wissensmanagement im Umfeld der industriellen Produktion
FAPS, xi u. 255 Seiten, 77 Bilder, 33 Tab.
2020. ISBN: 978-3-96147-275-8.

Band 338: Stephan Purr
Datenerfassung für die Anwendung lernender Algorithmen bei der Herstellung von Blechformteilen
LFT, ix u. 165 Seiten, 48 Bilder, 4 Tab.
2020. ISBN: 978-3-96147-281-9.

Band 339: Christoph Kiener
Kaltfließpressen von gerad- und schrägverzahnten Zahnrädern
LFT, viii u. 151 Seiten, 81 Bilder, 3 Tab.
2020. ISBN 978-3-96147-287-1.

Band 340: Simon Spreng
Numerische, analytische und empirische Modellierung des Heißcrimpprozesses
FAPS, xix u. 204 Seiten, 91 Bilder, 27 Tab.
2020. ISBN 978-3-96147-293-2.

Band 341: Patrik Schwingenschlögl
Erarbeitung eines Prozessverständnisses zur Verbesserung der tribologischen Bedingungen beim Presshärten
LFT, x u. 177 Seiten, 81 Bilder, 8 Tab.
2020. ISBN 978-3-96147-297-0.

Band 342: Emanuela Affronti
Evaluation of failure behaviour of sheet metals
LFT, ix u. 136 Seiten, 57 Bilder, 20 Tab.
2020. ISBN 978-3-96147-303-8.

Band 343: Julia Degner
Grundlegende Untersuchungen zur Herstellung hochfester Aluminiumblechbauteile in einem kombinierten Umform- und Abschreckprozess
LFT, x u. 172 Seiten, 61 Bilder, 9 Tab.
2020. ISBN 978-3-96147-307-6.

Band 344: Maximilian Wagner
Automatische Bahnplanung für die Aufteilung von Prozessbewegungen in synchrone Werkstück- und Werkzeugbewegungen mittels Multi-Roboter-Systemen
FAPS, xxi u. 181 Seiten, 111 Bilder, 15 Tab.
2020. ISBN 978-3-96147-309-0.

Band 345: Stefan Härter
Qualifizierung des Montageprozesses hochminiaturisierter elektronischer Bauelemente
FAPS, ix u. 194 Seiten, 97 Bilder, 28 Tab.
2020. ISBN 978-3-96147-314-4.

Band 346: Toni Donhauser
Ressourcenorientierte Auftragsregelung in einer hybriden Produktion mittels betriebsbegleitender Simulation
FAPS, xix u. 242 Seiten, 97 Bilder, 17 Tab.
2020. ISBN 978-3-96147-316-8.

Band 347: Philipp Amend
Laserbasiertes Schmelzkleben von Thermoplasten mit Metallen
LPT, xv u. 154 Seiten, 67 Bilder
2020. ISBN 978-3-96147-326-7.

Band 348: Matthias Ehlert
Simulationsunterstützte funktionale Grenzlagenabsicherung
KTmfk, xvi u. 300 Seiten, 101 Bilder,
73 Tab. 2020. ISBN 978-3-96147-328-1.

Band 349: Thomas Sander
Ein Beitrag zur Charakterisierung und Auslegung des Verbundes von Kunststoffsubstraten mit harten Dünnschichten
KTmfk, xiv u. 178 Seiten, 88 Bilder, 21 Tab. 2020. ISBN 978-3-96147-330-4

Band 350: Florian Pilz
Fließpressen von Verzahnungselementen an Blechen
LFT, x u. 170 Seiten, 103Bilder, 4 Tab.
2020. ISBN 978-3-96147-332-8

Band 351: Sebastian Josef Katona
Evaluation und Aufbereitung von Produktsimulationen mittels abweichungsbehafteter Geometriemodelle
KTmfk, ix u. 147 Seiten, 73 Bilder, 11 Tab.
2020. ISBN 978-3-96147-336-6

Band 352: Jürgen Herrmann
Kumulatives Walzplattieren. Bewertung der Umformeigenschaften mehrlagiger Blechwerkstoffe der ausscheidungshärtbaren Legierung AA6014
LFT, x u. 157 Seiten, 64 Bilder, 5 Tab.
2020. ISBN 978-3-96147-344-1

Band 353: Christof Küstner
Assistenzsystem zur Unterstützung der datengetriebenen Produktentwicklung
KTmfk, xii u. 219 Seiten, 63 Bilder, 14 Tab.
2020. ISBN 978-3-96147-348-9

Band 354: Tobias Gläßel
Prozessketten zum Laserstrahlschweißen von flachleiterbasierten Formspulenwicklungen für automobile Traktionsantriebe
FAPS, xiv u. 206 Seiten, 89 Bilder, 11 Tab.
2020. ISBN 978-3-96147-356-4.

Band 355: Andreas Meinel
Experimentelle Untersuchung der Auswirkungen von Axialschwingungen auf Reibung und Verschleiß in Zylinderrollenlagern
KTmfk, xii u. 162 Seiten, 56 Bilder, 7 Tab.
2020. ISBN 978-3-96147-358-8

Band 356: Hannah Riedle
Haptische, generische Modelle weicher anatomischer Strukturen für die chirurgische Simulation
FAPS, xxx u. 179 Seiten, 82 Bilder, 35 Tab.
2020. ISBN 978-3-96147-367-0

Band 357: Maximilian Landgraf
Leistungselektronik für den Einsatz dielektrischer Elastomere in aktorischen, sensorischen und integrierten sensomotorischen Systemen
FAPS, xxiii u. 166 Seiten, 71 Bilder, 10 Tab.2020. ISBN 978-3-96147-380-9

Band 358: Alireza Esfandyari
Multi-Objective Process Optimization for Overpressure Reflow Soldering in Electronics Production
FAPS, xviii u. 175 Seiten, 57 Bilder, 23 Tab.
2020. ISBN 978-3-96147-382-3

Band 359: Christian Sand

Prozessübergreifende Analyse komplexer Montageprozessketten mittels Data Mining

FAPS, XV u. 168 Seiten, 61 Bilder, 12 Tab. 2021. ISBN 978-3-96147-398-4

Band 360: Ralf Merkl

Closed-Loop Control of a Storage-Supported Hybrid Compensation System for Improving the Power Quality in Medium Voltage Networks

FAPS, xxvii u. 200 Seiten, 102 Bilder, 2 Tab. 2021. ISBN 978-3-96147-402-8

Kurzzusammenfassung

Sowohl mit dem Betrieb von leistungselektronischen Einspeisern sowie Verbrauchern in elektrischen Netzen als auch dem Übergang zu einer elektrischen Energieerzeugung auf Basis regenerativer Kraftwerke gehen Herausforderungen für die Spannungsqualität in elektrischen Netzen einher. Daher wird im Rahmen dieser Arbeit ein Regelungskonzept einer speicherunterstützten hybriden Kompensationsanlage zur gleichzeitigen Bereitstellung verschiedener Systemdienstleistungen erarbeitet, analysiert und bewertet. Darüber hinaus wird ein Ansatz für das Energie- und Leistungsmanagement des Energiespeichersystems dieser Anlage vorgestellt. Wesentliche Themen der Untersuchung sind die Ermittlung des aktuellen Niveaus der Spannungsqualität, die Berechnung geeigneter Indikatoren der Spannungsqualität sowie die Leistungsverteilung auf die Systemdienstleistungen. Darüber hinaus werden die Speichertechnologien Redox-Flow-Batterie und Schwungmassenpeicher modellhaft umgesetzt und zu einem hybriden Speichersystem kombiniert. Für den Betrieb des Speichersystems mit maximalem Wirkungsgrad wird ein Ansatz in Abhängigkeit der Leistungswerte und Ladezustände der Speicher untersucht.

Both the operation of power electronic feeders as well as consumers in electrical grids and the transition to electricity generation based on renewable plants create challenges with regard to voltage quality in electrical grids. Therefore within this thesis a control concept of a storage supported device for the simultaneous provision of various system services is elaborated, analyzed and evaluated. Moreover, an approach for the energy and power management of the energy storage of this plant is presented. Essential topics of the examination are the determination of the present level of power quality, the derivation of suitable power quality indicators as well as the power distribution to the system services. In addition, the storage technologies redox-flow battery and flywheel storage, are implemented using models and combined into a hybrid storage system. For operation of the storage system with maximum efficiency an approach depending on the power values and state of charge values of the stores is investigated.

ISBN 978-3-96147-402-8

9 783961 474028

FAU UNIVERSITY PRESS 2021